HIGH-THROUGHPUT SYNTHESIS AND APPLICATION DEVELOPMENT OF WATER-STABLE MOFS

A Dissertation
Presented to
The Academic Faculty

by

Paul M. Schoenecker

In Partial Fulfillment
of the Requirements for the Degree
Doctorate of Philosophy in the
School of Chemical and Biomolecular Engineering

Georgia Institute of Technology
December 2012

HIGH-THROUGHPUT SYNTHESIS AND APPLICATION DEVELOPMENT OF WATER-STABLE MOFS

Approved by:

Dr. Krista S. Walton, Advisor
School of Chemical and Biomolecular Engineering
Georgia Institute of Technology

Dr. Lakeshia J. Taite
School of Chemical and Biomolecular Engineering
Georgia Institute of Technology

Dr. William J. Koros
School of Chemical and Biomolecular Engineering
Georgia Institute of Technology

Dr. Haskell W. Beckham
School of Materials Science and Engineering
Georgia Institute of Technology

Dr. Christopher W. Jones
School of Chemical and Biomolecular Engineering
Georgia Institute of Technology

Dr. Catherine Thibaud-Erkey
United Technologies Research Center
United Technologies

Date Approved: November 12, 2012

ACKNOWLEDGEMENTS

I would first like to acknowledge my advisor, Associate Professor Krista S. Walton, for all her help and for allowing me to transition to Georgia Tech. with her. The advice and opportunities that she has provided me with have forever shaped my career and life.

I would also like to thank my Georgia Tech. committee members, Drs. Lakeshia J. Taite, William J. Koros, Christopher W. Jones, and Haskell W. Beckham for their active roles in directing my research toward higher-impact areas. Dr. Catherine Thibaud-Erkey from United Technologies has been a great collaborator and always provided constructive feedback on my projects.

Outside of my committee, Dr. Ronald W. Rousseau, current School Chair, took the time out of his overbooked schedule to meet with a lowly PhD candidate and provided great encouragement and constructive criticism on my crystallizer design.

Many present Walton Group members have provided substantial help throughout my studies. Grace Belancik was the best undergraduate researcher and was great help with the batch scale-up experiments. Bogna Grabicka has been willing to help out with any experiment without hesitation. You-gui Huang has helped with multiple synthesis problems and crystallographic questions throughout my studies, including the crystal phase-change of ZIF-65 (Chapter 7). Katrina Stults collected the microscopy images presented in this work. Greg Cmarik and Himanshu Jasjuja provided great feedback on the ZIF-65 adsorption (Chapter 8). Yang Cai suggested and helped with the statistical

analysis of Chapter 6, and Mike Mangarella pulled many late night kinetic samples for my kinetic experiments.

Last but not least, I would like to thank my family starting with my wife, Lindsey, for her dedication to all my wild ideas including coming back to grad. school, my Dad for always pushing the importance of science and math education even to an unreceptive wan-a-be body builder, and my Mom and Sister for being patient listeners to all my struggles. This would not be possible without any of you.

TABLE OF CONTENTS

LIST OF TABLES

LIST OF FIGURES

LIST OF SYMBOLS AND ABBREVIATIONS

Symbols

A	Total Surface Area
b	Toth Parameter for Adsorbate-Adsorbent Interactions
c	BET Parameter
d	Lattice Spacing
E_i	Heat of Adsorption for Layer i
m	Toth Parameter for Heterogeneity
n	Integer Values
N	Rotations per Minute
N	Adsorption Loading
Ns	Monolayer Capacity
P	Pressure
P_0	Vapor Pressure
Q_{ST}	Isosteric Heat of Adsorption
R	Ideal Gas Constant
Re	Reynolds Number
$S_{i/j}$	Selectivity of Material for Component i over j
s_i	Surface Area of Layer i
T	Temperature
v	Volume Adsorbed Phase
v_m	Volume of Monolayer Adsorbed
x_i	Mole Fraction of i in Adsorbed Phase
y_i	Mole Fraction of i in Gas Phase

λ	Wavelength
μ	Viscosity
ν	Kinematic Viscosity
ρ	Density
θ	Angle of Incidence
τ	Retention Time

Abbreviations

ATPA	Amino-Terephthalic Acid
A.U.	Arbitrary Units
BET	Brunauer Emmett Teller
BTB	Benzene TriBenzoic Acid
cc	Cubic Centimeters
.cif	Crystallographic Information File
CSTR	Continuous-Stirred Tank Reactor
CUS	Coordinatively Unsaturated Site
DABCO	Di-Aza-BiCycloOctane
Ea_{Nuc}	Activation Energy of Nucleation
g	gram
h	Hour(s)
IAST	Ideal Adsorbed Solution Theory
I.D.	Inside Diameter
IGA	Intelligent Gravimetric Adsorption
IRMOF	Isoreticular Metal-Organic Framework
K	Kelvin
kJ	kilo-Joule
m	meter
MFC	Mass-Flow Controller
min	Minute(s)
mL	Milliliter
MOF	Metal-Organic Framework
mol	gram-mole

NONO	Diazeniumdiolate
NMR	Nuclear-Magnetic Resonance
O.D.	Outside Diameter
PALS	Positron-Annihilation Lifetime Spectroscopy
PFA	PerFluoroAlkoxy
PRV	Pressure Relief Valve
PSM	Post-Synthetic Modification
PTFE	PolyTetraFluoroEthylene
pXRD	Powder X-Ray Diffraction
%RH	Percent Relative Humidity
S.A.	Surface Area
SEM	Scanning Electron Microscopy
SS	Stainless Steel
TEM	Transmission Electron Microscopy
TIC	Toxic Industrial Chemicals
TT	Temperature Transducer
UTRC	United Technologies Research Center
Vol.	Volume
XRD	X-Ray Diffraction
ZIF	Zeolitic Imidazolate Framework

SUMMARY

Metal-organic frameworks (MOFs) are porous networks of metal-centers connect by organic ligands, which have potential for an array of applications including gas separations and storage, drug delivery, and molecular sensing. A multitude of structures are reported with specific pore geometries and functionalities, but MOFs are not currently implemented in consumer or industrial applications. Two major setbacks have hindered their transition to the applied level. 1) Many MOFs are not stable in the presence of ambient moisture. 2) Most syntheses are costly and take place under batch-style solvothermal conditions.

This thesis addresses both of these setbacks and examines the performance potential of water-stable MOFs for selective gas adsorption. A representative set of MOFs are exposed to water, and structural effects are monitored from a before and after comparison to identify properties of water-stable MOFs. A novel continuous-flow MOF synthesis process is reported along with preliminary optimization experiments, which yield direct suggestions for future process improvements. Batch-style scale-up experiments are also conducted for three other MOFs, which provide insight into synthesis phenomena. Application specific results are reported for toxic chemical filtration and carbon dioxide removal from flue gas using MOFs.

The thesis concludes by summarizing the experimental findings, discussing the application potential of specific MOFs, and recommending topics for future research projects. Pitfalls observed during this research are also directly discussed along with potential solutions.

CHAPTER 1

INTRODUCTION

1.1 Metal-Organic Frameworks: A Class of Porous Materials

Metal-organic frameworks (MOFs) are porous crystalline structures consisting of metal centers connected via multidentate-ligands. The term metal-organic framework is credited to Yaghi et al.,[1] and overlapping nomenclature includes porous-coordination polymers,[2,3] organic zeolite analogues,[4] hybrid organic-inorganic materials,[5] and modular porous solids.[6] Unhindered by the ongoing discrepancies in naming,[7] the development of MOFs has increased rapidly over the past two decades. In this work, all highly-ordered (crystalline) porous materials with metal-organic moieties are considered MOFs.

1.1.1 Development of MOF Structures

Over the past few decades, publication of MOF structures has grown prolifically.[8] This research has provided a fundamental understanding of the building-block approach to crystal engineering MOFs.[3,6,9] The ability to manipulate the pore space by selecting the

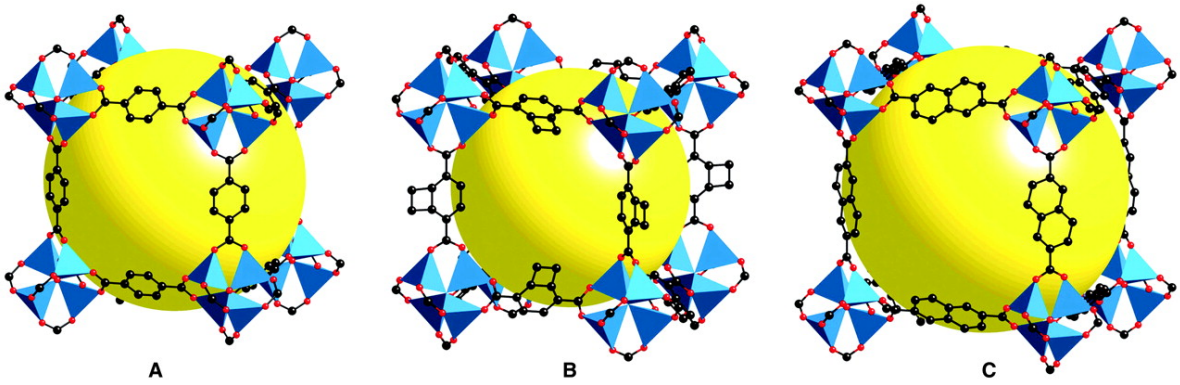

Figure 1.1. MOF-5 (A), IRMOF-6 (B), and IRMOF-8 (C) from Rosi et al.[9]

organic constituent for length and/or functionality (Figure 1.1) is shown in the isoreticular MOFs (IRMOFs)[10-13] and paves the way for future MOF crystal engineering. This approach utilizes a known coordination environment with multiple ligands to synthesize a family of MOFs and increase the rate of MOF structure development. Other applications of this approach include the zeolitic imidazolate frameworks (ZIFs)[14] and the UiO materials from the University of Oslo.[15,16]

Synthesizing isostructural MOFs with differing metal-centers also added to the proliferation of published MOF structures. Many of the aforementioned ZIF materials have been synthesized as zinc or cobalt-containing materials,[14] which simply bifurcates the structural possibilities. However, other MOFs are reported with a multitude of metal-centers e.g. MOF-74 or CPO-27 with Mg,[17] Zn,[9] Co,[18] and Ni.[19]

With many MOF structures reported, the value of particular functional-sites within the materials becomes apparent. MOFs containing open-metal sites or coordinatively unsaturated metal sites (CUSs) include HKUST-1[20] or CuBTC and MOF-74.[9] These unsaturated metal-centers possess Lewis-acid functionality and lead to some of the most attractive MOF structures from an application perspective. Other functionalities including amino,[21] bromo,[16] and methyl[22] have been introduced to MOFs by selecting modified ligands.

In addition to directly introducing functional groups during synthesis, post-synthetic modification (PSM) is shown to provide another avenue for engineering a MOF structure. PSM can be accomplished by using existing functional groups as reactive sites for gas or liquid-phase reactions. Examples of this include using CUSs to facilitate 'grafting' of diamines[23] and gas-phase reactions with 4-methyl amino-pyridine[24] or using amine-

functionalized MOFs to support anhydride substitution[21,25,26] and diazeniumdiolate[27] formation. Another recently reported PSM method is ligand-exchange, which does not rely on functionalized structures and makes use of the dynamic nature of MOF structures. This technique permits modification of an existing MOF without changing the overall structure, providing another method for incorporating the desired functionality.[28]

1.1.2 Water Stability

Despite the multitude of MOF structures available, many degrade in the presence of water,[29-33] and water stability is often considered a major weakness of MOFs. Structures formed via zinc-carboxylate bonding often exhibit such degradation (e.g. MOF-5, MOF-177,[34] and DMOF-1[35]), which is attributed to the relatively weak coordination bond-strength. However, other sources of water sensitivity are not as clear-cut. The presence of oxygen seems to play an integral role in the degradation of CUS-containing MOFs. Three analogues of MOF-74/CPO-27/M-DOBDC (Ni, Mg, and Co) show cyclic water vapor adsorption stability with inert carrier gases,[17,36,37] but exposure to humid air is shown to degrade the Ni[37] and Mg[35] forms of MOF-74 as well as another CUS-containing MOF, HKUST-1 or CuBTC.[35,38]

$$\text{M-L} + \text{H}_2\text{O} \rightarrow \text{M-(OH}_2\text{)}\cdots\text{L} \qquad (1.1)$$

$$\text{M-L} + \text{H}_2\text{O} \rightarrow \text{M-(OH)} + \text{LH} \qquad (1.2)$$

A firm understanding of the mechanism for hydration-induced MOF degradation is not available and is likely not identical for all MOF structures. UOP proposes two mechanisms for the degradation of MOFs in the presence of water, a ligand-displacement reaction (Eq. 1.1) and a hydrolysis reaction (Eq. 1.2).[39] Their study combines

experimental exposure of MOFs to saturated steam and modeling of the metal-oxide clusters to predict water stability. Born-Oppenheimer simulations are also used to model the degradation of IRMOF-1 and theoretical analogues with Mg and Be metal centers.[40] In addition to modeling of the coordination environment, interesting experimental techniques are also available to probe the pore-space and provide further insight. Matzger et al. utilize positron annihilation lifetime spectroscopy (PALS) to directly probe the MOF pore-space and provide insight into which pores have collapsed.[41]

Despite the lack of a unified theory on the hydration-induced decomposition mechanism, general trends have emerged for designing water-stable MOFs. In general, the metal-oxide coordination environment plays a significant role in water stability.[39,40] Higher pKa or more basic ligands tend to produce more water-stable MOFs. Pyrazolate[42] and imidazolate-based[14] MOFs exemplify this trend by demonstrating stability not only in humid air but also when immersed in harsh chemicals. More highly coordinated metal-centers also provide a more robust structure capable of withstanding exposure to moisture e.g. the UiO-66 materials[15,35] as well as several of the MIL materials.[38,43,44] Effect of the metal-centers on water stability was examined by LeVan et al., who report that, following steam conditioning, CO_2 adsorption of MOF-74 analogues tends to decrease more for MOFs with lower reduction potential metal-centers.[45] This trend is attributed to an increased affinity for polar molecules, which may occupy the CUSs. However, the influence on water stability likely follows a similar trend itself due to coupling of the water adsorption and stability of MOF-74. With many trends of MOF stability identified and stable structures developed, immediate preclusion of MOFs from humid environment applications is no longer a viable argument.

1.2 Potential Application of MOFs

With a semi-infinite set of plausible materials, and water-stable MOFs now reported, the application potential of MOFs is expansive. MOFs show high potential for selective gas adsorption due to the ability to tailor attributes including pore size,[10] functional groups,[21,46] and CUSs.[47] Larger pore MOFs are capable of providing record-high surface areas, which are of specific importance for gas storage applications.[48,49] CUS-containing MOFs and others with functionalized pore space are beneficial for selective adsorption and also promising for targeted drug delivery[50,51] and catalysis.[52-54] Other potential applications for MOFs include imaging enhancement,[51,55] sensor applications,[56] and membrane filtration.[56-59]

1.3 MOF Synthesis

In general, MOFs are synthesized by introducing a metal source and one or more ligands to a given system, providing energy to overcome an activation energy associated with nucleation, and allowing the materials to self assemble. Most early syntheses followed standard solvothermal techniques, and more recent focus has shifted to novel techniques that reduce synthesis times and environmental impact.

1.3.1 Conventional Synthesis Techniques

Typical lab-scale MOF syntheses take place solvothermally, which involves dissolving the metal-precursor and organic ligand(s) in a solvent or mixture of solvents, placing the solution in a sealed vessel, and heating to ca. 373-523K inside a convection oven for 1-6 days.[14,15] Polytetrafluoroethylene (PTFE)-lined acid digestions bombs are the most

common vessels,[60] but borosilicate glass vials are also frequently used for lower temperature syntheses. Often, an array of trials with different solvents and reactant concentrations is required in order to produce a new MOF. So, automated high throughput setups consisting of trays with micro-volume cavities are also implemented by groups focused on developing new structures.[61]

1.3.2 Non-Conventional Synthesis Techniques

Non-conventional synthesis techniques exist to address multiple aspects of MOF syntheses. To decrease the reaction time, microwave-assisted synthesis techniques are often implemented. Microwave irradiation more efficiently transfers energy to the reactant mixture via rotation of molecules possessing dielectric moments (e.g. H_2O)[62] and drastically reduces induction and synthesis times. Synthesis temperatures are typically on the same order as conventional heating, but times are usually 2 h or less.[62] Ni et al. report one of the fastest MOF synthesis times of 5 seconds in their patent.[63] Structures reportedly synthesized via microwave techniques include aluminum-based CAU-1 materials,[64] the zirconium based UiO-66 materials (Appendix A), IRMOFs-1,2, and 3;[63] CuBTC,[65] and Cr MIL-101.[66] In addition to reduced synthesis times, smaller particles are often reported with potential benefits for sensing applications. However, the rapid growth and nucleation can lead to higher amounts of crystal defects and lower internal surface areas.

Other MOF synthesis techniques exist to address specific goals. To alleviate safety concerns associated with large volumes of nitrate-containing organic solutions, BASF implements an electrochemical technique, which uses a metal electrode to provide metal-ions to a solution containing organic ligands.[67,68] The resultant MOF crystals form on the

electrode itself and are rinsed away with a recirculation pump. BASF also uses a 'solvent-free' synthesis technique,[69] which addresses a prominent environmental concern and cost of most MOF syntheses by forming the MOF directly in a liquid-ligand solution. Another method to reduce solvent use is the mechano-chemical synthesis technique, [70,71] which entails applying a mechanical force to the solid reactants with minimal solvent present. The development of non-conventional synthesis techniques is vital to the transition of MOFs from lab-scale research to industrial and consumer applications.

1.4 Overview of This Dissertation

The following work describes the development of MOFs for selective adsorption applications. Chapter 3 describes the synthesis of four materials UMCM-1-NH_2-COOH, Mg MOF-74, DMOF-1-NH_2, and UiO-66-NH_2 and subsequent testing for toxic industrial chemical (TIC) filtration. Structures are confirmed via pXRD and BET modeling of N_2 adsorption at 77 K. The functionalized UMCM-1 material is not successfully synthesized in the quantities required for filtration testing. The remaining materials are examined via breakthrough testing with select TICs and compared to commercially available adsorbents. The amine-functionalized MOFs show the best performance improvements for multiple TICs including NH_3 and CH_2O.

Chapter 4 is taken directly from a peer-reviewed article on the water stability of MOFs. Seven MOFs are selected and synthesized via previously published procedures; HKUST-1, Mg MOF-74, UMCM-1, DMOF-1(-NH_2), and UiO-66(-NH_2). Water adsorption isotherms are collected for each material, the samples are reactivated, and structure retention from before and after this treatment is examined. Crystal phase transformation is examined via pXRD comparison, and porosity retention is examined via BET modeling of N_2 adsorption at 77 K. The MOFs containing CUSs appear to lose significant porosity despite pXRD agreement. The Zn-carboxylate bound materials,

UMCM-1, DMOF-1, and DMOF-1-NH_2 display complete structure loss throughout the water adsorption cycle. The only materials showing practically no structure change throughout the process are the highly-coordinated UiO-66 and amine-functionalized analogue.

Following the water stability and TIC filtration performance of UiO-66-NH_2, scale-up synthesis is investigated and reported in Chapter 5 from another peer reviewed article. Batch style syntheses are examined to probe the use of PTFE or glass vessel materials and geometries. The mass-yield of MOF is directly proportional to the volume of reactant solution and independent of the wetted surface area to volume ratio. To understand the kinetics of the synthesis intermittent samples are collected at three temperatures (373, 383, and 393 K), and relative yields are compared. The maximum observed yield is obtained at 1/3 of the originally published synthesis time and all samples are confirmed to be of uniform crystal phase via pXRD, which leads to the development of a novel flow-through synthesis process. A proof-of-concept trial is completed and provisional patent application is filed on said process.

The batch-style scale-up MOF synthesis experiments developed for UiO-66-NH_2 are applied to three MOFs with specific application potential; Mg MOF-74, ZIF-65, and MIL-125-NH_2 and reported in Chapter 6. Hypotheses linking the water-stability and structure properties to the scale-up and kinetics behavior are sought. Mg MOF-74, which exhibits very hydrophilic adsorption character, also appears to prefer more hydrophilic synthesis vessel materials. ZIF-65 exhibits interesting kinetic behavior with yield reaching a local maximum and then asymptotically decreasing, which is indicative of instability under synthesis conditions. MIL-125-NH_2 scales-up similarly to UiO-66-NH_2, which is a nearly analogous structure.

Preliminary optimization of the flow-through synthesis process is reported in Chapter 7. The input variables for the optimization include number of impellers (1 or 2), agitation direction (up or down), and the use of the aforementioned draft-tube baffle. The main

figures of merit are mass-based yield, crystallinity, and porosity, which are examined via analytical weighing, pXRD, and BET modeling of N_2 adsorption at 77 K, respectively. The use of the current draft tube appears to stifle the mixing in the reactor and significantly reduce the yield. Using multiple impellers promotes better product crystallinity and BET surface area. The low outlet velocity is the apparent source of product stream plugging, which is difficult to mitigate given the current reactor design. However, suggestions for further revisions of the process are provided.

The pore size and functionality of ZIF-65 provides high potential for CO_2/N_2 separations, which are examined in Chapter 8. Single component isotherms for each analyte gas are collected from 0-20 bar at 298, 308, and 318 K. Isosteric heats of adsorption are predicted as a function of loading by using the experimental isotherms and the Clausius-Clapyeron equation. The ideal adsorbed solution theory (IAST) is used to predict mixture adsorption behavior, and the selectivity of CO_2 over N_2 is found to be sufficiently high for applications such as flue gas filtration. The water stability of ZIF-65 is examined using the procedure described in Chapter 4. Although the material appears very hydrophobic, which is advantageous for many applications, the crystallinity and porosity appear to change during water exposure and may preclude ZIF-65 from target applications.

Chapter 9 outlines conclusions from specific studies presented in this work and MOF research as a whole. Topics include TIC adsorption, water stability, and synthesis scale-up for MOFs. Suggestions for further work and potential pitfalls of MOFs and MOF synthesis scale-up are provided.

1.5 References

1. Yaghi OM, Li HL. Hydrothermal synthesis of a metal-organic framework containing large rectangular channels. *Journal of the American Chemical Society.* Oct 18 1995;117(41):10401-10402.

2. Moulton B, Zaworotko MJ. Coordination polymers: toward functional transition metal sustained materials and supermolecules. *Current Opinion in Solid State & Materials Science.* Apr 2002;6(2):117-123.

3. Kitagawa S, Kondo M. Functional micropore chemistry of crystalline metal complex-assembled compounds. *Bull. Chem. Soc. Jpn.* Aug 1998;71(8):1739-1753.

4. Aoyama Y. Functional organic zeolite analogues. *Design of Organic Solids.* 1998;198:131-161.

5. Rowsell JLC, Yaghi OM. Metal-organic frameworks: a new class of porous materials. *Microporous Mesoporous Mat.* Aug 2004;73(1-2):3-14.

6. Yaghi OM, Li HL, Davis C, Richardson D, Groy TL. Synthetic strategies, structure patterns, and emerging properties in the chemistry of modular porous solids. *Accounts of Chemical Research.* Aug 1998;31(8):474-484.

7. Batten SR, Champness NR, Chen XM, et al. Coordination polymers, metal-organic frameworks and the need for terminology guidelines. *Crystengcomm.* 2012;14(9):3001-3004.

8. Zhou HC, Long JR, Yaghi OM. Introduction to Metal-Organic Frameworks. *Chem. Rev.* Feb 2012;112(2):673-674.

9. Rosi NL, Kim J, Eddaoudi M, Chen BL, O'Keeffe M, Yaghi OM. Rod packings and metal-organic frameworks constructed from rod-shaped secondary building units. *Journal of the American Chemical Society.* Feb 2005;127(5):1504-1518.

10. Eddaoudi M, Li HL, Yaghi OM. Highly porous and stable metal-organic frameworks: Structure design and sorption properties. *Journal of the American Chemical Society.* Feb 23 2000;122(7):1391-1397.

11. Eddaoudi M, Moler DB, Li HL, et al. Modular chemistry: Secondary building units as a basis for the design of highly porous and robust metal-organic carboxylate frameworks. *Accounts of Chemical Research.* Apr 2001;34(4):319-330.

12. Eddaoudi M, Kim J, Rosi N, et al. Systematic design of pore size and functionality in isoreticular MOFs and their application in methane storage. *Science.* Jan 18 2002;295(5554):469-472.

13. Rowsell JLC, Millward AR, Park KS, Yaghi OM. Hydrogen sorption in functionalized metal-organic frameworks. *Journal of the American Chemical Society.* May 2004;126(18):5666-5667.

14. Park KS, Ni Z, Cote AP, et al. Exceptional chemical and thermal stability of zeolitic imidazolate frameworks. *Proc. Natl. Acad. Sci. U. S. A.* Jul 2006;103(27):10186-10191.

15. Cavka JH, Jakobsen S, Olsbye U, et al. A new zirconium inorganic building brick forming metal organic frameworks with exceptional stability. *Journal of the American Chemical Society.* Oct 2008;130(42):13850-13851.

16. Garibay SJ, Cohen SM. Isoreticular synthesis and modification of frameworks with the UiO-66 topology. *Chem. Commun.* 2010;46(41):7700-7702.

17. Dietzel PDC, Blom R, Fjellvag H. Base-induced formation of two magnesium metal-organic framework compounds with a bifunctional tetratopic ligand. *European Journal of Inorganic Chemistry.* Aug 2008(23):3624-3632.

18. Dietzel PDC, Johnsen RE, Blom R, Fjellvag H. Structural changes and coordinatively unsaturated metal atoms on dehydration of honeycomb analogous microporous metal-organic frameworks. *Chem.-Eur. J.* 2008;14(8):2389-2397.

19. Bonino F, Chavan S, Vitillo JG, et al. Local structure of CPO-27-Ni metallorganic framework upon dehydration and coordination of NO. *Chem. Mat.* Aug 2008;20(15):4957-4968.

20. Chui SSY, Lo SMF, Charmant JPH, Orpen AG, Williams ID. A chemically functionalizable nanoporous material Cu-3(TMA)(2)(H2O)(3) (n). *Science.* Feb 1999;283(5405):1148-1150.

21. Garibay SJ, Wang ZQ, Tanabe KK, Cohen SM. Postsynthetic Modification: A Versatile Approach Toward Multifunctional Metal-Organic Frameworks. *Inorganic Chemistry.* Aug 2009;48(15):7341-7349.

22. Cai Y, Zhang YD, Huang YG, Marder SR, Walton KS. Impact of Alkyl-Functionalized BTC on Properties of Copper-Based Metal-Organic Frameworks. *Cryst. Growth Des.* Jul 2012;12(7):3709-3713.

23. Hwang YK, Hong DY, Chang JS, et al. Amine grafting on coordinatively unsaturated metal centers of MOFs: Consequences for catalysis and metal encapsulation. *Angew. Chem.-Int. Edit.* 2008;47(22):4144-4148.

24. Ingleson MJ, Heck R, Gould JA, Rosseinsky MJ. Nitric Oxide Chemisorption in a Postsynthetically Modified Metal-Organic Framework. *Inorganic Chemistry.* Nov 2009;48(21):9986-9988.

25. Wang ZQ, Tanabe KK, Cohen SM. Accessing Postsynthetic Modification in a Series of Metal-Organic Frameworks and the Influence of Framework Topology on Reactivity. *Inorganic Chemistry.* Jan 2009;48(1):296-306.

26. Roy P, Schaate A, Behrens P, Godt A. Post-Synthetic Modification of Zr-Metal-Organic Frameworks through Cycloaddition Reactions. *Chem.-Eur. J.* May 2012;18(22):6979-6985.

27. Nguyen JG, Tanabe KK, Cohen SM. Postsynthetic diazeniumdiolate formation and NO release from MOFs. *Crystengcomm.* 2010;12(8):2335-2338.

28. Kim M, Cahill JF, Su YX, Prather KA, Cohen SM. Postsynthetic ligand exchange as a route to functionalization of 'inert' metal-organic frameworks. *Chem. Sci.* 2012;3(1):126-130.

29. Huang LM, Wang HT, Chen JX, et al. Synthesis, morphology control, and properties of porous metal-organic coordination polymers. *Microporous Mesoporous Mat.* Mar 2003;58(2):105-114.

30. Greathouse JA, Allendorf MD. The interaction of water with MOF-5 simulated by molecular dynamics. *Journal of the American Chemical Society.* Aug 2006;128(33):10678-10679.

31. Kaye SS, Dailly A, Yaghi OM, Long JR. Impact of preparation and handling on the hydrogen storage properties of Zn4O(1,4-benzenedicarboxylate)(3) (MOF-5). *Journal of the American Chemical Society.* Nov 2007;129(46):14176-+.

32. Wu TJ, Shen LJ, Luebbers M, et al. Enhancing the stability of metal-organic frameworks in humid air by incorporating water repellent functional groups. *Chem. Commun.* 2010;46(33):6120-6122.

33. Hausdorf S, Wagler J, Mossig R, Mertens F. Proton and water activity-controlled structure formation in zinc carboxylate-based metal organic frameworks. *Journal of Physical Chemistry A.* Aug 2008;112(33):7567-7576.

34. Cychosz KA, Matzger, Adam J. Water Stability of Microporous Coordination Polymers and the Adsorption of Pharmaceuticals from Water. *Langmuir.* August 13, 2010 2010;26(22):17198-17202.

35. Schoenecker PM, Carson CG, Jasjuja H, Flemming CJJ, Walton KS. Effect of Water Adsorption on Retention of Structure and Surface Area of Metal-Organic Frameworks *Ind. Eng. Chem. Res.* 2012.

36. Dietzel PDC, Morita Y, Blom R, Fjellvag H. An in situ high-temperature single-crystal investigation of a dehydrated metal-organic framework compound and field-induced magnetization of one-dimensional metaloxygen chains. *Angew. Chem.-Int. Edit.* 2005;44(39):6354-6358.

37. Dietzel PDC, Panella B, Hirscher M, Blom R, Fjellvag H. Hydrogen adsorption in a nickel based coordination polymer with open metal sites in the cylindrical cavities of the desolvated framework. *Chem. Commun.* 2006(9):959-961.

38. Kusgens P, Rose M, Senkovska I, et al. Characterization of metal-organic frameworks by water adsorption. *Microporous Mesoporous Mat.* Apr 2009;120(3):325-330.

39. Low JJ, Benin AI, Jakubczak P, Abrahamian JF, Faheem SA, Willis RR. Virtual High Throughput Screening Confirmed Experimentally: Porous Coordination Polymer Hydration. *Journal of the American Chemical Society.* Nov 2009;131(43):15834-15842.

40. Bellarosa L, Calero S, Lopez N. Early stages in the degradation of metal-organic frameworks in liquid water from first-principles molecular dynamics. *Phys. Chem. Chem. Phys.* 2012;14(20):7240-7245.

41. Liu M, Wong-Foy AG, Vallery RS, et al. Evolution of Nanoscale Pore Structure in Coordination Polymers During Thermal and Chemical Exposure Revealed by Positron Annihilation. *Adv. Mater.* Apr 2010;22(14):1598-+.

42. Choi HJ, Dinca M, Dailly A, Long JR. Hydrogen storage in water-stable metal-organic frameworks incorporating 1,3-and 1,4-benzenedipyrazolate. *Energy Environ. Sci.* 2010;3(1):117-123.

43. Ehrenmann J, Henninger SK, Janiak C. Water Adsorption Characteristics of MIL-101 for Heat-Transformation Applications of MOFs. *European Journal of Inorganic Chemistry.* Feb 2011(4):471-474.

44. Akiyama G, Matsuda R, Kitagawa S. Highly Porous and Stable Coordination Polymers as Water Sorption Materials. *Chemistry Letters.* Apr 2010;39(4):360-361.

45. Liu J, Benin AI, Furtado AMB, Jakubczak P, Willis RR, LeVan MD. Stability Effects on CO(2) Adsorption for the DOBDC Series of Metal-Organic Frameworks. *Langmuir.* Sep 2011;27(18):11451-11456.

46. Magee RW. Evaluation of the external surface-area of carbon-black by nitrogen adsorption. *Rubber Chemistry and Technology.* Sep-Oct 1995;68(4):590-600.

47. T.Grant Glover GWP, Bryan J. Schindler, David, Brittand OY. 'MOF-74 building unit has a direct impact on toxic gas adsorption'
Chem. Eng. Sci. 3 October 2010 2010.

48. Morris RE, Wheatley PS. Gas storage in nanoporous materials. *Angew. Chem.-Int. Edit.* 2008;47(27):4966-4981.

49. Mu B, Schoenecker PM, Walton KS. Gas Adsorption Study on Mesoporous Metal-Organic Framework UMCM-1. *Journal of Physical Chemistry C.* Apr 2010;114(14):6464-6471.

50. Horcajada P, Gref R, Baati T, et al. Metal-Organic Frameworks in Biomedicine. *Chem. Rev.* Feb 2012;112(2):1232-1268.

51. Keskin S, Kizilel S. Biomedical Applications of Metal Organic Frameworks. *Ind. Eng. Chem. Res.* Feb 2011;50(4):1799-1812.

52. Opelt S, Krug V, Sonntag J, Hunger M, Klemm E. Investigations on stability and reusability of Pd(2-pymo)(2) (n) as hydrogenation catalyst. *Microporous Mesoporous Mat.* Jan 2012;147(1):327-333.

53. Wang C, Xie ZG, deKrafft KE, Lin WL. Doping Metal-Organic Frameworks for Water Oxidation, Carbon Dioxide Reduction, and Organic Photocatalysis. *Journal of the American Chemical Society.* Aug 2011;133(34):13445-13454.

54. Babu KF, Kulandainathan MA, Katsounaros I, et al. Electrocatalytic activity of Basolite (TM) F300 metal-organic-framework structures. *Electrochem. Commun.* May 2010;12(5):632-635.

55. Horcajada P, Chalati T, Serre C, et al. Porous metal-organic-framework nanoscale carriers as a potential platform for drug delivery and imaging. *Nature Materials.* Feb 2010;9(2):172-178.

56. Shekhah O, Liu J, Fischer RA, Woll C. MOF thin films: existing and future applications. *Chem. Soc. Rev.* 2011;40(2):1081-1106.

57. Thompson JA, Chapman KW, Koros WJ, Jones CW, Nair S. Sonication-induced Ostwald ripening of ZIF-8 nanoparticles and formation of ZIF-8/polymer composite membranes. *Microporous Mesoporous Mat.* Aug 2012;158:292-299.

58. Yoo Y, Varela-Guerrero V, Jeong HK. Isoreticular Metal-Organic Frameworks and Their Membranes with Enhanced Crack Resistance and Moisture Stability by Surfactant-Assisted Drying. *Langmuir.* Mar 2011;27(6):2652-2657.

59. Liu YY, Hu EP, Khan EA, Lai ZP. Synthesis and characterization of ZIF-69 membranes and separation for CO2/CO mixture. *Journal of Membrane Science.* May 2010;353(1-2):36-40.

60. Parr. Acid Digestion http://www.parrinst.com/products/sample-preparation/acid-digestion/. Accessed August 25th, 2012.

61. Banerjee R, Phan A, Wang B, et al. High-throughput synthesis of zeolitic imidazolate frameworks and application to CO2 capture. *Science.* Feb 2008;319(5865):939-943.

62. Klinowski J, Paz FAA, Silva P, Rocha J. Microwave-Assisted Synthesis of Metal-Organic Frameworks. *Dalton Trans.* 2011;40(2):321-330.

63. Ni Z, Masel RI. Rapid Metal Organic Framework Molecule Synthesis Method. *United States Patent Application Publication.* 2009;11/785,102.

64. Ahnfeldt T, Stock N. Synthesis of isoreticular CAU-1 compounds: effects of linker and heating methods on the kinetics of the synthesis. *Crystengcomm.* 2012;14(2):505-511.

65. Seo YK, Hundal G, Jang IT, Hwang YK, Jun CH, Chang JS. Microwave synthesis of hybrid inorganic-organic materials including porous Cu-3(BTC)(2) from Cu(II)-trimesate mixture. *Microporous Mesoporous Mat.* Mar 2009;119(1-3):331-337.

66. Jhung SH, Lee JH, Yoon JW, Serre C, Ferey G, Chang JS. Microwave synthesis of chromium terephthalate MIL-101 and its benzene sorption ability. *Adv. Mater.* Jan 2007;19(1):121-+.

67. Ulrich Muller, Hermann Putter, Michael Hesse, et al. Method for Electrochemical Production of a Crystalline Porous Metal Organic Skeleton Material. *United States Patent Application Publication.* 2004;10/580,407.

68. Mueller U, Schubert M, Teich F, Puetter H, Schierle-Arndt K, Pastre J. Metal-organic frameworks - prospective industrial applications. *J. Mater. Chem.* Feb 2006;16(7):626-636.

69. Leung E, Muller U, Cox G. Solvent-Free Preparation of Magnesium Formate-Based Porous Metal-Organic Framework. *United States Patent Application Publication.* 2012;US 2012/0016160 A1.

70. Yang HW, Orefuwa S, Goudy A. Study of mechanochemical synthesis in the formation of the metal-organic framework Cu(3)(BTC)(2) for hydrogen storage. *Microporous Mesoporous Mat.* Aug 2011;143(1):37-45.

71. James SL, Adams CJ, Bolm C, et al. Mechanochemistry: opportunities for new and cleaner synthesis. *Chem. Soc. Rev.* 2012;41(1):413-447.

CHAPTER 2
EXPERIMENTAL METHODS AND MATERIALS

2.1 Characterization Methods

2.1.1 Optical Techniques

Multiple optical techniques were implemented to examine the crystal size and lattice structure of the synthesized MOFs. Powder X-ray diffractograms were collected and directly compared to previously published results to confirm crystal structure congruency. Microscopy techniques were used to examine the crystal morphology and size distributions.

2.1.1.1 Powder X-Ray Diffraction

Powder X-ray diffraction (pXRD) experiments were conducted using an X'Pert Pro PANalytical X-Ray Diffractometer.[1] All scans were aquired with both the source and detector scanning at θ° to the sample pan. An X'Celerator detector was used to provide faster scan rates without sacrificing data refinement via Real Time Multiple Strip

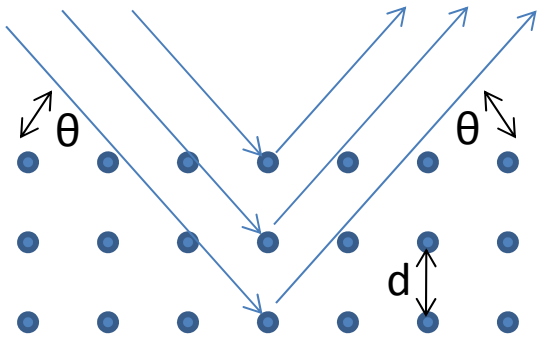

Figure 2. 1. Illustration of Bragg's Law reproduced from Skoog et al.[3]

technology.[2] Analysis of the XRD data comparison for crystal-structures is governed by the Bragg's Equation (Eq. 1),[4] which describes the relationship between the angles at which diffracted X-rays constructively interfere and the lattice spacing of the crystal structure, *d*, and is illustrated in Figure 2.1.

$$n\lambda = 2\mathrm{d}\sin(\theta) \qquad (1)^4$$

The remaining variables include *n*, which represents integer values; λ, which is the wavelength of the incident radiation; and θ, which is the angle of incidence. At all other angles, the diffracted radiation destructively interferes, which provides specific information about the lattice parameters. Throughout this work, pXRD diffractograms are collected and peak positions are compared with published data for the MOF structure or an isostructural material.

2.1.1.2 Scanning Electron Microscopy

The Hitachi S-800 Field Emission Gun Scanning Electron Microscope (SEM) available from *Georgia Tech's Center for Nanostructure Characterization* was used to examine crystallite morphology, thin film growth and approximate crystallite size. All samples were considered non-conducting and therefore sputter-coated with Au prior to SEM analysis.

2.1.2 Adsorption Testing

Characterizing porous media by adsorption behavior provided a deeper understanding of multiple material attributes. Specific surface area and pore volume were examined via modeling of nitrogen (N_2) adsorption isotherms at 77 K. Single component gas isotherms

provided insight into application-specific performance and were used to predict mixture adsorption behavior. Water vapor adsorption was also beneficial for examining application performance in the presence of humidity, especially with MOFs, which may degrade in humid conditions.[5-8]

2.1.2.1 Nitrogen Adsorption at 77 K

Nitrogen adsorption measurements at 77 K were performed using a QUADRASORB™ SI volumetric analyzer manufactured by Quantachrome Instruments.[9] Adsorption isotherms were collected over the range of relative pressures from 10^{-6} to 0.995 using ultra high purity nitrogen from Airgas, and the amount adsorbed was determined as a function of the equilibrium pressure. Prior to each adsorption measurement, the sample was outgassed via a FloVac Degasser under elevated temperatures, typically 423-523 K, and under dynamic vacuum of <0.1 torr. Then, the mass of the activated sample was recorded and used for normalization of the uptake.

With highly-ordered structures, such as MOFs, weight normalized surface areas [=] m^2/g were the main attribute examined via N_2 adsorption at 77 K. The modelling technique utilized for surface area prediction was the Brunauer Emmett Teller (BET) method,[10] which was developed for modelling of multilayer adsorption of gases at temperatures near their condensation points and is more appropriate for MOFs than the Langmuir method, which was developed for solely monolayer adsorption modelling and will typically overestimate the available surface area of MOFs.[10] Reproducibility of BET surface areas for the aforementioned instrument and experimental technique was predicted to be conservatively within 5% absolute error.

BET Method and Applicability to MOFs

The following is a summary of the originally described BET method, taken directly from Brunauer et al., and used to characterize MOFs throughout this work:[10]

For multilayer adsorption, the surface area of the material is defined as;

$$A = \sum_{i=0}^{\infty} s_i \qquad (2)$$

With *A* being the total surface area of the material, *i* representing the layer of the adsorbed phase, and s_i the surface area of layer *i*. Assuming that only the first layer of adsorbate molecules interact with the adsorbent surface, all other layers only interact homogeneously.

$$E_2 = E_3 = \cdots E_i = E_L \qquad (3)$$

E_i represents the heat of adsorption of the layer *i*, and E_L is the heat of liquefaction for the adsorbate. Therefore, E_1 is the only heat of adsorption dependent upon the material-adsorbate interaction. Further derivation of the relationships between the relative pressure of the system (p/p_o), volume of adsorbed phase (v), volume of the adsorbed monolayer (v_m), and surface area of each adsorbed layer results in the following equation:

$$\frac{p}{v(p_o - p)} = \frac{1}{v_m c} + \frac{c-1}{v_m c}\frac{p}{p_o} \qquad (4)$$

Equation (4) is fit to experimental data by plotting $p/(v(p_o-p))$ versus p/p_o. The linear plot should have a positive y-intercept equal to $(1/v_m c)$, which must be positive to accurately utilize the model.

MOF-specific use of the BET method for modelling surface area has been addressed via Walton and Snurr.[11] In addition to careful sample preparation and activation, selecting the appropriate relative pressure range for applying the BET

method is specifically important for MOFs. More specifically, the linear fit of the BET plot must be verified and the quantity $v(1-(p/p_o))$ must be increasing with increasing p/p_o over the selected pressure range.[11]

2.1.2.2 Single Component Gas Adsorption

Single component gas isotherms were collected using an Intelligent Gravimetric Analyser (IGA-001) from Hiden Isochema.[5] The apparatus consisted of a micro-balance and counter-balance within a 316 SS vessel with automated pressure and temperature control. Samples of ca. 10-50 mg were loaded into wire mesh sample buckets, attached to the balance, and sealed within the reactor with a new copper gasket. Then, the samples were activated *in situ* until their weights reached equilibrium, typically 8-24 h depending upon solvent volatility and activation temperature. A 'Fast Response' furnace from Hiden was used to provide elevated temperatures up to 523 K and dynamic vacuum of ca. <1E-06 torr was achieved via a Pfeiffer Turbomolecular Pump. Isotherms were collected using a water jacket for near-ambient temperature control and using the IGAswin software for pressure control and programmable monitoring of the adsorption kinetics. Single component gas isotherms were collected with periodic dosing of the analyte gas to maintain the desired pressure but without continuous-flow, which lead to more precise performance from the microbalance. The asymptote values measured at each pressure over the range of 12-20,000 mBar corresponded to the equilibrium uptake and were combined to produce the single component isotherm.

2.1.2.3 Water Vapor Adsorption

Water vapor adsorption isotherms were collected using an IGA-003,[12] which was similar to the aforementioned IGA-001 with the addition of four mass-flow controllers (MFCs) to control the composition of the analyte gases and a vapor generator canister to introduce the desired vapor to the system. Air Zero Grade from Airgas was used as the carrier gas and bubbled through the vapor generator canister, which is immersed in a water bath for temperature control. Following *in situ* activation, the samples were exposed to incrementally increasing amounts of moisture by controlling the ratio of air exposed to the vapor generator and dry air. The air passing through the vapor generator is assumed saturated. Therefore, the volumetric flow-rate of the saturated stream to the total flow-rate was considered equivalent to percent relative humidity (%RH). Data were not collected above 90% RH due to bulk condensation within the apparatus, which lead to artificially high uptakes and erroneous desorption hystereses. The total flow-rate was maintained at 200 cc/min and the resultant equilibrium points produce the water adsorption isotherm as a function of % RH.

2.1.2 Thermo-Gravimetric Analysis

A Netszch STA 449 F1 Jupiter[13] was used to examine the thermal degradation of synthesized MOFs. Samples of ca. 10-20 mg were loaded in an alumina crucible with lid and placed on the microbalance within the furnace. Two external MFCs were used to maintain the flow of inert gas, N_2 or He, at ca. 20 cc/min total through the furnace, 10 cc/min through the 'protective' and 'purge' MFCs. After the gas flow was initiated, and the balance came to equilibrium; a programmed temperature ramp-rate, typically 5-10

K/min, was applied and the sample mass was recorded. Solvent loss and decomposition temperatures were gathered from the resultant weight and temperature data.

2.2 Materials and Vessels

All syntheses took place using previously published reactant concentrations and conditions unless otherwise noted. Polytetrafluoroethylene (PTFE)-lined acid digestion bombs from Parr Instrument Co.;[14] 23, 46, and 125 mL, were primarily used when synthesis temperatures were significantly higher than the solvent boiling point. The inconel rupture disks and spring-loaded lids safely alleviate any unanticipated over-pressuring. If syntheses took place well below the solvent boiling point, 20 mL borosilicate-glass scintillation vials were typically used. Exceptions to these guidelines were specifically mentioned and include MIL-125-NH_2 and Mg MOF-74. In these cases, glass vials were used to accurately reproduce the published synthesis conditions.[15,16]

2.3 References

1. Panalytical. X-ray Diffraction Systems. 2012; http://www.panalytical.com/index.cfm?pid=154. Accessed August 24th, 2012.

2. Panalytical. X'Celerator. 2012; http://www.panalytical.com/index.cfm?pid=377. Accessed August 24th, 2012.

3. Douglas A. Skoog FJH, Stanley R. Crouch. *Instrumental Analysis.* Brooks/Cole; 2007.

4. Bragg WL. The structure of some crystals as indicated by their diffraction of x-rays. *Proc. R. soc. Lond. Ser. A-Contain. Pap. Math. Phys. Character.* Sep 1913;89(610):248-277.

5. HidenIsochema. IGA-001 Gas Sorption Analyser. 2012; http://www.hidenisochema.com/products/iga-series/iga-001-gravimetric-gas-sorption-analyser.html. Accessed August 24th, 2012.

6. Kusgens P, Rose M, Senkovska I, et al. Characterization of metal-organic frameworks by water adsorption. *Microporous Mesoporous Mat.* Apr 2009;120(3):325-330.

7. Matzger KACaAJ. Water Stability of Microporous Coordination Polymers and the Adsorption of Pharmaceuticals from Water. *Langmuir.* 2010;26(22):177198-117202.

8. Schoenecker PM, Carson CG, Jasjuja H, Flemming CJJ, Walton KS. Effect of Water Adsorption on Retention of Structure and Surface Area of Metal-Organic Frameworks *Ind. Eng. Chem. Res.* 2012.

9. Quantachrome. QUADRASORB SI. http://www.quantachrome.com/gassorption/quadrasorbsi.html. Accessed Aug. 27th, 2012.

10. Brunauer S, Emmett PH, Teller E. Adsorption of gases in multimolecular layers. *Journal of the American Chemical Society.* Jan-Jun 1938;60:309-319.

11. Walton KS, Snurr RQ. Applicability of the BET method for determining surface areas of microporous metal-organic frameworks. *Journal of the American Chemical Society.* Jul 11 2007;129(27):8552-8556.

12. HidenIsochema. IGA-003 Multicomponent Analyser. 2012; http://www.hidenisochema.com/products/iga-series/iga-003-multicomponent-gravimetric-gas-sorption-analyser.html. Accessed August 24th, 2012.

13. NETZSCH. Fascinating Flexibility in Thermal Analysis

STA 449 F1 Jupiter® – Simultaneous TGA-DSC. http://www.netzsch-thermal-analysis.com/en/products/detail/pid,42.html. Accessed August 24th, 2012.

14. Parr. Acid Digestion http://www.parrinst.com/products/sample-preparation/acid-digestion/. Accessed August 25th, 2012.

15. Dan-Hardi M, Serre C, Frot T, et al. A New Photoactive Crystalline Highly Porous Titanium(IV) Dicarboxylate. *Journal of the American Chemical Society.* Aug 2009;131(31):10857-+.

16. Caskey SR, Wong-Foy AG, Matzger AJ. Dramatic tuning of carbon dioxide uptake via metal substitution in a coordination polymer with cylindrical pores. *Journal of the American Chemical Society.* Aug 2008;130(33):10870-+.

CHAPTER 3

TOXIC INDUSTRIAL CHEMICAL ADSORPTION USING MOFS

This work was conducted in collaboration with United Technologies Research Center and partially funded by Combatting Terrorism Technical Support Office (CTTSO)-

Joshua A. Sheffel, Norberto O. Lemcoff, and Catherine Thibaud-Erkey

3.1 Toxic Industrial Chemicals

Although often less toxic than specifically designed chemical warfare agents, Toxic Industrial Chemicals (TICs) pose a legitimate safety threat due to the ease of procuring large quantities. The specific threat of TICs are evaluated by the International Task Force-25 (ITF-25) based on both toxicity and quantity availability.[1] Down-selected from the ITF-25 list the specific target chemicals of this project include ammonia, dihydrogen-sulfide, chlorine, methyl-amine, sulfur dioxide, and formaldehyde. Current filters composed of impregnated-activated carbons such as ASZM-TEDA exhibit poor protection from a number of dangerous TICS.[2] The goal of this project is to select and synthesize previously reported MOFs with potential to selectively adsorb TICs, which current activated carbons have performance deficiencies with.

3.2 ASZM-TEDA

Activated carbons,[2] zeolites,[3] and other porous adsorbents[4] are often used to filter TICs. ASZM-TEDA is an activated carbon impregnated with copper (A), silver (S), zinc (Z), molybdenum (M), and triethylenediamine (TEDA). Marketed by Calgon Carbon Corporation, ASZM-TEDA is currently used in many military and industrial applications

including personal respirators and collective filtration units.[2] Due to the sensitive nature of ASZM-TEDA applications, quantitative performance data are not readily available. However, general proficiencies with blood and nerve agents as well as some TICs including SO_2 and H_2S are published by Calgon, but poor performance is reported for others including NH_3, CH_3NH_2, and CH_2O.[2]

3.3 MOF Selection Criteria

MOFs exhibit potential for TIC adsorption applications with highly porous structures and a multitude of available functional sites, including coordinatively unsaturated metal sites (CUSs) and amine-functionalized sites.[5-8] Due to the often defense-based nature of toxic gas adsorption, few public articles address this application of MOFs. Britt et al.[6] examine the adsorption performance of select MOFs in the presence toxic gases including SO_2, NH_3, and Cl_2. Results are gathered by breakthrough apparatus and compared to BPL activated carbon. Of the eight toxic gases tested, the selected MOFs perform as well if not better than the BPL activated carbon for each case. The most improved case is NH_3 adsorption by the amine-functionalized MOF, IRMOF-3, which is likely an attribute of hydrogen-bonding and shows 105x improvement over the BPL carbon. Also noteworthy, the Zn MOF-74 analogue demonstrated the best SO_2 uptake and outperformed BPL carbon by ca. 5.9 fold. However, the results of this study do not account for exposure of the MOFs to water vapor,[6] which will be present during or prior to use for most target applications.

Work by Glover et al.[5] demonstrates the ability of MOFs to preferentially adsorb highly reactive gases. Toxic gas breakthrough curves are generated using MOF-74 analogues

(Ni, Mg, Co, and Zn) as an adsorbent, which contain CUSs. Attributed mainly to the Lewis-acid functionality of the CUSs, MOF-74 exhibits significantly higher uptake of NH_3 compared to both BPL activated carbon and zeolite 13X. However, the MOF performance is significantly impeded by water vapor presence.[5] Mg MOF-74 specifically shows the best ammonia uptake of all materials tested under dry conditions of 7.6 mmol/g, but the worst uptake of 1.7 mmol/g from the MOF-74 analogues under 50% RH exposure. Even with the diminished performance, Mg MOF-74 equilibrium loadings are at least 2.6-fold higher than BPL carbon and Zeolite 13X under both wet and dry conditions, which demonstrates the ability of open-metal site MOFs to selectively adsorb reactive gases via their specific functional sites. Both of these published studies on MOFs for removal of toxic gases[5,6] note a more irreversible adsorption behavior from MOFs versus traditional adsorbents for analyte gases including NH_3 and SO_2, which is highly advantageous for safe filtration and removal.

This work in collaboration with United Technologies Research Center (UTRC) focuses on synthesizing previously reported MOFs and investigating their potential for TIC adsorption. The end goal of the project is to produce a prototype filter consisting of a MOF or multiple MOFs to run in series with current ASZM filters and remove TICs that ASZM-TEDA failed to capture. My responsibilities include synthesis, characterization, and delivery of previously reported MOFs, which show high potential for TIC removal.

3.4 Selected MOFs

Initially, the following three MOFs were selected; DMOF-1-NH_2, Mg-MOF-74, and UMCM-1-NH_2-COOH. These three materials represented multiple properties including

micropores, mesopores, CUSs, amine-groups, and carboxyl groups, which had high potential for selective TIC adsorption. Of the initial MOFs DMOF-1-NH_2 and Mg MOF-74 were successfully synthesized in the required quantities for testing (>/= 100 mg). Therefore, a fourth material, UiO-66-NH_2, was also synthesized and characterized. MOF structures were confirmed via p-XRD and BET modeling of N_2 adsorption at 77 K.

3.4.1 DMOF-1-NH_2

DMOF-1-NH_2 was synthesized via the procedure published by Cohen et al.,[9] and is a mixed ligand MOF with Zn centers connected by 2-amino terephthalic acid (ATPA)

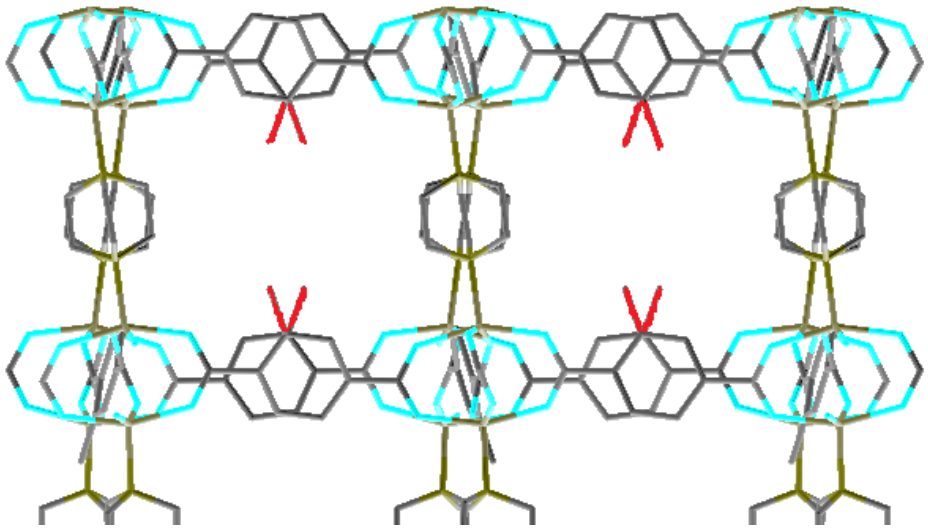

Figure 3. 1. DMOF-1-NH_2 structure illustration. (C-C Grey, O- Teal, NH_2-red, and Zn-N Green)

and diazabicyclo-octane (DABCO). The resultant structure, illustrated in Figure 3.1, consisted of 2-D sheets formed via a Zn paddlewheel structure and ATPA ligands, which were connected via pillar-like coordination of DABCO ligands. The pore diameters were ca. 7.5x7.5 Å and 4.8x3.2 Å.[10] The amine-functionalized ligand was expected to give the

MOF basic properties in order to facilitate adsorption of TICs including SO_2 and H_2S as well as provide a hydrogen-bonding site for TICs such as CH_2O and NH_3.

3.4.2 UMCM-1-NH_2-COOH

Synthesis of UMCM-1-NH_2 also followed the published procedure of Cohen et al.[9] with slight modifications based on communications with Dr. Cohen's group. The goal was to take advantage of the mixed acidic and basic properties of a MOF containing both carboxylic acid and amine functional sites for reactive gas adsorption. The synthesis procedure consisted of initial synthesis of UMCM-1-NH_2,[9] which contained meso- and micropores of 27x32 Å and 14x17 Å,[10] respectively with Zn metal centers and mixed-ligand character from the 1,3,5-benzene tribenzoic acid (BTB) and ATPA. The resultant product underwent post-synthetic modification (PSM) via substitution with succinic anhydride, a five-membered cyclic anhydride.

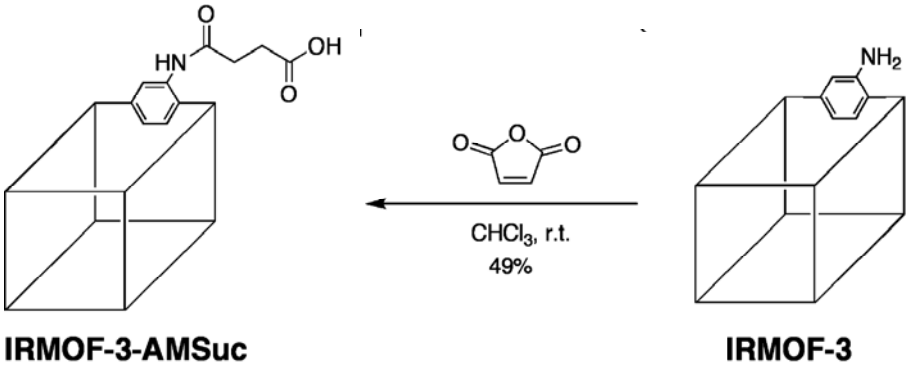

Figure 3. 2. Illustration or PSM via succinic anhydride to provide carboxylic acid functionality taken from Cohen et al.[11]

The procedure was taken from Cohen et al.[11] using a 2:1 ratio of anhydride to free amine-group ratio recommended via email from first author, Sergio J. Garibay. The anhydride bonded to the amine site and unraveled resulting in an accessible carboxylic acid group,

analogous to that shown in Figure 3.2.[11] For simplicity, we chose a slightly different nomenclature, UMCM-1-NH_2-COOH v. UMCM-1-AMSuc.

3.4.3 Mg MOF-74

Mg MOF-74 consisted of 2,5-dihydroxy terephthalic acid ligands connecting Mg metal centers with CUSs inside 11 Å cylindrical pores[12] (Figure 3.3). The Lewis-acid properties of CUSs were expected to preferentially adsorb ammonia and methyl-amine. Mg-MOF-74 synthesis was conducted solvothermally via the published procedure from Matzger et al.[12]

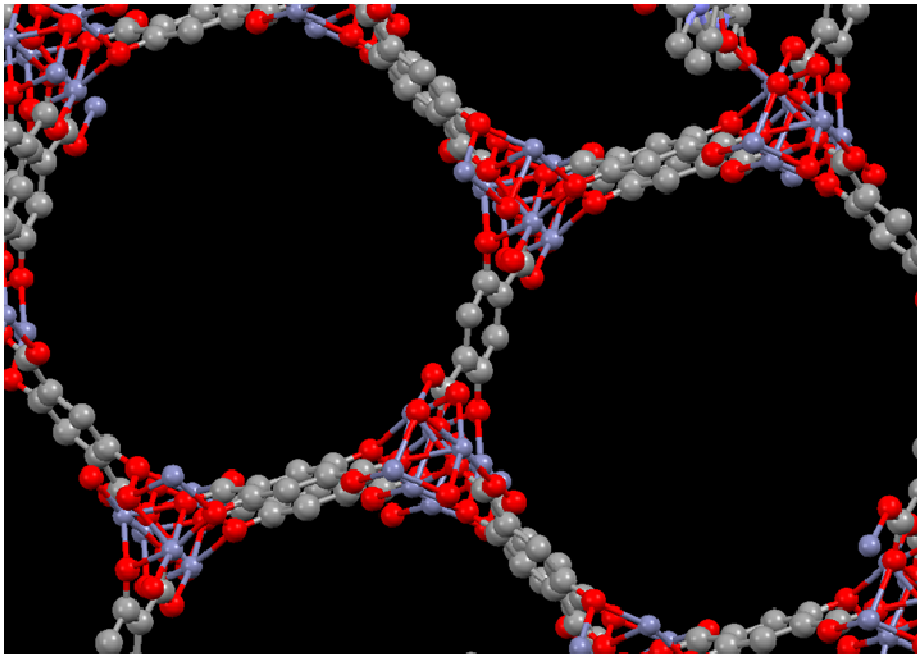

Figure 3. 3. Mg MOF-74 structure illustration (C -Grey, O- Red, and Mg-Blue).

3.4.4 UiO-66-NH_2

UiO-66, which was reported by Cavka et al.[13] consisted of 8-coordinated Zr connected via terephthalic acid and was reported to be stable in water and under mechanical pressures up to 10,000 kg/cm^2.[13] With the reported stability in mind and the predicted benefits of amine groups, an amine-functionalized version of the structure, UiO-66-NH_2, was sought. Unpublished at the time, synthesis of UiO-66-NH_2 was attempted following an identical procedure to that reported by Cavka et al. for UiO-66.[13] However, equimolar amounts of ATPA were substituted for the original terephthalic acid. The resultant cubic structure[13] was illustrated in Figure 3.4 and had pore diameters of ca. 6 Å.[10] Later this material was published and also shown to facilitate PSM.[14]

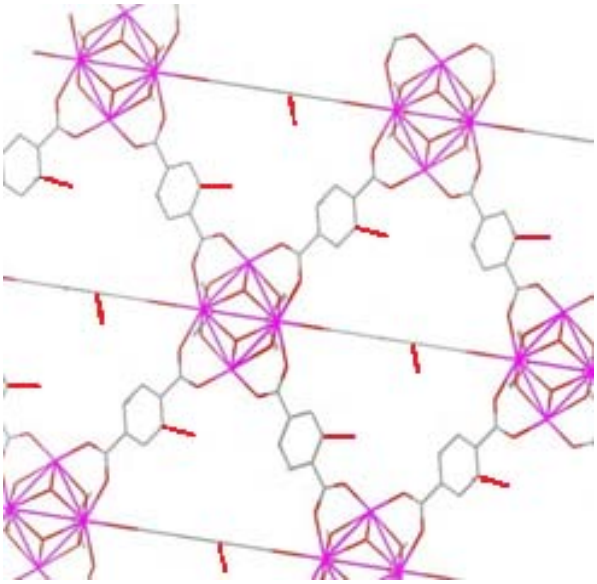

Figure 3. 4. UiO-66-NH_2 structure illustration. (C-C Grey, Zr-O Pink, and NH_2-red)

3.5 Synthesis Results

DMOF-1-NH_2 and Mg MOF-74 were successfully synthesized and characterized by p-XRD and BET modeling of N_2 adsorption at 77 K. The synthesis procedure for

UMCM-1-NH_2 required multiple attempts and was successfully confirmed via powder XRD, and the PSM with succinic annhydride was confirmed via H^1 NMR. Successful product was created from small scale synthesis attempts ca. 10mg. However, PSM of larger batches required for breakthrough testing, ca. 500 mg, lead to complete structure degradation as visible by XRD and N_2 adsorption at 77 K. Due to the need to scale up further and time constraints of the project, UMCM-1-NH_2-COOH synthesis was aborted and other potential MOFs were sought.

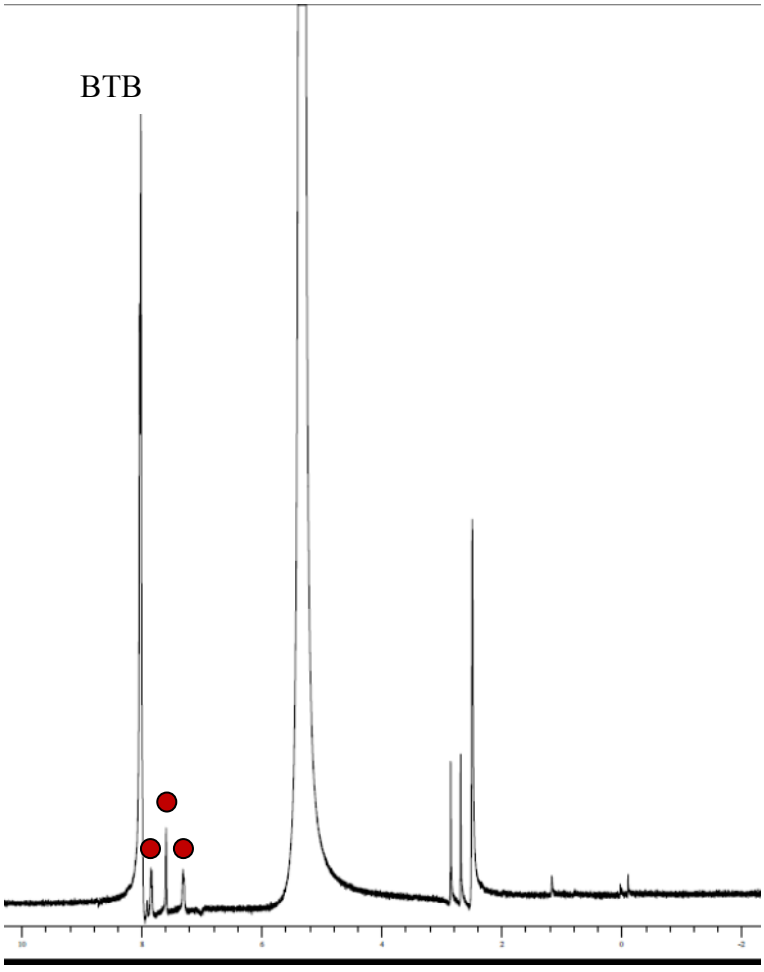

Figure 3.5 H^1 NMR from digested sample of UMCM-1-NH_2-COOH. Unmodified benzene tribenzoic acid (BTB) peak is labeled and red circles indicate peaks corresponding to successful succinic anhydride modification.

The next MOF of interest for the TIC adsorber project was Zr-based MOF, UiO-66-NH_2. The amine-functionalized MOF was successfully prepared and confirmed to be isostructural to the parent material, UiO-66. Also noteworthy is high mechanical stability of UiO-66-NH_2, demonstrated by the successful pelletizing reported by UTRC, which was potentially useful for reducing pressure drop across the filter via increasing particle size.

3.6 Filtration Performance Testing

Due to the extensive safety procedures and equipment required to experiment with TICs, UTRC conducted most of the adsorption experiments for the project via breakthrough adsorption testing, Figure 3.6. Throughout the investigation of adsorbents

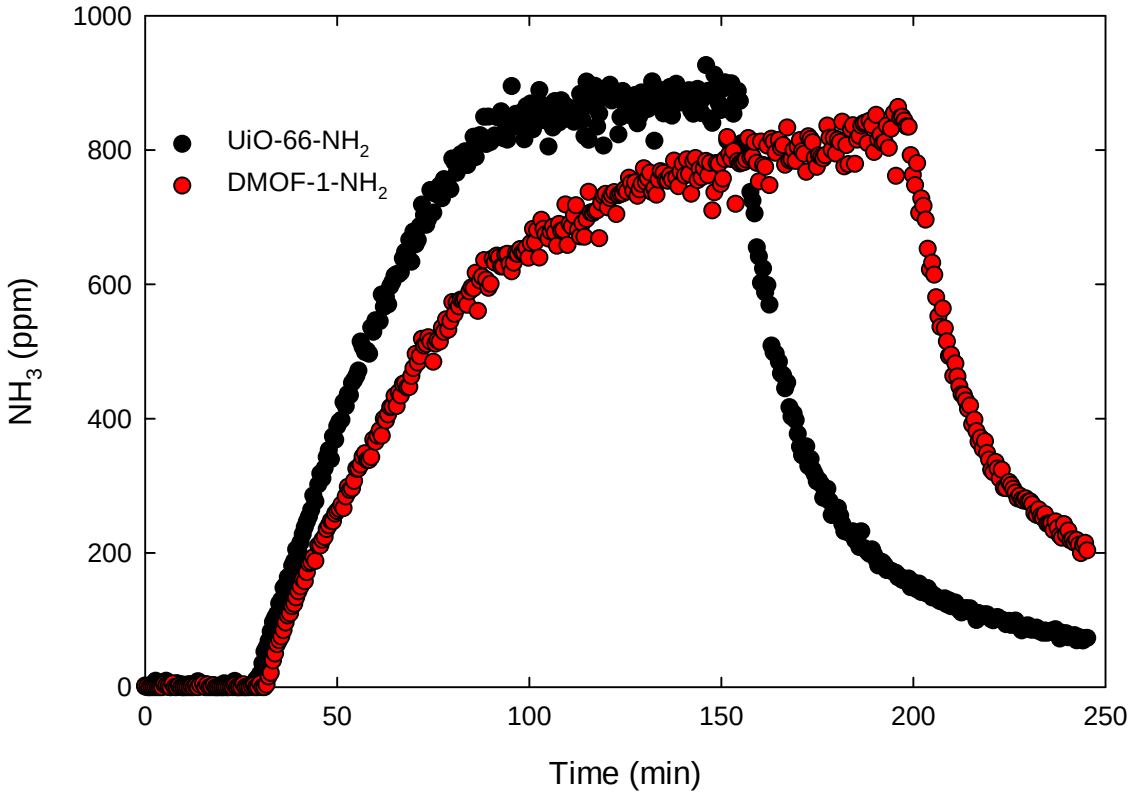

Figure 3.6 Breakthrough data for amine-functionalized MOFs with NH_3 as the adsorbate. Samples were exposed to 50% RH prior to adsorption testing. ***Collected by UTRC***

for TIC filtration a total of six MOFs and five activated carbons were examined. The three MOFs supplied by the above syntheses and three commercially sourced (Sigma Aldrich) MOFs, C300 (HKUST-1 or CuBTC), F300, and Z1200 (ZIF 8) were tested.[15] Since the target application would require exposure to ambient air prior to potential TIC exposure, the adsorbents were tested at 23-35°C and after exposure to 50-65% relative humidity (RH).

Despite structure confirmation via pXRD, Mg MOF-74 exhibited little or no uptake of select TICs. One potential source of the poor performance may be the strong affinity of Mg MOF-74 for water vapor. Glover et al. reported the affinity for water during their water adsorption studies,[5] and in this work, suspicions of water adsorption interference were validated by collecting CO_2 adsorption isotherms at 298K and up to 1 bar, Figure 3.7. In order to duplicate the reported record uptake of 35 wt% of CO_2 at 1bar and 298 K.[12] Mg MOF-74 was loaded into the IGA-001 in solution, *wet,* and activated *in situ* at 523 K. Analogous trials with a dried powder sample, *dry*, and minimal exposure to lab atmosphere prior to *in situ* activation resulted in drastically reduced uptakes of ca. 10 wt% under the same conditions.

Also noteworthy are the water stability results for Mg MOF-74 (Chapter 4),[10] which demonstrate a substantial loss of porosity following water adsorption with air as a carrier gas and regeneration. Comparison of the water adsorption results in Chapter 4 with those reported by Glover et al.[5] may also inadvertently illustrate the inherent sensitivity of MOF-74 when exposed to humid air. The water loading reported at 80%RH humidity for Mg MOF-74 differ by 59%, 21.7 and 36.7 mmol/g for Glover et al.[5] and our study,[10]

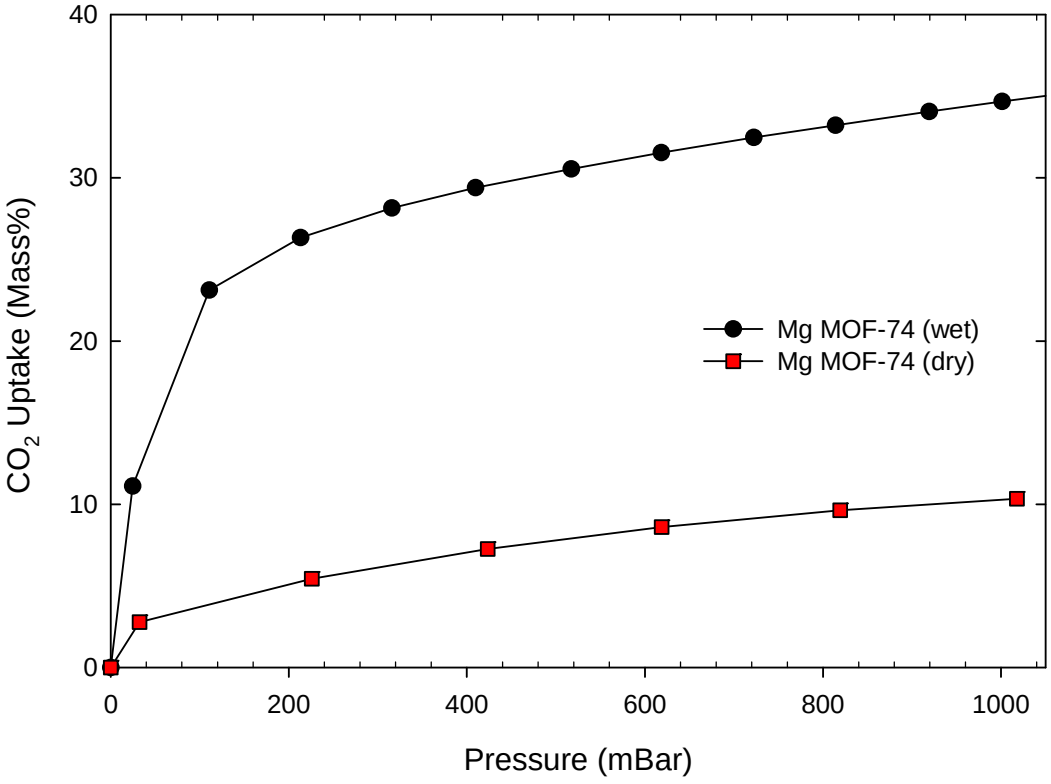

Figure 3.7 CO_2 adsorption data for Mg MOF-74 collected at 298 K. 'Wet' sample was loaded in solution and activated *in situ*. 'Dry' sample was allowed to dry under ambient conditions before *in situ* activation

respectively. The BET surface areas of the samples may account for some of the variance with a 16% lower surface area reported by Glover et al.[5] (1,400 v 1,206 m^2/g),and the differences in apparatuses (breakthrough[5] v. gravimetric[10]) may affect the results. However, another potential source of the discrepancy is degradation occurring prior to the water adsorption trial conducted via Glover et al.,[5] which is not easily identified via pXRD.[10] With initial the target application requiring water vapor exposure prior to adsorbate exposure, further synthesis and testing of Mg MOF-74 was aborted.

Exhibiting the best overall MOF performance, the two amine-functionalized MOFs described above showed the highest uptake of three selected TICs; methyl amine,

ammonia, and formaldehyde with improvements of 1.7, 5, and 2x, respectively versus the current filter media. The promising results sparked interest in further investigation of the application potential of the amine-functionalized MOFs, DMOF-1-NH_2 and UiO-66-NH_2.

Table 3.1 Summary of amine-functionalized MOF filtration performance for NH_3, CH_2O, and CH_3NH_2 and best improvement compared to baseline filter. ***Collected by UTRC***

	UiO-66-NH_2	DMOF-1-NH_2	Performance Increase
NH_3	Improved	Best	1.5X
CH_2O	Best	Improved	5X
CH_3NH_2	Best	Best	2X

With the relatively low analyte gas fugacities, the pore volume (0.57 and 0.58 cc/g for DMOF-1-NH_2 and UiO-66-NH_2, respectively)[10] and BET surface areas (ca. 2,000 and 1,000 m^2/g for DMOF-1-NH_2 and UiO-66-NH_2, respectively)[10] are not likely to account for the attractive adsorption behavior. However, amine-functional groups are beneficial for site-selective adsorption of molecules capable of hydrogen bonding, which includes NH_3, CH_2O, and CH_3NH_2. So, the preferential adsorption is likely governed by the number of accessible amine-sites for a given analyte gas and the dipole moment afforded by the functional group.

Since both materials utilize the same ligand, ATPA, the hydrogen-bonding capabilities of the functional group should be nearly identical. However, Yaghi et al.[16] have demonstrated via solid-state ^{15}N NMR that the amine-functional groups of UiO-66-NH_2 are not solely –NH_2. The metal salt used in the synthesis, $ZrCl_4$, provides an abundance of Cl^- ions, which forms $NH_3^+Cl^-$ sites accounting for ca. 33% of the functional groups. A similar study has not been performed on DMOF-1-NH_2, which is required for a direct

functional group comparison. However, the nitrate-salt complex used in the synthesis would likely form some $NH_3^+NO_3^-$ sites, which could significantly affect adsorption site preferences.

3.7 Conclusions

During the selection and subsequent TIC filtration testing of MOFs, amine-functionalization demonstrates the highest potential to selectively remove reactive gases from air including ammonia, formaldehyde, and methyl amine. UMCM-1-NH_2-COOH was not successfully synthesized on the scale required for filtration experiments, and due to suspected structural instabilities was not deemed a viable option for the target application. Mg MOF-74 was successfully synthesized in the quantities required for breakthrough testing but exhibited little or no uptake of target TICs, which is likely attributed to instability in the presence of water.[10]

The final goal of the UTRC TIC filtration project was to synthesize the most promising MOFs, DMOF-1-NH_2 and UiO-66-NH_2, at a commercial level and apply them following ambient air exposure. Thus, a more in depth understanding of MOF water stability and development of large-scale MOF synthesis methods was deemed imperative.

3.8 References

1. Hincal F, Erkekoglu P. Toxic Industrial Chemicals (TICs)-Chemical Warfare Without Chemical Weapons. *FABAD J. Pharm. Sci.* 2006;31:220-229.

2. Corporation CC. Respirators and Human Protection: Technologies for Purification, Separation, Recovery and Synthesis. 2003; http://www.calgoncarbon.com/documents/RespiratorsandHumanProtection.pdf.

3. Lee SK, Jang YN, Bae IK, Chae SC, Ryu KW, Kim JK. Adsorption of Toxic Gases on Iron-Incorporated Na-A Zeolites Synthesized from Melting Slag. *Materials Transactions.* Oct 2009;50(10):2476-2483.

4. Furtado AMB, Wang Y, Glover TG, LeVan MD. MCM-41 impregnated with active metal sites: Synthesis, characterization, and ammonia adsorption. *Microporous Mesoporous Mat.* Jul 2011;142(2-3):730-739.

5. T.Grant Glover GWP, Bryan J. Schindler, David, Brittand OY. 'MOF-74 building unit has a direct impact on toxic gas adsorption' *Chemical Engineering Science.* October 2010.

6. Britt D, Tranchemontagne D, Yaghi OM. Metal-organic frameworks with high capacity and selectivity for harmful gases. *Proc. Natl. Acad. Sci. U. S. A.* Aug 2008;105(33):11623-11627.

7. Kreno LE, Hupp JT, Van Duyne RP. Metal-Organic Framework Thin Film for Enhanced Localized Surface Plasmon Resonance Gas Sensing. *Analytical Chemistry.* Oct 2010;82(19):8042-8046.

8. Ariga K, Ishihara S, Abe H, Li M, Hill JP. Materials nanoarchitectonics for environmental remediation and sensing. *J. Mater. Chem.* 2012;22(6):2369-2377.

9. Wang ZQ, Tanabe KK, Cohen SM. Accessing Postsynthetic Modification in a Series of Metal-Organic Frameworks and the Influence of Framework Topology on Reactivity. *Inorg. Chem.* Jan 2009;48(1):296-306.

10. Schoenecker PM, Carson CG, Jasjuja H, Flemming CJJ, Walton KS. Effect of Water Adsorption on Retention of Structure and Surface Area of Metal-Organic Frameworks *Ind. Eng. Chem. Res.* 2012.

11. Garibay SJ, Wang ZQ, Tanabe KK, Cohen SM. Postsynthetic Modification: A Versatile Approach Toward Multifunctional Metal-Organic Frameworks. *Inorg. Chem.* Aug 2009;48(15):7341-7349.

12. Caskey SR, Wong-Foy AG, Matzger AJ. Dramatic tuning of carbon dioxide uptake via metal substitution in a coordination polymer with cylindrical pores. *Journal of the American Chemical Society.* Aug 2008;130(33):10870-+.

13. Cavka JH, Jakobsen S, Olsbye U, et al. A new zirconium inorganic building brick forming metal organic frameworks with exceptional stability. *Journal of the American Chemical Society.* Oct 2008;130(42):13850-13851.

14. Garibay SJ, Cohen SM. Isoreticular synthesis and modification of frameworks with the UiO-66 topology. *Chemical Communications.* 2010;46(41):7700-7702.

15. BASF. BASF 051908 BASOLITE Handout. *www.Sigma-Aldrich.com.*

16. Morris W, Doonan CJ, Yaghi OM. Postsynthetic Modification of a Metal-Organic Framework for Stabilization of a Hemiaminal and Ammonia Uptake. *Inorg. Chem.* Aug 2011;50(15):6853-6855.

CHAPTER 4

WATER STABILITY OF MOFS

Reproduced from P. M. Schoenecker, C. G. Carson, H. Jasuja, C. J. J. Flemming, and K. S. Walton. *Ind. and Chem. Engg. Research.* 2012, 51 (18), 6513–6519.

4.1 Introduction

The ability to synthesize metal-organic frameworks (MOFs) with prescribed structural features has led to intense interest in the materials for selective adsorption processes. The hybrid nature of MOFs provides an almost infinite set of building blocks that can be manipulated to target specific adsorption behavior by introducing open metal sites and functional groups, or by further modulating the properties by post-synthetic modification.[1-8] To date, much of the experimental and theoretical research on MOF applications has centered on adsorption simulations and measurements. Investigations of gas storage (hydrogen/methane) and carbon dioxide capture from flue gas have been a particular focus.[2,3,8]

Aside from good adsorption loadings and high selectivities, the stability of an adsorbent in humid environments is a critical property that must be considered when designing an adsorption process. The water sensitivity of certain MOFs has been well-documented,[9-13] but a variety of MOFs including pyrazolate[14] and imidazolate[15] frameworks and zirconium-based MOFs[16] have been reported in recent years that do not lose structural integrity in the presence of water. Long and coworkers have reported pyrazolate-based MOFs that show remarkable structural integrity after exposure to boiling water and other solvents due to the high pK_a value of the ligands. These materials

also possess open metal sites.[14] Lillerud and coworkers have reported an interesting family of isoreticular zirconium MOFs built from various aromatic carboxylates.[16] UiO-66 shows no change in PXRD pattern after exposure to liquid water and other solvents. The stability is attributed to the strength of the inorganic unit; each zirconium atom is 8-coordinated via terephthalic acid ligands. Several MIL materials are known to maintain good structural integrity after water exposure due to high coordination numbers,[17-19] and the zeolitic imidazolate frameworks (ZIFs) have also been shown good stability under aqueous conditions.[15,19]

Cychosz and Matzger[20] recently reported an investigation of the stability of several MOFs after exposure to aqueous solutions with varying amounts of DMF. MOF structures utilizing Zn-carboxylate connectivity (MOF-5, MOF-177) were found to be unstable after exposure to liquid water, while copper paddle-wheel MOFs (HKUST-1, MOF-505) showed good structure retention after similar testing. An investigation by Low et al.[21] using high throughput steam treatment found that metal-ligand bond strength and oxidation state of the metal cluster are important contributors to MOFs stability. Kaskel et al.[19] reported water adsorption isotherms for several MOFs; HKUST-1, ZIF-8, DUT-4, MIL-100, and MIL-101. Water stability was analyzed following the water vapor adsorption as well as after immersing the MOFs in liquid water at 323 K. The Dietzel group has investigated the stability of the MOF-74/CPO-27 materials (Co, Mg, Ni) throughout dehydration/rehydration cycling.[22-24] The MOF-74 analogues were found to be stable during cyclic adsorption testing while using inert gases (Ar/N_2). However, when the same experiment was conducted in air the Ni MOF-74 degraded.[23]

Sensitivity to water vapor is widely considered to be a major weakness of MOFs that could negate potential advantages of the hybrid materials from an applications perspective. Previous studies have focused largely on understanding structural changes in MOFs after immersion in liquid water. However, understanding the behavior of MOFs under humid conditions is also quite important for applications such as CO_2 capture from flue gas or air purification. The importance of MOF performance in humid environments cannot be overstated, and understanding the parameters that contribute to this sensitivity is critical for elevating MOFs to the applied level. Nevertheless, few systematic studies on the stability of MOFs after exposure to humid streams have been reported. In this work, we present an experimental investigation of water adsorption in MOFs at room temperature and up to 90% relative humidity (RH), followed by an analysis of structural degradation and surface area change. Specifically, we examine structure retention after water exposure and regeneration via dynamic vacuum and elevated temperature, due to the direct link with many gas separation applications.

Seven MOFs were selected for this study to represent a range of features that are common in MOFs. These include open-metal sites (HKUST-1,[25] Mg-MOF-74[26]), amine-functional groups (UiO-66,[27] DMOF-1[5,28]), carboxylate coordination (UMCM-1,[29] HKUST-1, Mg-MOF-74), and nitrogen coordination (DMOF-1). There are also differences in the metal coordination as these MOFs are synthesized from zinc, copper, magnesium, or zirconium. The isoreticular family of UiO-66 materials also contain open-metal sites upon activation or dehydroxylation.[16,30,31] However, Llewellyn et. al.[32] shows that these open Zr sites do not interact with gases like CO and CO_2 in the same

fashion as other open-metal site MOFs e.g. HKUST-1. So, UiO-66 and UiO-66-NH_2 are not considered in the same category as Mg-MOF-74 and HKUST-1 for this study.

HKUST-1 or Cu-BTC is one of the most widely studied MOFs over the past decade.[19,33-36] This material is synthesized by coordination of copper with 1,3,5-benzene tricarboxylic acid. The secondary building unit is formed by the copper paddlewheel, in which two copper atoms coordinate with four BTC ligands. The large pore diameter is 9 Å, and the small pores are around 6 Å. An open coordination site is generated at each copper upon activation of the material. Wang et al.[36] reported the first water isotherm for HKUST-1, but no structure or surface area analyses were performed. Low et. al.[21] reported that HKUST-1 is stable up to 200 ^{o}C when exposed to 50 mol% steam, and Cychosz and Matzger[20] found that HKUST-1 exhibits good structure retention in a 7:1 mixture of H_2O:DMF even after 21 months of exposure. In contrast, Kaskel et al.[19] determined from powder X-ray diffraction that HKUST-1 breaks down after immersion in pure water at 323 K for 24 h.

Mg-MOF-74 is synthesized from magnesium and 2,5-dihydroxyterephthalic acid. It possesses one-dimensional channels of approximately 11 Å diameter in a honeycomb topology, with removable solvent molecules coordinating at the metal sites. Of the open-metal site MOFs, Mg MOF-74 exhibits among the highest loadings of CO_2 at low pressure (e.g. 35.2 wt% uptake of CO_2 at 298K and 1atm).[3] It also has been reported to exhibit a strong affinity for water,[34,36,38] but the effect of water adsorption and regeneration on available surface area has not been investigated.

UiO-66 contains $[Zr_6O_4(OH)_4]$ clusters linked with twelve terephthalate moieties. The pore diameters are approximately 6 Å. Upon dehydroxylation $[Zr_6O_4(OH)_4]$ clusters

change to [Zr_6O_6], and the Zr metal-centers undergo a transition from the as-synthesized 8-coordinated state to 7-coordinated state.[31] Previous studies have shown that UiO-66 maintains its structure after immersion in water and other solvents, but no water isotherms were reported.[16]

Nitrogen-coordinated DMOF-1 ($Zn_2(BDC)_2(DABCO)$) has square-shaped channels of 7.5 Å diameter that are interconnected by smaller pores with diameters of 4.8 x 3.2 Å. It has been shown to be hydrophobic up to 42% RH, but no structure analysis was performed post-exposure.[28] On the other hand, Liang et al.[38] investigated the water tolerance of zinc and nickel versions of this material and found that both appear to lose structural integrity after exposure to relative humidity above 60%. The corresponding surface area analysis was not performed.

MOFs with amine-functionalized ligands often provide the functional sites capable of facilitating post-synthetic modification (PSM),[7,39] and therefore, are of great importance when considering PSM materials for humid gas separation processes. There have been no water adsorption or stability studies reported for the amine containing analogues, UiO-66-NH_2 and DMOF-1-NH_2.

UMCM-1 is a mesoporous MOF synthesized from zinc and two organic ligands, terephthalic acid and 1,3,5-tris(4-carboxyphenyl)benzene (BTB). This MOF has shown some promise for dry gas separation applications.[40] However, with a coordination environment similar to MOF-5, it is unlikely that UMCM-1 will exhibit great water stability.

4.2 Experimental

4.2.1 Synthesis Methods

All chemicals were procured from commercial sources (Fisher and Sigma Aldrich) and used without further purification. Samples are stored in sealed vials prior to use.

UMCM-1: A modified version of the previously reported synthesis method[29] is used. $Zn(NO_3)_2 \cdot 6H_2O$ (3.87 g, 13.0 mmol), terephthalic acid (TPA) (0.540 g, 3.25 mmol), and 1,3,5-tris (carboxyphenyl) benzene (1.28 g, 2.92 mmol) are dissolved in 120 mL of diethylformamide (DEF). The solution is then filtered twice to remove undissolved solids and divided into twelve 20 mL scintillation vials in a sand bath. The sand bath is heated to 85°C for 48 h. The product is rinsed with dimethylformamide (DMF) three times before solvent exchanging with dichloromethane (CH_2Cl_2) for 96 h via Sohxlet extraction prior to activation at 150°C.

Mg MOF-74: The reported synthesis method[3] is implemented as follows: $Mg(NO_3)_2 \cdot 6H_2O$ (1.90 g, 7.4 mmol) and 2,5-dioxido-1,4-benzenedicarboxylic acid (H_4DOBDC) (0.444 g, 7.40 mmol) are placed in a 200 mL of DMF:ethanol:water (15:1:1, by volume). The resultant mixture is sonicated until homogenous. Ten mL portions of the solution are placed in 20mL scintillation vials and placed in a sand bath. The sand bath is heated to 125°C and the solution is allowed to react for 20 h. The resultant product is collected and placed in a Sohxlet extractor for 96 h to exchange with methanol before activation at 250°C.

HKUST-1: HKUST-1 is synthesized as follows: $Cu(NO_3)_2 \cdot 3H_2O$ (4.55 g, 18.8 mmol) is dissolved in 60 mL of de-ionized water, and trimesic acid (2.10 g, 9.99 mmol)

is dissolved in 60 mL of ethanol via sonication. The solutions are added together and placed in 23 mL PTFE lined acid digestion vessels. The reaction is conducted at 100°C for 18 h. The product is rinsed with methanol and water before activation at 150°C.

UIO-66: The previously reported synthesis method[16] is implemented as follows: $ZrCl_4$ (0.636 g, 2.73 mmol) and terephthalic acid (TPA) (0.453 g, 2.73 mmol) are dissolved via stirring in 106 mL of DMF. The solution is divided up equally and placed in ten 20 mL scintillation vials. The vials are placed in a sand bath at 120°C and reacted for 20h. The resultant product is rinsed with DMF three times before activation at 200°C. The amino version of UiO-66 is synthesized following the same procedure, substituting terephthalic acid with amino-terephthalic acid (ATPA).

DMOF-1: The procedure reported by Wang et al. [5] is used to solvothermally synthesize DMOF-1. $Zn(NO_3)_2 \cdot 6H_2O$ (1.74 g, 6.00 mmol), TPA (1.02 g, 6.00 mmol), and 1,4-diazabicyclo[2.2.2]octane or DABCO (1.08 g, 9.63 mmol) are dissolved in 150 mL of DMF. The solution is then filtered three times to remove the white precipitate and placed in ten 20 mL scintillation vials in a sand bath. The sand bath is heated from 35°C to 120°C at a rate of 2.5°C/min and reacted for 12 h. The product is rinsed with DMF three times and activated at 110°C.

DMOF-1-NH_2: Again, the procedure reported by Wang et al.[5] is used to solvothermally synthesize DMOF-1-NH_2. $Zn(NO_3)_2 \cdot 6H_2O$ (1.79 g, 6.02 mmol), ATPA (1.10 g, 6.09 mmol), and DABCO (1.08 g, 9.63 mmol) are dissolved in 150 mL of DMF. The solution is then filtered three times to remove the white precipitate and placed in fifteen 20 mL scintillation vials in a sand bath. The sand bath is heated from 35°C to 120°C at a rate of 2.5°C/min, and the vials are allowed to react for 12 h. The product is

rinsed with DMF three times, and then placed in a Sohxlet extractor for solvent exchange with chloroform for 72 h at 90°C.

4.2.2 Adsorption Isotherm Measurement

Water adsorption isotherms were measured at 298 K and 1bar on an IGA-003 microbalance from Hiden Isochema. All MOF samples were activated in situ to remove residual solvent and water adsorbed during sample loading, which requires brief exposure (c.a. 3 min.) to ambient air. Dry air was used as the carrier gas, with a portion of the carrier gas being bubbled through a vessel of deionized water. The relative humidity (RH) was controlled by varying the ratio of saturated air and dry air via two mass flow controllers. Experiments were conducted up to 90% RH due to water condensation in the apparatus at higher humidities. The total gas flow rate was 200 cc/min for the entire experiment. Variable timeouts were used with a maximum limit of 24 h per isotherm point. Due to fluctuating climate control of the laboratory itself, condensation inside the gravimetric adsorption apparatus can occur at 90% RH. In this case, equilibrium was not reached due to continued mass gain from condensation, and desorption data were not reported. After the isotherms were collected, the samples were regenerated under dynamic vacuum and elevated temperature. Reactivation temperatures for each MOF are given in the supporting information (Table 4.1).

Table 4.1. Reactivation temperatures of samples used for water adsorption prior to pXRD and N_2 adsorption at 77 K.

Reactivation Temp °C	UiO-66	UiO-66-NH_2	DMOF-1	DMOF-1-NH_2	HKUST-1	Mg MOF-74	UMCM-1
Initial	200	200	110	100	150	250	150
Final	200	250	110	150	200	300	200

4.2.3 Characterization

Powder X-ray diffractograms are collected using a PANalytical X-ray diffractometer. Initial sample sizes for each material are on the order of 200 mg and are able to fill a bulk XRD sample holder and are collected prior to activation. However, due to size limitations of the gravimetric adsorption sample pan, reactivated samples are on the order of 50mg. With the available p-XRD equipment, the smaller sample size required the use of a low-background sample holder for the reactivated samples. From previous experience with the equipment we have noted that the intensities often vary with the change in XRD sample pan size. Therefore, the peak position and relative peak heights are examined to confirm structure retention. Diffractograms are collected under ambient conditions, and humidity exposure is minimized via storage in sealed vials. Nitrogen adsorption isotherms at 77 K were measured for each MOF before and after water exposure using a Quantachrome Quadrasorb system.

4.3 Results and Discussion

Figure 4.1 shows water adsorption and desorption isotherms for HKUST-1 and Mg MOF-74 at 298 K. As expected, both open metal site materials exhibit a strong affinity for water, with loadings of 33 and 37 mmol/g for HKUST-1 and Mg MOF-74,

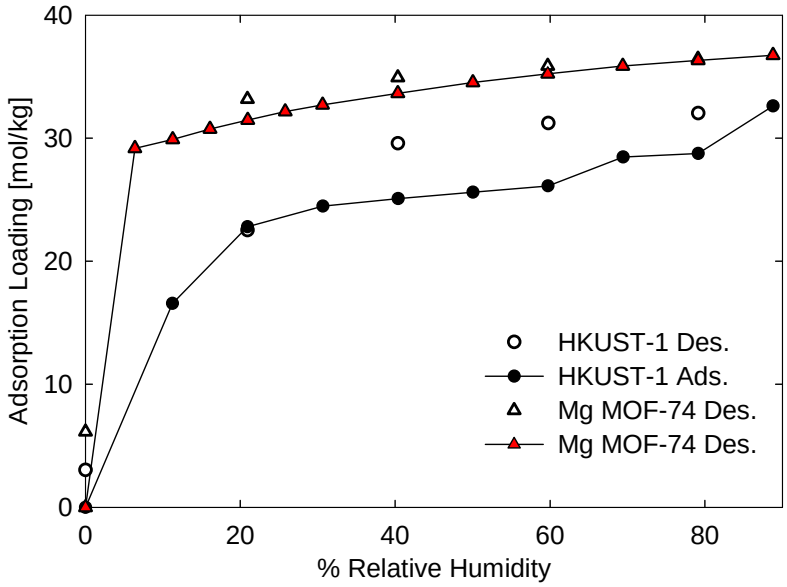

Figure 4.1. Water adsorption and desorption isotherms for open-metal site MOFs, HKUST-1 and Mg MOF-74, at 298 K and 1 bar.

respectively at ~ 90% RH. These results are consistent with previous reports that open-metal site MOFs have high affinities for small molecules containing accessible lone pairs of electrons such as CO_2 and H_2O.[3,19,33,34,38] In agreement with the findings of Kaskel et al.,[19] the hysteresis curves show that a portion of the water cannot be desorbed under flowing dry air. At 0% relative humidity Mg MOF-74 retains more water than HKUST-1 upon desorption; Mg MOF-74 retains 17% of maximum uptake compared to 9% retained by HKUST-1.

Water adsorption plots for UiO-66, DMOF-1, and the amine-functionalized analogues are shown in Figure 4.2. Of these four MOFs the zirconium based UiO-66 and amine-functionalized analogue exhibit the highest water uptake at humidity levels greater than or equal to 30% RH. UiO-66 adsorbs relatively little water below 20% RH but then exhibits a sharp step in the isotherm in which adsorption loadings increase from 3 to 16

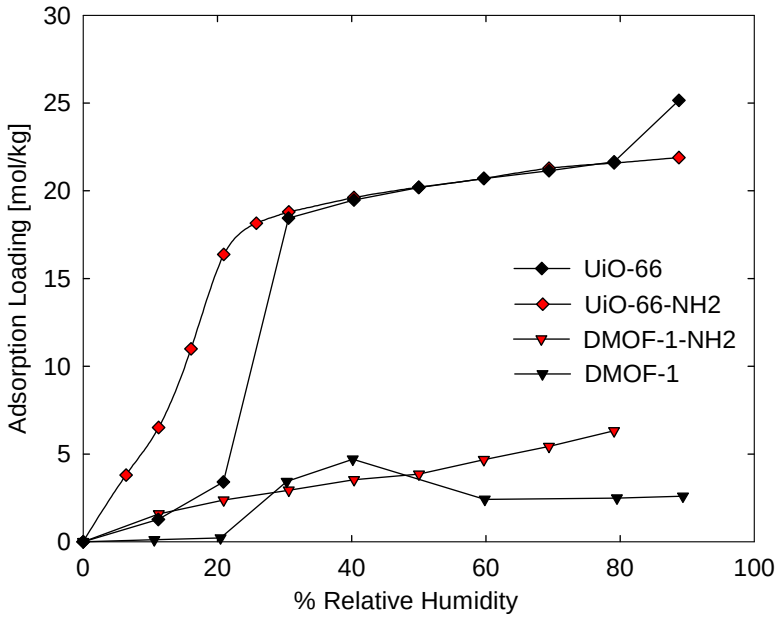

Figure 4.2. Water adsorption isotherms for parent materials, UiO-66 and DMOF-1, along with their amine-functionalized analogues, UiO-66-NH_2 and DMOF-1-NH_2, at 298 K and 1 bar.

mmol/g. This MOF has been reported to undergo a transition from the as-synthesized 8-coordinated state to 7-coordinated upon dehydroxylation.[16] The observed step in the isotherm may correspond to a transition back to the 8-coordinated state, but the step is more likely attributed to capillary condensation also reported by Llewellyn et al.[32] This

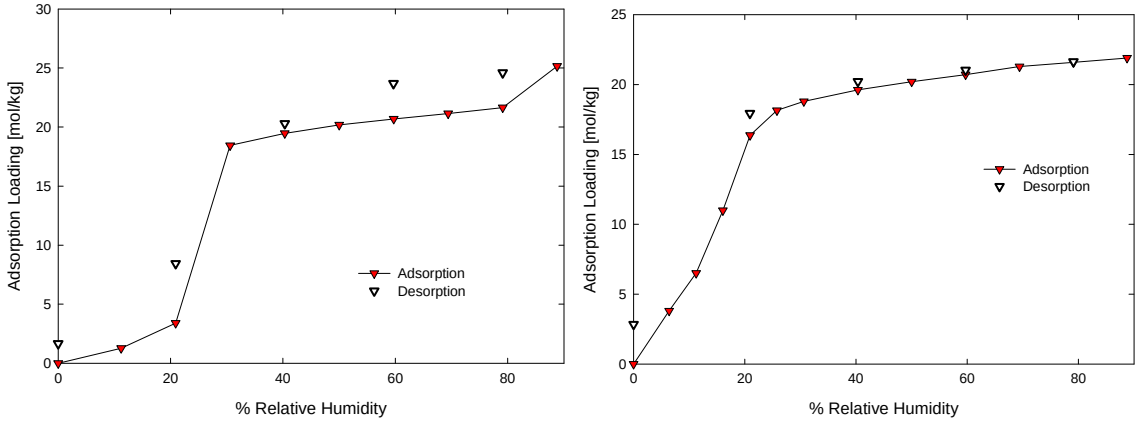

Figure 4.3. Water adsorption and desorption for materials, UiO-66 (left) and UiO-66-NH_2 (right) at 298 K and 1 bar.

point will be revisited in later discussion. The desorption isotherms of UiO-66 and UiO-6-NH_2, Figure 4.3, exhibit hysteresis indicative of the inability to remove a portion of the water under flowing dry air. At 0% RH, UiO-66 and UiO-66-NH_2 retain 1.7 and 2.8 mmol H_2O/g, respectively, which suggests rehydroxylation of the samples during water adsorption and is in agreement with the reported results from Llewellyn and coworkers.[32] For UiO-66-NH_2, the adsorption isotherm exhibits more rectangular or Type I behavior below 20% RH compared to the parent material, which along with the increased water retention under dry air flow are indicative of the preferred amine-water interactions. In agreement with what others have reported,[28,38,41] we find that DMOF-1 displays the most hydrophobic character of all the materials in this study up to 20% RH. Above this concentration we see atypical adsorption behavior in agreement with the findings of Liang et al.[38] More specifically, a sharp increase in uptake, which is likely due to capillary condensation occurs at 30% RH followed by a decrease from 40-60% RH. In this case, the loss of adsorbed water despite increasing water vapor concentration is likely an attribute of both the structure loss of the adsorbent itself and the hydrophobic properties of the degradation product, DABCO. DMOF-1-NH_2 exhibits an increase in water adsorption compared to the hydrophobic parent material and does not demonstrate the same loss of adsorbed water. This is likely due to the hydrophilic character of the proposed degradation product, ATPA.

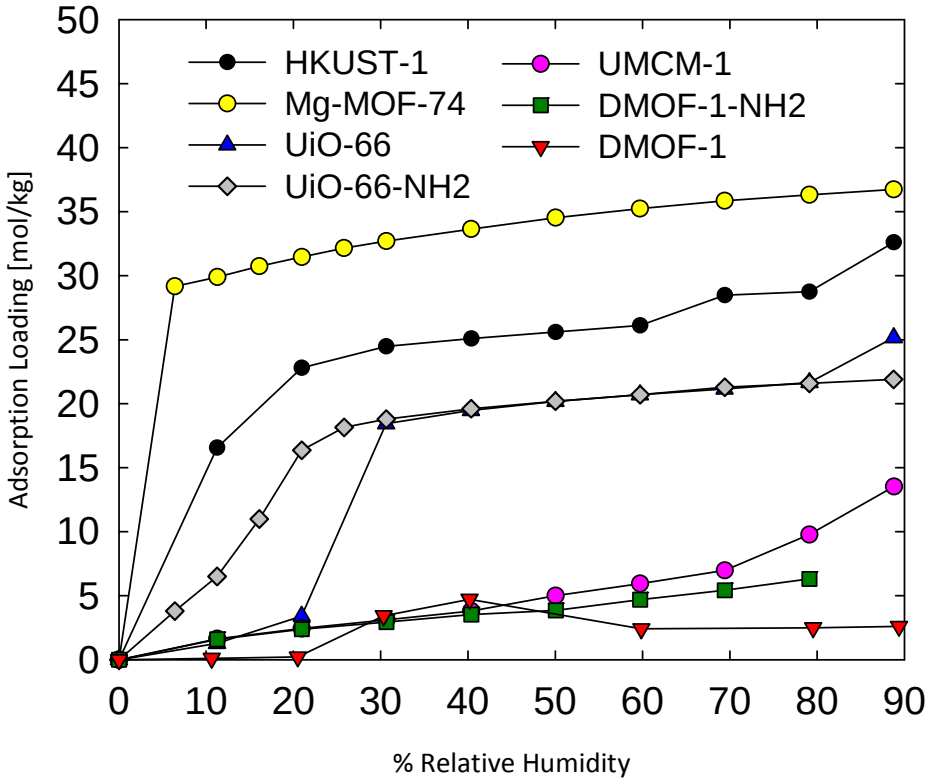

Figure 4.4. Water adsorption isotherms for seven representative MOFs measured at 298 K and 1 bar.

The compilation of adsorption isotherms is shown in Figure 4.4. For the zinc-carboxylate MOF, UMCM-1, the adsorption isotherm nearly mirrors DMOF-1-NH_2 adsorption until 40% RH, but at higher humidity levels there is a more rapid increase in uptake. From a pore volume perspective (2.41 cc/g), the low uptake results for UMCM-1 are surprising.

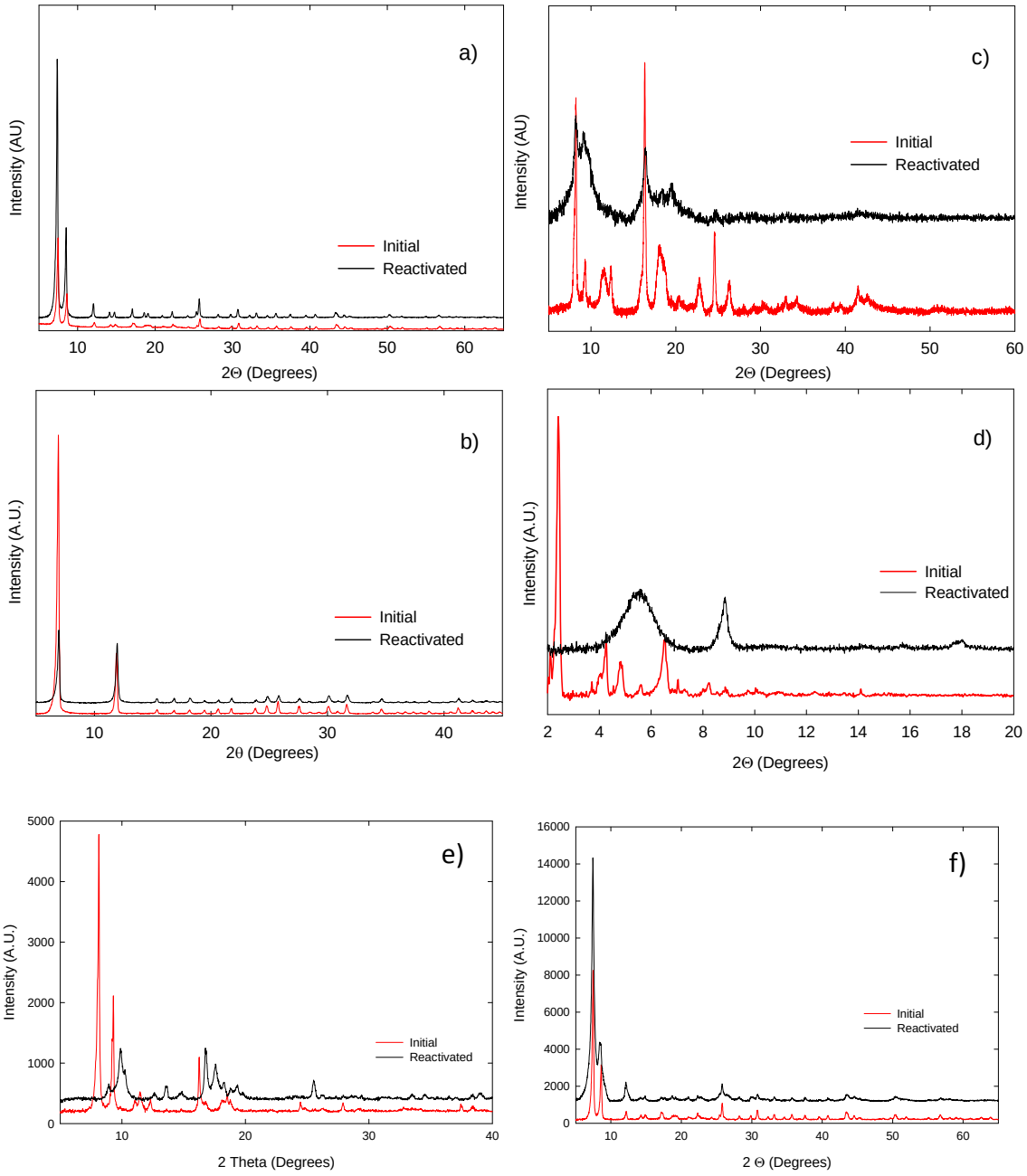
a)
Intensity (AU)
Initial
Reactivated
2Θ (Degrees)
c)
Intensity (AU)
Initial
Reactivated
2Θ (Degrees)
b)
Intensity (A.U.)
Initial
Reactivated
2θ (Degrees)
d)
Intensity (A.U.)
Initial
Reactivated
2Θ (Degrees)
e)
Intensity (A.U.)
Initial
Reactivated
2 Theta (Degrees)
f)
Intensity (A.U.)
Initial
Reactivated
2 Θ (Degrees)

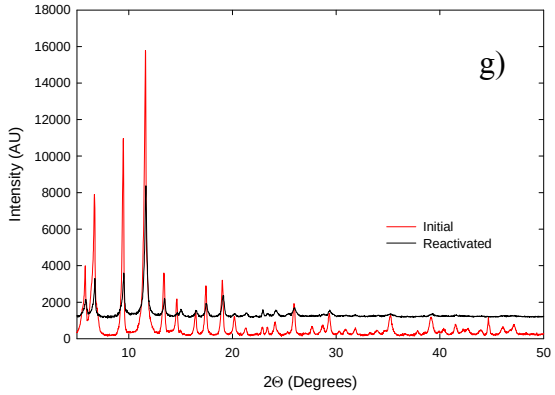

Figure 4.5. pXRD results for (a) UiO-66-NH_2, (b) Mg-MOF-74, (c) DMOF-1-NH_2,(d) UMCM-1, (e) DMOF-1, (f) HKUST-1, and (g) HKUST-1

To examine the possible degradation of the tested materials, powder XRD data were collected for the as-synthesized samples and for the samples exposed to humid conditions and reactivated. Figure 4.5 illustrates the apparent structure retention of UiO-66-NH_2 and Mg-MOF-74 and the significant loss of crystallinity for DMOF-1-NH_2, and UMCM-1. UiO-66 and HKUST-1 also retained their crystallinity based on pXRD, but it is important to note that slight degradation of the structure may not show up in the powder X-ray patterns due to high intensities of the peaks at low angles. The hydrolysis degradation reaction appears to describe the UMCM-1 structure loss; at higher values of 2Θ there is evidence of $Zn(OH)_2$, which is a direct product of this reaction.[21] The degradation of UMCM-1 is not surprising considering that the coordination environment (zinc acetate) is identical to MOF-5, which is well known to decompose under humid conditions. The significant loss of crystallinity in the DMOF-1 materials is somewhat surprising considering the hydrophobic nature of the parent material under low relative humidity and the relatively high pK_a of the DABCO ligand. However, the zinc-carboxylate coordination is notoriously unstable and likely the weakest link which initiates the framework collapse, in spite of the Zn-N coordination from the DABCO ligand.

Further support of the stability analysis is captured by BET surface area analysis of the initial and reactivated samples. These results are shown in Table 2. The water uptake at 80% RH for each MOF does not directly correlate with pore volume or diameter.

Table 4.2. Adsorption loadings at 80% relative humidity and BET surface area comparison of samples before water exposure and after isotherm measurement and reactivation.

Material	Pore Volume[†] (cc/g)	Pore Diameter (Å)	Loading, 80%RH[‡] (cc/g)	Surface Area (m^2/g) Before	After	% Loss
Mg-MOF-74*	0.65	11	0.62	1400	238	83
UiO-66-NH_2	0.57	< 6	0.37	1040	1050	0
UiO-66	0.52	~ 6	0.37	1160	1130	2
DMOF-1	0.58	7.5 x 7.5; 4.8 x 3.2	0.04	1960	7	100
DMOF-1-NH_2	0.58	7.5 x 7.5; <4.8 x 3.2	0.11	2010	0	100
HKUST-1*	0.62	9; 6	0.49	1270	945	26
UMCM-1	2.41	27 x 32; 14 x 17	0.11	6010	205	97

*Contains open metal sites

[†]Obtained from the Dubinin-Astakov model of N_2 adsorption at 77K

[‡]Condensation effects observed at higher humidity levels

Instead, site preferences and degradation dictate the water adsorption. For example, the open metal site materials with relatively small pore volumes, HKUST-1 and Mg MOF-74, show significantly higher uptake than UMCM-1. This is due to the open-metal site MOFs' affinity for water and also due to the degradation of UMCM-1. Similarly, DMOF-1 and DMOF-1-NH_2 have significantly lower water uptakes of 0.04 and 0.11 cc/g at 80% RH, respectively compared to their accessible pore volumes of 0.58 cc/g from N_2 adsorption at 77 K. This is attributed to the degradation of DMOF-1 and DMOF-1-NH_2 throughout the water isotherm collection, which is in agreement with the PXRD data

(Figure 4.5). The increased water uptake exhibited by the amine-functionalized version is likely due to the hydrophilic character of the ATPA ligand itself. In agreement with PXRD results, UiO-66 and the amine-functionalized analogue display negligible loss of surface area. Water uptakes of 0.37 cc/g at 80% RH for both UiO-66 and UiO-66-NH_2 match well with the value previously reported.[32] Nevertheless, these water uptakes are less than pore volumes obtained via N_2 adsorption. This is likely an attribute of the rehydroxylation of the materials during water exposure. BET modeling of the N_2 adsorption at 77 K for UMCM-1 confirm the degradation apparent in the XRD analysis, showing almost total loss in surface area. Despite structure confirmation via XRD, both of the open metal site MOFs undergo significant reduction in surface area. HKUST-1 and Mg MOF-74 show 26 and 83% loss, respectively. Kaskel et al.[19] also report a significant loss in BET surface area, 48%, for HKUST-1 following water adsorption and reactivation. The Dietzel group show the complete stability of MOF-74 materials during cyclic dehydration/rehydration experiments under inert atmosphere, [22,24] but Ni MOF-74 was shown to degrade during identical testing in the presence of oxygen.[23] The dehydration or reactivation procedure of our study utilized dynamic vacuum, which may have prevented oxygen exposure from contributing to structure degradation. However, since air was used as a carrier gas, the entrained oxygen in the adsorbed water appears to sufficiently supply the degradation reaction during reactivation. However, this could not be determined conclusively from the available data.

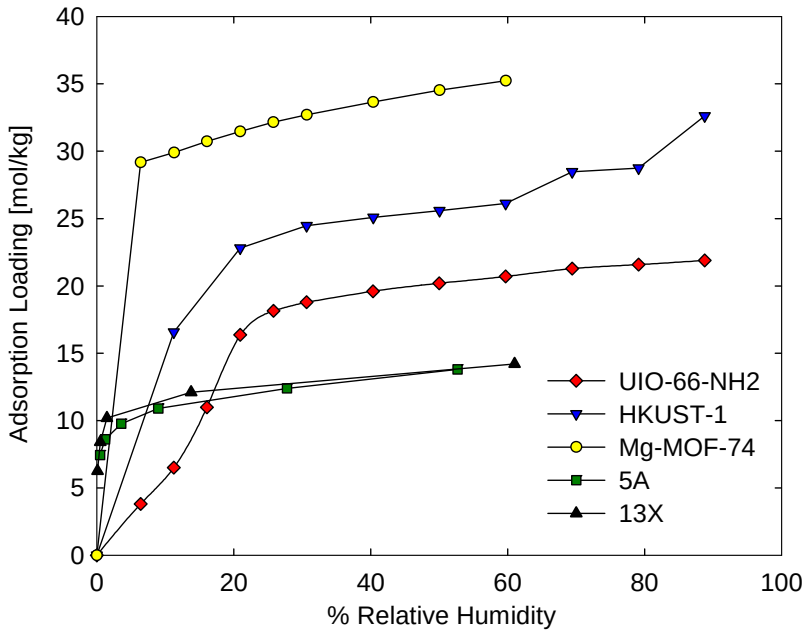

Figure 4.6. Water adsorption isotherms for UiO-66-NH_2, HKUST-1, and Mg MOF-74 compared with zeolites 5A and 13X from Wang et. al.,[37] all at 298 K.

Greater insight into water adsorption behavior of MOFs can be gained by comparing our results with adsorption in traditional porous materials. Adsorption isotherms for UiO-66-NH_2, Mg MOF-74, and HKUST-1 are compared in Figure 4.6. with water adsorption in zeolites[42] 5A and 13X. The calcium and sodium cations in 5A and 13X, respectively, provide strong adsorption sites for water at low relative pressure. The more rectangular Type I isotherms are indicative of this behavior. The MOFs with open-metal sites show analogous hydrophilicity but have much higher saturation loadings compared to the zeolites due to larger pore volumes. The rectangular Type I isotherm for UiO-66-NH_2 compared to the parent material (Figure 4.2) illustrates the favorable impact of amino functional groups on water adsorption.

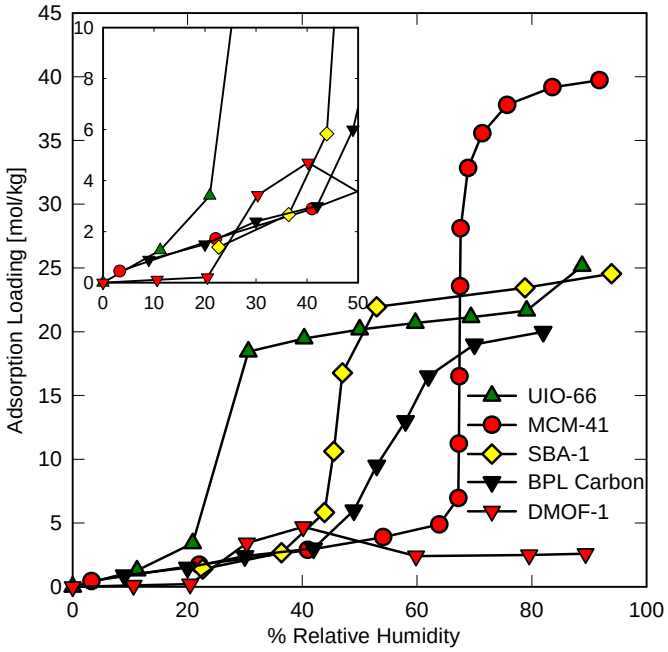

Figure 4.7. Water adsorption isotherms for UiO-66 (298 K) compared with MCM-41 (293 K), SBA-1 (293 K) and BPL carbon (298 K).

A comparison of water isotherms for UiO-66 and DMOF-1 with BPL carbon[43] and mesoporous silicas[44] MCM-41 and SBA-1 is shown in Figure 5. These materials exhibit Type V isotherms, which are characteristic of water adsorption by capillary condensation. The condensation step occurs first for UiO-66, which has pore sizes of ca. 6 Å and is immediately followed by DMOF-1, with 7.5 Å and 4.5 x 3.8 Å pores. SBA-1 (21 Å pores) undergoes condensation at the next lowest pressure, followed by BPL carbon, which possesses a distribution of pore sizes (6-18 Å). Capillary condensation occurs last for the largest-pore material (30 Å) MCM-41. It is difficult to decouple the effects of pore size, local functionalization, and wetting on the adsorption behavior. However, in the absence of highly favorable adsorption sites (e.g., cations or open metal sites), adsorption of water within a porous structure will occur primarily though capillary condensation. This condensation arises due to the overlapping potential of the pore walls

and will be dictated by the size of the pore. Thus, capillary condensation, or the step in the isotherm, will occur at the lowest relative pressure of water for the material with the smallest pores. For materials with no local functionalization of the pore space, water will have stronger interactions within the bulk liquid state than with the surface. Because of this, condensation will not occur until the bulk pressure is higher than the saturation vapor pressure (i.e., $P/P_0 > 1$).[45,46] On the other hand, local functionalization or heterogeneity of the surface will lead to adsorption of water at lower pressures. The adsorbed water molecules then provide stable hydrogen-bonding networks within the pores, which consequently lead to adsorption saturation below P_0.[45,46]

Mesoporous silicas and activated carbons typically have some degree of local functionalization in the form of silanol groups, carbonyls, etc. UiO-66 has no analogous functionalization, but the small pore size and metal oxide cluster most likely contribute to apparent condensation at 20% RH. The desorption isotherm of UiO-66 (Fig. S8) exhibits low pressure hysteresis that is similar to the H1 classification, which indicates the presence of micropores.[47] DMOF-1 possesses micropores with diameters similar to UiO-66 and exhibits capillary condensation at nearly the same point, ca. 20% RH. However, the indicative water adsorption step is less significant in DMOF-1, and the desorption data are not capable of confirming the capillary condensation due to the complete framework collapse which occurs during the water adsorption above 40% RH.

4.4 Conclusion

In summary, we have performed an investigation of water vapor adsorption and subsequent structural analysis of a representative set of metal-organic frameworks. The

crystal structure of UMCM-1 was completely degraded after water exposure and regeneration. This instability is attributed to the four-coordinated zinc-carboxylate system. The amine-functionalized and parent forms of DMOF-1 also exhibited a complete loss of crystallinity after water exposure at 90% RH. Both the parent and functionalized UiO-66 show good structural stability via complete pXRD peak agreement and negligible BET surface area loss. This is attributed to the higher stability of the Zr inorganic cluster. The adsorption behavior of UiO-66 and DMOF-1 are analogous to capillary condensation in heterogeneous pore spaces of mesoporous silicas and carbons. MOFs with open-metal sites strongly bind water and exhibit isotherm shapes similar to zeolites 5A and 13X. These MOFs are difficult to regenerate after water exposure by heating under vacuum. PXRD patterns suggest that the crystalline structures are retained to some extent, but BET surface areas of the materials decreased substantially and are indicative of some structure loss during the adsorption-reactivation process likely due to the use of dry air as the carrier gas. Oxygen exposure itself or the presence of entrained oxygen in the adsorbed water phase may facilitate the degradation. Additional studies of water adsorption in MOFs with a wide range of metals and ligands are necessary to truly develop design criteria for synthesizing stable materials. Nevertheless, this work proves that careful choice of coordination environment can lead to robust MOFs with water adsorption behavior that is comparable to conventional adsorbents such as zeolites and activated carbon.

4.5 References

1. Ferey, G. Some Suggested Perspectives for Multifunctional Hybrid Porous Solids. *Dalton Trans.* **2009**, 4400.

2. Kuppler, R. J.; Timmons, D. J.; Fang, Q. R.; Li, J. R.; Makal, T. A.; Young, M. D.; Yuan, D. Q.; Zhao, D.; Zhuang, W. J.; Zhou, H. C. Potential Applications of Metal-Organic Frameworks. *Coord. Chem. Rev.* **2009**, *253*, 3042.

3. Caskey, S. R.; Wong-Foy, A. G.; Matzger, A. J. Dramatic Tuning of Carbon Dioxide Uptake via Metal Substitution in a Coordination Polymer with Cylindrical Pores. *J. Am. Chem. Soc.* **2008**, *130*, 10870.

4. Rowsell, J. L. C.; Yaghi, O. M. Effects of Functionalization, Catenation, and Variation of the Metal Oxide and Organic Linking Units on the Low-Pressure Hydrogen Adsorption Properties of Metal-Organic Frameworks. *J. Am. Chem. Soc.* **2006**, *128*, 1304.

5. Wang, Z. Q.; Tanabe, K. K.; Cohen, S. M. Tuning Hydrogen Sorption Properties of Metal-Organic Frameworks by Postsynthetic Covalent Modification. *Chem.-Eur. J.* **2010**, *16*, 212.

6. Farha, O. K.; Hupp, J. T. Rational Design, Synthesis, Purification, and Activation of Metal-Organic Framework Materials. *Acc. Chem. Res.* **2010**, *43*, 1166.

7. Tanabe, K. K.; Cohen, S. M. Postsynthetic Modification of Metal-Organic Frameworks-a Progress Report. *Chem. Soc. Rev.* **2011**, *40*, 498.

8. Li, J. R.; Kuppler, R. J.; Zhou, H. C. Selective Gas Adsorption and Separation in Metal-Organic Frameworks. *Chem. Soc. Rev.* **2009**, *38*, 1477.

9. Huang, L. M.; Wang, H. T.; Chen, J. X.; Wang, Z. B.; Sun, J. Y.; Zhao, D. Y.; Yan, Y. S. Synthesis, Morphology Control, and Properties of Porous Metal-Organic Coordination Polymers. *Microporous Mesoporous Mat.* **2003**, *58*, 105.

10. Greathouse, J. A.; Allendorf, M. D. The Interaction of Water with MOF-5 Simulated by Molecular Dynamics. *J. Am. Chem. Soc.* **2006**, *128*, 10678.

11. Kaye, S. S.; Dailly, A.; Yaghi, O. M.; Long, J. R. Impact of Preparation and Handling on the Hydrogen Storage Properties of Zn4O(1,4-benzenedicarboxylate)(3) (MOF-5). *J. Am. Chem. Soc.* **2007**, *129*, 14176.

12. Wu, T. J.; Shen, L. J.; Luebbers, M.; Hu, C. H.; Chen, Q. M.; Ni, Z.; Masel, R. I. Enhancing the Stability of Metal-Organic Frameworks in Humid Air by Incorporating Water Repellent Functional Groups. *Chem. Commun. (Cambridge, U.K.)* **2010**, *46*, 6120.

13. Hausdorf, S.; Wagler, J.; Mossig, R.; Mertens, F. Proton and Water Activity-Controlled Structure Formation in Zinc Carboxylate-Based Metal Organic Frameworks. *J. Phys. Chem. A* **2008**, *112*, 7567.

14. Choi, H. J.; Dinca, M.; Dailly, A.; Long, J. R. Hydrogen Storage in Water-Stable Metal-Organic Frameworks Incorporating 1,3-and 1,4-benzenedipyrazolate. *Energy & Environmental Science* **2010**, *3*, 117.

15. Park, K. S.; Ni, Z.; Cote, A. P.; Choi, J. Y.; Huang, R. D.; Uribe-Romo, F. J.; Chae, H. K.; O'Keeffe, M.; Yaghi, O. M. Exceptional Chemical and Thermal Stability of Zeolitic Imidazolate Frameworks. *Proc. Natl. Acad. Sci. U. S. A.* **2006**, *103*, 10186.

16. Cavka, J. H.; Jakobsen, S.; Olsbye, U.; Guillou, N.; Lamberti, C.; Bordiga, S.; Lillerud, K. P. A New Zirconium Inorganic Building Brick Forming Metal Organic Frameworks with Exceptional Stability. *J. Am. Chem. Soc.* **2008**, *130*, 13850.

17. Ehrenmann, J.; Henninger, S. K.; Janiak, C. Water Adsorption Characteristics of MIL-101 for Heat-Transformation Applications of MOFs. *Eur. J. Inorg. Chem.* **2011**, 471.

18. Akiyama, G.; Matsuda, R.; Kitagawa, S. Highly Porous and Stable Coordination Polymers as Water Sorption Materials. *Chem. Lett.* **2010**, *39*, 360.

19. Kusgens, P.; Rose, M.; Senkovska, I.; Frode, H.; Henschel, A.; Siegle, S.; Kaskel, S. Characterization of Metal-Organic Frameworks by Water Adsorption. *Microporous Mesoporous Mat.* **2009**, *120*, 325.

20. Cychosz, K. A.; Matzger, A. J. Water Stability of Microporous Coordination Polymers and the Adsorption of Pharmaceuticals from Water. *Langmuir* **2010**, *26*, 17198.

21. Low, J. J.; Benin, A. I.; Jakubczak, P.; Abrahamian, J. F.; Faheem, S. A.; Willis, R. R. Virtual High Throughput Screening Confirmed Experimentally: Porous Coordination Polymer Hydration. *J. Am. Chem. Soc.* **2009**, *131*, 15834.

22. Dietzel, P. D. C.; Morita, Y.; Blom, R; Fjellvag, H. An In Situ High-Temperature Single-Crystal Investigation of a Dehydrated Metal-Organic Framework Compound and Field-Induced Magnetization of One-Dimensional Metal-Oxide Chains. *Angew. Chem., Int. Ed.* **2005**, 44, 6354-6358.

23. Dietzel, P. D. C.; Panella, B.; Hirscher, M.; Blom, R.; Fjellvag, H. Hydrogen Adsorption in a Nickel Based Coordination Polymer with Open Metal Sites in the Cylindrical Cavities of the Desolvated Framework. *Chem. Commun. (Cambridge, U.K.)* **2006**, 959-961.

24. Dietzel, P. D. C.; Blom, R.; Fjellvag, H. Base-Induced Formation of Two Magnesium Metal-Organic Framework Compounds with a Bifunctional Tetratopic Ligand. *Eur. J. Inorg. Chem.* **2008**, 3624-3632.

25. Chui, S. S. Y.; Lo, S. M. F.; Charmant, J. P. H.; Orpen, A. G.; Williams, I. D. A Chemically Functionalizable Nanoporous Material Cu-3(TMA)(2)(H2O)(3) (n). *Science (Washington, DC, U. S.)* **1999**, *283*, 1148.

26. Rosi, N. L.; Kim, J.; Eddaoudi, M.; Chen, B. L.; O'Keeffe, M.; Yaghi, O. M. Rod Packings and Metal-Organic Frameworks Constructed from Rod-Shaped Secondary Building Units. *J. Am. Chem. Soc.* **2005**, *127*, 1504.

27. Garibay, S. J.; Cohen, S. M. Isoreticular Synthesis and Modification of Frameworks with the UiO-66 Topology. *Chem. Commun. (Cambridge, U.K.)* **2010**, *46*, 7700.

28. Lee, J. Y.; Olson, D. H.; Pan, L.; Emge, T. J.; Li, J. Microporous Metal-Organic Frameworks with High Gas Sorption and Separation Capacity. *Adv. Funct. Mater.* **2007**, *17*, 1255.

29. Koh, K.; Wong-Foy, A. G.; Matzger, A. J. A Crystalline Mesoporous Coordination Copolymer with High Microporosity. *Angew. Chem., Int. Ed.* **2008**, *47*, 677.

30. Zlotea, C.; Phanon, D.; Mazaj, M.; Heurtaux, D.; Guillerm, V.; Serre, C.; Horcajada, P.; Devic, T.; Magnier, E.; Cuevas, F.; Ferey, G.; Llewellyn, P. L.; Latroche, M. Effect of NH(2) and CF(3) functionalization on the hydrogen sorption properties of MOFs. *Dalton Trans.*, **2011**, 40, 4879.

31. Valenzano, L.; Civalleri, B.; Chavan, S.; Bordiga, S.; Nilsen, M. H.; Jakobsen, S.; Lillerud, K. P.; Lamberti, C. Disclosing the Complex Structure of UiO-66 Metal Organic Framework: A Synergic Combination of Experiment and Theory. *Chem. Mater.* **2011**, 23, 7, 1700-1718.

32. Wiersum, A. D.; Soubeyrand-Lenoir, E.; Yang, Q. Y.; Moulin, B.; Guillerm, V.; Ben Yahia, M.; Bourrely, S.; Vimon, A.; Miller, S.; Vagner, C.; Daturi, M.; Clet, G.; Serre, C.; Maurin, G.; Llewellyn, P. L. An Evaluation of UiO-66 for Gas-Based Applications. *Chem.--Asian J.* **2011**, 6, 12, 3270-3280.

33. Keskin, S.; van Heest, T. M.; Sholl, D. S. Can Metal-Organic Framework Materials Play a Useful Role in Large-Scale Carbon Dioxide Separations? *ChemSusChem* **2010**, *3*, 879.

34. Liu, J.; Wang, Y.; Benin, A. I.; Jakubczak, P.; Willis, R. R.; LeVan, M. D. CO2/H2O Adsorption Equilibrium and Rates on Metal-Organic Frameworks: HKUST-1 and Ni/DOBDC. *Langmuir* **2010**, *26*, 14301.

35. Millward, A. R.; Yaghi, O. M. Metal-Organic Frameworks with Exceptionally High Capacity for Storage of Carbon Dioxide at Room Temperature. *J. Am. Chem. Soc.* **2005**, *127*, 17998.

36. Wang, Q. M.; Shen, D. M.; Bulow, M.; Lau, M. L.; Deng, S. G.; Fitch, F. R.; Lemcoff, N. O.; Semanscin, J. Metallo-Organic Molecular Sieve for Gas Separation and Purification. *Microporous Mesoporous Mat.* **2002**, *55*, 217.

37. Glover, T. G.; Peterson, G. W.; Schindler, B. J.; Britt, D.; Yaghi, O. MOF-74 Building Unit Has a Direct Impact on Toxic Gas Adsorption. *Chem. Eng. Sci.* **2011**, *66*, 163.

38. Liang, Z. J.; Marshall, M.; Chaffee, A. L. CO2 Adsorption, Selectivity and Water Tolerance of Pillared-Layer Metal Organic Frameworks. *Microporous MesoporousMat.* **2010**, *132*, 305.

39. Wang, Z. Q.; Tanabe, K. K.; Cohen, S. M. Accessing Postsynthetic Modification in a Series of Metal-Organic Frameworks and the Influence of Framework Topology on Reactivity. *Inorg. Chem. (Washington, DC, U. S.)* **2009**, *48*, 296.

40. Mu, B.; Schoenecker, P. M.; Walton, K. S. Gas Adsorption Study on Mesoporous Metal-Organic Framework UMCM-1. *J. Phys. Chem. C* **2010**, *114*, 6464.

41. Chen, Y. F.; Lee, J. Y.; Babarao, R.; Li, J.; Jiang, J. W. A Highly Hydrophobic Metal Organic Framework Zn(BDC)(TED)(0.5) for Adsorption and Separation of CH3OH/H2O and CO2/CH4: An Integrated Experimental and Simulation Study. *J. Phys. Chem. C* **2010**, *114*, 6602.

42. Wang, Y.; Levan, M. D. Adsorption Equilibrium of Carbon Dioxide and Water Vapor on Zeolites 5A and 13X and Silica Gel: Pure Components. *J. Chem. Eng. Data* **2009**, *54*, 2839.

43. Rudisill, E. N.; Hacskaylo, J. J.; Levan, M. D. Coadsorption of Hydrocarbons and Water on BPL Activated Carbon. *Ind. Eng. Chem. Res.* **1992**, *31*, 1122.

44. Oh, J. S.; Shim, W. G.; Lee, J. W.; Kim, J. H.; Moon, H.; Seo, G. Adsorption Equilibrium of Water Vapor on Mesoporous Materials. *J. Chem. Eng. Data* **2003**, *48*, 1458.

45. Liu, J. C.; Monson, P. A. Does Water Condense in Carbon Pores? *Langmuir* **2005**, *21*, 10219.

46. Monson, P. A. Contact Angles, Pore Condensation, and Hysteresis: Insights from a Simple Molecular Model. *Langmuir* **2008**, *24*, 12295.

47. Sing, K. S. W.; Everett, D. H.; Haul, R. A. W.; Moscou, L.; Pierotti, R. A.; Rouquerol, J.; Siemieniewska, T. Reporting Physisorption Data for Gas Solid Systems with Special Reference to the Determination of Surface-Area and Porosity (Recommendations 1984). *Pure Appl. Chem.* **1985**, *57*, 603.

CHAPTER 5

UIO-66-NH_2 SYNTHESIS SCALE-UP AND CRYSTALLIZATION PROCESS DESIGN

Reproduced from Paul M. Schoenecker, G. A. Belancik, B. E. Grabicka, and K.S. Walton. AIChE Journal. doi: AIChE-12-14240.R1

5.1 Introduction

Metal-organic framework (MOF) synthesis and characterization have increased exponentially in recent years. As a family of porous-crystalline materials, MOFs provide a multitude of pore geometries, connectivities, and chemical functionalities that can be further tuned by post-synthetic modification (PSM). Due in part to the nearly infinite structure possibilities, MOFs exhibit potential for a plethora of applications including gas separation and storage,[1-5] catalysis,[6,7] drug delivery,[8-10] and thin film applications.[11,12] Amine-functionalized MOFs including IRMOF-3, DMOF-1-NH_2, and UiO-66-NH_2 are of particular importance for many applications. The amine-functionality proves beneficial for selective gas adsorption[13] and NO delivery[14] as well as facilitating PSM via anhydride substitution.[15,16]

The reported water sensitivity of certain MOFs[17-20] and the subsequent concern that MOF performance tends to decrease under humid conditions has hindered the transition of these materials to an applied level. However, recent reports have emerged of materials capable of withstanding water exposure, including nitrogen-coordinated and highly-coordinated MOFs.[13,21-23] In addition to a high degree of water stability, the amine-

functionalized analogue of UiO-66 is expected to exhibit a similar degree of chemical and mechanical stability reported for the parent material.[24] This will be highly advantageous not only for harsh environment applications but filtration applications in general, where the ability to press pellets of materials with minimal or no binder required can significantly reduce the pressure drop across the filter without sacrificing adsorption capacity.

Despite being a viable option for many applications, few MOFs are currently commercially available.[25] Sigma-Aldrich currently offers four MOFs from BASF: Basolite® A100, C300, F300, and Z1200, which are priced up to $28.75/g.[26] With the exception of C300, these MOFs are versions of well known structures from the literature: Al MIL-53[27] (A100), HKUST-1[28] or CuBTC (C300), FeBTC (F300), and ZIF-8[22] (Z1200). ZIF-8 (Z1200) is one of the most well known chemically stable MOFs and is reportedly resistant to humid environments,[29] aqueous solutions,[30] as well as heated alkanes and other organic solvents.[22] FeBTC (F300) shows potential for separation applications,[31] but little is reported on the structure itself, except that it shows amorphous XRD behavior[32] with an empirical formula, which is not analogous to C300.[31] Two of the commercially available structures demonstrate some degree of instability during water exposure. Al MIL-53 (A100) has recently been shown to lose crystallinity and surface area upon immersion in deionized water and is reportedly less chemically stable than the Cr-analogue of MIL-53.[33] After solvent removal, HKUST-1 (C300) exhibits Lewis-acid behavior via open-metal sites, which demonstrates specific benefits for selective gas adsorption[34] but is reported to degrade in the presence of water vapor.[23,29,35]

From a current literature review, it is apparent that further MOF synthesis process development is necessary to decrease the cost of manufacturing if MOFs are to compete in the adsorbent market, which is valued around $3 billion annually.[36] Most current patent literature regarding MOF synthesis applies to the use of particular ligands or metals to form families of MOFs. Other patents and patent applications cover particular applications of MOFs (e.g. Liquid adsorption,[37] CO_2 separation[38], nano-MOFs[39]). A few others apply to non-conventional MOF synthesis techniques including microwave[40] and electrochemical.[41,42] However, to the best of our knowledge there are no current research articles, patents, or patent applications covering the synthesis of MOFs via conventional heating in continuous-flow reactors. The design and implementation of continuous-flow MOF synthesis processes will lead to significant cost reduction and increased material production via reduced down-time.

BASF has made significant contributions to the scale-up of MOF syntheses by developing two novel methods for synthesizing MOFs[41-44] and successfully conducting the 'First Industrial-Scale MOF Synthesis.'[44] The electrochemical synthesis technique[41,42] patented by BASF is reportedly able to provide a continuous-flow of products via a recirculation pump with only periodic interruptions to replenish the metal anode. Alleviated safety concerns are cited as a main benefit compared to standard solvothermal synthesis techniques. Specifically, nitrate-containing metal-salts in large quantities of heated organic solvents pose a significant industrial hazard. However, many other metal-salts are used to synthesize MOFs. Also, metal anodes can be a less cost effective source of metal ions compared to their metal-salts analogues. The 'solvent-free' synthesis technique[43] addresses a prominent cost and environmental concern of many

MOF syntheses by forming the MOF directly in the organic acid itself, therefore eliminating the use of large quantities of solvents required for most solvothermal syntheses, which can be cost prohibitive and require additional waste disposal costs and concerns. However, certain organic ligands are difficult if not impossible to maintain in a liquid phase (e.g. terephthalic acid).[45] Despite the direct significance of these techniques, the applicability of any one synthesis method to all MOF structures is unlikely. Therefore, further development of alternative high-throughput MOF synthesis techniques is of paramount importance.

As with development of any novel material, to scale up and optimize a MOF synthesis requires a detailed understanding of the reaction kinetics as well as the characteristics of the intermediate products. Currently a handful of papers address the determination of MOF nucleation and crystal growth rates. Kinetic data for Fe MIL-53 solvothermal syntheses are reported under conventional oven (CE), ultrasound (US), and microwave (MW) heating.[46] From XRD peak area analysis, relative crystallinity plots are used to model the crystal growth and nucleation. They report that nucleation and crystal growth rates trend as follows; US > MW >> CE and exhibit activation energies (E_a) for the convection oven syntheses of 39.2 and 66.4 kJ/mol for the nucleation and growth rates, respectively. Intermediate products undergo further characterization via SEM and appear to be more or less uniform. Others have reported kinetic synthesis results for copper carboxylate structures, HKUST-1 and MOF-14.[47] Modeling of the *in situ* energy-dispersive X-ray diffraction (EDXRD) data also provides nucleation and growth rates for both materials and estimates the nucleation activation energies to be 71.6 and 113.9 kJ/mol for HKUST-1 and MOF-14 respectively. The higher E_{aNuc} of MOF-14 is

attributed to the interpenetrated structure. The importance of synthesis time as well as temperature is demonstrated by the reported degradation of MOF-14 following prolonged exposure to synthesis conditions. Recently, the crystal growth kinetics have been reported for the water-stable Al-based MOFs, CAU-1-NH_2 and CAU-1-$(OH)_2$.[48] The materials were synthesized under microwave-assisted and standard solvothermal methods. Via EDXRD characterization, microwave-assisted syntheses reportedly decreased the crystal growth Ea of both materials slightly. Adsorption characterization was reported for the final CAU-1 products. However, these papers did not characterize the intermediate materials via adsorption testing, which can directly indicate performance differences for specific applications such as gas separation and storage and may differ vastly from the final product despite XRD congruency. A comprehensive understanding of product quality over a range of synthesis times is also vital, when considering the use of traditional flow-through crystallization reactors, which inherently have some degree of non-uniform residence time.

This work aims to develop a systematic approach to scale-up of solvothermal synthesis of UiO-66-NH_2 via convection heating. With the aforementioned benefits of water-stable and amine-functionalized MOFs, we examine the scalability of synthesis techniques within sealed vessels as well as the potential to implement a continuous-flow through reactor. A threefold approach is used to gain insight into the optimal synthesis conditions and process design for this specific MOF. Glass and polytetrafluoroethylene (PTFE) walled vessels are used to examine nucleation site preferences. A kinetic study is conducted by collecting and characterizing intermediate synthesis products at three specific temperatures, and a continuous-flow solvothermal synthesis process is

developed, which incorporates a basic draft-tube type crystallization reactor. Understanding the crystal growth behavior of specific MOFs can facilitate coupling with the well-established field of 'reactive-crystallizers'[49] and provide more efficient means of commercial MOF production. We are convinced that similar iterations of this approach will prove successful for scale-up of other MOF syntheses and identification of potential pitfalls for crystallization of specific MOFs.

5.2 Experimental

5.2.1 Reactant Solution Preparation

All chemicals are procured from Sigma-Aldrich and used without any further purification. Reactant solutions containing equimolar amounts of zirconium(IV) chloride ($ZrCl_4$) and amino-terephthalic acid (ATPA) are dissolved in dimethyl formamide (DMF) with final concentrations identical to those reported for the parent material, UiO-66.[24] The reactant solution is stirred for approximately 15 minutes or until solids are dissolved before being placed in the chosen vessels.

5.2.2 Reaction Vessel Geometry and Material Investigation

To examine the effect of vessel materials and geometries on UiO-66-NH_2 product quantity and quality, solvothermal syntheses are conducted in sealed borosilicate glass and PTFE-lined vessels. From visually noted MOF syntheses trends, vessel material as well as wetted surface area are expected to affect the total product yield and quality. Therefore, vessel dimensions are selected to provide a range of wetted surface area to reactant solution volume ratios (SA/V), and glass and PTFE vessels are chosen to

investigate crystal growth interactions with the representative MOF synthesis vessel materials. In total, nineteen sealed vessels are used for each material including; 5, 10, 20, and 250 mL glass vessels as well as 23, 46, and 125 mL PTFE lined vessels.

An aliquot of the reactant solution described above is placed in each vessel and the solution volume is recorded. All vessels are sealed, placed in a preheated isothermal convection oven, and reacted simultaneously at 393K for the published reaction time of 24 h. After cooling, the resultant products are collected using filter paper and allowed to air-dry. The products are then weighed separately to determine a relative yield (g MOF/ Vol. solution) and characterized via powder XRD (pXRD) to confirm the desired crystal phase. BET modeling of N_2 adsorption at 77K is conducted on the largest scale vessels for comparison to original synthesis results. This initial portion of the study provides direct insight into the UiO-66-NH_2 synthesis scalability and the resultant product characteristics.

5.2.3 Kinetic Study

Two experiments are conducted to examine the crystal-growth reaction kinetics of the solvothermal synthesis. Ten mL aliquots of the reactant solution are placed in 20 mL glass scintillation vials and arranged in three identical sand baths. The baths are then placed in separate preheated convection ovens at 373, 383, and 393 K respectively. Every four hours a triplet set of vials are removed from each sand bath and allowed to cool at ambient temperature. The samples are then transferred from the vials to 15 mL centrifuge tubes and centrifuged using a VanGuard V6500 centrifuge at 3,400 ± 100 rpm[50] for c.a. 10 minutes. The original solvent, DMF, is decanted and replaced with

methanol. The centrifuging, decanting, and solvent exchange process is repeated two days later. The solvent-exchanged samples are allowed to air-dry uniformly and then activated in a vacuum oven for approximately 24 h at 373 K. The activated samples are weighed under ambient conditions to understand the time and temperature dependence of the total product yield. From previous studies of UiO-66-NH_2,[23] weighing under lab ambient conditions will permit significant water vapor adsorption. Therefore, the presented yields are for relative comparison only. All samples are then characterized via pXRD, and the initial and final samples collected at each temperature are characterized by BET modeling of N_2 adsorption at 77 K.

In order to examine the nucleation rate and its temperature dependence, syntheses are conducted under identical conditions to those above, but samples are removed every 15 min before solvent exchange with methanol. Following previously published procedures,[46,47] nucleation rates are determined by the inverse of the synthesis time needed to produce the first Bragg XRD peak and plotted as an Arrhenius plot to predict the activation energy of nucleation, E_{aNuc}.

5.2.4 Continuous-Flow Reactor Design

Stirred-sealed vessel trials are conducted in a 20 mL scintillation vial, 250 mL glass jar, and 2 L PTFE reactor. All vessels are filled with an appropriate amount of the aforementioned reactant solution. Both the vial and jar trials are conducted at 393 K for approximately 24 h. The 20 mL vial synthesis utilizes a magnetic stir bar, hot plate with temperature probe, and sand bath to provide agitation and promote uniform heating respectively. The glass jar synthesis trial is conducted by immersing the jar in a heated

mineral oil bath with temperature probe. Stirring is accomplished using a magnetic stir bar and stir plate. The 2 L PTFE reactor is manufactured from a 6" PTFE bar, and the stirred-sealed synthesis trial is conducted with only a pressure-relief valve (PRV) installed, and no inlet or outlet. The vessel is filled with approximately 1.8 L of reactant solution and sealed by clamping between two aluminum plates. Thermal energy is provided via a drum heater and manually controlled with a variable power supply. The reactant solution temperature is monitored via infrared temperature sensor and maintained at 378-398 K for 12 h. Stirring is accomplished using a large magnetic stir bar and stir plate. The effects of dynamic synthesis conditions on the UiO-66-NH_2 production are examined via pXRD and BET modeling of the N_2 adsorption.

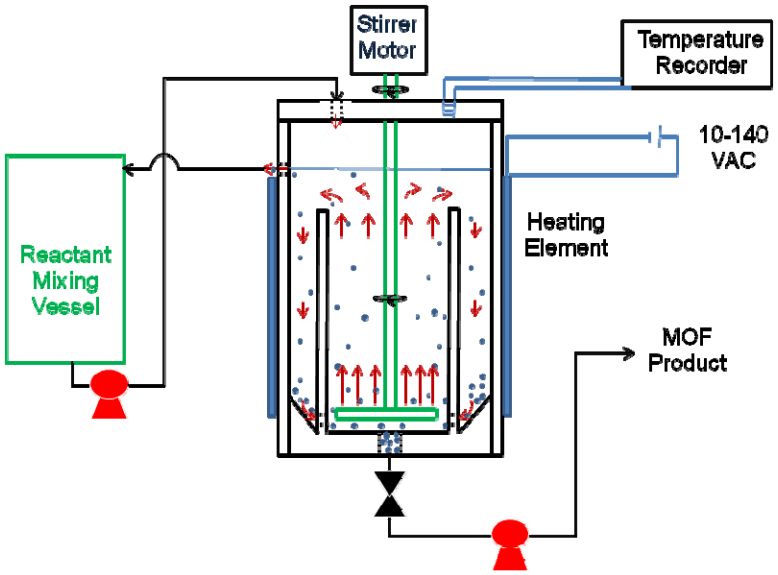

Figure 5.1. Preliminary PFD of the proposed DTB crystallizer-based MOF synthesis process *GTRC ID 5907 Provisional Patent Application: 61/616,746.*

As final proof of the concept presented in invention disclosure *GTRC ID 5970 (Provisional Patent Application: 61/616,746)* illustrated in Figure 5.1, "Continuous-Flow Metal-Organic Framework Crystallization Reactor," the inlet and outlet are drilled and tapped in the 2 L PTFE vessel and a 3" concentric PTFE tube with ¼" holes near the base is added to form an rudimentary draft-tube baffled (DTB) crystallization reactor. Due to materials compatibility concerns ¼" perfluoroalkoxy (PFA) tubing and tube fittings from Swagelok® are utilized throughout the process. The aforementioned drum heater and power supply are again used for heating the continuous-flow crystallization trial. Stir bar agitation is abandoned for an overhead mixer and PTFE coated impeller to provide upward-directed axial flow within the draft-tube with the intent of selectively recirculating the small crystals and mother liquor. The temperature is recorded every 5 minutes via an Extech EasyView 15 Datalogger connected to a Raytech® CI1A infrared temperature sensor with air-purge collar. The reaction vessel is filled with approximately 2 L of reactant solution and heated to 373-393 K for 12 h before flow commences. Then, the inlet from a glass reactant mixing tank containing the reactant solution is opened and the flowrate is set to c.a. 3 mL/min with a calibrated Cole Parmer Masterflex® peristaltic pump equipped with PTFE tubing. Overflow from the reactor is recycled to the reactant mixing tank as a form of level control, reactant tank heating, and source of MOF seed crystals, which may promote a more rapid nucleation rate. The product flow is also initiated and maintained via an identical peristaltic pump at ~2.8 mL/min to maintain an average retention time (τ) of approximately 12 hours and c.a. 7% overflow to feed ratio. The total product is collected in a large vessel and intermediate samples are collected directly from the outlet line every 6 hours, 0.5τ. The synthesis commences under flowing

conditions for 36 h or 3τ following the initial 'priming' of the reactor. Powder XRD patterns are measured for the total bulk product, intermediate samples, and the product retained in the DTB crystallizer upon synthesis completion. Surface area modeling of N_2 adsorption at 77K is reported for the total bulk product and the UiO-66-NH_2 retained within the crystallizer itself. Further optimization and intermediate product characterization are the subjects of ongoing research in our group.

5.2.5 Characterization

All powder X-ray diffractograms were collected using a PANalytical X-ray Diffractometer. For samples less than 100 mg the MOF sample was suspended in methanol and a few drops of the solution were placed on a low-background sample holder. Larger samples were placed in standard pXRD trays. Nitrogen adsorption measurements were performed using a Quadrasorb SI volumetric analyzer manufactured by Quantachrome Instruments. Adsorption isotherms were measured at 77 K over the range of relative pressures from 10^{-6} to 0.995 using high purity nitrogen of 99.998% from Airgas, and the amount adsorbed was determined as a function of the equilibrium pressure. Prior to each adsorption measurement, the sample was outgassed via a FloVac Degasser for approximately 16 h at 473 K and under dynamic vacuum.

5.3 Results and Discussion

5.3.1 Reaction Vessel Geometry and Material Investigation

The results of the reaction vessel material investigation are illustrated in Figure 5.2. The strong linear correlation between yield of UiO-66-NH_2 and reactant solution volume

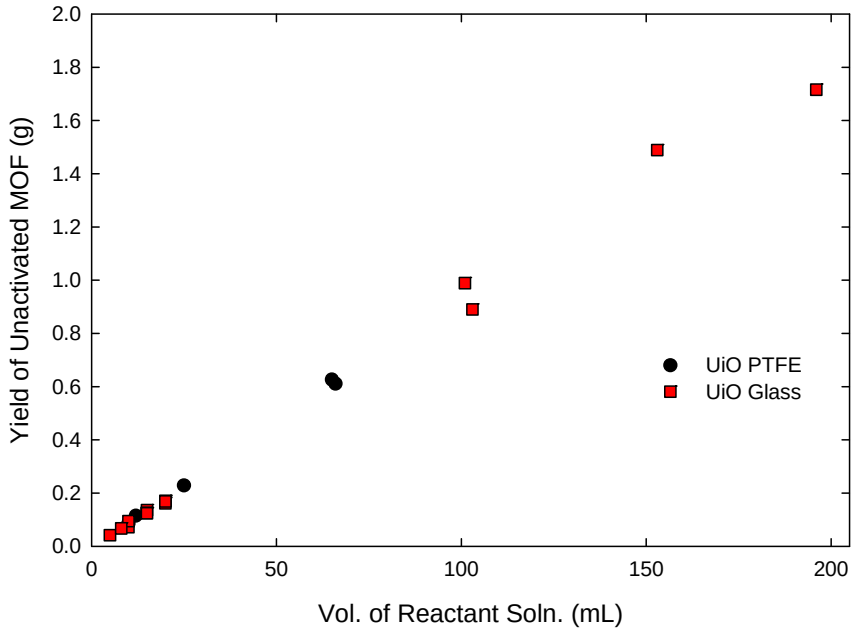

Figure 5.2. Plot of UiO-66-NH_2 yield illustrating direct proportionality to volume of reactant solution

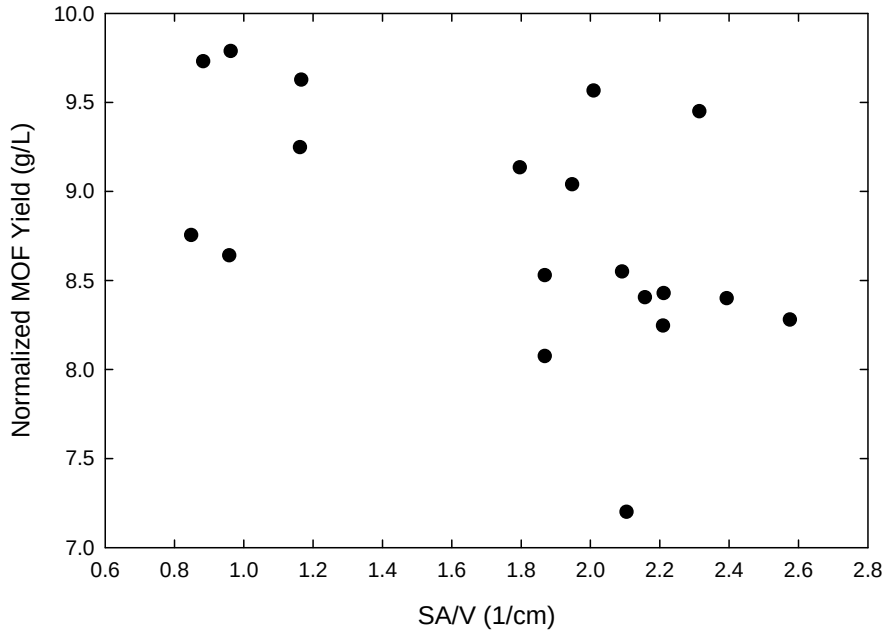

Figure 5.3. Normalized yield of UiO-66-NH_2 (per liter of reactant solution) as a function of SA/V illustrates that the yield is independent of SA/V.

(R^2 = 0.995) confirms that the crystallization reaction is directly scalable under the conditions examined, which is a nontrivial first step in MOF synthesis process design. The largest sample consists of 200 mL of reactant solution in a 250 mL glass jar, and the smallest sample is 1 mL of solution in a 5 mL vial. So, scalability is confirmed over more than two orders of magnitude. Figure 5.2 also illustrates that yield is not dependent upon vessel material when considering PTFE and glass vessels. However, this conclusion is drawn from solely a yield basis and does not demonstrate how the hydrophobic and hydrophilic behavior of the PTFE and borosilicate glass vessels, respectively, may influence the nucleation and crystal growth mechanics. The reaction vessel geometry experimental results are illustrated in the Figure 5.3. The yield of UiO-66-NH_2 appears to be independent of the wetted surface area to reactant solution volume ratio for both PTFE and glass vessels. Therefore, nucleation and growth appear to take place primarily in the reactant solution itself. Increasing vessel volume is apparently the only means for increasing the reaction output for this specific MOF under the tested batch-style conditions.

5.3.2 Kinetic Study

Figure 5.4 (a) shows the normalized yield of UiO-66-NH_2 as a function of time at 373, 383, and 393 K. The points and error bars represent the mean and 95% confidence interval of the triplet samples, respectively. The trials all appear to asymptote to the same maximum of approximately 2.6 g MOF/ L solution. In comparison to the originally published synthesis conditions of the parent UiO-66, which are 393 K for 24 h, we note a

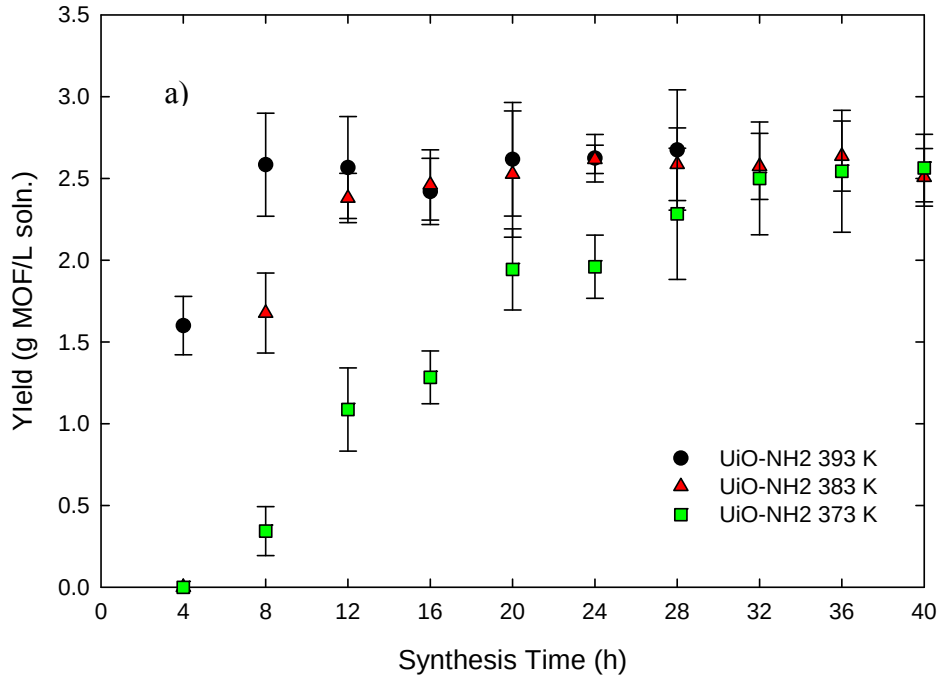
a)
Yield (g MOF/L soln.)
Synthesis Time (h)
UiO-NH2 393 K
UiO-NH2 383 K
UiO-NH2 373 K

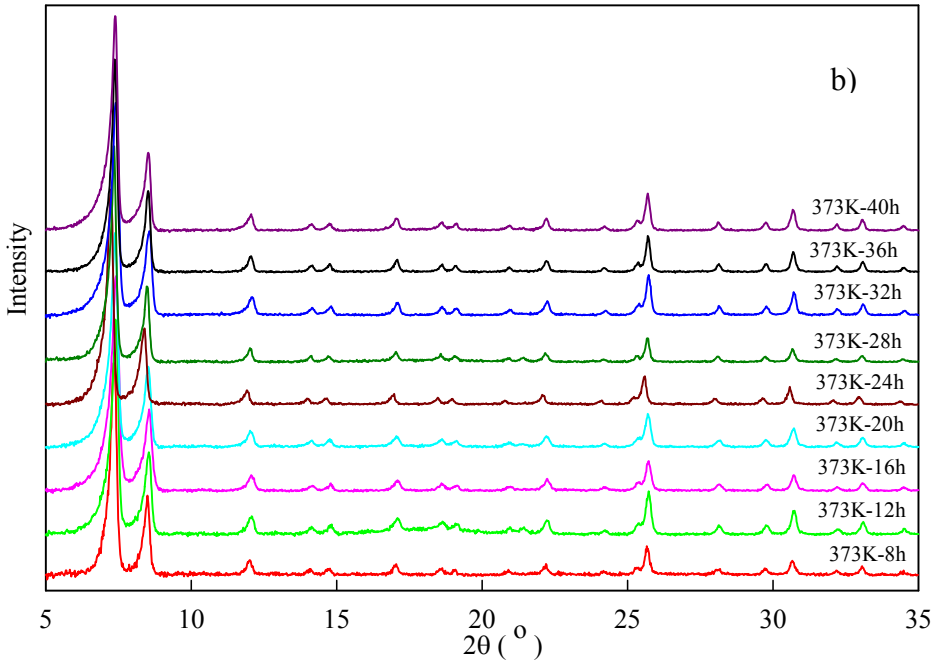
b)
Intensity
373K-40h
373K-36h
373K-32h
373K-28h
373K-24h
373K-20h
373K-16h
373K-12h
373K-8h
2θ (o)

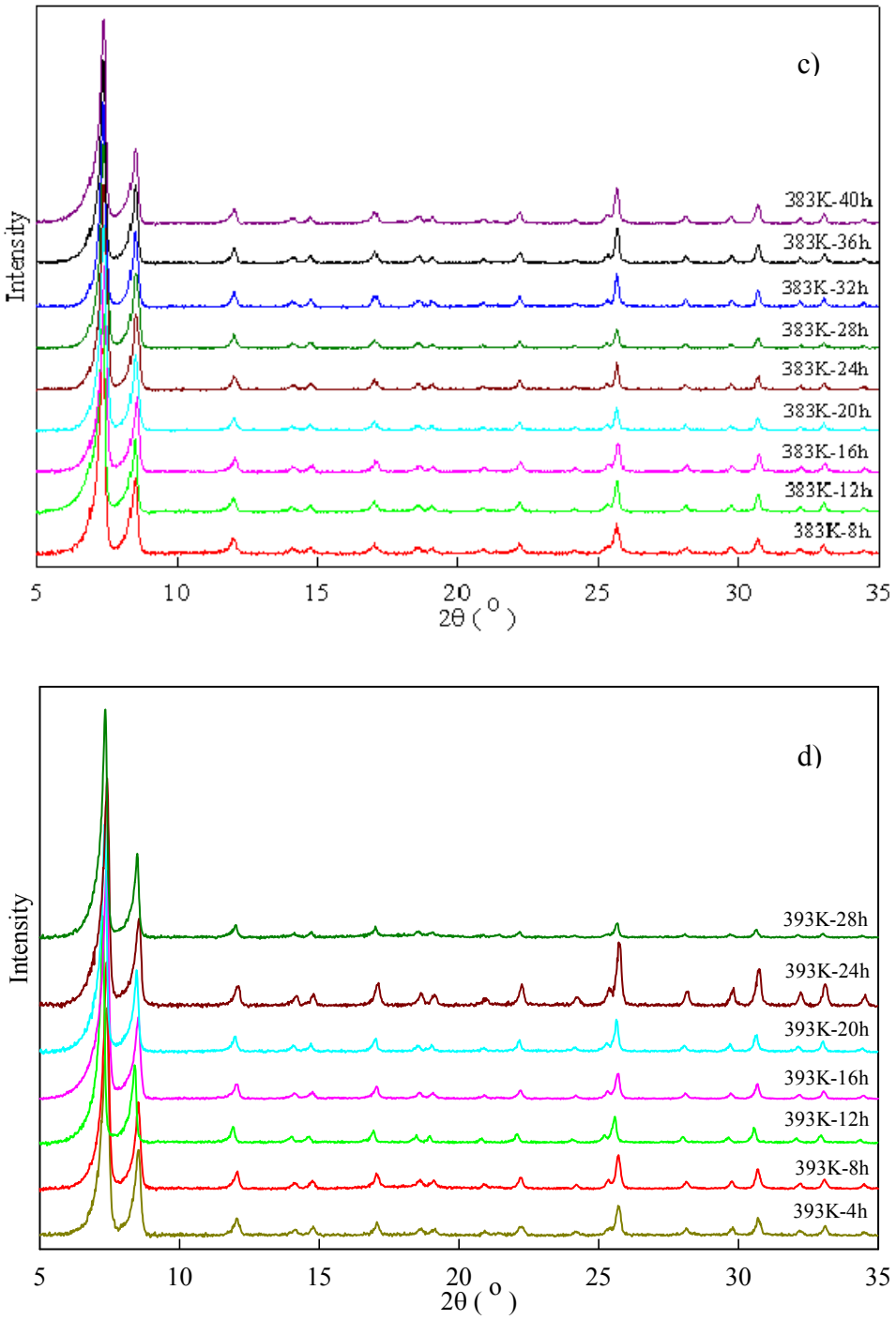

Figure 5.4. (a) UiO-66-NH2 yield from triplicate samples collected every 4 h at 373, 383, and 393K. pXRD comparison of (b) 373 K samples, (c) 383 K samples, and (d) 393 K samples.

67% decrease in the reaction time required to reach the maximum product yield at the same temperature. The 24 h original synthesis time was likely chosen for convenience. However, the difference amounts to a significant increase in throughput from a process vantage point. Figure 5.4 (b),(c), and (d) illustrate the pXRD diffractograms collected for the 393 K synthesis products. Under all temperatures examined and for all samples collected, we do not note any discernible differences in pXRD patterns, which are consistent with those of the desired product, UiO-66-NH_2. Each triplet of samples is then

Table 5.1. BET Surface Areas (m^2/g) of UiO-66-NH_2 synthesis products at 373, 383, and 393 K. *Min.* and *Max.* times are the shortest and longest times, respectively, at which an appropriate amount of product was obtained for adsorption testing.

BET Surface Areas (m^2/g) from N_2 Adsorption at 77 K			
	373 K	383 K	393 K
Min. Time	$1{,}070^{(8)}$	$947^{(8)}$	$1{,}000^{(4)}$
Max. Time	$855^{(40)}$	$1{,}010^{(40)}$	$1{,}010^{(28)}$

( ), Hours of respective synthesis

combined, and further structure confirmation is accomplished via BET modeling of the N_2 adsorption at 77 K. Table 5.1 shows the resultant BET surface areas of the initial and final samples at each synthesis temperature, which are relatively consistent except for the 373 K, 40 h sample, which is c.a. 15% lower than the final samples at 383 and 393 K. An independent 373 K 40 h trial is generated to confirm the lower BET surface area, yielding 867 m^2/g, which is within 1.4% of the first trial. The reduced BET surface area of the 373 K, 40 h sample may be a result of larger crystal formation or more tightly packed agglomerates, which may form under longer synthesis times and reduce the BET surface area contributions from the geometric properties of the crystal particles

themselves. This reasoning would be directly congruent with the idea patented by UOP[39] concerning the synthesis of MOF nanoparticles with higher effective surface areas. However, the yield, pXRD, and N_2 adsorption results still demonstrate that there are multiple temperatures and synthesis times capable of producing UiO-66-NH_2 with nearly identical performance characteristics. From a flow-through reactor design viewpoint, this is highly advantageous and is reportedly not the case for some MOFs.[47]

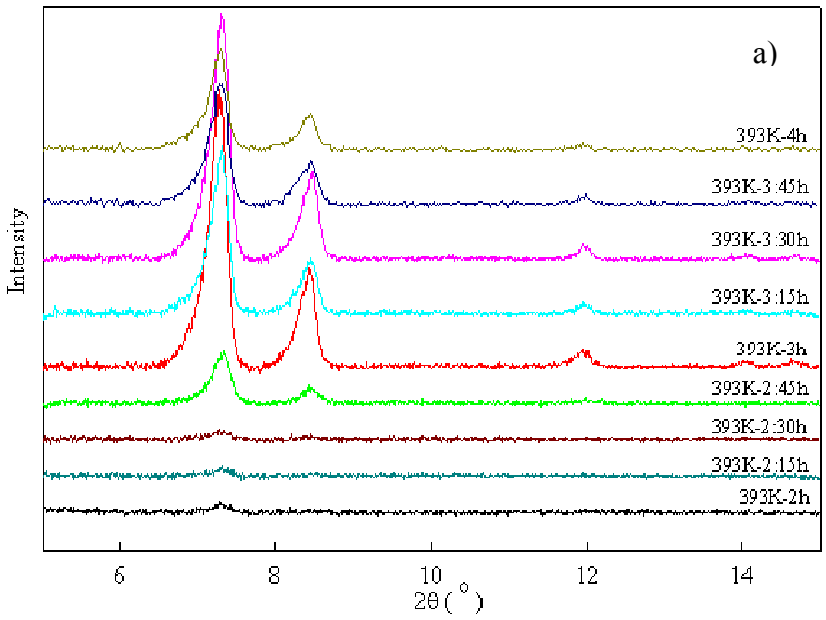

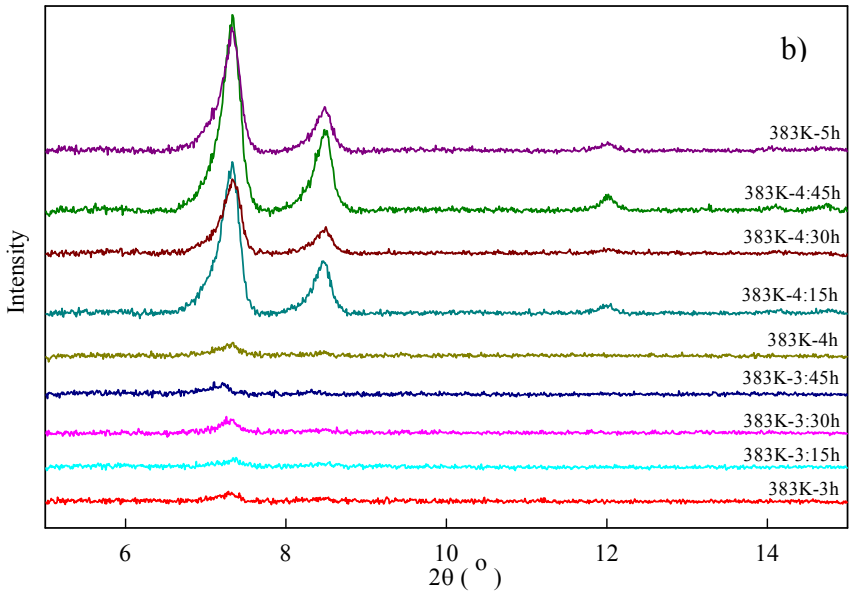
b)
383K-5h
383K-4:45h
383K-4:30h
383K-4:15h
383K-4h
383K-3:45h
383K-3:30h
383K-3:15h
383K-3h
Intensity
6
8
10
12
14
2θ (o)

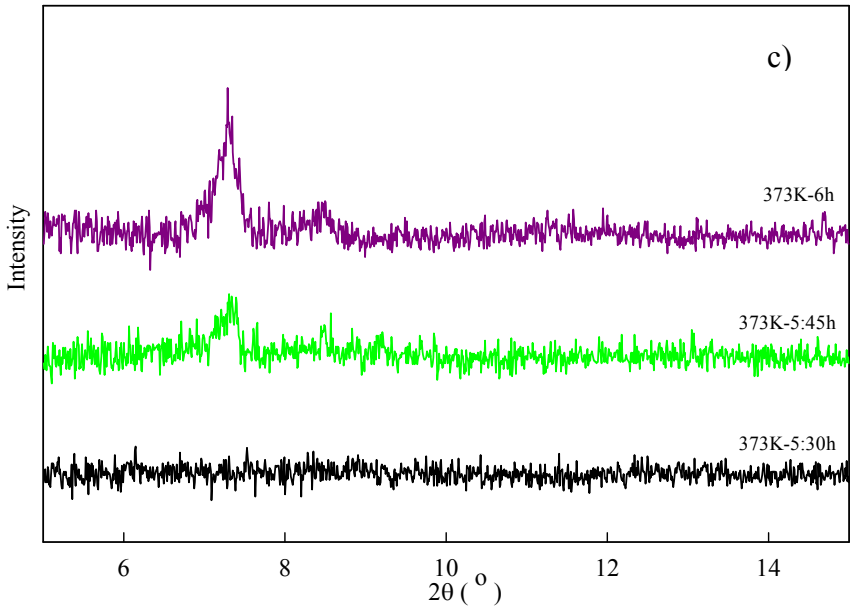
c)
373K-6h
373K-5:45h
373K-5:30h
Intensity
6
8
10
12
14
2θ (o)

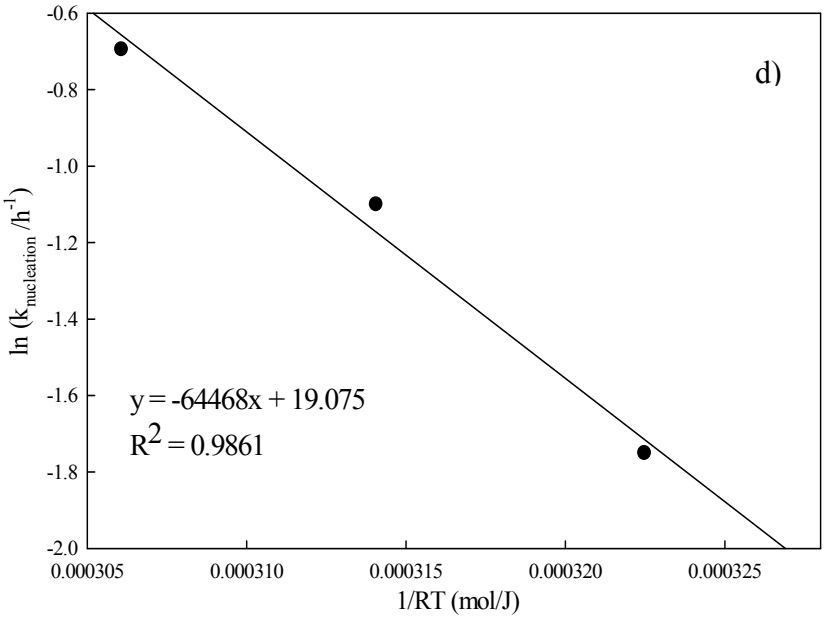

Figure 5.5. UiO-66-NH_2 pXRD used to determine nucleation rate ((a) 393 K, (b) 383 K, (c) 373 K) (d) Arrhenius plot of experimentally determined nucleation rates.

The XRD diffractograms used to identify the time at which nucleation occurs at 393 K, 383 K, and 373 K and the resultant nucleation rate are shown in Figure 5.5. The resultant Arrhenius plot is produced by comparing the nucleation rates determined at 373, 383, and 393 K (Figure 5.5(d)). The activation energy of UiO-66-NH_2 nucleation (Ea_{Nuc}) predicted by the Arrhenius plot is approximately 64.5 kJ/mol. A higher value compared to the Ea_{Nuc} reported for Fe MIL-53, 39.2 kJ/mol,[46] may be indicative of the difference in coordination environments. UiO-66-NH_2 consists of highly-coordinated clusters, which form an eight-coordinated state when hydrated and seven-coordinated upon dehydroxylation,[24,51] requiring a higher Ea to facilitate nucleation compared to the 4-coordinated Fe MIL-53 framework.[52] Furthermore, the Ea_{Nuc} for UiO-66-NH_2 is still significantly lower than that of MOF-14, which is 113.9 kJ/mol for convection oven synthesis and is expected to be relatively high as an attribute of the framework

interpenetration.[47] HKUST-1 E_{aNuc} of 71.6 kJ/mol[47] is within 11% of the value predicted for UiO-66-NH_2. The nucleation rates and predicted Ea_{Nuc} for UiO-66-NH_2 solvothermal synthesis are congruent with reported values for other MOFs, which not only validate our findings but also predict that UiO-66-NH_2 continuous-flow crystallization may be representative of a typical MOF crystallization process. Crystal size distribution, a common figure of merit for crystal growth kinetics, is not examined in this work. From an fixed-bed adsorption perspective, the ability to press pellets without affecting the structure[24] diminishes the need to control MOF particle size. Also, UiO-66 crystallites are typically sub-micron, [24] suggesting that the main dominant mechanism is nucleation.

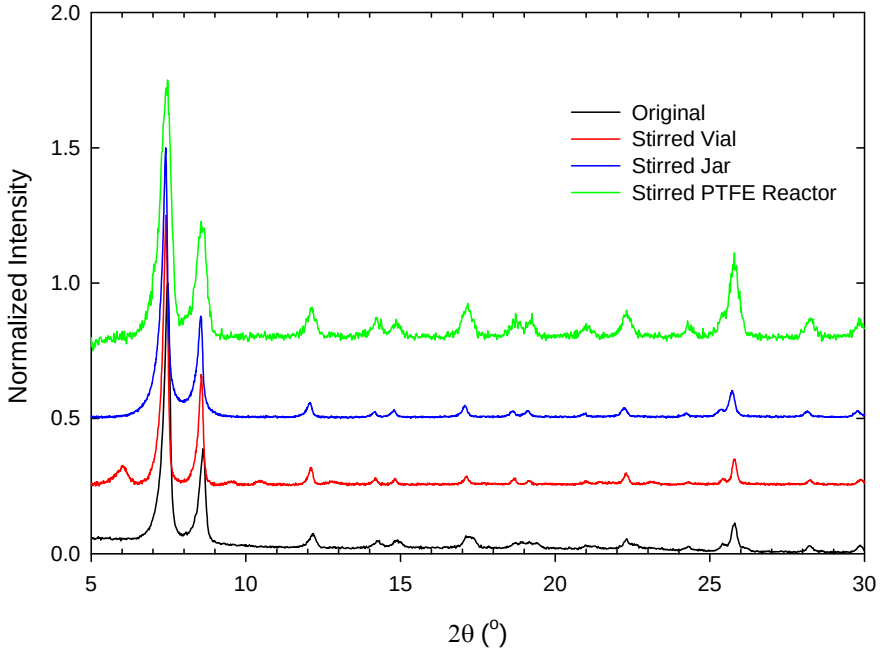

Figure 5.6. pXRD of stirred-sealed synthesis trials. Intensities are normalized to account for the differences in sample and sample pan sizes.

5.3.3 Continuous-Flow Reactor Design

The pXRD comparisons of the stirred-sealed synthesis trials are presented in Figure 5.6. From peak position comparison, all diffractograms appear to have consistent

crystallinity as UiO-66-NH_2. The difference in relative peak heights for the stirred-PTFE reactor compared to the other trials is attributed to pXRD sample and sample pan size differences. More specifically, the 2L PTFE reactor provides a sample approximately two orders of magnitude larger than the 20 mL vial, and a larger XRD sample pan is selected to accurately examine the cumulative sample. BET modeling of the N_2 adsorption at 77 K predicts effective surface areas of 630, 680, and 830 m^2/g for the 20 mL vial, 250 mL jar, and 2 L PTFE reactor, respectively. The surprising increase of surface area with increasing reaction vessel volume may be attributed to more accurate temperature control during the 2 L PTFE trial, in which the solution temperature itself is monitored with an infrared temperature sensor. The temperatures of the jar and vial trials are monitored by placing the hot plate probe in the oil and sand baths, respectively, instead of the actual reactant solution. Fluid dynamics within the vessel may also influence the stirred-trial product quality. The general definition of the Reynolds number is as follows:[53]

$$Re = \left[\frac{l_0 v_0 \rho}{\mu}\right] \quad (1)$$

Since the reaction solutions and reaction conditions are nearly identical, we assume that the fluid properties (μ and ρ) are constant for all trials. Also, we substitute in the diameter of the stir bar (D) and convert the angular velocity of the stir bar to linear velocity by $v_o = N*D$, where N[=]rotations/minute and get:

$$Re \propto ND^2 \quad (2)$$

Using (2) Table 5.2 is generated to illustrate the large range of Re involved in the stirred-sealed synthesis trials.

Table 5.2. Relative Reynolds numbers calculated for the three stirred-sealed syntheses.

Vessel	Stir Bar D (in.)	N (r.p.m.)	Normalized Re
Vial (20 mL)	0.563	150	1.00
Jar (250 mL)	1.500	200	9.48
PTFE Reactor (2,000 ml)	2.000	150	12.6

The normalized Reynolds numbers cover a 12-fold range of values presented in Table 5.2, which will need to be investigated in more detail to predict any specific relationship between fluid dynamics and MOF product quality. However, the trend is in agreement with the claim of UOP's patent application[39] for nano-MOF synthesis, which utilizes agitation to decrease particle size as well as agglomeration and increase the resultant effective surface area. The stirred trial BET results are notably lower than the initial 20 mL vial synthesis conducted under static conditions. However, we note a similar decrease in surface area during the characterization of the larger samples collected during the reaction vessel geometry and material investigation. The largest volume sample of the scale-up synthesis work consists of 200 mL of reactant solution in a 250 mL glass jar, which yields a BET surface area of 810 m^2/g. In general, commercially available MOFs do not tend to have high degrees of precision associated with their BET surface areas (e.g. C300 from Sigma-Aldrich via BASF is reported to have BET surface areas from 1,500-2,100 m^2/g or 1,800 m^2/g +/-17%),[54] and the benefits of the proposed flow-through synthesis process may far outweigh any moderate reduction in surface area. Other studies conducted in our lab (see *Appendix A*) demonstrate how differences in BET surface areas of up to 25% for the same MOF result in very little difference in the adsorption behavior for carbon dioxide, especially at low pressure.

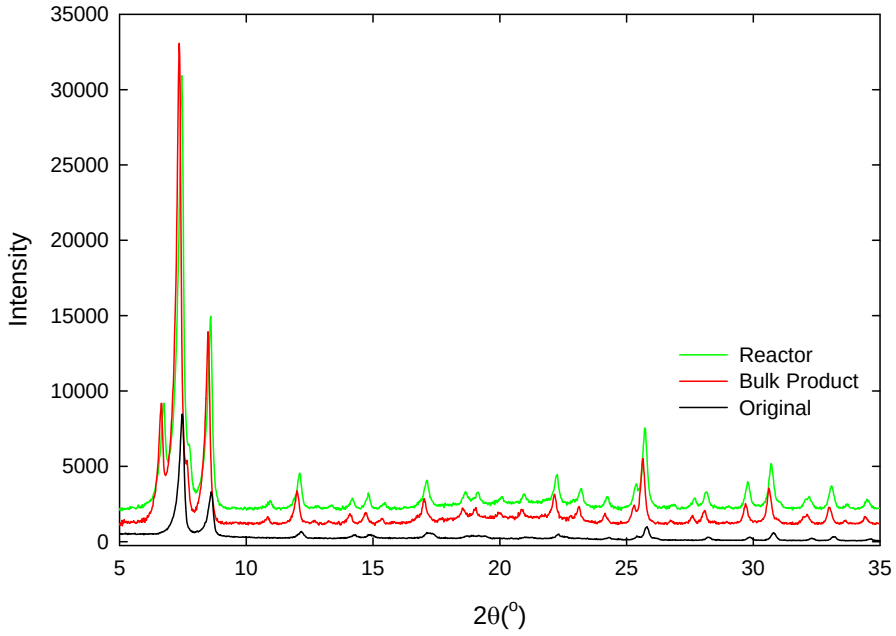

Figure 5.7. pXRD of the bulk product from the flow-through synthesis trial, 'Product,' and the material retained within the DTB crystallization reactor, 'Reactor,' compared with original UiO-66-NH_2 sample.

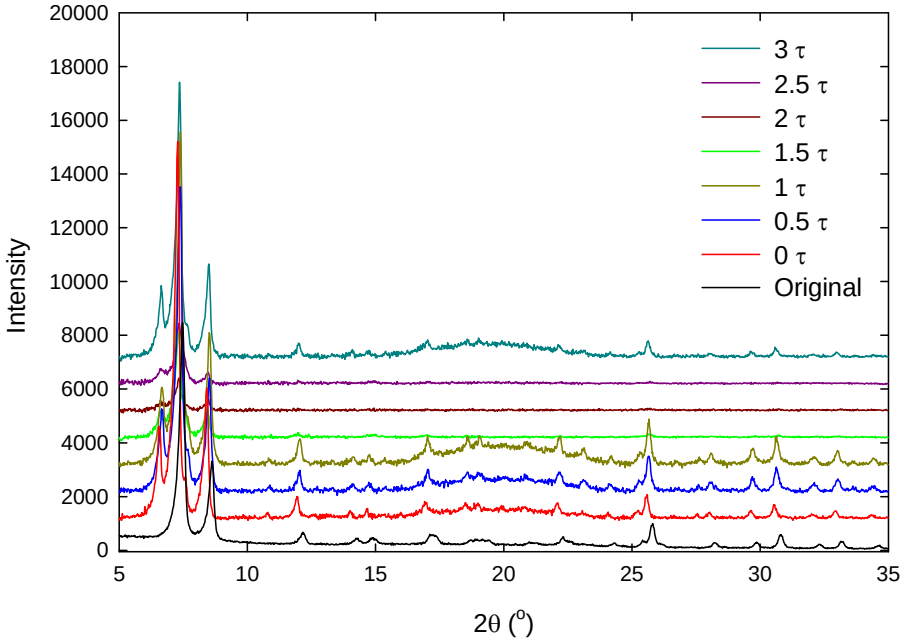

Figure 5.8. pXRD comparison of continuous-flow synthesis trial as a function of time. 0 t corresponds to the product present immediately following the reactor start-up.

Figure 5.7 illustrates the pXRD of the bulk product collected from the continuous-flow synthesis trial as well as the product retained within the crystallizer following the synthesis trial. PXRD of the intermediate samples are shown in Figure 5.8. and illustratepeak position and intensity agreement confirming formation of the desired product, UiO-66-NH_2. The BET surface areas of the bulk product and product from within the reactor are 530 and 640 m^2/g, respectively. Drastic reduction of surface area, which is a direct measure of product quality for many MOF applications, may be indicative of insufficient or non-uniform retention time or significant impurity concentration. However, we see relatively similar product quality with a 22% loss from the stirred-batch trial in the same reaction vessel. These novel results directly demonstrate the feasibility of continuous-flow MOF synthesis. Further optimization will be conducted in our lab to optimize crystalline-product yield and quality. However, these results are still of principal importance to the industrial scale-up of metal-organic frameworks and subsequent transition to potential applications.

5.4 Conclusion

In summary, we have developed and implemented a methodical approach to the scale-up synthesis of UiO-66-NH_2 and presented initial proof of concept results for a novel continuous-flow MOF synthesis process, which implements a flow-through crystallization reactor. During batch-style syntheses, we find that crystal yield is directly proportional to the volume of reactant solution in the vessel and independent of the wetted surface area to volume ratio. The yield also shows no preference for PTFE or borosilicate glass vessels. Collecting intermediate products during the sealed

solvothermal syntheses at three temperatures illustrates the bulk reaction kinetics. We find that the maximum yield is reached at all three temperatures, and at the originally published synthesis temperature we are able to obtain the maximum yield with a 67% decrease in reaction time. Relatively uniform product quality is noted from the first collectable product to the final product and is illustrated via pXRD and BET surface area comparison. The intermediate products are also characterized via pXRD, and nucleation rates are determined at each temperature. We find the nucleation rates follow the Arrhenius equation and predict a Ea_{Nuc} of 64.5 kJ/mol, which is in the range reported for other MOFs and appears to be representative of the highly-coordinated Zr-MOF structure. Stirred-synthesis trials are conducted over a 100-fold range of reaction vessel volumes and all products are compared via pXRD and BET modeling of the N_2 adsorption at 77 K. A novel continuous-flow MOF crystallization process is reported. Resultant pXRD of intermediate products show some intensity variance, which is likely attributed to accumulation of crystalline product within the reactor and lower concentration of MOF in the product stream. However, the bulk product is in good agreement with the pXRD found for the original UiO-66-NH_2 product, and BET surface area of the product retained within the reactor is within 22% of the 827 m^2/g found for the stirred-batch trial in the same vessel. Further optimization of the process is necessary in order to produce a more consistent concentration of MOF product. However, the importance of the novel crystallization method cannot be overstated. The reduction in down-time and increased throughput can directly aid in the transition of MOFs from the lab to an applied level.

5.5 References

1. Glover TG, Peterson GW, Schindler BJ, Brittand D, Yaghi O. MOF-74 building unit has a direct impact on toxic gas adsorption. Chem. Eng. Sci. Jan 2010; 66(2): 163-170.

2. Liu J, Benin AI, Furtado AMB, Jakubczak P, Willis RR, LeVan MD. Stability effects on CO(2) adsorption for the DOBDC series of metal-organic frameworks. Langmuir. Sep 2011;27(18):11451-11456.

3. Karra JR, Walton KS. Molecular simulations and experimental studies of CO2, CO, and N-2 adsorption in metal-organic frameworks. Journal of Physical Chemistry C. Sep 2010;114(37):15735-15740.

4. Mu B, Schoenecker PM, Walton KS. Gas adsorption study on mesoporous metal-organic framework UMCM-1. Journal of Physical Chemistry C. Apr 2010;114(14):6464-6471.

5. Millward AR, Yaghi OM. Metal-organic frameworks with exceptionally high capacity for storage of carbon dioxide at room temperature. Journal of the American Chemical Society. Dec 2005;127(51):17998-17999.

6. Wang C, Xie ZG, deKrafft KE, Lin WL. Doping metal-organic frameworks for water oxidation, carbon dioxide reduction, and organic photocatalysis. Journal of the American Chemical Society. Aug 2011;133(34):13445-13454.

7. Tanabe KK, Cohen SM. Engineering a metal-organic framework catalyst by using postsynthetic modification. Angew. Chem.-Int. Edit. 2009;48(40):7424-7427.

8. Horcajada P, Serre C, Ferey G, Couvreur P, Gref R. Porous materials, loading and release of antitumural and antiretroviral drugs. Actual Chim. Jan-Feb 2011(348-49):58-63.

9. McKinlay AC, Morris RE, Horcajada P, Ferey G, Gref R, Couvreur P, Serre C. BioMOFs: metal-organic frameworks for biological and medical applications. Angew. Chem.-Int. Edit. 2010;49(36):6260-6266.

10. Miller SR, Heurtaux D, Baati T, Horcajada P, Greneche JM, Serre C. Biodegradable therapeutic MOFs for the delivery of bioactive molecules. Chem. Commun. 2010;46(25):4526-4528.

11. Zacher D, Shekhah O, Woll C, Fischer RA. Thin films of metal-organic frameworks. Chem. Soc. Rev. 2009;38(5):1418-1429.

12. Shekhah O, Liu J, Fischer RA, Woll C. MOF thin films: existing and future applications. Chem. Soc. Rev. 2011;40(2):1081-1106.

13. Demessence A, D'Alessandro DM, Foo ML, Long JR. Strong CO2 binding in a water-stable, triazolate-bridged metal-organic framework functionalized with ethylenediamine. Journal of the American Chemical Society. Jul 2009;131(25):8784-+.

14. Nguyen JG, Tanabe KK, Cohen SM. Postsynthetic diazeniumdiolate formation and NO release from MOFs. Crystengcomm. 2010;12(8):2335-2338.

15. Wang ZQ, Tanabe KK, Cohen SM. Tuning hydrogen sorption properties of metal-organic frameworks by postsynthetic covalent modification. Chem.-Eur. J. 2010;16(1):212-217.

16. Garibay SJ, Cohen SM. Isoreticular synthesis and modification of frameworks with the UiO-66 topology. Chem. Commun. 2010;46(41):7700-7702.

17. Kaye SS, Dailly A, Yaghi OM, Long JR. Impact of preparation and handling on the hydrogen storage properties of Zn4O(1,4-benzenedicarboxylate)(3) (MOF-5). Journal of the American Chemical Society. Nov 2007;129(46):14176-+.

18. Wu TJ, Shen LJ, Luebbers M, Hu CH, Chen QM, Ni Z, Masel, RI. Enhancing the stability of metal-organic frameworks in humid air by incorporating water repellent functional groups. Chem. Commun. 2010;46(33):6120-6122.

19. Hausdorf S, Wagler J, Mossig R, Mertens F. Proton and water activity-controlled structure formation in zinc carboxylate-based metal organic frameworks. Journal of Physical Chemistry A. Aug 2008;112(33):7567-7576.

20. Greathouse JA, Allendorf MD. The interaction of water with MOF-5 simulated by molecular dynamics. Journal of the American Chemical Society. Aug 2006;128(33):10678-10679.

21. Choi HJ, Dinca M, Dailly A, Long JR. Hydrogen storage in water-stable metal-organic frameworks incorporating 1,3-and 1,4-benzenedipyrazolate. Energy & Environmental Science. 2010;3(1):117-123.

22. Park KS, Ni Z, Cote AP, et al. Exceptional chemical and thermal stability of zeolitic imidazolate frameworks. Proc. Natl. Acad. Sci. U. S. A. Jul 2006;103(27):10186-10191.

23. Schoenecker PM, Carson CG, Jasjuja H, Flemming CJJ, Walton KS. Effect of water adsorption on retention of structure and surface area of metal-organic frameworks. Ind. Eng. Chem. Res. 2012;51(18):6513–6519.

24. Cavka JH, Jakobsen S, Olsbye U, Guillou N, Lamberti C, Bordiga S, Lillerud KP. A new zirconium inorganic building brick forming metal organic frameworks with exceptional stability. Journal of the American Chemical Society. Oct 2008;130(42):13850-13851.

25. Ferey G. Some suggested perspectives for multifunctional hybrid porous solids. Dalton Trans. 2009(23):4400-4415.

26. Basolite®Pricing.Sigma-Aldrich. http://www.sigmaaldrich.com/catalog/product/aldrich/691348. Accessed May 14th 2012.

27. Loiseau T, Serre C, Huguenard C, Fink G, Taulelle F, Henry M, Bataille T, Ferey G. A rationale for the large breathing of the porous aluminum terephthalate (MIL-53) upon hydration. Chem.-Eur. J. Mar 2004;10(6):1373-1382.

28. Chui SSY, Lo SMF, Charmant JPH, Orpen AG, Williams ID. A chemically functionalizable nanoporous material Cu-3(TMA)(2)(H2O)(3) (n). Science. Feb 1999;283(5405):1148-1150.

29. Kusgens P, Rose M, Senkovska I, Frode H, Henshel A, Siegle S, Kaskel S. Characterization of metal-organic frameworks by water adsorption. Microporous Mesoporous Mat. Apr 2009;120(3):325-330.

30. Ge D, Lee HK. Water stability of zeolite imidazolate framework 8 and application to porous membrane-protected micro-solid-phase extraction of polycyclic aromatic hydrocarbons from environmental water samples. Journal of Chromatography A. Nov 2011;1218(47):8490-8495.

31. Centrone A, Santiso EE, Hatton TA. Separation of chemical reaction intermediates by metal-organic frameworks. Small. Aug 2011;7(16):2356-2364.

32. Babu KF, Kulandainathan MA, Katsounaros I, et al. Electrocatalytic activity of Basolite (TM) F300 metal-organic-framework structures. Electrochem. Commun. May 2010;12(5):632-635.

33. Kang IJ, Khan NA, Haque E, Jhung SH. Chemical and thermal stability of isotypic metal-organic frameworks: effect of metal ions. Chem.-Eur. J. May 2011;17(23):6437-6442.

34. Liu J, Wang Y, Benin AI, Jakubczak P, Willis RR, LeVan MD. CO2/H2O Adsorption equilibrium and rates on metal-organic frameworks: HKUST-1 and Ni/DOBDC. Langmuir. Sep 2010;26(17):14301-14307.

35. Low JJ, Benin AI, Jakubczak P, Abrahamian JF, Faheem SA, Willis RR. Virtual high throughput screening confirmed experimentally: porous coordination

polymer hydration. Journal of the American Chemical Society. Nov 2009;131(43):15834-15842.

36. Cychosz KA, Ahmad R, Matzger AJ. Liquid phase separations by crystalline microporous coordination polymers. Chem. Sci. Sep 2010;1(3):293-302.

37. Muller U, Hesse M, Putter H. Liquid absorption by metal-organic frameworks. United States Patent Application Publication. 2009;7534303.

38. Schubert M, Muller U, Kiener C. Method for the separation of carbon dioxide using a porous metal-organic framework. United States Patent Publication. 2009;7,556,673.

39. Benin A, Willis, R. R. Synthesis methodology to produce nano metal organic framework crystals. United States Patent Application Publication. 2012;US 2012/00033475 A1.

40. Ni Z, Masel RI. Rapid metal organic framework molecule synthesis method. United States Patent Application Publication. 2009;11/785,102.

41. Muller U, Putter H, Hesse M, Schuber M, Wessel H, Huff J, Guzmann M. Method for Electrochemical Production of a Crystalline Porous Metal Organic Skeleton Material. United States Patent Application Publication. 2004;10/580,407.

42. Mueller U, Schubert M, Teich F, Puetter H, Schierle-Arndt K, Pastre J. Metal-organic frameworks - prospective industrial applications. J. Mater. Chem. Feb 2006;16(7):626-636.

43. Leung E, Muller U, Cox G. Solvent-free preparation of magnesium formate-based porous metal-organic framework. United States Patent Application Publication. 2012;US 2012/0016160 A1.

44. Kummeter M. First Industrial-Scale MOF Synthesis. Available at http://www.basf.com/group/pressrelease/P-10-428. Accessed May 14th, 2012.

45. Lucchesi CA, Lewis WT. Latent heat of sublimation of terephthalic acid from differential thermal analysis data. J. Chem. Eng. Data. 1968;13(3):389.

46. Haque E, Khan NA, Park JH, Jhung SH. Synthesis of a metal-organic framework material, iron terephthalate, by ultrasound, microwave, and conventional electric heating: a kinetic study. Chem.-Eur. J. 2010;16(3):1046-1052.

47. Millange F, El Osta R, Medina ME, Walton RI. A time-resolved diffraction study of a window of stability in the synthesis of a copper carboxylate metal-organic framework. Crystengcomm. 2011;13(1):103-108.

48. Ahnfeldt T, Moellmer J, Guillerm V, Staudt R, Serre C, Stock N. High-throughput and time-resolved energy-dispersive x-ray diffraction (edxrd) study of the formation of CAU-1-(OH)(2): microwave and conventional heating. Chem.-Eur. J. May 2011;17(23):6462-6468.

49. Myerson AS. Handbook of industrial crystallization (2nd Edition). Weburn, MA:Buttersorth-Heinemann, 2002.

50. Vanguard V6500 centrifuge. SCSI & Fiber Optic Connectivity Solutions. Available at http://www.cecocablingsystems.com/centrifuge.htm. Accessed May 14th 2012.

51. Valenzano L, Civalleri B, Chavan S, Bordiga S, Nilsen NH, Jakobsen S, Lillerud KP, Lamberti C. Disclosing the complex structure of UiO-66 metal organic framework: a synergic combination of experiment and theory. Chem. Mat. Apr 2011;23(7):1700-1718.

52. Millange F, Serre C, Ferey G. Synthesis, structure determination and properties of MIL-53 as and MIL-53ht: the first Cr-III hybrid inorganic-organic microporous solids: Cr-III(OH)center dot{O2C-C6H4-CO2}center dot{HO2C-C6H4-CO2H}(x). Chem. Commun. 2002(8):822-823.

53. Bird R, Stewart W, Lightfoot, E. Transport Phenomena Revised 2nd Edition. 2001: 846.

54. The world record in surface area BASOLITE metal organic frameworks. Available at http://www.sigmaaldrich.com/etc/medialib/docs/Aldrich/General_Information/basf_basolite_handout_051908.Par.0001.File.tmp/basf_basolite_handout_051908.pdf . Accessed on May 14th 2012.

CHAPTER 6

FLOW-THROUGH SYNTHESIS OPTIMIZATION

6.1 Introduction

Metal-organic framework (MOF) synthesis and characterization continues to progress rapidly, and MOFs exhibit potential to meet specific applications including selective removal of toxic gases[1-3] and CO_2,[4-6] targeted drug delivery,[7] and sensor applications.[8,9] Attention is shifting towards scale-up of MOF syntheses, which is imperative for applications outside of research laboratories.

Multiple techniques now exist with specific benefits and limitations for large scale synthesis. The electrochemical method developed by BASF[10,11] is designed to mitigate the environmental hazards from typical solvothermal methods, which often utilize metal-nitrates in heated solvents. However, this technique has not been reported for a wide range of MOFs and may not be cost effective for MOFs containing metals that are much less expensive as a salt precursor. Mechanochemical synthesis techniques[12,13] have been developed to reduce or eliminate the need of solvent in MOF synthesis. These techniques are based on a broad synthesis background and may be more applicable to many MOF syntheses. However, the ability to control phase purity and porosity, which are vital for many MOF applications could present a formidable challenge. Our group is currently developing flow-through reactive-crystallizers, which can provide a continuous output of MOF product and have a well-established background in the field of crystallization process design.[14] The first flow-through MOF synthesis process implements a reactive

crystallizer[15] and is used to synthesize UiO-66-NH_2. Potential benefits of the flow-through crystallization include *in situ* purification[16] and crystal size distribution control.

The following presents a preliminary optimization of the novel flow-through MOF synthesis reactor reported previously.[15] Multiple variables are manipulated to establish general hypotheses for future syntheses and reactor design including stirring rate, number of impellers, presence of a draft tube, and impeller flow direction. The reactor temperature and reactant concentrations are held constant for these trials but should have a significant impact specifically on yield and throughput. For further simplification, the previously described recycle stream is not implemented in this study. Specific attributes of the synthesis products are examined including crystallinity, mass-based yield, porosity, and crystal morphology. Following characterization of each flow-through synthesis trial, elementary experimental design methods are applied to determine specific operating parameters, which have significant effects on attributes including pXRD agreement, BET surface area, and the normalized yield of solids.

6.2 Experimental Procedure

All chemicals are procured from Sigma-Aldrich and used without further purification. Reactant solutions containing equimolar amounts of zirconium(IV) chloride ($ZrCl_4$) and amino-terephthalic acid (ATPA) are dissolved in dimethyl formamide (DMF) with final concentrations identical to those reported initially for the parent material, UiO-66.[17] The solution is then stirred for ca. 15 min and added to the flow-through process reactant tank.

The process (Figure 6.1) is operated under constant temperature, flow, and volume conditions throughout all trials. Heating is achieved via a variable power supply and insulated drum heater at a set-point of ca. 393 K (+/- 10 K) and recorded via an infrared temperature sensor and datalogger every 5 minutes.

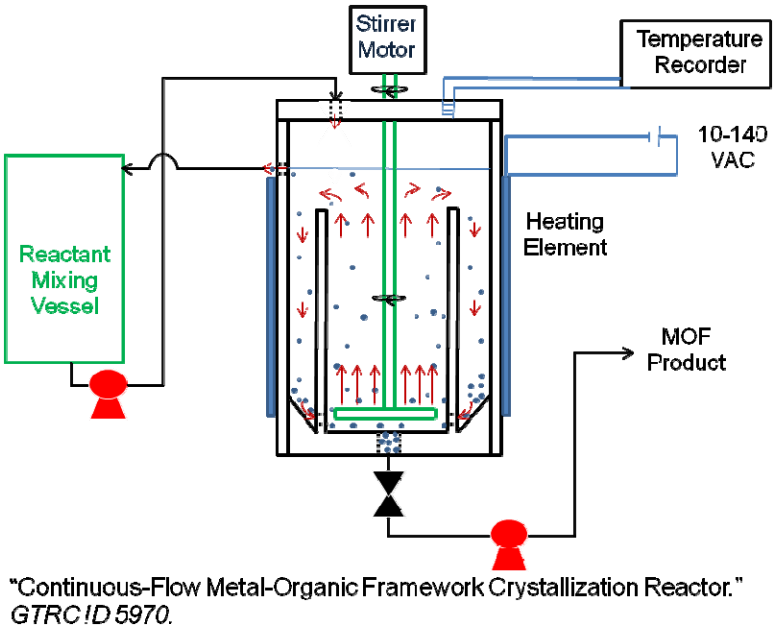

Figure 6.1. Preliminary PFD of the proposed DTB crystallizer-based MOF synthesis process *GTRC ID 5907 Provisional Patent Application: 61/616,746.*[15]

Flowrates of the inlet and outlet peristaltic pumps are calibrated prior to each trial and set at ca. 2.8 mL/min to achieve the desired retention time (τ), 12 h, which is long enough to achieve maximum observed yields at temperatures >/= 383 K.

Approximately 50 mL samples are pulled just upstream of a bulk product collection tank every 12 h or 1 τ. Each sample is centrifuged for ca. 10 min in a VanGuard 6500 centrifuge at 3,400 ± 100 rpm,[18] and the solvent is decanted and replaced with fresh methanol three times, over the course of three days. The samples are then allowed to air

dry prior to heating under vacuum at 373 K. After the samples cool and come to equilibrium under lab ambient conditions, they are weighed to determine the normalized yield (g/L) of solids and characterized via pXRD. BET modeling of N_2 adsorption at 77 K is conducted to examine porosity of the bulk product, and TEM images are collected from 1 τ and 6 τ samples to examine crystal morphology.

In order to quantify the pXRD agreement with the published UiO-66 pattern, the number of peaks and their respective positions from the crystallographic information file (.cif) are examined. From 5 to 35° 2θ the original .cif contains 19 peaks, whose quantity and positions are in direct agreement with UiO-66-NH_2 synthesized previously.[15] The peak positions from the flow-through samples collected once steady-state is assumed (i.e. 3, 4, 5, and 6 τ) are determined using the 2nd-derivative test in X'Pert HighScore Plus. Then, each peak is compared to the 19 peaks from the .cif, and the number of peaks with matching positions is recorded. This provides a pXRD-fit value (*P*) which has values between zero and one for trials having no agreement (0 matching peaks) and complete agreement (19 matching peaks), respectively. These *P* values are averaged for the trial and normalized by the maximum number of peaks (19)

6.2.1 Draft Tube Exclusion

More uniform crystal size and reduced encrustation are typical benefits of draft-tube crystallizers. However, with the noted ease of pressing pellets of UiO-66-NH_2 without a binder, crystal size distribution is not considered as vital as other crystallization processes (e.g. pharmaceuticals), and other methods exist for preventing encrustation including high-shear stirring and automated scraping of the reactor walls. Also, compared to a

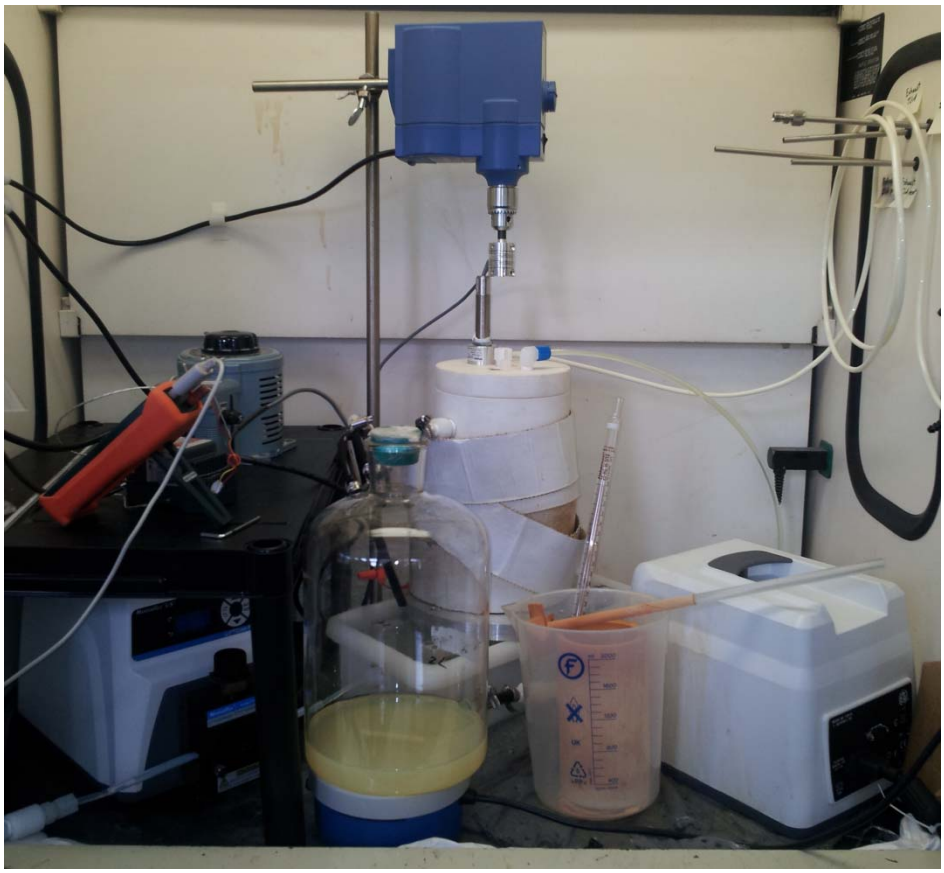

Figure 6.2. Flow-through synthesis process, *GTRC ID 5907 Provisional Patent Application: 61/616,746.*

standard CSTR, the draft-tube inherently hinders mixing of the reactor to accommodate crystal recirculation, which may change local concentrations within the reactor and synthesis process itself. Trials commence with and without the PTFE draft tube in place were performed to examine the effect on product quality and quantity.

6.2.2 Use of Multiple Impellers

To further examine the effects of mixing on solids yield and product quality the use of one and two PTFE impellers (2" O.D.) is examined. The impellers are procured from Southeastern Lab Apparatus (SLA) and consist of 4 blades, which are oriented ca. 45° to

horizontal and promote unidirectional axial flow (Fig 6.3). The increased mixing is expected to help with more consistent product formation but may negate the benefits of a settling region, which is provided via the draft tube.

Figure 6.3. Illustration of impellers used within the crystallization reactor with the draft tube and reactor in background.

6.2.3 Stirring Direction

Upward-directed axial flow is originally selected to promote retention of smaller crystallites and mother liquor and provide a higher outlet concentration of MOF. However, previous continuous-flow zeolite synthesis has shown that downward-directed flow may yield beneficial results including, increased rate of product removal.[19] Due to the symmetry of the current PTFE impeller(s) a reversible stirring motor is implemented to facilitate the desired flow direction and experimentally determine the optimal direction for this reactor.

6.2.4 Stirring Rate Manipulation

The aforementioned trials are conducted using a stirring rate, which is consistent within this study as well as the initial proof-of-concept trial ca. 150 r.p.m.[15] With insufficient viscosity and density data of the dissolved reactant solution at elevated temperature, relative Reynolds numbers (Re) are reported. A quick estimation of Re numbers is conducted using the fluid properties of DMF at 298 K (kinematic viscosity = 0.0085 cm^2/s) [20] predicts a mixed Re >80,000, for all trials at Re(relative) = 1. Following their completion, one trial is conducted to examine the effect of an increased stirring rate Re(relative) ca. 1.7. This serves as a preliminary experiment only, which will shape future agitation considerations.

6.3 Results and Discussion

6.3.1 General Results

In total, six optimization trials were conducted to examine the potential of the current flow-through reactor and determine key design criteria. The operational parameters and resultant product characteristics were summarized in Table 6.1

Trial 2.1 was nearly a direct reproduction of the reported proof-of-concept trial,[15] with only a reorientation of the outlet pump and tubing to mitigate product accumulation; the recycle stream was removed to simplify optimization. In addition, a more recent batch of metal precursor, $ZrCl_4$, was used in an attempt to alleviate the additional low-angle peak.

Table 6.1. Summary of reactor optimization trials controlled parameters (left) and resultant product characteristics (right).

Synthesis Parameters					**Product Characterization**		
Trial Name	Flow Direction	Impellers	Re(relative)	Draft Tube	XRD-fit (P)[+*]	Normalized Yield (g/L)[*]	BET (m^2/g)[#]
2.1	Up	1	1	Yes	0.092	0.92	220
2.2	Up	1	1	No	0.092	2.6	310
3.1	Up	2	1	Yes	0.55	0.087	550
3.2	Up	2	1	No	0.55	0.82	480
3.3	Down	2	1	No	0.58	1.8	780
4.1	Down	2	1.7	No	0.66	0.56	370

+ Normalized parameter based on number of peaks with correct °2θ positions
* Average from samples after steady state is assumed (3, 4, 5, 6 τ)
# From bulk product

The formation of Zr-hydroxide or oxide was likely the aforementioned phase impurity (extra peak) and was also reported by others.[21] Figure 6.4 illustrates the normalized solids yield and pXRD results obtained during trial 2.1. Normalized yield was nearly unappreciable until well after steady state is expected (5 τ v. 3τ until steady state).[22] The pXRD diffractograms consistently exhibit the first two peaks but any further agreement was less predictable. Surface area prediction using the BET method yields 220 m^2/g, which was significantly lower than the 530 m^2/g of the published proof-of-concept trial and may be due to eliminating the recycle stream during this optimization phase.

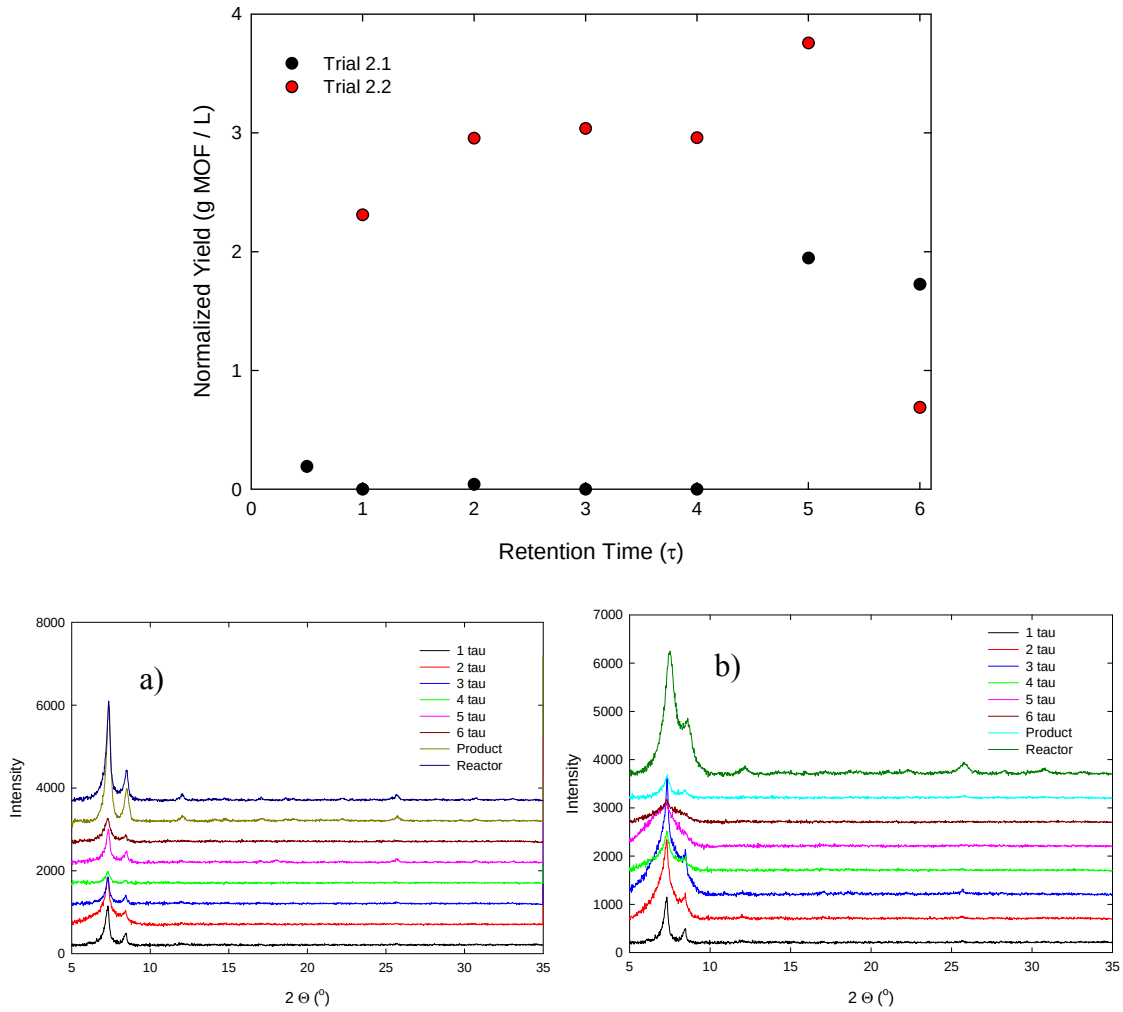

Figure 6.4. Yield (top) and pXRD comparison (bottom) of continuous-flow synthesis trials 2.1 (a) and 2.2 (b).

Trial 2.2 was identical to 2.1 with the exclusion of the draft-tube and provides higher normalized yields of ca. 3 g/L until the last sample at 6 τ, which was less than 1 g/L (Figure 6.4). This sharp decrease in yield was the first sign of plugging within the reactor and appears to be the most significant problem of the current design. PXRD results were similar to trial 2.1, and the BET surface area had increased slightly to 310 m^2/g but was still well below the initial trial. Trials 2.1 and 2.2 demonstrated the least amount of

pXRD agreement with the originally reported structure. *P* was 0.092, which illustrated that less than 10% of the original peaks are present in the samples examined.

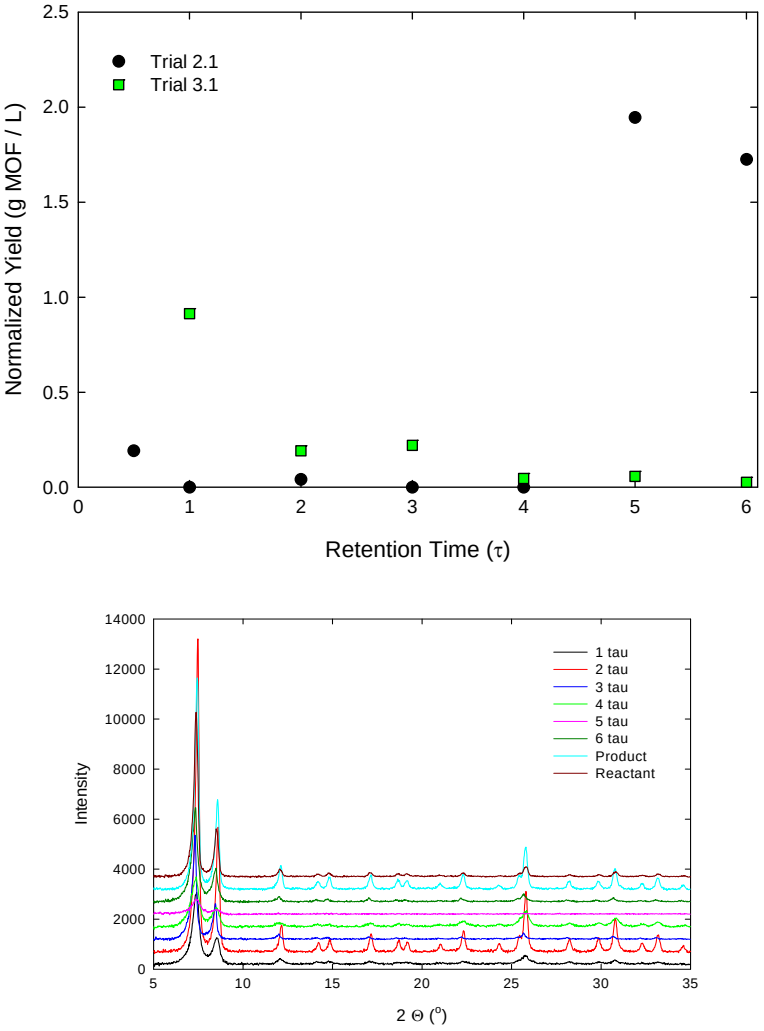

Figure 6.5. Yield (top) and pXRD results (bottom) of continuous-flow synthesis trial 3.1.

Figure 6.5 illustrated trial 3.1, which was congruent with 2.1 but with two impellers within the draft tube. Multiple impellers provided more thorough mixing and a more consistent product. Low yields < 1 g/L were observed throughout the trial, and plugging of the outlet apparently occurred again after only 1 τ. However, the product quality

increased significantly with P = 0.55 and 550 m^2/g of surface area predicted via BET modeling.

Trials 3.2 and 3.3 were illustrated in Figure 6.6 and used two impellers, no draft tube, and upward and downward directed axial flow, respectively. Yield remained inconsistent for the continuous-flow trials. However, the average normalized yield following steady-state improved from 0.82 to 1.8 g/L (Table 6.1) when both impellers were directing flow downward (Trial 3.3). PXRD agreement was better than either of the 1-impeller trials and did not appear to be significantly affected by flow-direction with P = 0.55 and 0.58 for trials 3.2 and 3.3, respectively. Trial 3.3 provided the highest BET S.A. from these trials of 780 m^2/g, which was 47% and 63% higher than the proof-of concept trial and analogous trial with upward directed flow (3.2), respectively.

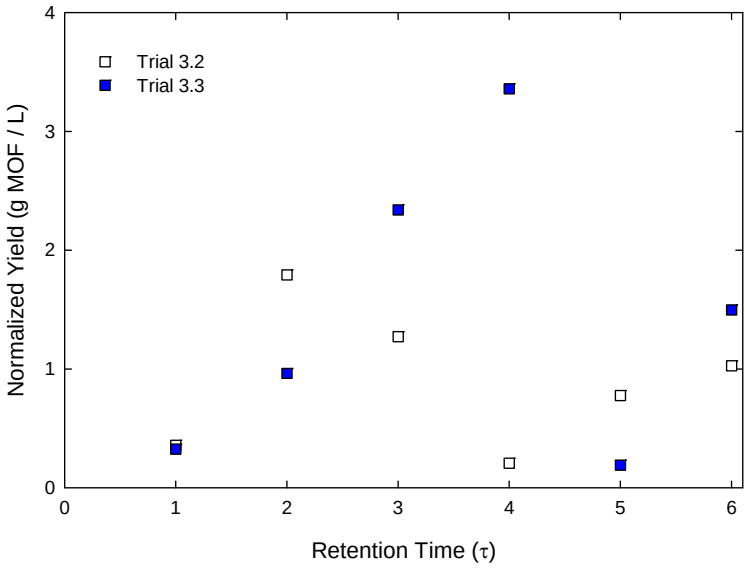

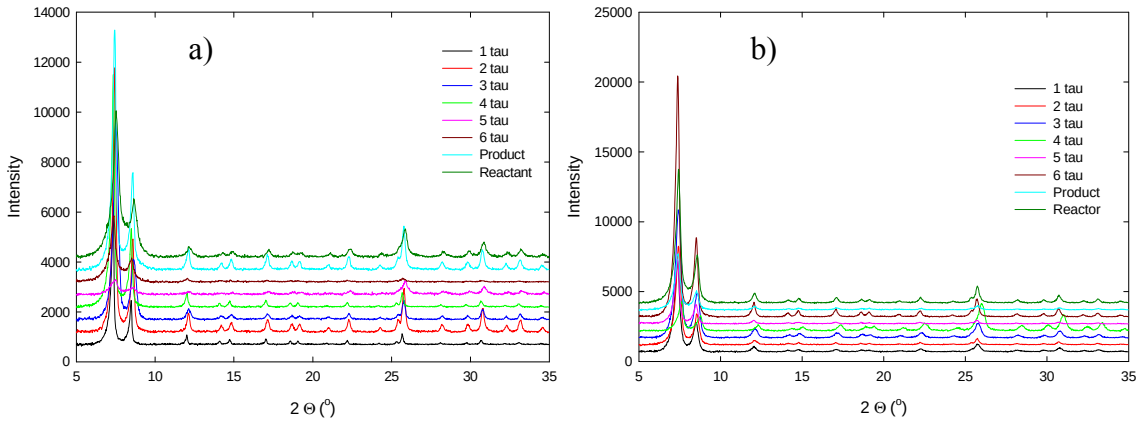

Figure 6.6. Yield (top) and pXRD comparison (bottom) of continuous-flow synthesis trials 3.2 (a) and 3.3 (b).

Following the five initial optimization trials, which examined multiple impellers, draft tube, and flow-direction effects, one final optimization trial commenced using the knowledge gained. The draft tube was removed, both impellers were installed with downward-directing rotation, and the stir-rate was increased to ca. 1.7X the previous trials. Figure 6.7 illustrated the unexpected results and a compilation of all normalized yield results. The yield of trial 4.1 again was not consistent, and the average normalized yield was only 0.56 g/L, which was lower than four of the previous trials. *P* was at the highest value of this study, 0.66, which was surprising considering the relatively low surface area, 370 m^2/g.

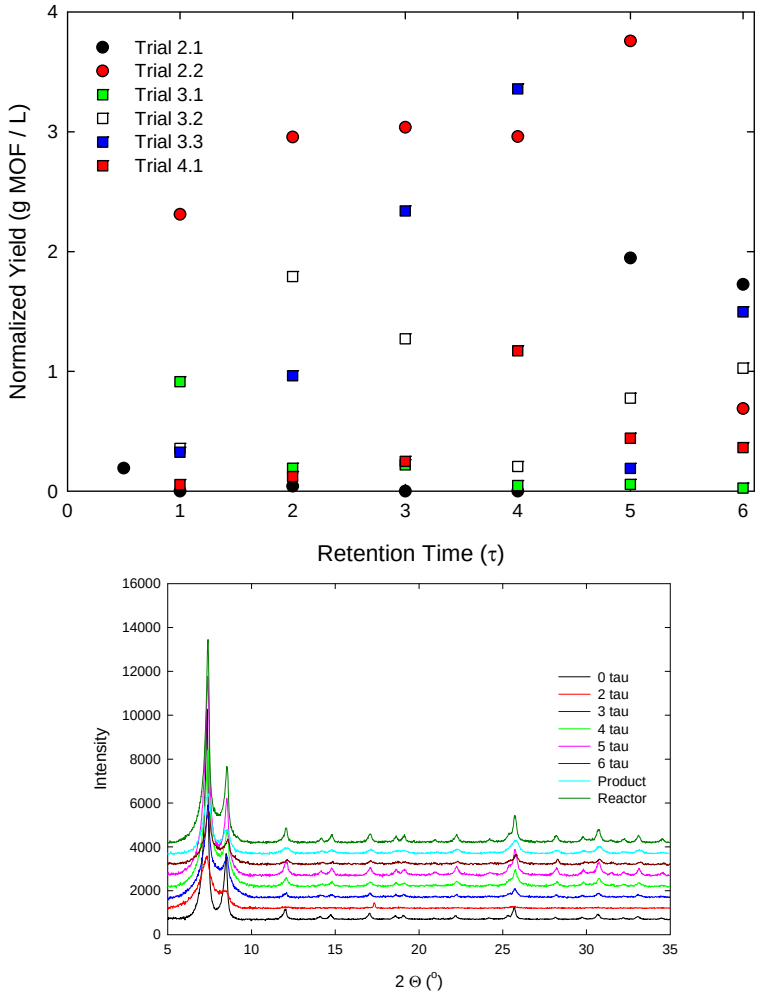

Figure 6.7. Yield compilation including trial 4.1 (top) and pXRD comparison of continuous-flow synthesis trial 4.1 (bottom).

6.3.2 Microscopy

In an effort to characterize the crystal-size effects of the process parameters, initial samples and final samples (1 and 6 τ) were examined via TEM and presented in Figure 6.8. The original synthesis of UiO-66 reported sub-micron intergrown cubic crystals, which required that the structure was solved via pXRD data instead of single-crystal XRD.[17] The trials of this study showed similar behavior on even smaller length scales (< 100 nm), which prohibited discerning particular crystals for crystal-size distribution analyses via the available TEM (e.g. 3.2, 1 τ). Significant aggregation was also noted

and attempts to alleviate it using multiple solvents (Methanol, Toluene, and DMF) were not successful. However, qualitative differences were noted between the one impeller trials (2.1 and 2.2) and two impeller trials (3.1, 3.2, 3.3, and 4.1), which corresponded with the pXRD and BET results. The TEM images for 2.1 and 2.2 illustrated a less-crystalline gel phase, which still exhibited some X-ray diffraction but appeared significantly less-ordered than the two-impeller products.

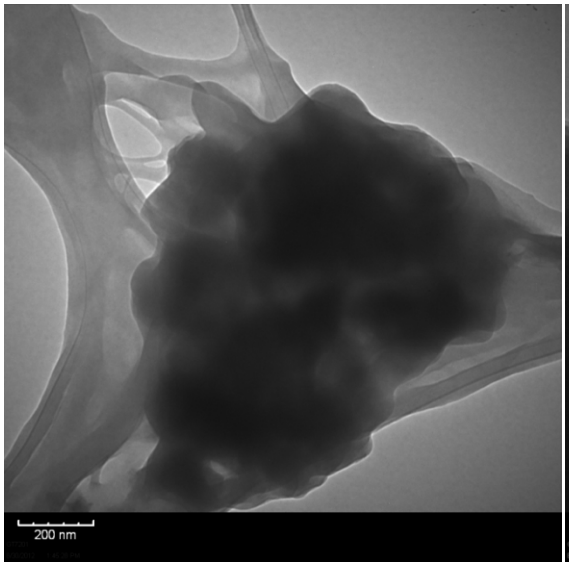

Trial 2.1 (1 τ)

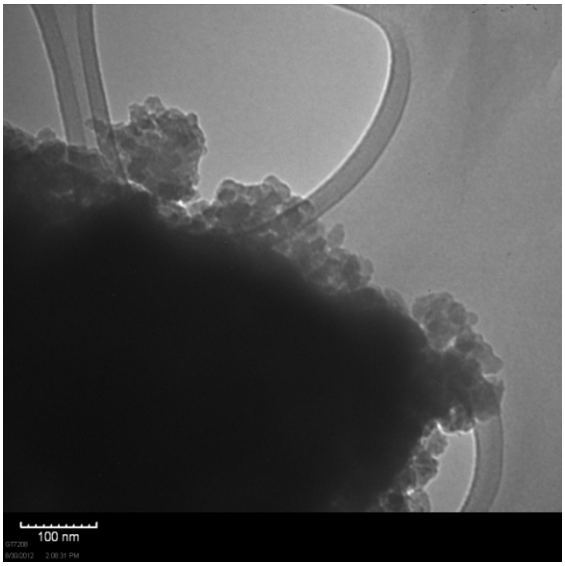

Trial 2.1 (6 τ)

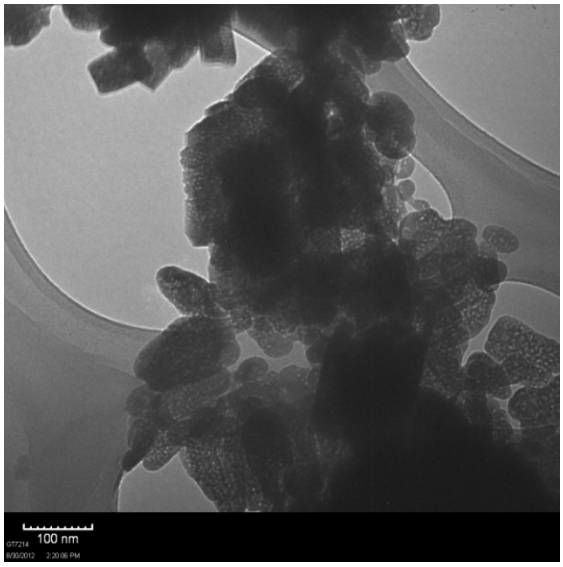

Trial 2.2 (1 τ)

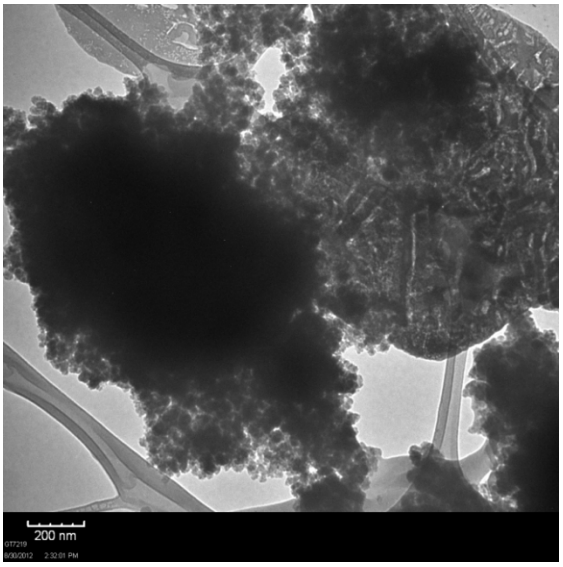

Trial 2.2 (6 τ)

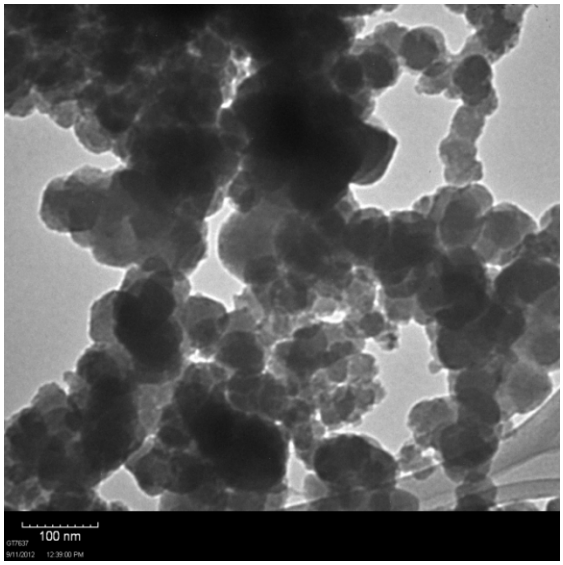

Trial 3.1 (1 τ)

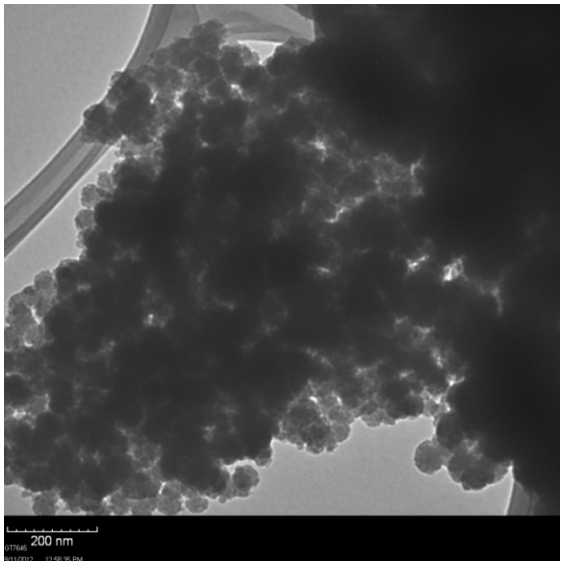

Trial 3.1 (6 τ)

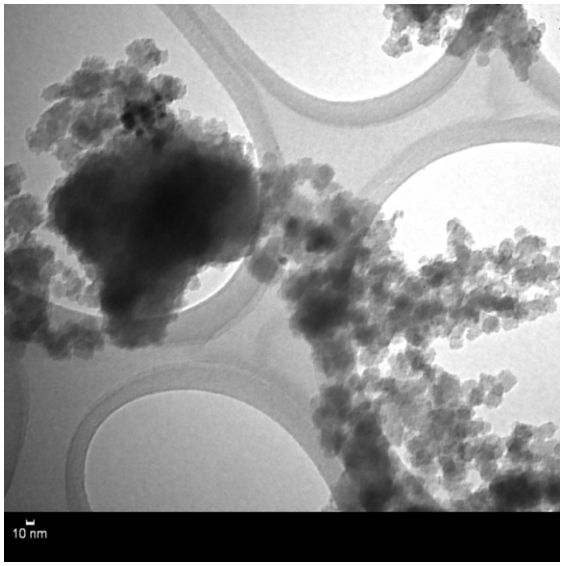

Trial 3.2 (1 τ)

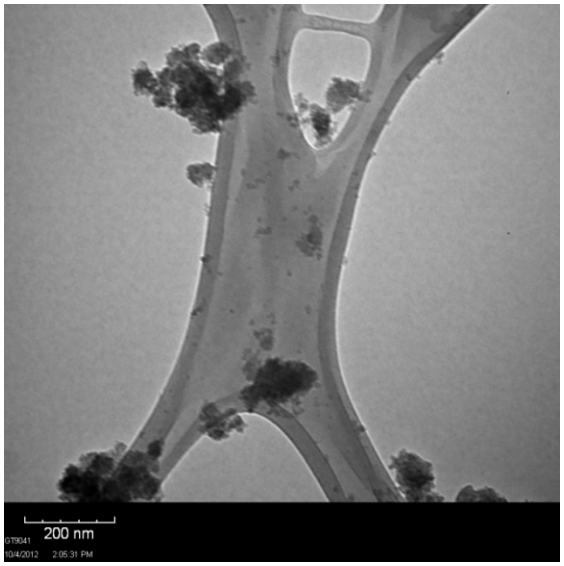

Trial 3.2 (6 τ)

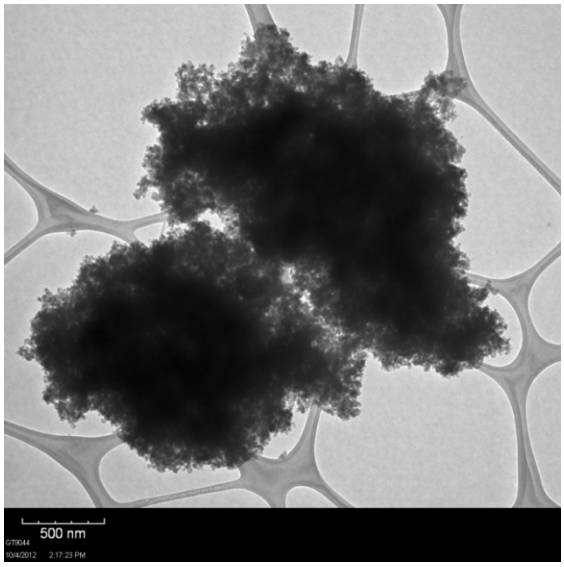

Trial 3.3 (1 τ)

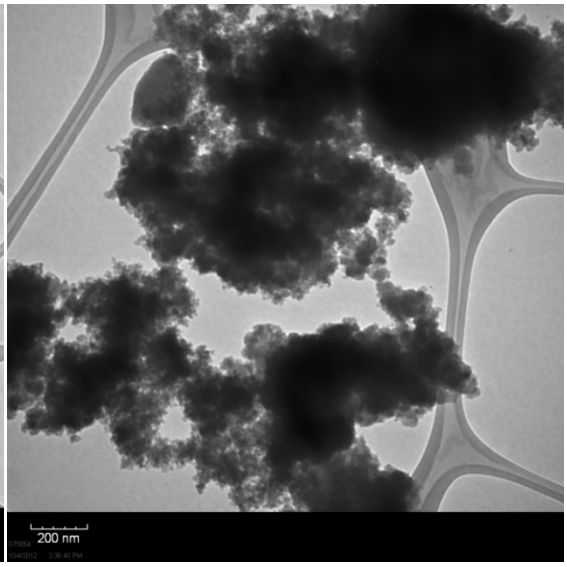

Trial 3.3 (6 τ)

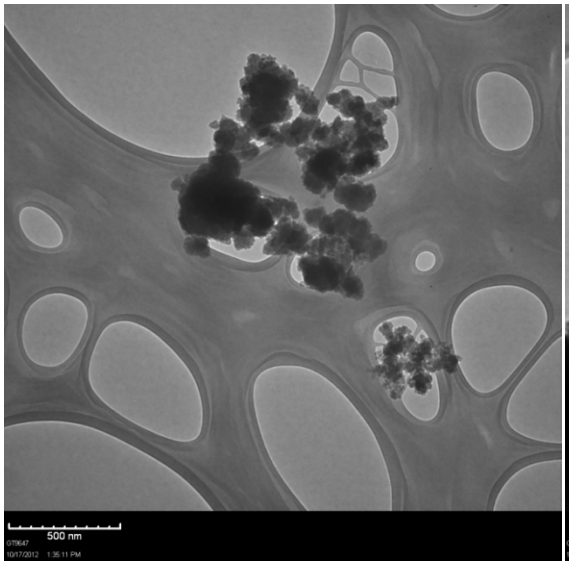

Trial 4.1 (1 τ)

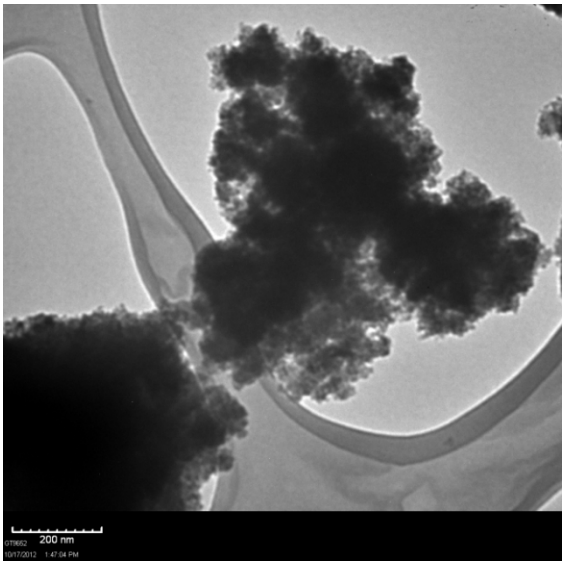

Trial 4.1 (6 τ)

Figure 6.8. TEM images of each flow-through synthesis trial at 1 and 6 τ.

6.3.3 Analysis and Parameter Effect Investigation

With the novel nature of this flow-through synthesis process, confirming the presence of the desired product is imperative. Crystal phase of the product is considered the most important figure of merit for this initial optimization followed by normalized yield,

porosity, and crystal size/morphology. Without significant evidence of the correct crystal phase, it is not possible to determine if the desired product, UiO-66-NH_2, has been synthesized.

Once product phase consistency is established the normalized yield has an obvious impact on the success of this scale-up endeavor. Others in our group have shown reactant concentration to have a significant effect on MOF yield, and the kinetic studies of Chapter 5 directly demonstrate the potential of increased synthesis temperature. Since both of these parameters remain constant throughout this optimization, normalized yields are expected to be less than optimal.

Effects on porosity and crystal size/morphology are important to understand from a fundamental standpoint but depending on the specific target application. Large pore volumes and BET surface areas are important for maximizing performance near saturation loading and indicate a crystalline-phase with less defects. However, higher surface areas should not be considered directly-proportional to adsorption performance without experimental evidence. The CO_2 adsorption comparison of UiO-66 from microwave and conventional syntheses (Appendix A) demonstrates only a slight adsorption capacity difference despite 24% surface area loss. The amine-functional groups of UiO-66-NH_2 play a more direct role for low fugacity TIC filtration than BET surface area, which was apparent when a lower surface area UiO-66-NH_2 sample (ca. 500 m^2/g) was analyzed by UTRC for TIC filtration and showed better breakthrough performance than a higher surface area sample (ca. 1,000 m^2/g) of the same material.

Also, the crystal size and morphology are important for MOFs that require a binder to pelletize or applications requiring a specific size of crystallites. However, UiO-66-NH_2

can be pelletized without a binder and with no apparent performance loss, which also negates the importance of crystal size for applications such as pressure-swing adsorption (PSA). Also, most UiO-66 syntheses typically result in sub-micron crystals,[21,23] and the use of modulators requires attention if crystal size distribution is of particular importance.[7]

Table 6.2. Summary of data used for generating main-effect experimental design plots, which are based on average values from trials 2.1, 2.2, 3.1, and 3.2 for a given parameter
(e.g. Average values for using 2 impellers are from trials 3.1 and 3.2)

		Yield (g/L)	*P*	BET (m^2/g)
Impellers	1	1.76	0.1	265
	2	0.45	0.6	515
Draft Tube	Yes	0.5	0.3	385
	No	1.71	0.3	395

The experimental results are analyzed to determine each operating parameter's effect on a particular product attribute (main effect) as well as interaction effects between multiple parameters (interaction effect). 2^N experiments are required to examine main and interaction effects for N parameters. So, the main effects and interaction effects of using the draft-tube and the second impeller are examined via trials 2.1, 2.2, 3.1, and 3.2, which provides direct insight into further reactor design and experimentation in the field of continuous-flow crystallization of MOFs.

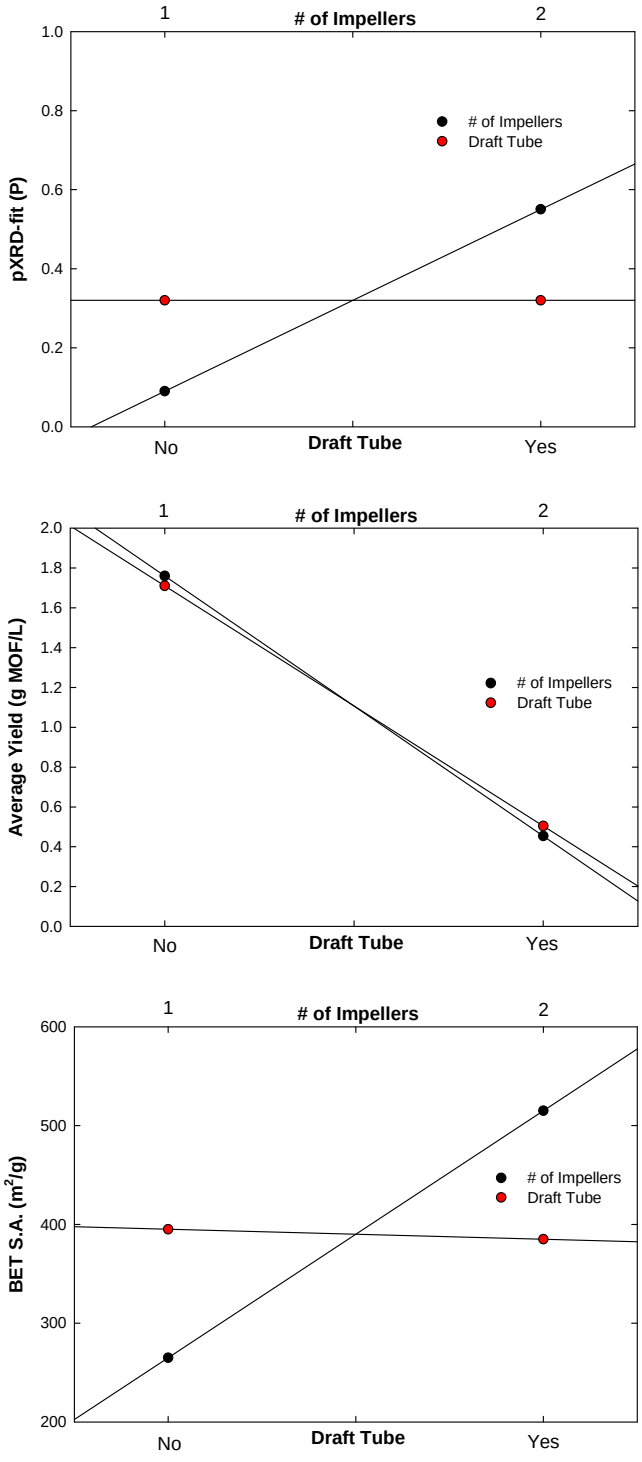

Figure 6.9. Main effects of # of impellers and draft tube presence on *P* (top), average yield (middle), and BET surface area (bottom).

The main effects on the previously defined pXRD-fit value, *P;* the average yield, and BET surface areas are tabulated in Table 6.2 and illustrated in Figure 6.9. Inclusion of the draft-tube appears to have no effect on *P* and an adverse effect on the average yield. Using two impellers appears to significantly increase *P*, which is likely attributed to more uniform crystallization within the reactor due to more thorough mixing. However, an adverse effect on yield is also observed when using two impellers and may be intrinsic to the current reactor design. Even though the impellers are designed to provide mainly axially directed flow (up/down), they will also exhibit a centrifugal effect, which could push the MOF products away from the concentric outlet. Similar to the main effects for *P*, the main effects on BET surface area (S.A.) demonstrates appreciably no dependence on the presence of the draft tube. The average surface areas from the trials with the draft tube present and removed, 2.1/3.1 and 2.2/3.2, are 395 m^2/g and 385 m^2/g, respectively, which are within the estimated experimental error of 5%. However, the average BET surface areas increase significantly when utilizing two impellers versus one impeller from 265 m^2/g and 515 m^2/g, respectively, which demonstrates a significant main effect of the number of impellers on BET surface area.

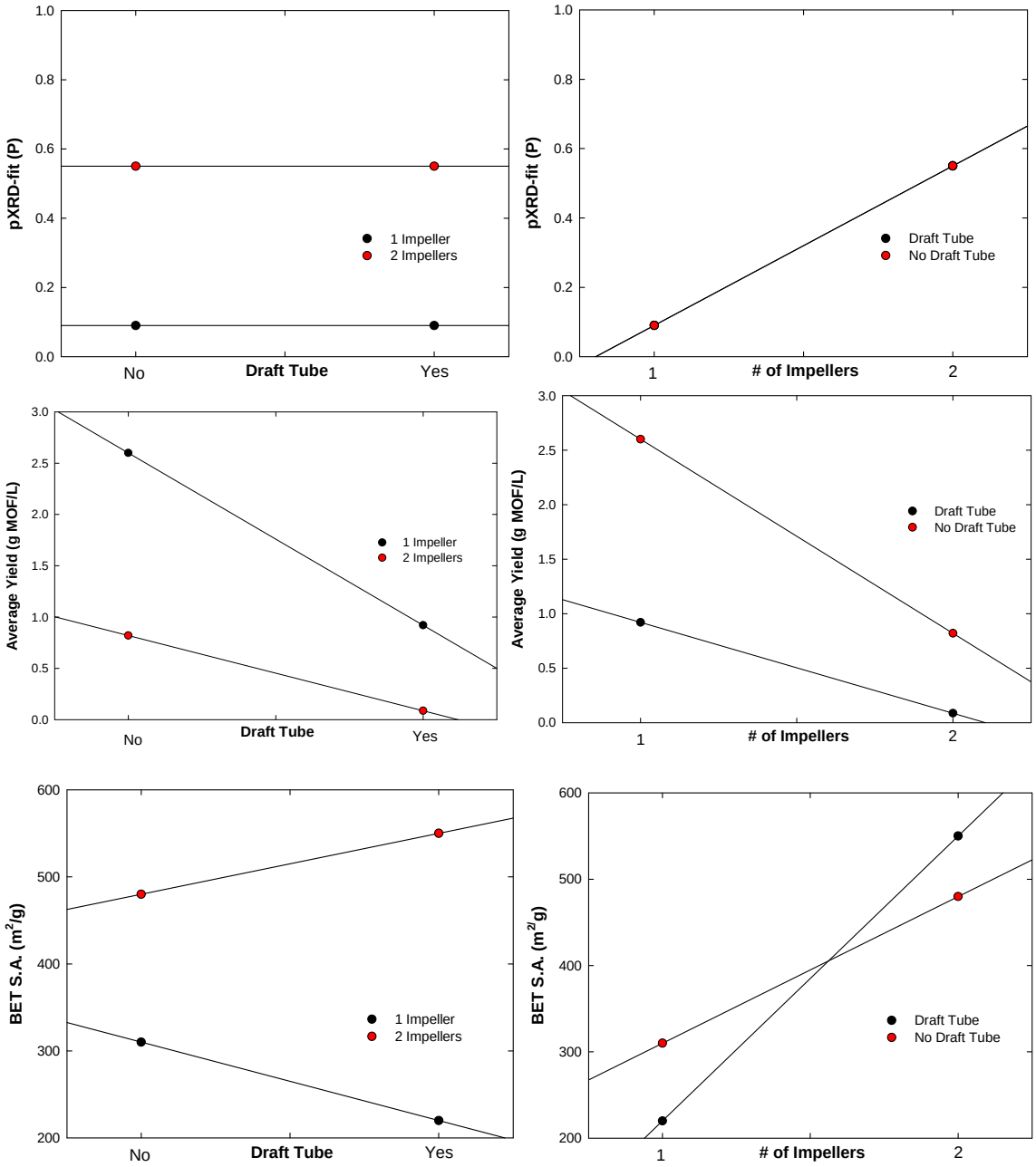

Figure 6.10. Interaction effects; draft tube given # of impellers (left) and # of impellers given draft tube (right) on *P*(top), average yield(middle), and BET surface area (bottom).

The interaction effects for draft tube implementation and use of one or two impellers are graphically illustrated in Figure 6.10. These plots are generated from the individual experiment data given in table 6.1. For example, the top-left graph in Figure 6.10, which

illustrates the draft-tube effect on *P* given the number of impellers, uses the *P*-values for trials 2.1 and 2.2 for the 1-impeller plot and trials 3.1 and 3.2 for the 2-impeller plot. The interactive effects on *P* illustrate again that the draft-tube has no measurable effect on the pXRD results. Synergistic results are seen for the yield comparisons with increasing the number of impellers and implementing the draft-tube both reducing average yield. The draft-tube effect given the number of impellers on the BET surface area (Fig. 6.10 bottom, left) exhibits the only antagonistic interaction effect of this study. This illustrates that using the draft tube with only one impeller decreases the BET surface area of the product but increases the surface area when two impellers are in place. Also, the effect of using two impellers increases the BET surface area for each trial but does so more drastically when the draft-tube is in place.

6.3.4 General Discussion

Crystallinity is the most important figure of merit, and crystals large enough for single-crystal XRD are not likely with UiO-66-NH_2. So, a quantitative measure of pXRD agreement with the published structure is necessary. Development of the *P* parameter to examine the pXRD results appears to be a useful approach to quantify the level of crystal-phase agreement. Analysis of the trials demonstrate that optimizing the pXRD agreement of the product is straight-forward. More thorough mixing via increasing the number of impellers (2.1,2.2 v. 3.1,3.2) or the stirring rate (3.3 v. 4.1) produces more consistent pXRD results. The presence of the draft tube appears to have essentially no effect on pXRD results, which may be indicative of minimal impedance of the reactor mixing despite significantly changing the flow.

Yield is obviously important for reactor optimization but currently secondary to crystallinity because of the novel nature of flow-through MOF synthesis. The yield is inconsistent throughout the reported trials (average % variance = 59%) and appears to be strongly affected by plugging within the reactor outlet, which is observed during cleaning between trials. These inconsistencies minimize the applicability of identified trends. Assuming that the bulk flow at the outlet is not affected by the stirring, the Re is ca. 34. So, outlet plugging may be overcome using a variety of techniques including increasing the outlet velocity, inert gas sparging, sonicating, or agitating the outlet stream. Specific recommendations are discussed in Chapter 9. Despite the variable results, yields at or above the previously published maximum yields from the kinetic study (ca. 2.6 g/L)[15] are observed for points in trial 2.2 and 3.3, which illustrates one of the potential benefits of flow-through syntheses.

The porosity of the products measured via BET analysis of N_2 adsorption at 77 K appears to nearly mirror the pXRD fit (except trial 4.1), which indicates that the crystal phase development of the product is mainly governing the resultant surface area. The presence of undissolved reactants or amorphous impurities may reduce the BET surface area but can be addressed via post-synthesis solvent washing or separations.

Trials 3.3 and 4.1 are not included in the determination of main and interactive effects due to the need of 2^N trials for N parameter optimization. However, they can be used to guide further design and experimentation. Trial 3.3 yields the best BET surface area of 780 m^2/g and slightly better *P*-value than the analogous upward flow trial, 3.2, (0.58 v. 0.55). Trial 4.1, which utilizes a 1.7X stir-rate and downward-directed flow shows the best pXRD fit (P=0.66) but surprisingly low BET S.A. of 370 m^2/g, which is repeated

using the same sample and confirmed within 3%. Multiple phenomena govern the self-assembly of MOFs in general such as temperature, concentration, solvent, water presence, etc. Stirred and continuous-flow systems add to this complexity by introducing shear effects and complex fluid and heat transfer with entrained solids. Trial 4.1 exemplifies this and illustrates how thorough optimization of just one parameter for such a novel process may require an array of trials. Further ideas of reactor design and optimization experiments are given in Chapter 9.

6.3.5 Future Potential

Estimated costs of manufacturing UiO-66-NH_2 at the current yields (g/L) are ca. $22/g assuming the maximum observed concentration of 2.6 g/L is achieved consistently, which is not directly competitive with current commercially available MOFs, Basolites, with prices up to $28.75/g.[24] The larger scale potential for UiO-66-NH_2 versus current Basolites and ability to readily reduce the operating costs preclude abandonment of further optimization.

The current design and retention times would produce ca. 9.4 g of UiO-66-NH_2 per day. However, simply increasing the temperature to 413 K can reduce the required retention

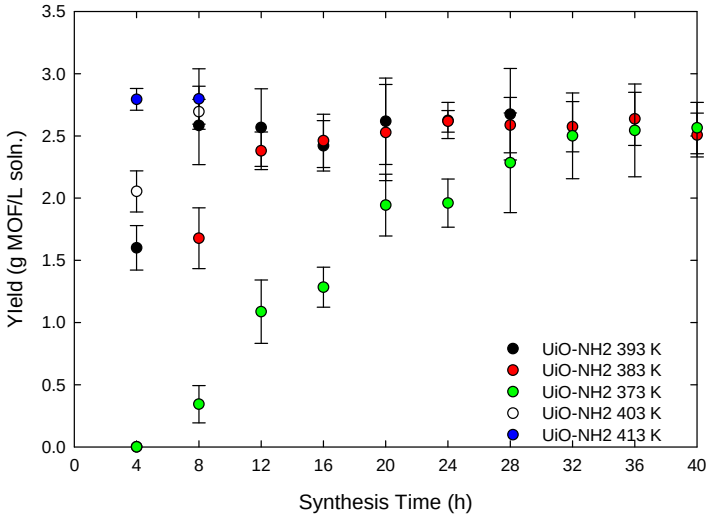

Figure 6.11. Previously published kinetic yield results[15] with additional data for 403 K and 413 K.

time from 12 h to 4 h and increase throughput 3-fold (Fig. 6.11). Also, based on concentrations reported for the parent material,[25] increased reactant concentrations can be employed to drastically increase yield. More specific design suggestions are given in Chapter 9.

Other benefits of flow-through solvothermal crystallization include recycling the solvent and seed crystals and *in situ* purification of the desired crystalline phase. The solvent recycling can significantly reduce operating costs and environmental impact of the synthesis. Often MOFs are formed with impurities with different densities compared to the desired product. In a batch-style synthesis, this requires another processing step consisting of immersion in a solvent with density between the two phases and decanting the solution. However, with advanced flow-through reactors such as the oscillatory-baffled flow reactor (OBR) the separation and reaction can occur simultaneously.[16]

6.4 Conclusions

This work provides a preliminary optimization of a novel continuous-flow MOF synthesis process. Six trials are reported, which allow the identification of main and interactive effects of using one or two impellers and draft tube implementation. PXRD and BET results from the bulk products show increased crystallinity and porosity, respectively, with the use of two impellers and improvements from the initial proof-of concept trial. The draft tube presence does not have a significant effect on either crystallinity or porosity. Increased yields are observed compared to the maximum yield from a prior batch style kinetic study. However, the yield results show inconsistent behavior, which is attributed to a design flaw in the current reactor/process conditions that promotes plugging of the outlet stream. Methods to alleviate this problem are proposed including increasing the operating temperature and outlet flow rate. Although major limitations of the current reactor have been identified, the continued development of flow-through MOF crystallizers has the potential to advance the industrial and commercial applicability of MOFs in the near future.

6.5 References

1. Britt D, Tranchemontagne D, Yaghi OM. Metal-organic frameworks with high capacity and selectivity for harmful gases. *Proc. Natl. Acad. Sci. U. S. A.* Aug 2008;105(33):11623-11627.

2. Galli S, Masciocchi N, Colombo V, et al. Adsorption of Harmful Organic Vapors by Flexible Hydrophobic Bis-pyrazolate Based MOFs. *Chem. Mat.* Mar 2010;22(5):1664-1672.

3. Furtado AMB, Wang Y, Glover TG, LeVan MD. MCM-41 impregnated with active metal sites: Synthesis, characterization, and ammonia adsorption. *Microporous Mesoporous Mat.* Jul 2011;142(2-3):730-739.

4. Keskin S, van Heest TM, Sholl DS. Can Metal-Organic Framework Materials Play a Useful Role in Large-Scale Carbon Dioxide Separations? *ChemSusChem.* 2010;3(8):879-891.

5. Liu J, Benin AI, Furtado AMB, Jakubczak P, Willis RR, LeVan MD. Stability Effects on CO(2) Adsorption for the DOBDC Series of Metal-Organic Frameworks. *Langmuir.* Sep 2011;27(18):11451-11456.

6. Samanta A, Zhao A, Shimizu GKH, Sarkar P, Gupta R. Post-Combustion CO2 Capture Using Solid Sorbents: A Review. *Ind. Eng. Chem. Res.* Feb 2012;51(4):1438-1463.

7. Horcajada P, Gref R, Baati T, et al. Metal-Organic Frameworks in Biomedicine. *Chem. Rev.* Feb 2012;112(2):1232-1268.

8. Allendorf MD, Houk RJT, Andruszkiewicz L, et al. Stress-induced Chemical Detection Using Flexible Metal-Organic Frameworks. *Journal of the American Chemical Society.* Nov 2008;130(44):14404-+.

9. Shekhah O, Liu J, Fischer RA, Woll C. MOF thin films: existing and future applications. *Chem. Soc. Rev.* 2011;40(2):1081-1106.

10. Ulrich Muller, Hermann Putter, Michael Hesse, et al. Method for Electrochemical Production of a Crystalline Porous Metal Organic Skeleton Material. *United States Patent Application Publication.* 2004;10/580,407.

11. Mueller U, Schubert M, Teich F, Puetter H, Schierle-Arndt K, Pastre J. Metal-organic frameworks - prospective industrial applications. *J. Mater. Chem.* Feb 2006;16(7):626-636.

12. Yang HW, Orefuwa S, Goudy A. Study of mechanochemical synthesis in the formation of the metal-organic framework Cu(3)(BTC)(2) for hydrogen storage. *Microporous Mesoporous Mat.* Aug 2011;143(1):37-45.

13. James SL, Adams CJ, Bolm C, et al. Mechanochemistry: opportunities for new and cleaner synthesis. *Chem. Soc. Rev.* 2012;41(1):413-447.

14. Myerson AS. *Handbook of Industrial Crystallization, Second Edition*. *Handbook of Industrial Crystallization, Second Edition.* 2002.

15. Schoenecker PM, Belancik GA, Grabicka BE, Walton KS. Amine-Functionalized Zr-Based MOF Synthesis Kinetics and Process Design. *AIChE Journal.* 2012.

16. Mackley MR, Smith KB, Wise NP. THE MIXING AND SEPARATION OF PARTICLE SUSPENSIONS USING OSCILLATORY FLOW IN BAFFLED TUBES. *Chemical Engineering Research & Design.* Nov 1993;71(A6):649-656.

17. Cavka JH, Jakobsen S, Olsbye U, et al. A new zirconium inorganic building brick forming metal organic frameworks with exceptional stability. *Journal of the American Chemical Society.* Oct 2008;130(42):13850-13851.

18. SCSI FOCS. Vanguard V6500 Centrifuge. [Website]. http://www.cecocablingsystems.com/centrifuge.htm. Accessed July 1st, 2010, 2010.

19. Valyocsik EW. Apparatus for a Continuous Down-Flow Zeolite Production. *United States Patent* 1983;4,368,174.

20. National Center for Biotechnology Information USNLoM. Dimethylformamide-Compound Summary. 2012; http://pubchem.ncbi.nlm.nih.gov/summary/summary.cgi?cid=6228&loc=ec_rcs#x27.

21. Abid HR, Ang HM, Wang SB. Effects of ammonium hydroxide on the structure and gas adsorption of nanosized Zr-MOFs (UiO-66). *Nanoscale.* 2012;4(10):3089-3094.

22. Zhang M, Karjala TW, Kolthammer BWS. Delayed dynamics of polymer properties in continuous stirred tank polymerization reactors. *Ind. Eng. Chem. Res.* Aug 2007;46(18):5922-5935.

23. Devautour-Vinot S, Maurin G, Serre C, et al. Structure and Dynamics of the Functionalized MOF Type UiO-66(Zr): NMR and Dielectric Relaxation Spectroscopies Coupled with DFT Calculations. *Chem. Mat.* Jun 2012;24(11):2168-2177.

24. Sigma-Aldrich. *http://www.sigmaaldrich.com/united-states.html.* 2010.

25. Garibay SJ, Cohen SM. Isoreticular synthesis and modification of frameworks with the UiO-66 topology. *Chem. Commun.* 2010;46(41):7700-7702.

CHAPTER 7

METAL-ORGANIC FRAMEWORK SCALE-UP: TRENDS AND CHALLENGES

7.1 Introduction

Metal-organic framework (MOF) research has grown at an impressive rate, and MOFs are shown to have high potential for applications at the consumer and industrial levels including CO_2 removal from flue gas,[1-3] H_2 storage,[4] and targeted drug delivery.[5] With the vast number of MOFs and relatively few high-throughput synthesis methods reported, development of a comprehensive understanding of synthesis scale-up is of paramount importance.

Most scale-up work appears to be driven by synthesis of a particular material and/or reduction of environmentally unfavorable synthesis components. For example, the electrochemical method developed by BASF[6,7] eliminates the need for hazardous nitrate-containing solvents but is limited to MOFs containing metals, which are electrochemically ionizable under appropriate synthesis conditions. Mechanochemical synthesis techniques[8,9] greatly reduce the amount of solvent required to synthesize a given MOF, which has significant environmental and economic benefits. However, as with any new synthesis mechanism, the product quality obtained may vastly differ from reported solvothermal techniques and present new obstacles to overcome. Another viable option is to implement the existing solvothermal synthesis methods with the well developed field of crystallization process design.[10] Reactive crystallization processes

may provide benefits not currently reported in the alternative synthesis routes including fine-tuned crystal size distributions and *in situ* product purification.

Recently, we reported the development of a novel flow-through synthesis process for the metal-organic framework, UiO-66-NH_2.[11] The water stability of UiO-66 materials[12,13] and the amine-functionality made this material a propitious candidate for multiple applications.[14,15] A thorough investigation of the batch-style synthesis of UiO-66-NH_2 provided important process design criteria. This work sought to apply the same batch-style experiments to a representative set of three MOFs; ZIF-65, MIL-125-NH_2, and Mg MOF-74, in order to develop a more thorough understanding of MOF synthesis scale-up potential.

With well known chemical and thermal stability,[16-20] ZIFs have attractive application potential for multiple industrial and consumer applications including gas[17,21,22] and liquid adsorption,[23] membranes,[24-27] and thin-films.[28] In this study, we examine ZIF-65, which consists of nitro-functionalized 10.4 Å cages accessible through 3.4 Å pores and exhibits specific potential for CO_2/N_2 and CO_2/CH_4 separations.[27,29]

MIL-125 is a Ti-based cubic MOF with photochromic properties from titanium-oxo compound formation during alcohol adsorption.[30] Titanium containing MOFs are relatively rare and in addition to their unique complexing abilities offer a less-toxic metal center for biological applications. The amine-functionalized form, MIL-125-NH_2 may provide additional benefits for selective adsorption of more polar molecules, e.g. CO_2. The 12-coordinated structure is thermally stable up to 360 °C under air atmosphere[30] and potentially resistant to degradation during water exposure.

MOF-74, M-DOBDC or CPO-27 is an open-metal site MOF with cylindrical pores and is reported using metal centers including Zn,[31] Co,[32] Ni,[33] and Mg.[34] With Lewis acid behavior of the open-metal sites, MOF-74 demonstrates high application potential for multiple uses including catalysis[35] and selective adsorption of toxic gases[36] and CO_2.[2,34,37,38] The Mg form of MOF-74 specifically demonstrates an affinity for CO_2 at low pressures by adsorbing ca. 35 wt% at 1 bar,[34] which is advantageous for flue gas separations and significantly higher than a key competitor, Zeolite 13X, which reportedly adsorbs ca. 21 wt% under identical conditions.[39,40] Also, water adsorption has been shown to diminish the CO_2 adsorption performance of MOF-74 to a lesser extent than 13X.[2]

7.2 Materials and Methods

All materials are procured from Sigma-Aldrich and used without further purification unless otherwise noted in the below procedures. The vessel studies utilize Parr polytetrafluoroethylene (PTFE)-line acid digestion bombs of 23, 46, and 125 mL volumes[41] and borosilicate glass vessels of 5-250 mL volumes. Kinetic studies utilize 20 mL borosilicate glass scintillation vials, which are removed in triplicate sets at intermediate times to examine product yield and quality throughout the synthesis. During every kinetic trial, at least one *control* vial is left under lab ambient conditions during the solvothermal syntheses. The vessel examination and kinetic studies reported herein use identical procedures to those reported for UiO-66-NH_2[11] in hopes of identifying underlying trends of batch-style MOF scale-up. All reported mass-yields are measured under lab ambient conditions after the samples have been dried or desolvated and allowed

to reach adsorption equilibrium with the ambient water vapor. These data are sufficient for identifying relative yields and synthesis trends. However, absolute yields are significantly lower and require weighing under vacuum or inert atmosphere for accurate data. Absolute yield could be estimated by subtracting the appropriate amount of adsorbed water from prior water adsorption data and ambient conditions during weighing, but the water adsorption data itself could vary significantly under different synthesis conditions and depending upon pore volume of each individual sample.

Powder X-ray diffraction (pXRD) experiments are collected using a PANalytical X-ray Diffractometer. For samples less than 100 mg, the MOF samples are placed on a low-background sample holder, and larger samples are placed in standard pXRD trays. The peak positions of each sample are compared to examine the bulk crystal-phase purity.

7.2.1 ZIF-65

ZIF-65 synthesis follows the originally reported procedure[42] with the substitution of Zn-metal centers instead of Co-metal centers. ZIF-65 consists of nitro-functionalized 10.4 Å cages accessible through 3.4 Å pores (Figure 7.1). The original procedure does not specify if N,N-dimethyl formamide (DMF) or N,N-diethyl formamide (DEF) is the required solvent. So, an initial trial is conducted with each solvent under the published conditions of 373 K and 72 h. The pXRD results are shown in Figure 7.1 and clearly illustrate a higher degree of peak position agreement between the DMF synthesized material and the pattern generated from the Crystallographic Information File (.cif) compared to the DEF analogue. So, all subsequent trials use DMF and the same concentrations originally published but on a significantly larger scale.[42]

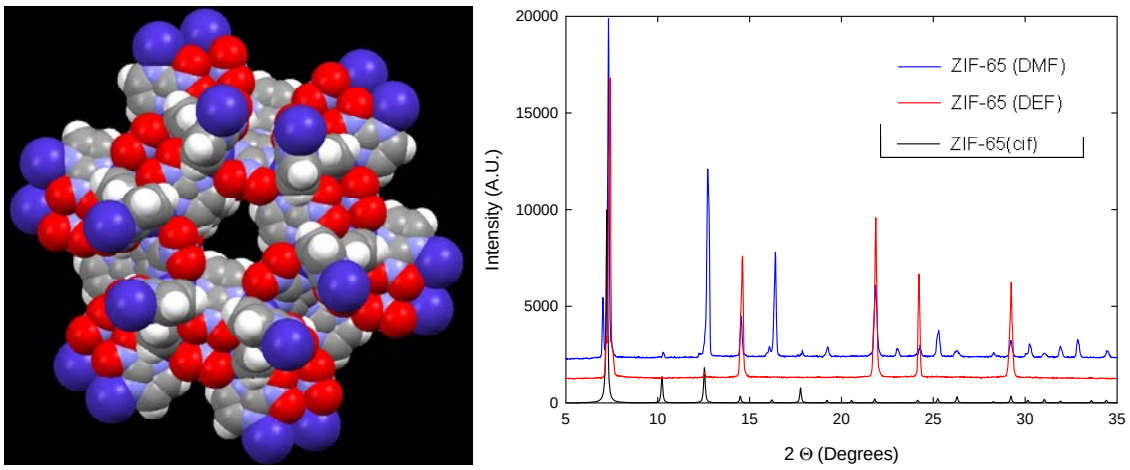

Figure 7.1. Structure of ZIF-65: C-grey, H-white, O-red, N-light blue, and Zn-dark blue (left) and pXRD results from initial synthesis of ZIF-65 to compare published solvents DMF and DEF (right).

To examine the vessel geometry and material preferences of ZIF-65, the aforementioned vessels were filled with recorded volumes of the following solution after dissolving the following solid constituents via stirring: 12.38g of 2-nitroimidazole (NIm) procured from Oakwood Products, 7.52g of ($Zn(NO_3)_2$ $6H_2O$), and 674 mL of DMF. The vessels were placed in a preheated isothermal oven at 373 K for 24h. These synthesis conditions were selected following the kinetic study.

The kinetic portion of this study utilized 11.76 g of NIm and 7.14 g of $Zn(NO_3)_2$ $6H_2O$ in 640 mL of DMF. Sixty four scintillation vials were filled with 10 mL aliquots of the reactant solution. The vials were divided equally into three sand baths and placed in isothermal ovens at 373, 383, and 393 K. The first two samples were collected every 6 hours in anticipation of the reaction occurring more rapidly than the published 72 h. Then, the remaining samples were collected every 12 h.

All samples were collected with filter paper, rinsed with DMF 3x, and dried overnight under ambient temperature and dynamic vacuum. Finally, each individual sample was

weighed using an analytical balance. Kinetic samples from each time and temperature were combined prior to further characterization via pXRD.

7.2.2 MIL-125-NH_2

The previously reported synthesis[30,43] was modified and implemented as follows. For the kinetic study, 15.3g of 2-amino-terephthalic acid (ATPA) and 12.75ml of titanium tetraisopropoxide (TiPr) were introduced in a solution of methanol (MeOH) and dimethylformamide (DMF) (352.75ml; 1:1 ratio). The reactant solution was stirred for 15 minutes at room temperature. The obtained mixture was divided into 10 mL aliquots, transferred to glass vials, and placed in three sand baths. Next, the baths were placed in an isothermal oven at 373, 383, and 393K, and the intermediate samples were collected at 4, 8, 12, 18, 24, 36 and 48h. For the vessel material and geometry study, identical concentrations to those above were used with 25.2 g of ATPA and 21 mL of TiPr in 1,160 mL of the DMF/MeOH solution. The synthesis was conducted at 383 K for 24 h. All samples were then cooled down at room temperature, washed twice by methanol, and air dried at room temperature.

7.2.3 Mg MOF-74

The reactant concentrations for Mg MOF-74 syntheses were taken from Caskey et al.[34] For the vessel material and geometry experiment 9.50 g of magnesium nitrate hexahydrate ($Mg(NO_3)_2$ $6H_2O$) and 2.22 g of 2,5-dioxido-1,4-benzenedicarboxylic acid (DOBDC) were placed in 1,000 mL mixture of DMF:ethanol:water (15:1:1, by volume). The reactant mixture was then sonicated until all solid constituents were dissolved. The

solution was then divided, placed in the respective vessels, sealed, and reacted at 393 K for 20h in a programmable isothermal oven.

The Mg MOF-74 kinetic study used a similar batch of reactant solution containing 10.45 g of $Mg(NO_3)_2$ $6H_2O$ and 2.44 g of DOBDC in 1,100 mL of the solvent mixture. Again the solution was sonicated until homogenous, and 10 mL aliquots were placed in glass vials divided evenly in three sand baths. Then, the sand baths were placed in three isothermals ovens at 378, 388, and 398 K for 28 h.

All resultant products were collected with filter paper, rinsed with methanol volumes equivalent to the original reactant solution 3x, and allowed to air dry prior to weighing. Air drying without desolvation was specifically selected for Mg MOF-74 from prior work,[13] which demonstrated that exposure to humid ambient air and reactivation appears to be degrade the material.

7.3 Results and Discussion

7.3.1 ZIF-65

The vessel material experimental results are shown in Fig. 7.2 and illustrate a direct proportionality between the yield of ZIF-65 and the volume of reactant solution. There is

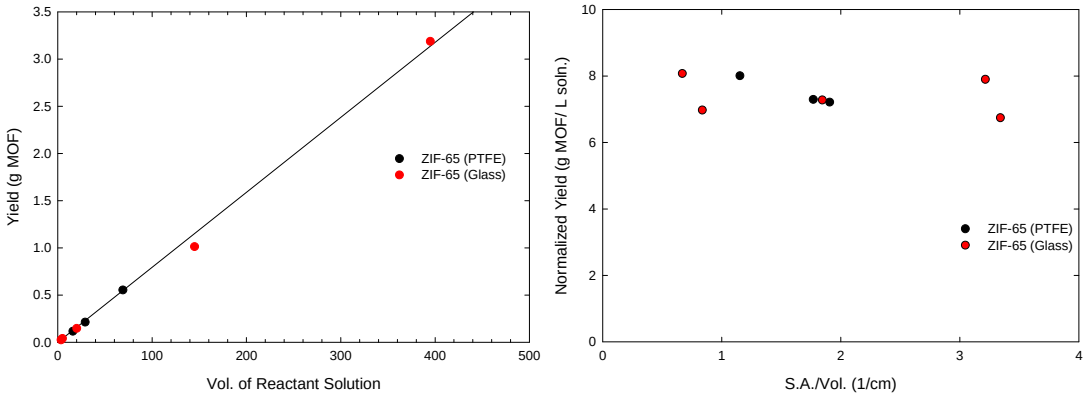

Figure 7.2. ZIF-65 vessel material (left) and geometry results (right).

no preference for PTFE or glass vessels demonstrated, which likely is a sign of nucleation and growth occurring mainly in the solution itself. These results show the same trends as the UiO-66-NH_2 work published earlier.[44] However, the kinetic results (Fig. 7.3) are in stark contrast. Instead of asymptotically approaching the same equilibrium yield at all synthesis temperatures, ZIF-65 equilibrium yield decreases with increasing temperature. The presence and positions of local maximum yields at each temperature is also interesting.

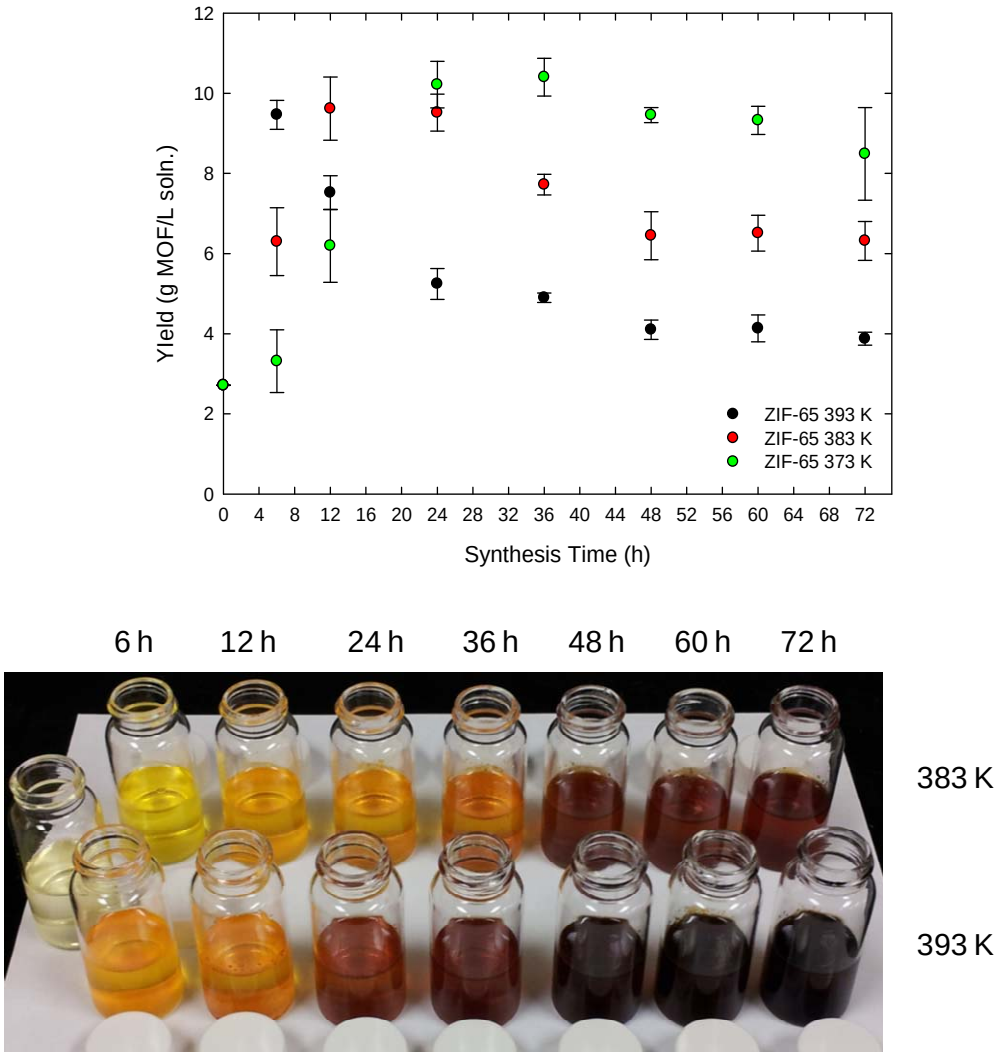

Figure 7.3. ZIF-65 kinetic yield results at 373, 383, and 393 K (top). Picture of kinetic samples (bottom) with the control sample at left-center.

The local maximums are located between samples 0 - 4 h, 12 - 24 h, and 24 - 36 h for 393, 383, and 373 K, respectively. The kinetic samples also exhibit a significant color transition from a nearly clear reactant solution to yellow, orange, red, and dark red with increasing time and temperature.

These results are likely an attribute of the degradation of ZIF-65 under the given synthesis conditions, which is also reported for MOF-14.[45] Despite the specific color change and decreased yield of the kinetic products, the pXRDs of all samples are very consistent exhibiting nearly perfect peak-agreement with the .cif file throughout the study (Figure 7.4). However, for MOF-14 the EDXRD results demonstrate a complete loss of crystallinity.[45] If the decrease in ZIF-65 equilibrium yield with increasing synthesis temperature is the result of degradation, the degradation reaction appears to be kinetically limited, and with no discernible XRD pattern change, the degradation product is likely non-crystalline.

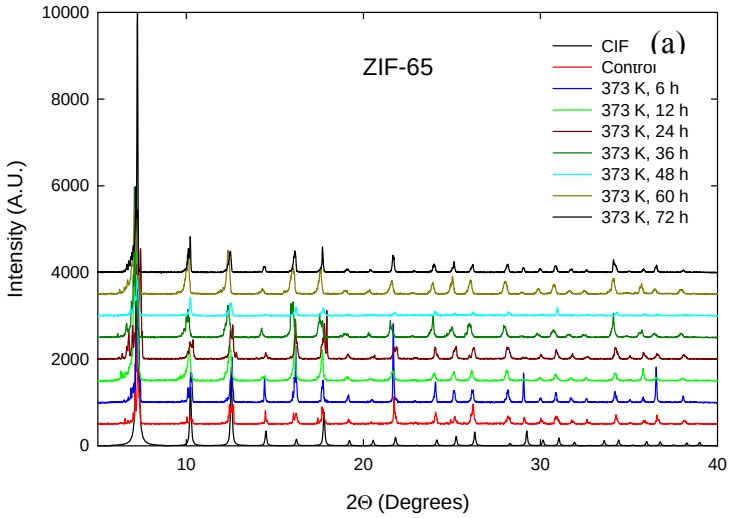

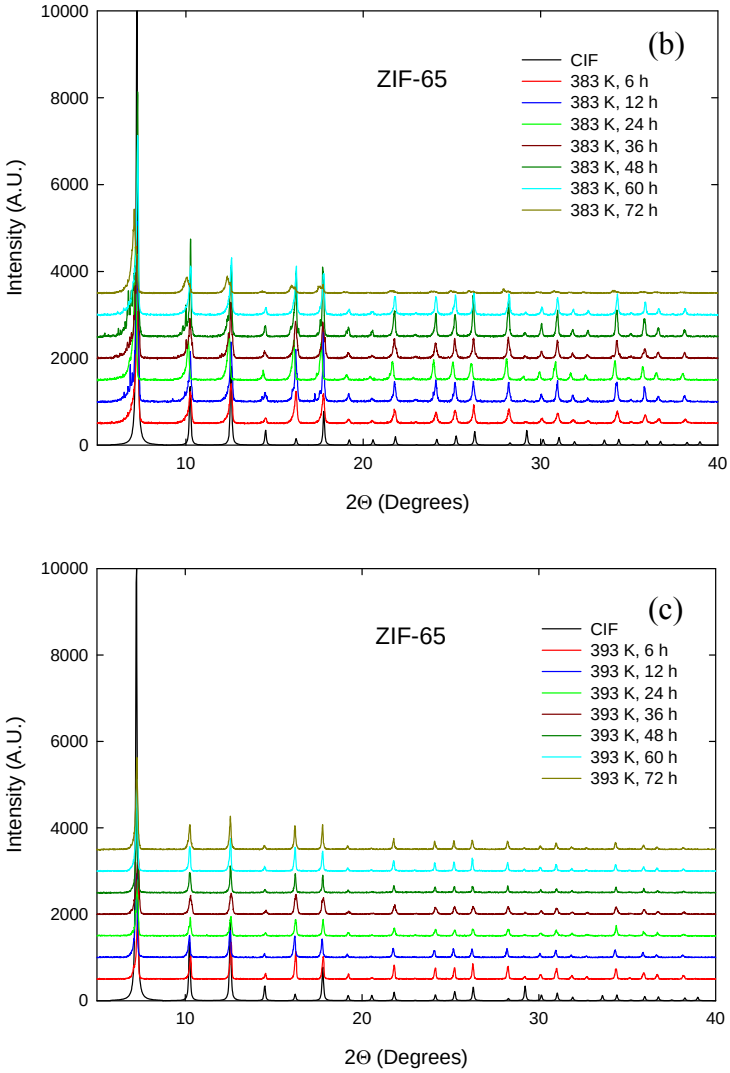

Figure 7.4. ZIF-65 pXRD kinetic results at 373(a), 383(b), and 393 K (c).

Transmission electron microscopy is used to examine select kinetic samples, 383 K-6 h and 383 K-24 h, in hopes of gaining further insight into the atypical kinetic behavior. These samples are selected due to their chronologic positions before and after the maximum yield. Figure 7.5 shows similar sub-micron crystallites for both samples with some cubic crystals as well as less-defined aggregates or intergrown crystallites. At six hours there is a significant population of ZIF-65 crystals with length scales of ca. 20 nm, which are no longer present at twenty four hours. This could be indicative of dissolution

of the smaller crystallites back into the mother liquor, which could explain the subsequent decrease in yield. However, it may also be just the early stages of the crystal growth process. In order to clarify further, an accurate crystal-size distribution as well as count

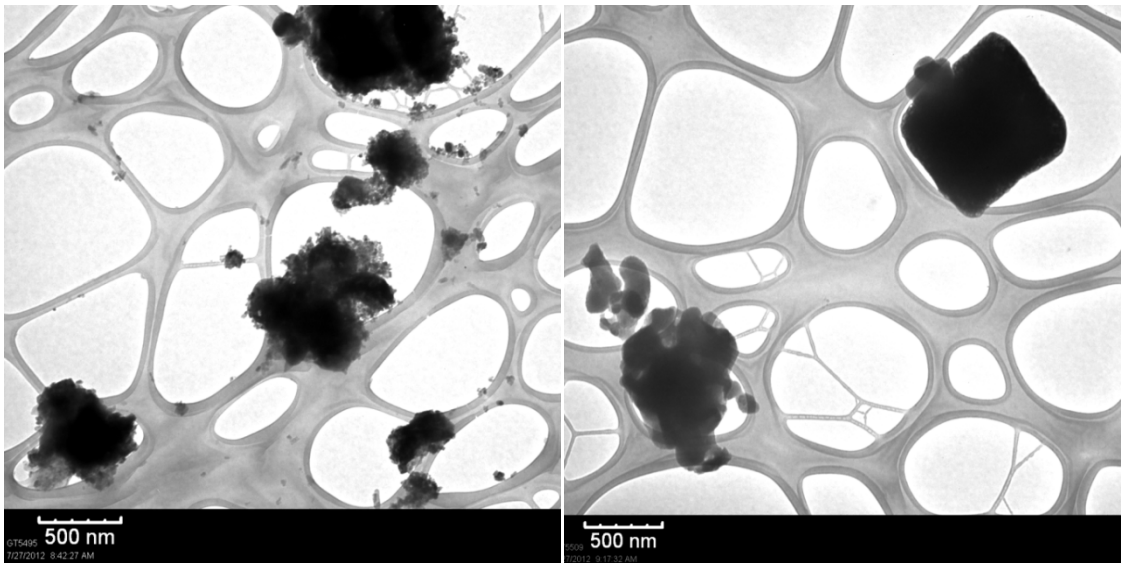

Figure 7.5. ZIF-65 TEM images of kinetic samples 383 K 6h (left) and 24 h (right).

of the total crystal population for each sample is required. Without both one cannot determine if the crystal size change is merely due to crystal growth, or if dissolution is taking place and is significant enough to affect the total yield.

7.3.2 MIL-125-NH_2

The vessel material and geometry results for MIL-125-NH_2 are illustrated in Figure 7.6 and show a similar trend to ZIF-65 and UiO-66-NH_2.[11] More specifically, a direct proportionality between synthesis volume or reactant solution and yield of unactivated MOF and no identifiable trend between the wetted surface area and volume of reactant solution are observed.

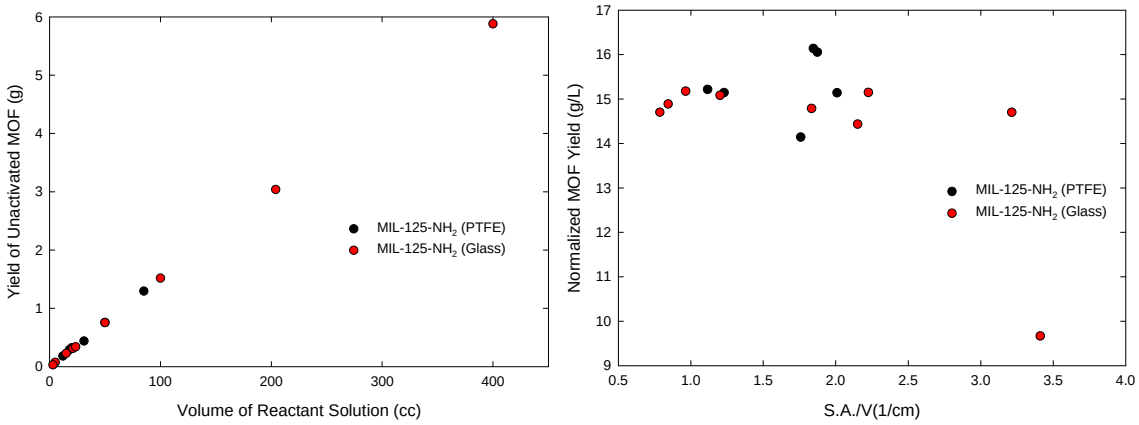

Figure 7.6. MIL-125-NH_2 vessel material (left) and geometry results (right).

The yield results from the kinetic study of MIL-125-NH_2 are illustrated in Figure 7.7 and show a less notable trend than the other materials examined. The significantly larger error bars are attributed to two sources. First, the metal source, TiOPr, which forms a solid precipitate when placed in the solvent solution and is included in the mass of

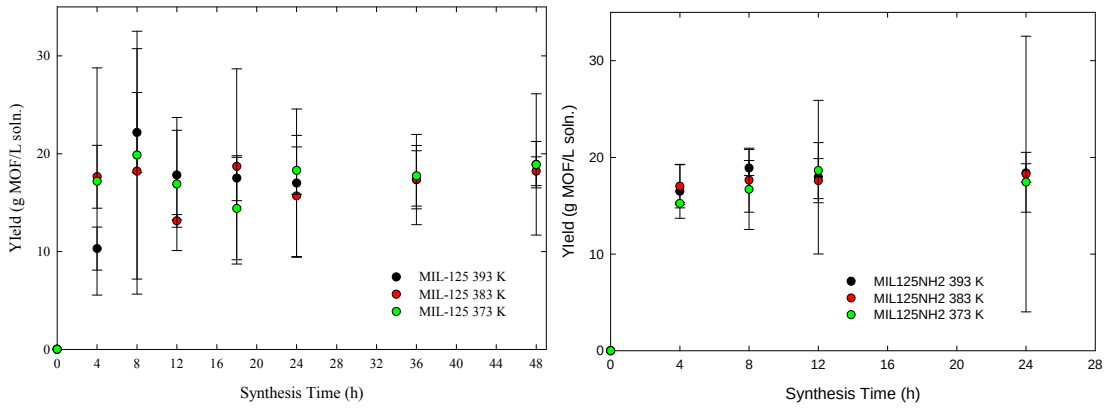

Figure 7.7. MIL-125-NH_2 initial kinetic synthesis trial (left) and repeated trial (right).

sample gathered at short times. This artificially raises the yield results before product formation. The pXRDs from the kinetic study (Figure 7.8) verify that the product collected at shorter times is non-crystalline. Second, the more volatile solvent mixture (1:1 ratio of DMF/Methanol) will lead to higher pressure buildup than the other syntheses of this study. The vials are apparently unable to contain a significant amount of the solvent solution as synthesis time progresses, which can detrimentally affect the precision of sample masses collected. To confirm that this experiment is intrinsically imprecise, the trial is repeated and significantly large error bars (95% C.I.) are obtained again.

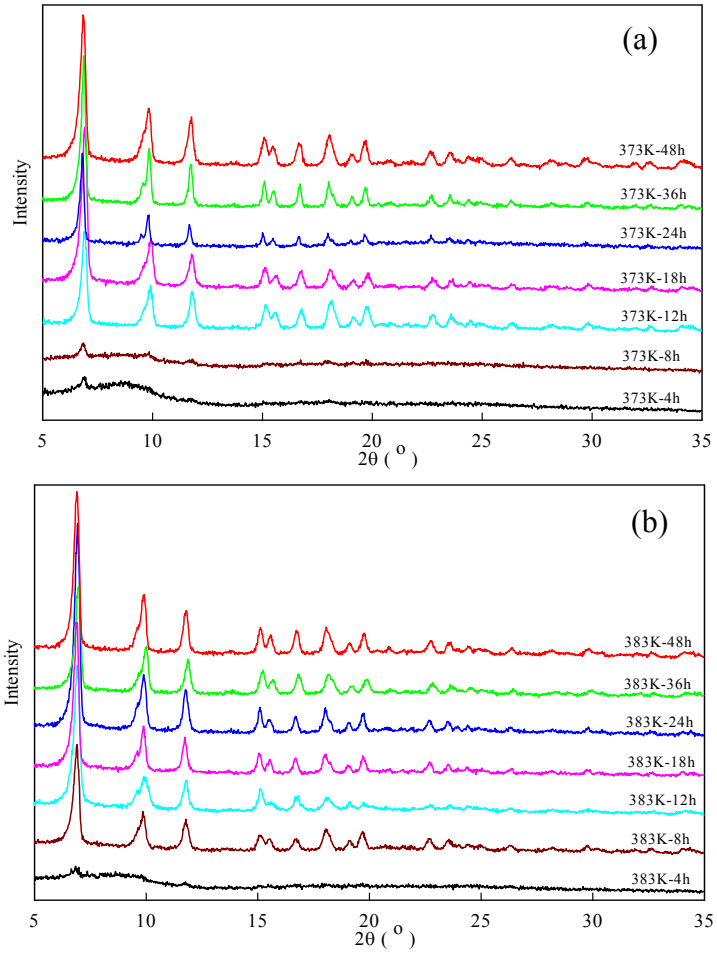

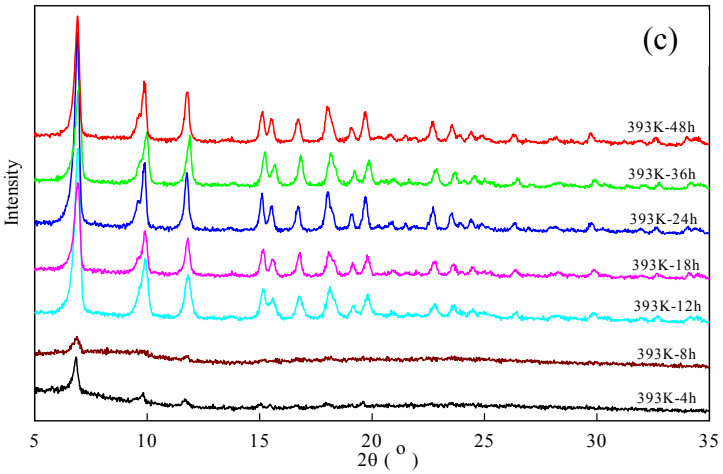

Figure 7.8. MIL-125-NH_2 kinetic pXRD results from 373(a), 383(b), and 393K (c).

In addition to the difficulties in precise determination of MIL-125-NH_2 yield, pXRD diffractograms also demonstrate inconsistencies. For example, at 393 K the first Bragg peak is discernible at 4 h but diminishes at 8 h, but at 383 K the complete diffractogram is visible at 8 h. Inherent with the TiPr metal-source, the large amount of amorphous solids in these samples negatively affects the consistency of pXRD analysis during the shorter synthesis times.

7.3.3 Mg MOF-74

The vessel material experimental results for Mg MOF-74 are shown in Figure 7.9 and demonstrate a significantly different trend than shown for the other MOFs of this study. Two distinctly different slopes are noted for the yield v. volume of reactant solution plot with the glass vessels demonstrating a better yield per given volume of reactant solution. This merely demonstrates some preference for the glass vessels. However, the normalized yield is inversely proportional to the S.A./V when using PTFE lined vessels

whose linear regression predicts that for S.A./V values above ca. 2.64 no appreciable amount of Mg MOF-74 product will be formed. This directly demonstrates that nucleation and growth of Mg MOF-74 occurs significantly on the vessel walls and the hydrophilic adsorption behavior of Mg MOF-74 reported earlier[13] dictates the nucleation-substrate interaction.

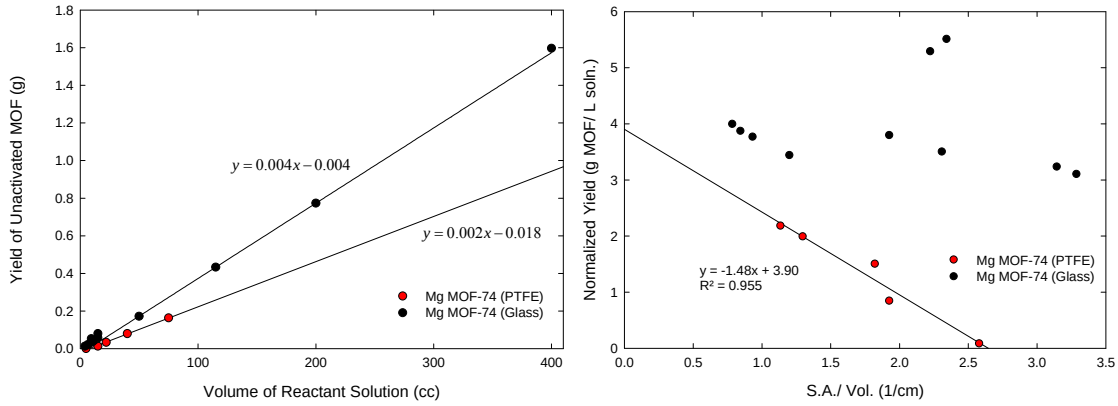

Figure 7.9. Mg MOF-74 vessel material (left) and geometry results (right).

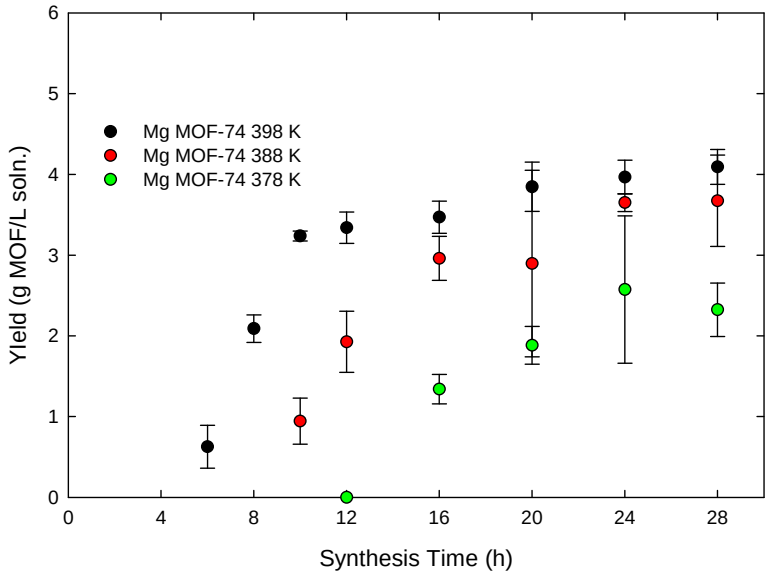

Figure 7.10. Mg MOF-74 kinetic yield results.

The mass-based yield examination of the intermediate samples (Figure 7.10) illustrates that different equilibrium yields are obtained at each of the three temperatures examined, with higher yields coming at increased temperatures. This is similar to what was seen for ZIF-65, but with inverse temperature dependence. This particular trend indicates that the synthesis is kinetically limited, and the product appears stable under the synthesis conditions. The pXRDs (Fig 7.11) confirm that the correct crystalline phase has been formed and is consistent for all discernible yields.

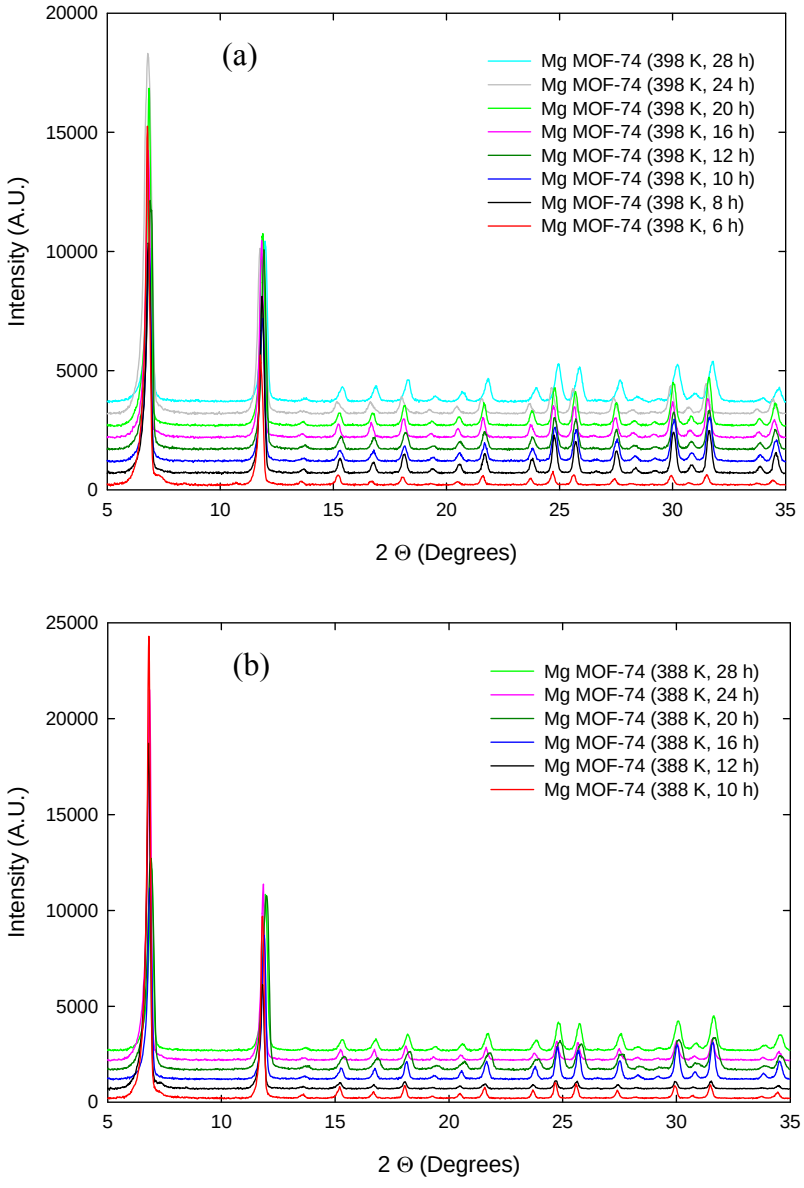

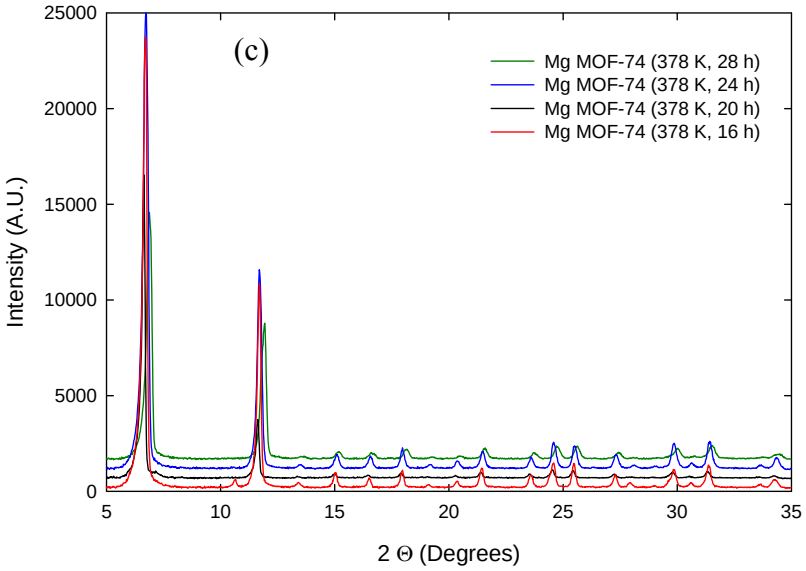

Figure 7.11. Mg MOF-74 kinetic pXRD results 398 K (a), 388 K (b), and 378 K (c).

7.3.4 General Hypotheses

These results lead to the development of the following two hypotheses:

1. *If nucleation and growth of a MOF occurs sufficiently at the vessel surface, then the yield-based material preference will be governed by the same surface properties as adsorption.*

2. *Solvothermal synthesis conditions provide a complex and dynamic chemical environment, which may lead to MOF degradation despite a robust coordination environment.*

7.4 Conclusions

This study has demonstrated commonalities with MOF synthesis behavior as well as some of the complex behavior of solvothermal scale-up. All three materials examined and UiO-66-NH_2[11] showed mass-based yields, which were directly proportional to the volume of reactant solution during the vessel geometry and material investigation. This followed general intuition of synthesis reactions. However, with the self-assembly

processes of MOF syntheses not sufficiently understood, even intuitive results required validation. Increasing the wetted S.A./V for PTFE-lined Mg MOF-74 synthesis trials detrimentally affected yield results. Even though ZIF-65 was selected from a very robust family of materials, the synthesis conditions caused a kinetically governed degradation or dissolution to a non-crystalline phase. MIL-125-NH_2 was more challenging to characterize via yield-based methods due to the immediate precipitate formed by the metal-ion source. Novel hypotheses are given for these results, which can be applied to scale-up of further MOF syntheses.

7.5 References

1. Keskin S, van Heest TM, Sholl DS. Can Metal-Organic Framework Materials Play a Useful Role in Large-Scale Carbon Dioxide Separations? *ChemSusChem.* 2010;3(8):879-891.

2. Liu J, Benin AI, Furtado AMB, Jakubczak P, Willis RR, LeVan MD. Stability Effects on CO(2) Adsorption for the DOBDC Series of Metal-Organic Frameworks. *Langmuir.* Sep 2011;27(18):11451-11456.

3. Samanta A, Zhao A, Shimizu GKH, Sarkar P, Gupta R. Post-Combustion CO2 Capture Using Solid Sorbents: A Review. *Ind. Eng. Chem. Res.* Feb 2012;51(4):1438-1463.

4. Song LF, Zhang J, Sun LX, et al. Mesoporous metal-organic frameworks: design and applications. *Energy Environ. Sci.* Jun 2012;5(6):7508-7520.

5. Horcajada P, Gref R, Baati T, et al. Metal-Organic Frameworks in Biomedicine. *Chem. Rev.* Feb 2012;112(2):1232-1268.

6. Ulrich Muller, Hermann Putter, Michael Hesse, et al. Method for Electrochemical Production of a Crystalline Porous Metal Organic Skeleton Material. *United States Patent Application Publication.* 2004;10/580,407.

7. Mueller U, Schubert M, Teich F, Puetter H, Schierle-Arndt K, Pastre J. Metal-organic frameworks - prospective industrial applications. *J. Mater. Chem.* Feb 2006;16(7):626-636.

8. Yang HW, Orefuwa S, Goudy A. Study of mechanochemical synthesis in the formation of the metal-organic framework Cu(3)(BTC)(2) for hydrogen storage. *Microporous Mesoporous Mat.* Aug 2011;143(1):37-45.

9. James SL, Adams CJ, Bolm C, et al. Mechanochemistry: opportunities for new and cleaner synthesis. *Chem. Soc. Rev.* 2012;41(1):413-447.

10. Myerson AS. *Handbook of Industrial Crystallization, Second Edition*. *Handbook of Industrial Crystallization, Second Edition.* 2002.

11. Schoenecker PM, Belancik GA, Grabicka BE, Walton KS. Amine-Functionalized Zr-Based MOF Synthesis Kinetics and Process Design. *AIChE Journal.* 2012.

12. Cavka JH, Jakobsen S, Olsbye U, et al. A new zirconium inorganic building brick forming metal organic frameworks with exceptional stability. *Journal of the American Chemical Society.* Oct 2008;130(42):13850-13851.

13. Schoenecker PM, Carson CG, Jasjuja H, Flemming CJJ, Walton KS. Effect of Water Adsorption on Retention of Structure and Surface Area of Metal-Organic Frameworks *Ind. Eng. Chem. Res.* 2012.

14. Ingleson MJ, Heck R, Gould JA, Rosseinsky MJ. Nitric Oxide Chemisorption in a Postsynthetically Modified Metal-Organic Framework. *Inorganic Chemistry.* Nov 2009;48(21):9986-9988.

15. Garibay SJ, Wang ZQ, Tanabe KK, Cohen SM. Postsynthetic Modification: A Versatile Approach Toward Multifunctional Metal-Organic Frameworks. *Inorganic Chemistry.* Aug 2009;48(15):7341-7349.

16. Park KS, Ni Z, Cote AP, et al. Exceptional chemical and thermal stability of zeolitic imidazolate frameworks. *Proc. Natl. Acad. Sci. U. S. A.* Jul 2006;103(27):10186-10191.

17. Hayashi H, Cote AP, Furukawa H, O'Keeffe M, Yaghi OM. Zeolite a imidazolate frameworks. *Nature Materials.* Jul 2007;6(7):501-506.

18. Diao HM, Ren SZ. *Synthesis and Stability of Zeolitic Imidazolate Framework ZIF-8.* 2010.

19. Kusgens P, Rose M, Senkovska I, et al. Characterization of metal-organic frameworks by water adsorption. *Microporous Mesoporous Mat.* Apr 2009;120(3):325-330.

20. Ge D, Lee HK. Water stability of zeolite imidazolate framework 8 and application to porous membrane-protected micro-solid-phase extraction of polycyclic aromatic hydrocarbons from environmental water samples. *Journal of Chromatography A.* Nov 2011;1218(47):8490-8495.

21. Wang B, Cote AP, Furukawa H, O'Keeffe M, Yaghi OM. Colossal cages in zeolitic imidazolate frameworks as selective carbon dioxide reservoirs. *Nature.* May 2008;453(7192):207-U206.

22. Phan A, Doonan CJ, Uribe-Romo FJ, Knobler CB, O'Keeffe M, Yaghi OM. Synthesis, Structure, and Carbon Dioxide Capture Properties of Zeolitic Imidazolate Frameworks. *Accounts of Chemical Research.* Jan 2010;43(1):58-67.

23. Centrone A, Santiso EE, Hatton TA. Separation of Chemical Reaction Intermediates by Metal-Organic Frameworks. *Small.* Aug 2011;7(16):2356-2364.

24. Thompson JA, Chapman KW, Koros WJ, Jones CW, Nair S. Sonication-induced Ostwald ripening of ZIF-8 nanoparticles and formation of ZIF-8/polymer composite membranes. *Microporous Mesoporous Mat.* Aug 2012;158:292-299.

25. Bux H, Liang FY, Li YS, Cravillon J, Wiebcke M, Caro J. Zeolitic Imidazolate Framework Membrane with Molecular Sieving Properties by Microwave-Assisted Solvothermal Synthesis. *Journal of the American Chemical Society.* Nov 2009;131(44):16000-+.

26. Li YS, Bux H, Feldhoff A, Li GL, Yang WS, Caro J. Controllable Synthesis of Metal-Organic Frameworks: From MOF Nanorods to Oriented MOF Membranes. *Adv. Mater.* Aug 2010;22(30):3322-+.

27. Atci E, Keskin S. Atomically Detailed Models for Transport of Gas Mixtures in ZIF Membranes and ZIF/Polymer Composite Membranes. *Ind. Eng. Chem. Res.* Feb 2012;51(7):3091-3100.

28. Demessence A, Boissiere C, Grosso D, et al. Adsorption properties in high optical quality nanoZIF-8 thin films with tunable thickness. *J. Mater. Chem.* 2010;20(36):7676-7681.

29. Amrouche H, Aguado S, Perez-Pellitero J, et al. Experimental and Computational Study of Functionality Impact on Sodalite-Zeolitic Imidazolate Frameworks for CO2 Separation. *Journal of Physical Chemistry C.* Aug 2011;115(33):16425-16432.

30. Dan-Hardi M, Serre C, Frot T, et al. A New Photoactive Crystalline Highly Porous Titanium(IV) Dicarboxylate. *Journal of the American Chemical Society.* Aug 2009;131(31):10857-+.

31. Rosi NL, Kim J, Eddaoudi M, Chen BL, O'Keeffe M, Yaghi OM. Rod packings and metal-organic frameworks constructed from rod-shaped secondary building units. *Journal of the American Chemical Society.* Feb 2005;127(5):1504-1518.

32. Dietzel PDC, Morita Y, Blom R, Fjellvag H. An in situ high-temperature single-crystal investigation of a dehydrated metal-organic framework compound and field-induced magnetization of one-dimensional metaloxygen chains. *Angew. Chem.-Int. Edit.* 2005;44(39):6354-6358.

33. Dietzel PDC, Panella B, Hirscher M, Blom R, Fjellvag H. Hydrogen adsorption in a nickel based coordination polymer with open metal sites in the cylindrical cavities of the desolvated framework. *Chem. Commun.* 2006(9):959-961.

34. Caskey SR, Wong-Foy AG, Matzger AJ. Dramatic tuning of carbon dioxide uptake via metal substitution in a coordination polymer with cylindrical pores. *Journal of the American Chemical Society.* Aug 2008;130(33):10870-+.

35. Yang DA, Cho HY, Kim J, Yang ST, Ahn WS. CO2 capture and conversion using Mg-MOF-74 prepared by a sonochemical method. *Energy Environ. Sci.* Apr 2012;5(4):6465-6473.

36. T.Grant Glover GWP, Bryan J. Schindler, David, Brittand OY. 'MOF-74 building unit has a direct impact on toxic gas adsorption.' *Chem. Eng. Sci.* 3 October 2010 .

37. Herm ZR, Krishna R, Long JR. Reprint of: CO2/CH4, CH4/H-2 and CO2/CH4/H-2 separations at high pressures using Mg-2(dobdc). *Microporous Mesoporous Mat.* Jul 2012;157:94-100.

38. Liu J, Wang Y, Benin AI, Jakubczak P, Willis RR, LeVan MD. CO2/H2O Adsorption Equilibrium and Rates on Metal-Organic Frameworks: HKUST-1 and Ni/DOBDC. *Langmuir.* Sep 2010;26(17):14301-14307.

39. Cavenati S, Grande CA, Rodrigues AE. Adsorption equilibrium of methane, carbon dioxide, and nitrogen on zeolite 13X at high pressures. *J. Chem. Eng. Data.* Jul-Aug 2004;49(4):1095-1101.

40. Franchi RS, Harlick PJE, Sayari A. Applications of pore-expanded mesoporous silica. 2. Development of a high-capacity, water-tolerant adsorbent for CO2. *Ind. Eng. Chem. Res.* Oct 12 2005;44(21):8007-8013.

41. Parr. Acid Digestion http://www.parrinst.com/products/sample-preparation/acid-digestion/. Accessed August 25th, 2012.

42. Banerjee R, Phan A, Wang B, et al. High-throughput synthesis of zeolitic imidazolate frameworks and application to CO2 capture. *Science.* Feb 2008;319(5865):939-943.

43. Zlotea C, Phanon D, Mazaj M, et al. Effect of NH(2) and CF(3) functionalization on the hydrogen sorption properties of MOFs. *Dalton Trans.* 2011;40(18):4879-4881.

44. Bass CR, Darvish K, Bush B, et al. Material properties for modeling traumatic aortic rupture. *Stapp Car Crash J.* 2001 2001;45:143-160.

45. Millange F, El Osta R, Medina ME, Walton RI. A time-resolved diffraction study of a window of stability in the synthesis of a copper carboxylate metal-organic framework. *Crystengcomm.* 2011;13(1):103-108.

CHAPTER 8

ZIF-65 (SOD) ADSORPTION AND STABILITY

8.1 Introduction

Metal-organic frameworks have high potential for multiple gas separation and storage applications.[1-4] Mesoporous-MOFs with high surface areas are typically the best candidates for high pressure storage of gases including CH_4, CO_2, and H_2.[5] For separations occurring at lower pressures, such as CO_2 capture from flue gas, smaller pore MOFs containing functionalized pore-space typically show the best performance. With Lewis acid functionality, open-metal site MOFs are often considered the most propitious candidates for CO_2 separations.[6,7] However, their affinity for water and instability under humid conditions may prove detrimental for flue gas applications;[8-10] unless a guard bed is implemented.

MOFs with size-selective properties are also viable options for gas separations. Recently, Atci and Keskin[11] modeled pure and polymer composite membranes of ZIF-90 and ZIF-65 for H_2/CO_2 separations. Both ZIFs showed similar adsorption of the smaller H_2 molecules and ZIF-65 demonstrated higher uptakes of CO_2, which is attributed to the slightly smaller 3.4 Å pores size. Permeation modeling predicts that both ZIFs should also exceed the present Robeson's limit[12] and ZIF-65 will demonstrate higher H_2/CO_2 selectivity. Amrouche et al.[13] modeled adsorption in the more famous ZIF-8 and hypothetical analogues containing -COOH, -HCO, -NO_2, and -Cl functional groups, which share a sodalite-like topology with ZIF-65. The simulations predicted that the dipole moment of the nitro-functional group would yield the highest isosteric heats of adsorption for CO_2 and highest CO_2/N_2 selectivity among the functionalized ZIF-8s.[13]

Originally reported by Yaghi et al.,[14] ZIF-65(SOD) consists of Co metal-centers and 2-nitro-imidazole ligands, which form 10.4 Å cages accessible through 3.4 Å pores. The pores are conveniently sized between the kinetic diameters for N_2 and CO_2 of 3.64 and 3.3 Å, respectively.[15] In addition to the potential advantages of the pore structure itself, the reported water-stability and hydrophobic nature of ZIFs are appealing for flue gas separations applications and drive the following experimental study of ZIF-65. Water adsorption and subsequent structure retention is examined via exposure to humid air and characterization of the material before and afterwards using BET modeling of the N_2 adsorption at 77 K, powder X-ray diffraction (pXRD), and transmission electron microscopy (TEM). Pure-component CO_2 and N_2 adsorption isotherms are collected at 298, 308, and 318 K to examine the potential for flue gas separations. Isosteric heats of adsorption are predicted for ZIF-65 using the Clausius-Clapyeron equation, and mixture adsorption performance is predicted via the ideal adsorbed solution theory (IAST),[16] which is reportedly applicable for other ZIFs.[17]

8.2 Water Adsorption and Stability

Synthesis follows the originally reported procedure[14] except Zn-metal centers are implemented instead of Co. A sample of ZIF-65, ca. 50 mg, is loaded into an IGA-003 from Hiden Isochema and activated *in situ* at 423 K and under dynamic vacuum of <1E-06 mmHg until the sample mass reaches equilibrium.

Then, a water isotherm is collected using air as the carrier gas and following the previously published procedure,[9] which shows a relatively hydrophobic nature (Figure 8.1) similar to that reported for ZIF-8.[8] The Type V adsorption behavior of the materials

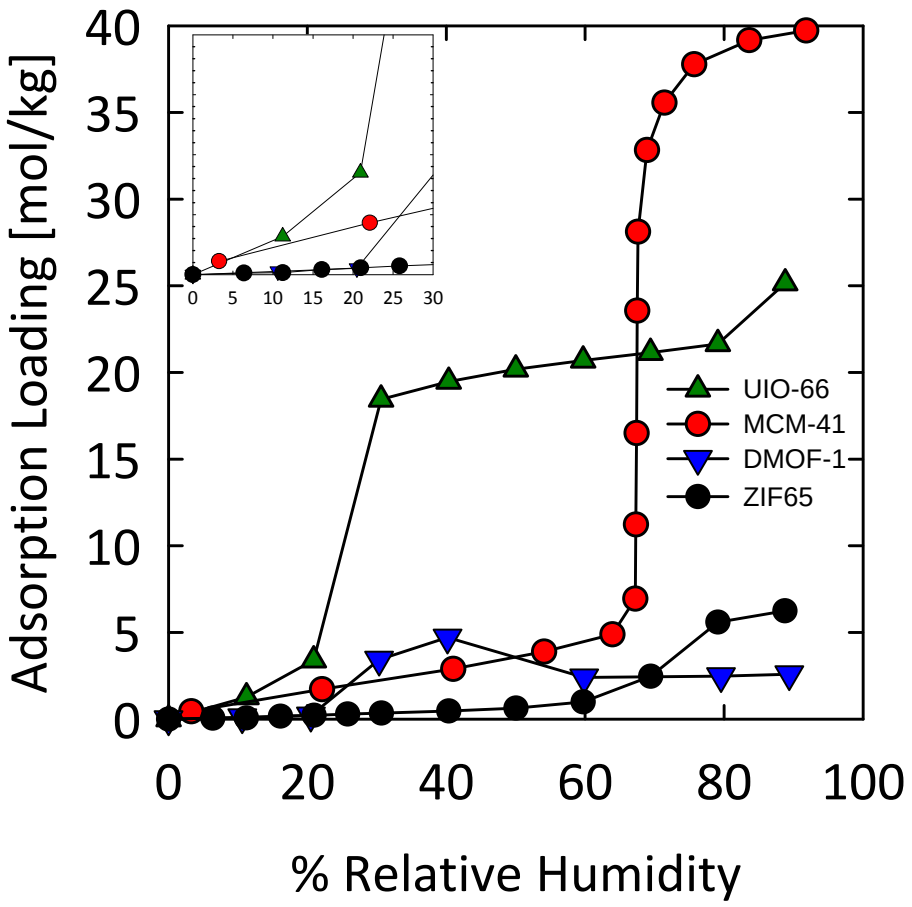

Figure 8.1. Water adsorption results for ZIF-65 compared with UiO-66 and DMOF-1.[9]

in Figure 8.1 indicates capillary condensation is occurring. Upon comparison to previously published hydrophobic MOFs[9] and mesoporous silica, MCM-41,[18] UiO-66 and MCM-41 show higher uptake of water even below 20% relative humidity (RH), which is before capillary condensation occurs. When compared to DMOF-1[19], another well-known hydrophobic MOF, ZIF-65 demonstrates nearly identical uptake up to 20% RH and remarkably less uptake at higher humidities. Assuming similar adsorbate-surface interactions, capillary condensation typically occurs first for smaller pore materials. This trend is followed for the previously reported UiO-66, DMOF-1, and MCM-41 materials,

which have ca. 6 Å, 7.5 Å and 4.5 x 3.8 Å, and 30 Å pores, respectively. However, ZIF-65 with 10.4 Å cages does not fit the trend, with practically no uptake until ca. 65% RH, which is approximately where MCM-41 capillary condensation begins. This behavior may be an attribute of the hydrophobic nature of the ZIF material itself, but a crystal-structure transition may also play a significant role in the water adsorption.

PXRD and N_2 adsorption at 77 K are collected to examine the retention of crystal phase and porosity, respectively. Using a previously reported modeling technique,[20] the predicted accessible surface area for ZIF-65, assuming a perfect crystal, is found to be 680 m^2/g. BET modeling of N_2 adsorption at 77 K predicts an experimental surface area

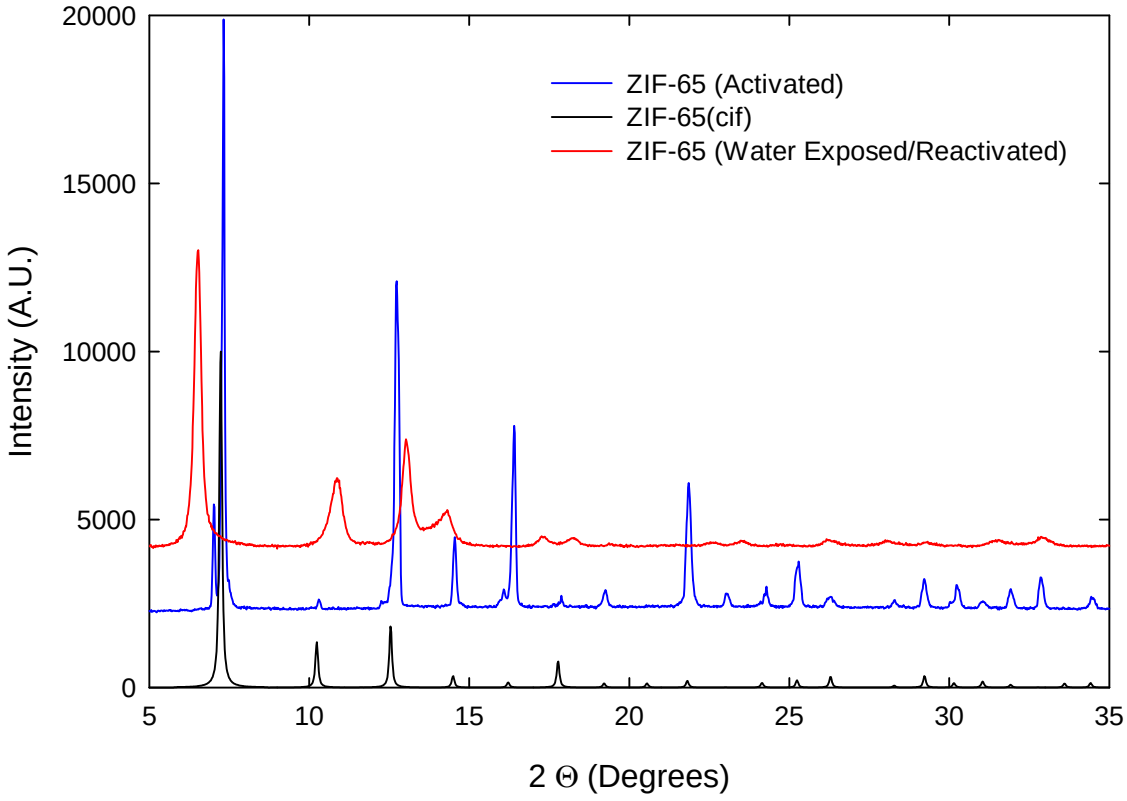

Figure 8.2. pXRD results from predicted pattern (cif), initial synthesis (DMF), and water exposed sample.

of 560 m^2/g (18% less), which is likely an attribute of crystal structure defects associated with synthesis and desolvation. Following reactivation, the post-water exposure experiment yields only 430 m^2/g. In general, ZIFs are known for having very robust structures under harsh chemical environments.[8,21-23] So, the 23% loss of surface area following water exposure is perplexing. A possible source of the structure change or degradation is the nitro-functionalized ligand, which incorporates a much stronger dipole moment than the methyl-functionalized ZIF-8. This has an electron withdrawing effect on the heterocyclic ring and effectively reduces the pKa of the ligand from 7.86 to 7.15 for the methyl and nitro-functionalized versions, respectively,[24] which typically results in a less water-stable MOF.[9,25]

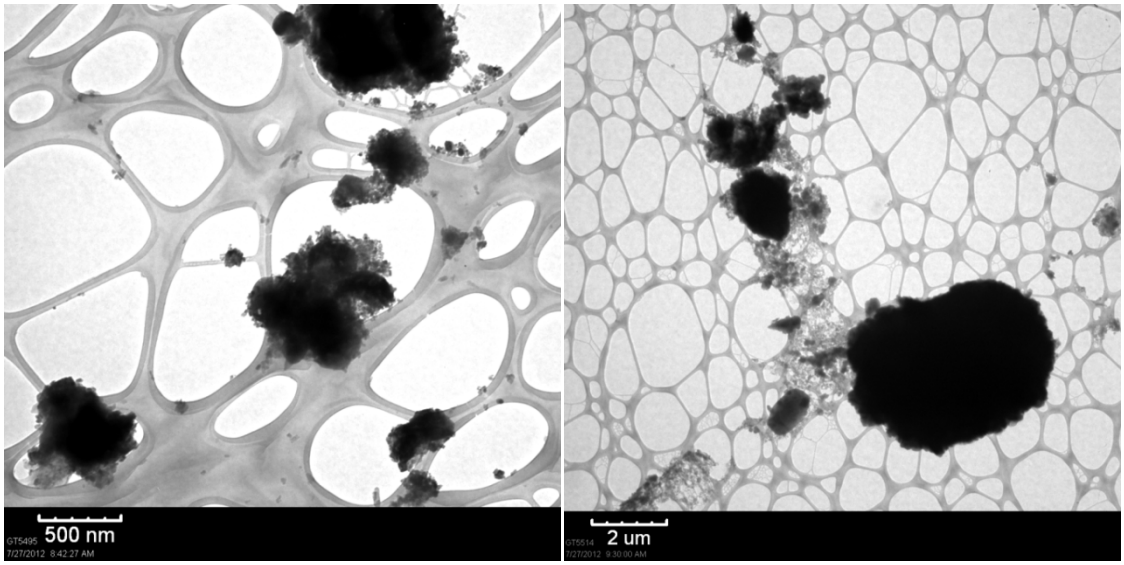

Figure 8.3. TEM images of ZIF-65 samples before (left) and after (right) water adsorption.

Comparison of the pXRD experiments from after initial activation and after water exposure and reactivation also illustrates a significant change in crystal phase (Figure 8.2). Attempts to solve the post-hydration crystal structure via Rietveld Refinement of

the pXRD diffractogram are not successful and likely require *in situ* data collection. TEM images of samples before and after water exposure are also collected but a trend in crystal morphology and/or size was not apparent (Figure 8.3).

8.3 CO_2 and N_2 Adsorption

8.3.1 Single Component Results

Pure component isotherms are collected for ZIF-65 using an IGA-001 from Hiden. After *in situ* activation at 423 K, isotherms are collected at 298, 308, and 318 K for each gas. Figure 8.4 illustrates the results of the adsorption experiments including the Type I behavior for the CO_2 adsorption and preferential adsorption of CO_2 over N_2. The loading

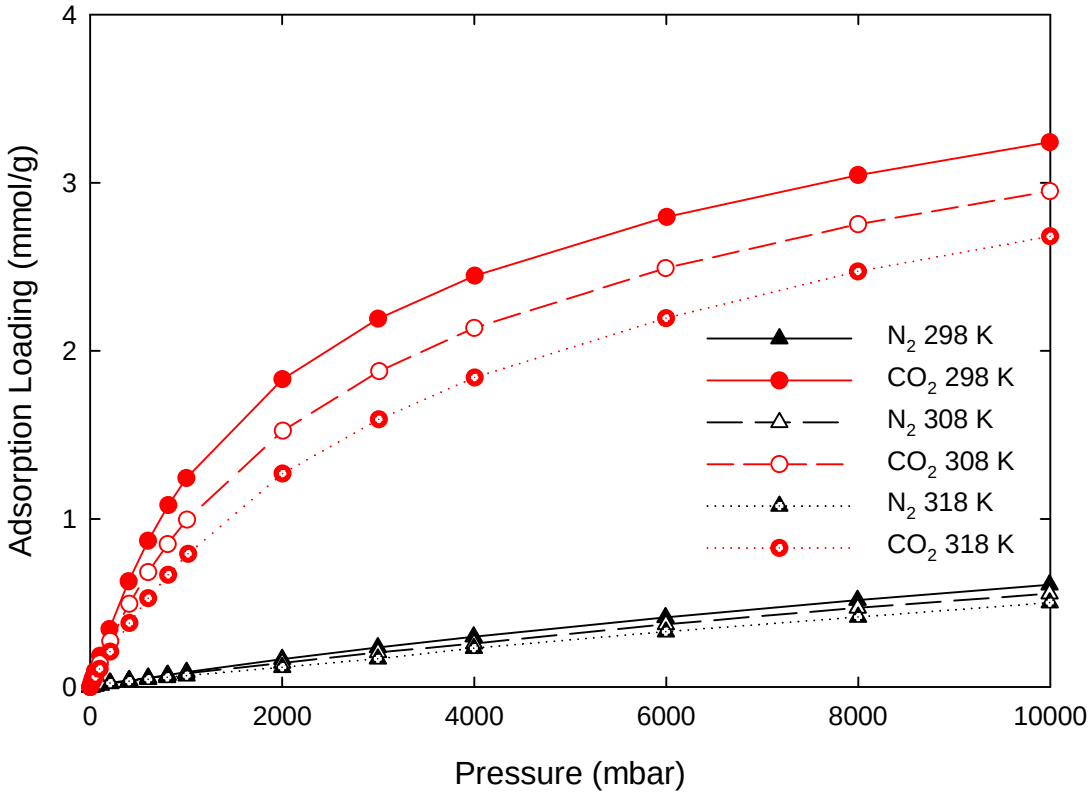

Figure 8.4. Experimental single component isotherms of ZIF-65 at 298 K, 308 K, and 318 K.

at low pressures, which is important for separating CO_2 from flue gas, is not record breaking compared to some MOFs (e.g. 298 K and 1 bar: ZIF-65 uptake = 1.24 mmol/g v. Mg MOF-74 = 8 mmol/g),[26] and significantly less than Zeolite 13X (4.66 v. 1.24 mmol/g at 298 K and 1 bar).[27] However, the benefits of the above reported hydrophobic behavior and the attractive CO_2/N_2 selectivity of ZIF-65 may still prove advantageous for the target application. Comparison to pure CO_2 adsorption predicted for the Co form of ZIF-65 via GCMC simulations[11] exhibit nearly identical results with adsorption loadings of 1.2 mmol/g reported in both cases at 298 K and 1 bar.

The single-component isotherms are fit with the Toth equation (Eq. 1), which facilitates interpolation to identify points of constant loading. The loading (N) is fit by two parameters b and m, which are attributed to the low loading adsorbent-adsorbate interactions and the heterogeneity of the system, respectively. P is the absolute pressure of the system, and N_S is the monolayer capacity of the adsorbent.

$$\mathbf{N} = \frac{\mathbf{Ns\ b\ P}}{[\mathbf{1}+(\mathbf{bP})^{\mathbf{m}}]^{\frac{\mathbf{1}}{\mathbf{m}}}} \qquad (1)$$

Using the loading data from all three temperatures, the Clasius-Clapeyron equation (Eq. 2) is implemented to predict isosteric heats of adsorption (Q_{ST}) as a function of loading (Figure 8.5). In Equation 2, R represents the ideal gas constant and T is absolute temperature. For ZIF-65, the Q_{ST} for CO_2 at zero loading is 29.8 kJ/mol, while N_2 is 16.9 kJ/mol. This demonstrates a particular preference for CO_2 but is low enough to facilitate

$$\mathbf{Q_{ST}} = -\mathbf{R}\left\{\frac{\partial \ln (\mathbf{P})}{\partial \frac{\mathbf{1}}{\mathbf{T}}}\right\}\Bigg|_{\mathbf{N}} \qquad (2)$$

desorption without the higher energy cost associated with open-metal site MOFs, which presents advantages for cyclic adsorption processes such as pressure swing adsorption

(PSA). This value is slightly higher than that predicted for the hypothetical NO_2-functionalized ZIF-8, 27 kJ/mol, and can be attributed to the stronger confinement effect afforded by the smaller cage of ZIF-65 (10.4 Å v. 10.61 Å).[13] Also, Q_{ST} for CO_2 illustrates a relatively constant behavior and ZIF-65's homogeneity towards CO_2 adsorption. Comparison of CO_2 Q_{ST}'s for open-metal site MOFs are significantly higher, e.g. Mg MOF-74 and Cu-BTTri are 47 and 90 kJ/mol, respectively,[26,28] and Zeolite 13X also demonstrates a stronger Q_{ST} of 37.2 kJ/mol for CO_2.[27]

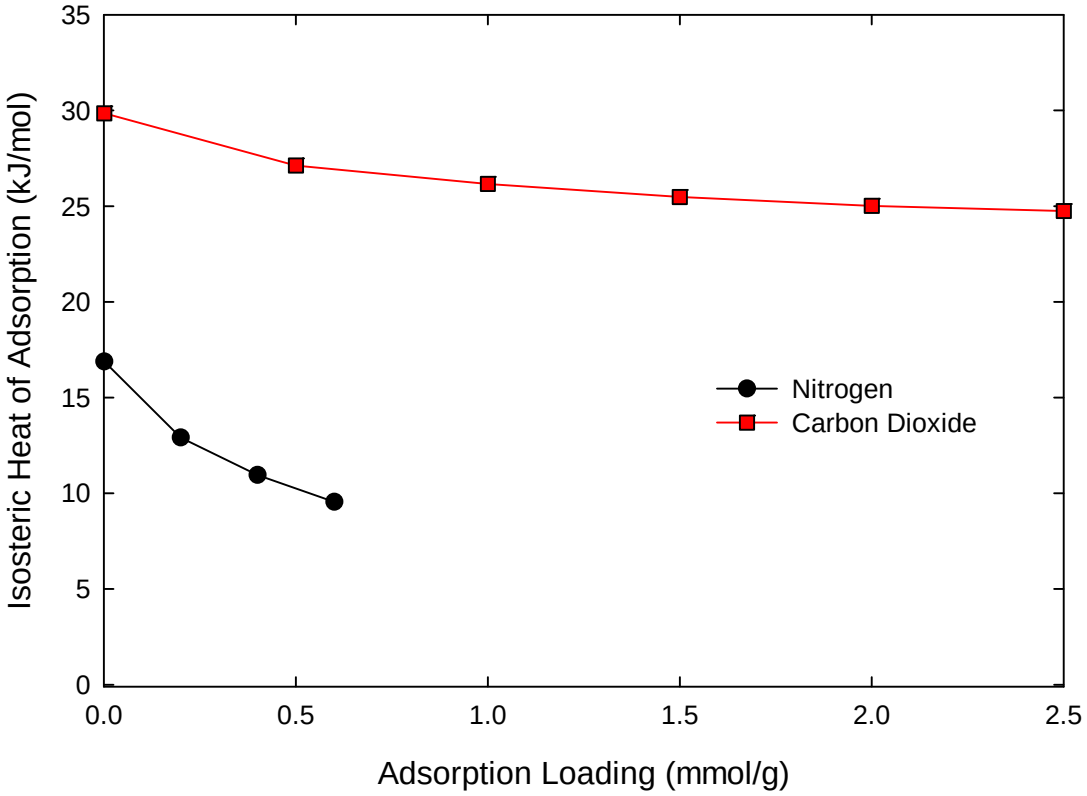

Figure 8.5. Isosteric heats of adsorption for ZIF-65 from Clausius-Clapyeron fitting.

8.3.2 Mixture Adsorption from IAST

In order to gain further insight into the competitive adsorption behavior of ZIF-65, IAST[16] is applied using the 298 K pure-component adsorption data. Figure 8.6 illustrates the predicted adsorption isotherms of a 50/50 mole ratio of N_2 and CO_2 and resultant CO_2/N_2 selectivity ($S_{CO2/N2}$) as defined in the following equation:

$$\mathbf{S}_{\frac{CO2}{N2}} = \frac{\mathbf{X_{CO2}}}{\mathbf{Y_{CO2}}} / \frac{\mathbf{X_{N2}}}{\mathbf{Y_{N2}}} \qquad (3)$$

X_i and Y_i refer to the mole fraction of component i in the adsorbed and bulk phases, respectively.

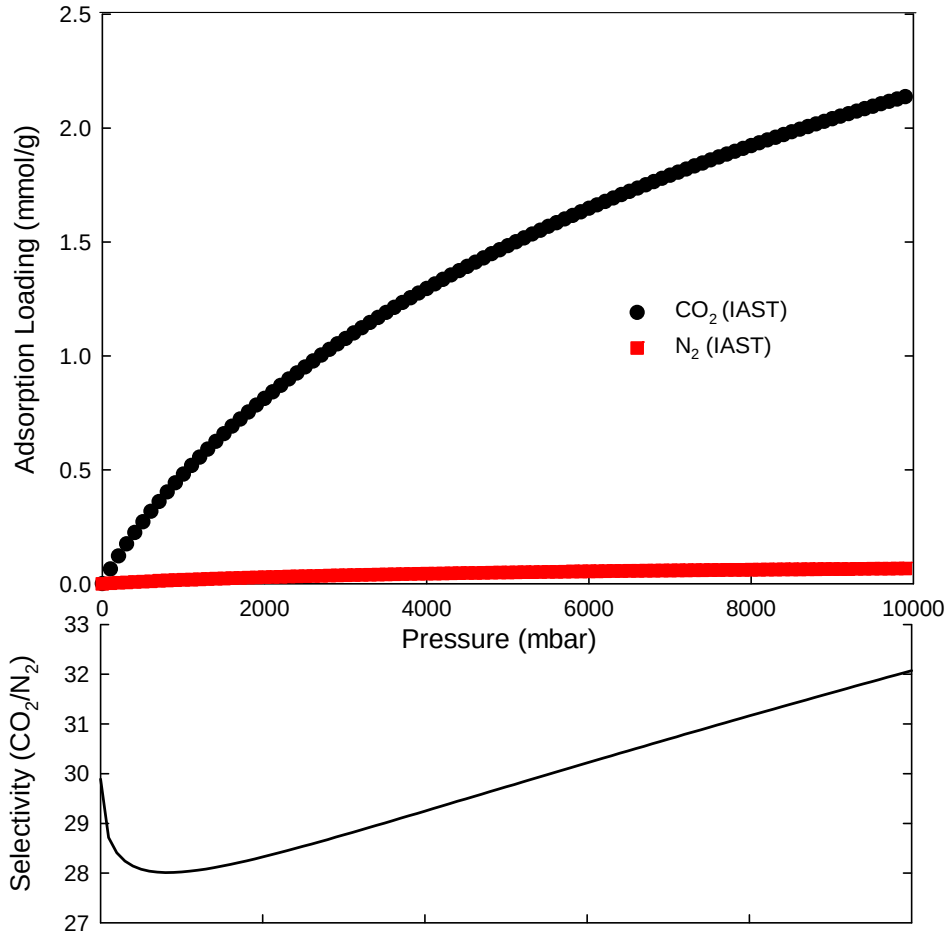

Figure 8.6. CO_2 and N_2 adsorption data predicted via IAST modeling of pure component data at 298 K.

As with the loading of ZIF-65, the selectivity of 29.8 at low loading is not record-setting but still potentially useful and congruent with that reported for the hypothetical ZIF-8-NO_2 of 29.[13] Others have reported CO_2/N_2 selectivity of MOFs up to ca. 80,[29] but the applied benefits of said selectivity difference are not directly proportional. When comparing the IAST predicted behavior for 50/50 mole ratios of CO_2/H_2 and CO_2/N_2, ZIF-65 shows more competitive adsorption of N_2 than H_2, which is likely attributed to an increase in confinement effects. For example the predicted CO_2 uptakes in these mixtures at 298 K and 1 bar are 0.48 and 0.65 mmol/g for the CO_2/N_2 and CO_2/H_2[11] mixtures, respectively. The Henry's constants from the mixture data also illustrate the less competitive nature of the CO_2/H_2 mixture with values of 0.0016 and 0.0012 mmol/g/mbar for the CO_2/N_2 and CO_2/H_2 mixtures, respectively.

8.4 Conclusions

This work presents an experimental adsorption study for ZIF-65, which directly probes this MOF's potential for CO_2/N_2 separations. ZIF-65 exhibits very hydrophobic water adsorption behavior common to ZIFs. However, ZIF-65 appears to degrade and/or undergo a structural transition following water adsorption and regeneration, which is attributed to the less-basic nitro-functionalized imidazole ligand. This phase transition was not reversed when the material is reactivated and results in a loss of surface area via BET modeling of experimental data. Single component CO_2 and N_2 isotherms demonstrate preferential adsorption of CO_2 with a low-loading isosteric heat of adsorption of 29.8 kJ/mol for CO_2 and selectivity of 29.8 for a 50/50 mixture CO_2/N_2. Although these adsorption results are not record setting, when combined with the

hydrophobic adsorption behavior they demonstrate potential for flue gas separations with ZIF-65. Cyclic multi-component experiments are necessary before additional conclusions can be drawn on application specific performance.

8.5 References

1. Wiersum AD, Soubeyrand-Lenoir E, Yang QY, et al. An Evaluation of UiO-66 for Gas-Based Applications. *Chem.-Asian J.* Dec 2011;6(12):3270-3280.

2. Han SG, Huang YG, Watanabe T, et al. High-Throughput Screening of Metal-Organic Frameworks for CO2 Separation. *Acs Combinatorial Science.* Apr 2012;14(4):263-267.

3. Herm ZR, Krishna R, Long JR. Reprint of: CO2/CH4, CH4/H-2 and CO2/CH4/H-2 separations at high pressures using Mg-2(dobdc). *Microporous Mesoporous Mat.* Jul 2012;157:94-100.

4. Samanta A, Zhao A, Shimizu GKH, Sarkar P, Gupta R. Post-Combustion CO2 Capture Using Solid Sorbents: A Review. *Ind. Eng. Chem. Res.* Feb 2012;51(4):1438-1463.

5. Song LF, Zhang J, Sun LX, et al. Mesoporous metal-organic frameworks: design and applications. *Energy Environ. Sci.* Jun 2012;5(6):7508-7520.

6. Liu J, Benin AI, Furtado AMB, Jakubczak P, Willis RR, LeVan MD. Stability Effects on CO(2) Adsorption for the DOBDC Series of Metal-Organic Frameworks. *Langmuir.* Sep 2011;27(18):11451-11456.

7. Liu J, Wang Y, Benin AI, Jakubczak P, Willis RR, LeVan MD. CO2/H2O Adsorption Equilibrium and Rates on Metal-Organic Frameworks: HKUST-1 and Ni/DOBDC. *Langmuir.* Sep 2010;26(17):14301-14307.

8. Kusgens P, Rose M, Senkovska I, et al. Characterization of metal-organic frameworks by water adsorption. *Microporous Mesoporous Mat.* Apr 2009;120(3):325-330.

9. Schoenecker PM, Carson CG, Jasjuja H, Flemming CJJ, Walton KS. Effect of Water Adsorption on Retention of Structure and Surface Area of Metal-Organic Frameworks *Ind. Eng. Chem. Res.* 2012.

10. Dietzel PDC, Panella B, Hirscher M, Blom R, Fjellvag H. Hydrogen adsorption in a nickel based coordination polymer with open metal sites in the cylindrical cavities of the desolvated framework. *Chem. Commun.* 2006(9):959-961.

11. Atci E, Keskin S. Atomically Detailed Models for Transport of Gas Mixtures in ZIF Membranes and ZIF/Polymer Composite Membranes. *Ind. Eng. Chem. Res.* Feb 2012;51(7):3091-3100.

12. Robeson LM. The upper bound revisited. *J. Membr. Sci.* Jul 2008;320(1-2):390-400.

13. Amrouche H, Aguado S, Perez-Pellitero J, et al. Experimental and Computational Study of Functionality Impact on Sodalite-Zeolitic Imidazolate Frameworks for CO2 Separation. *Journal of Physical Chemistry C.* Aug 2011;115(33):16425-16432.

14. Banerjee R, Phan A, Wang B, et al. High-throughput synthesis of zeolitic imidazolate frameworks and application to CO2 capture. *Science.* Feb 2008;319(5865):939-943.

15. Breck DW. *Zeolite Molecular Sieves: Structure, Chemistry, and Use.* John Wiley and Sons; 1974.

16. Myers AL, Prausnitz JM. Thermodynamics of mixed-gas adsorption. *AIChE Journal.* 1965;11(1):121-+.

17. Liu JC, Keskin S, Sholl DS, Johnson JK. Molecular Simulations and Theoretical Predictions for Adsorption and Diffusion of CH4/H-2 and CO2/CH4 Mixtures in ZIFs. *Journal of Physical Chemistry C.* Jun 2011;115(25):12560-12566.

18. Oh JS, Shim WG, Lee JW, Kim JH, Moon H, Seo G. Adsorption equilibrium of water vapor on mesoporous materials. *J. Chem. Eng. Data.* Nov-Dec 2003;48(6):1458-1462.

19. Chen YF, Lee JY, Babarao R, Li J, Jiang JW. A Highly Hydrophobic Metal Organic Framework Zn(BDC)(TED)(0.5) for Adsorption and Separation of CH3OH/H2O and CO2/CH4: An Integrated Experimental and Simulation Study. *Journal of Physical Chemistry C.* Apr 2010;114(14):6602-6609.

20. Walton KS, Snurr RQ. Applicability of the BET method for determining surface areas of microporous metal-organic frameworks. *Journal of the American Chemical Society.* Jul 11 2007;129(27):8552-8556.

21. Park KS, Ni Z, Cote AP, et al. Exceptional chemical and thermal stability of zeolitic imidazolate frameworks. *Proc. Natl. Acad. Sci. U. S. A.* Jul 2006;103(27):10186-10191.

22. Diao HM, Ren SZ. *Synthesis and Stability of Zeolitic Imidazolate Framework ZIF-8.* 2010.

23. Demessence A, Boissiere C, Grosso D, et al. Adsorption properties in high optical quality nanoZIF-8 thin films with tunable thickness. *J. Mater. Chem.* 2010;20(36):7676-7681.

24. Catalan J, Depaz JLG, Yanez M, Elguero J. Basicity of azoles .6. Calculated intrinsic basicities for methyl-substituted pyrazoles and imidazoles - comparison

to aqueous-solution data - n-methylation effect. *J. Org. Chem.* 1984;49(23):4379-4386.

25. Choi HJ, Dinca M, Dailly A, Long JR. Hydrogen storage in water-stable metal-organic frameworks incorporating 1,3-and 1,4-benzenedipyrazolate. *Energy Environ. Sci.* 2010;3(1):117-123.

26. Caskey SR, Wong-Foy AG, Matzger AJ. Dramatic tuning of carbon dioxide uptake via metal substitution in a coordination polymer with cylindrical pores. *Journal of the American Chemical Society.* Aug 2008;130(33):10870-+.

27. Cavenati S, Grande CA, Rodrigues AE. Adsorption equilibrium of methane, carbon dioxide, and nitrogen on zeolite 13X at high pressures. *J. Chem. Eng. Data.* Jul-Aug 2004;49(4):1095-1101.

28. Demessence A, D'Alessandro DM, Foo ML, Long JR. Strong CO2 Binding in a Water-Stable, Triazolate-Bridged Metal-Organic Framework Functionalized with Ethylenediamine. *Journal of the American Chemical Society.* Jul 2009;131(25):8784-+.

29. An JY, Fiorella RP, Geib SJ, Rosi NL. Synthesis, Structure, Assembly, and Modulation of the CO2 Adsorption Properties of a Zinc-Adeninate Macrocycle. *Journal of the American Chemical Society.* Jun 2009;131(24):8401-+.

CHAPTER 9

CONCLUSIONS AND RECOMMENDATIONS

9.1 TIC Adsorption Using MOFs (Chpt. 3)

Chapter 3 demonstrates the benefits of functionalized MOFs for selective adsorption of toxic chemicals, and the difficulties in selecting application specific MOFs. Mg MOF-74 is successfully synthesized and expected to yield great TIC adsorption results, but instability in the presence of water proves detrimental. Also, UMCM-1-NH_2-COOH was synthesized via a more complicated procedure but only in quantities too small for the desired testing. The –NH_2 groups of DMOF-1-NH_2 and UiO-66-NH_2 yielded the best filtration performance for adsorbates with H-bonding capabilities including NH_3, CH_2NH_3, and CH_2O.

The promising results of this work, other work ongoing within our group, and reported in literature[1-3] demonstrate the ability of some MOFs to outperform traditional adsorbent materials including zeolites, activated carbons,[1] etc. for TIC filtration. However, the instability of many of the same MOFs under ambient conditions and lack of commercial availability currently prohibits MOFs from most TIC filtration applications. More specifically, two of the more pertinent obstacles to overcome are long-term water stability and large quantity availability (tons v. grams).

In the near future, studies should implement commercially available MOFs and MOFs readily synthesized in at least pound quantities. These materials would have potential for more-rapid implementation. Further scale-up syntheses and process design is a valuable

area of research in order for MOFs to reach this target application and now has a firm basis in our research group.

Long-term and cyclic moisture stability studies are imperative for TIC adsorption applications, where performance degradation can result in a loss of life. The IGA-003 can be used to examine cyclic stability of potential MOFs. However, a more simplified and realistic experiment would be to store potential MOFs in controlled humidity chambers e.g. desiccators with salt buffer solution and periodically examine the crystallinity and porosity via pXRD and BET modeling of N_2 adsorption at 77 K. This directly simulates possible storage conditions and their affect on the structure properties. However, since most TIC filtration occurs at low analyte fugacity, the BET surface area is not necessarily directly indicative of TIC filtration performance. So, an even more relevant experiment would be to test the TIC filtration properties of said 'stored' samples periodically.

9.2 MOF Water Stability (Chpt. 4)

There are now a set of hypotheses governing MOF water stability. The two main ideas can be simplified as follows: 1) Stronger metal-ligand bonds via incorporation of more basic ligands and/or more acidic metals provide a more stable material. 2) Preventing access to the metal-ligand bond-site via a more hydrophobic ligand and/or by steric hindrances via catenation or shielding with the ligand itself increases the stability of the MOF *to a point*. However, the later hypothesis may not hold for many materials on a long time-scale or when exposed to liquid water. In general, the long-term water stability

of MOFs remains to be seen and must be addressed before many consumer or industrial applications can be met.

The degradation mechanism itself is still not clear and may differ drastically for specific MOFs. Current and future work in our group that combines *in situ* XRD of the water-exposed MOF and potential modeling of the adsorption/degradation behavior will be of paramount importance. A fundamental understanding of the degradation mechanism may lead to further methods of alleviating instability in the presence of water.

9.3 UiO-66-NH_2 Scale-Up and Reactor Development (Chpt. 5)

Over the past decades MOF research has been mainly targeted at synthesizing novel materials and more recently examining their application potential. Sifting through the current pool of MOF structures to select a few with high-potential for a particular application is already a daunting task. Now, research objectives should be redirected towards advanced synthesis techniques and scale-up of known materials if the most propitious MOFs are to reach the applied level.

Admittedly, BASF has patents on multiple synthesis techniques currently leading the way for industrial-scale production of MOFs.[4-8] However, the set of materials they have developed seem to be based mainly on popularity within the research journals and not on application potential. Further collaboration with more application-based research groups such as the Walton Group would lead to a more rapid advancement of materials capable of reaching consumer and industrial applications.

9.3.1 Batch Scale-Up

The set of rudimentary experiments developed in this work to determine MOF synthesis material and vessel geometry preferences as well as kinetics are a necessity for development of synthesis techniques using conventional heating techniques. A more fundamental understanding of MOF nucleation and growth could be examined via probing the effect of surface roughness on MOF nucleation and growth. TEM or SEM could be used to examine the roughness of particular vessel/substrate material as well as the resultant MOF particle size. Bulk properties such as yield, surface area, and crystallinity could be examined via the methods described in chapter 5, which would provide a fundamental understanding of the importance of vessel roughness on the synthesis of a representative set of MOFs.

9.3.2 Reactor Development

The development of the first continuous-flow MOF reactor has potentially the greatest impact of the experiments described herein. There are currently a wealth of publications in the field of crystallization process design,[9,10] which when combined with the findings of this work could be applied to drastically reduce synthesis costs and bring MOFs to the applied level more rapidly. However, development of a significantly more advanced reactor within an academic setting would likely require one or multiple PhD student's sole attention or a group member with prior process development experience.

9.4 Continuous-Flow Optimization (Chpt. 6)

The initial optimization of the flow-through MOF synthesis process of Chapter 5 does not result in a directly marketable reactor but important effects of operational parameters are identified. In particular, the draft-tube presence has little effect on the product crystallinity and porosity. Using two impellers versus one to improve mixing has the most beneficial effect on product quality. Significant BET surface area improvements are noted for trial 3.3, yielding a 47% increase over the proof-of concept trial, and yields above the maximum batch yield are reported during two trials. However, the primary challenge remaining is to alleviate reactor plugging and produce more consistent yields. Approaches are recommended to develop a new reactor with less potential for plugging. Figure 9.1 illustrates a recommended reactor design, which can be directly implemented in the current process with only slight modifications (additional thermocouples and heat tape). Additional thermocouples should be implemented to insure uniformity over the lengthened reactor. The new reactor should be made of glass or another transparent and chemically resistant material to allow direct observation of the fluid-particle dynamics within. The I.D. is reduced from ca 4.9" to ca. 2.5," which serves multiple purposes including increased external surface area for better heat transfer, higher shear at the wall due to less clearance around 2" impellers, and increased bulk flow velocity for better product removal (3.8x faster). Couple this improvement with the recommended increased temperature to 413 K and the bulk flow velocity increases by ca. 11x over the current reactor and increases the bulk Re by ca. 5.9x assuming that stirring does not affect the outlet flow. Also, an eccentric outlet is recommended to promote turbulence and mitigate product settling at the outlet. These modifications should improve product

removal at the studied concentrations and at increased concentrations, which are under investigation via other group members.

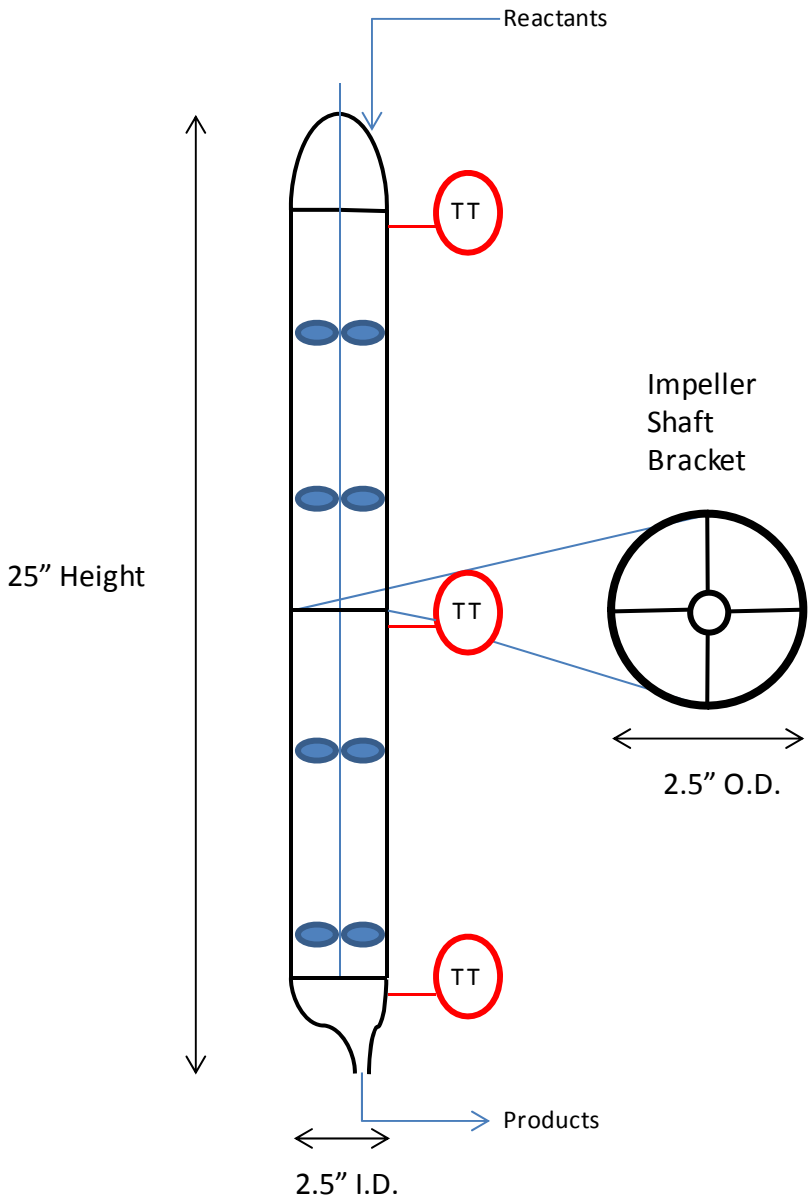

Figure 9.1. Second version of flow-through reactor.

Other alternatives to prevent product plugging include inert gas sparging of the outlet stream, vibrating the outlet stream, and oscillatory flow. Low flowrates of inert gas should not affect the synthesis results and can provide bubbles capable of clearing the solid products from the reactor outlet. Vibrating the outlet stream can be accomplished via attaching a linear actuator to the outlet fitting and adjusting the frequency to prevent product accumulation. Oscillatory flow can also be implemented and is a well known way of keeping solid crystals entrained in the bulk flow.[11] The effectiveness of these methods will be best understood with a transparent reactor, which facilitates direct observation of the outlet.

Other general reactor design recommendations include the use of alternative energy sources e.g. microwave-assisted synthesis combined with a flow-through reactor. Implementing the conventional microwave capable of synthesizing UiO-66 in 45 s (*Appendix A*) can potentially provide higher throughput via reducing the retention time by nearly three orders of magnitude. This can take place by simply running tubing through the existing microwave and using one of the current peristaltic pumps to feed the reactor. This alternative has been discussed with Environmental Health and Safety (EH&S) and remains a viable option if proper shielding and radiation testing take place. However, more sophisticated techniques have been reported for nanoparticle synthesis[12] which utilize a more uniform microwave source but appear significantly more challenging to design and implement.

Investigating the benefits of stage-tanks or directly-seeding the reactor may also prove beneficial. A significant portion of the crystallization process appears to be nucleation-based instead of growth-based, with the typical sub-micron crystals of UiO-66-NH_2

formed and relatively long nucleation times reported in Chapter 5 from 2 to 5 h for 393 K and 373 K batches, respectively. So, introducing seed-crystals to promote secondary nucleation and attrition-based nucleation has high potential for reducing reaction times within the described flow-through processes.

9.5 MOF Scale-Up Trends (Chpt. 7)

Specific hypotheses are developed in Chapter 7, which can be applied to MOF synthesis scale-up and process development. The affinity of Mg MOF-74 for H_2O results in a strong preference for hydrophilic vessel materials. This indicates that Mg MOF-74 is nucleating and growing mainly on the vessel surface and the adsorption properties are directly related to the synthesis material preference. However, for the other examined MOFs the hydrophilic/hydrophobic adsorption behavior does not seem to directly relate to the vessel material synthesis results. On a smaller scale, this is likely governed by how the MOF crystallites/particles are terminated at the surface and can be further examined via surface characterization techniques such as contact-angle measurements. Examining the affect of surface roughness on synthesis results is another valuable study to further explore the importance of synthesis vessel selection.

The kinetic examinations provide significant results for flow-through process development and are sufficient for characterizing bulk properties and understanding general synthesis trends. However, to more fundamentally understand what competitive reactions (degradation, etc.) are occurring and their respective rates more sophisticated *in situ* XRD techniques[13-15] capable of discerning relative crystallinity and phase proportions are better suited experiments.

9.6 ZIF-65 SOD (Chpt. 8)

The hydrophobic adsorption behavior of ZIF-65 as well as the relatively high CO_2/N_2 selectivity afforded by the nitro-functionalized 3.4 Å pores demonstrates direct application potential for selective adsorption of CO_2 from flue gas. However, the structural change noted upon water adsorption and reactivation may diminish the separation performance and should be evaluated via cyclic breakthrough studies.

In addition to the adsorption separations examined in Chapter 8, ZIF-65 has direct application potential for mixed-matrix membrane separations of CO_2/N_2 and CO_2/CH_4[16] and separation of larger molecules[17] provided it exhibits similar flexibility to ZIF-8. I recommend that future collaboration with the Koros Group is considered to examine the performance of said ZIF-65 mixed-matrix membrane.

9.7 REFERENCES

1. Britt D, Tranchemontagne D, Yaghi OM. Metal-organic frameworks with high capacity and selectivity for harmful gases. *Proc. Natl. Acad. Sci. U. S. A.* Aug 2008;105(33):11623-11627.

2. Galli S, Masciocchi N, Colombo V, et al. Adsorption of Harmful Organic Vapors by Flexible Hydrophobic Bis-pyrazolate Based MOFs. *Chem. Mat.* Mar 2010;22(5):1664-1672.

3. T.Grant Glover GWP, Bryan J. Schindler, David, Brittand OY. 'MOF-74 building unit has a direct impact on toxic gas adsorption' *Chem. Eng. Sci.* 3 October 2010.

4. Ulrich Muller, Hermann Putter, Michael Hesse, et al. Method for Electrochemical Production of a Crystalline Porous Metal Organic Skeleton Material. *United States Patent Application Publication.* 2004;10/580,407.

5. Mueller U, Schubert M, Teich F, Puetter H, Schierle-Arndt K, Pastre J. Metal-organic frameworks - prospective industrial applications. *J. Mater. Chem.* Feb 2006;16(7):626-636.

6. Leung E, Muller U, Cox G. Solvent-Free Preparation of Magnesium Formate-Based Porous Metal-Organic Framework. *United States Patent Application Publication.* 2012;US 2012/0016160 A1.

7. Kummeter M. First Industrial-Scale MOF Synthesis. *http://www.basf.com/group/pressrelease/P-10-428.* 2012.

8. Gaab M, Trukhan N, Maurer S, Gummaraju R, Muller U. The progression of Al-based metal-organic frameworks - From academic research to industrial production and applications. *Microporous Mesoporous Mat.* Jul 2012;157:131-136.

9. Myerson AS. *Handbook of Industrial Crystallization, Second Edition*. *Handbook of Industrial Crystallization, Second Edition.* 2002.

10. Lawton S, Steele G, Shering P, Zhao LH, Laird I, Ni XW. Continuous Crystallization of Pharmaceuticals Using a Continuous Oscillatory Baffled Crystallizer. *Org. Process Res. Dev.* Nov-Dec 2009;13(6):1357-1363.

11. Ni X, Gough P. On the discussion of the dimensionless groups governing oscillatory flow in a baffled tube. *Chem. Eng. Sci.* Sep 1997;52(18):3209-3212.

12. Horikoshi S, Abe H, Torigoe K, Abe M, Serpone N. Access to small size distributions of nanoparticles by microwave-assisted synthesis. Formation of Ag

nanoparticles in aqueous carboxymethylcellulose solutions in batch and continuous-flow reactors. *Nanoscale.* 2010;2(8):1441-1447.

13. Schmidt C, Feyand M, Rothkirch A, Stock N. High-throughput and in situ EDXRD investigation on the formation of two new metal aminoethylphosphonates - Ca(O3PC2H4NH2) and Ca(OH)(O3PC2H4NH3) center dot 2H(2)O. *J. Solid State Chem.* Apr 2012;188:44-49.

14. Schmidt C, Stock N. High-Throughput and in Situ Energy Dispersive X-ray Diffraction Investigation on the Formation of the New Metal Organogermanate Cu(OOCC(2)H(4)Ge)(2)O(3). *Cryst. Growth Des.* Dec 2011;11(12):5682-5687.

15. Ahnfeldt T, Moellmer J, Guillerm V, Staudt R, Serre C, Stock N. High-Throughput and Time-Resolved Energy-Dispersive X-Ray Diffraction (EDXRD) Study of the Formation of CAU-1-(OH)(2): Microwave and Conventional Heating. *Chem.-Eur. J.* May 2011;17(23):6462-6468.

16. Amrouche H, Aguado S, Perez-Pellitero J, et al. Experimental and Computational Study of Functionality Impact on Sodalite-Zeolitic Imidazolate Frameworks for CO2 Separation. *Journal of Physical Chemistry C.* Aug 2011;115(33):16425-16432.

17. Zhang C, Lively RP, Zhang K, Johnson JR, Karvan O, Koros WJ. Unexpected Molecular Sieving Properties of Zeolitic Imidazolate Framework-8. *Journal of Physical Chemistry Letters.* Aug 2012;3(16):2130-2134.

APPENDIX A

MICROWAVE SYNTHESIS OF UIO-66 AND UIO-66-NH2

Introduction

MOF syntheses are generally conducted solvothermally with the use of conventional ovens, which consists of placing a reactant mixture inside a sealed vessel and heating in a convection oven for 0.5 to 3 days. More rapid syntheses are reported using microwaves or ultrasound (US) assisted synthesis techniques,[1-4] with the fastest MOF synthesis reported of ca. 5 seconds via Ni et al.[4]

Results

The first portion of my scale-up efforts examined the use of microwave-assisted solvothermal syntheses to reduce reaction times of UiO-66 and UiO-66-NH_2. Initial trials were conducted using a rudimentary 1,000 W Panasonic NE-1024F commercial microwave oven and a 45 mL PTFE Parr digestion vessel model 4782.[5] The parent UiO-

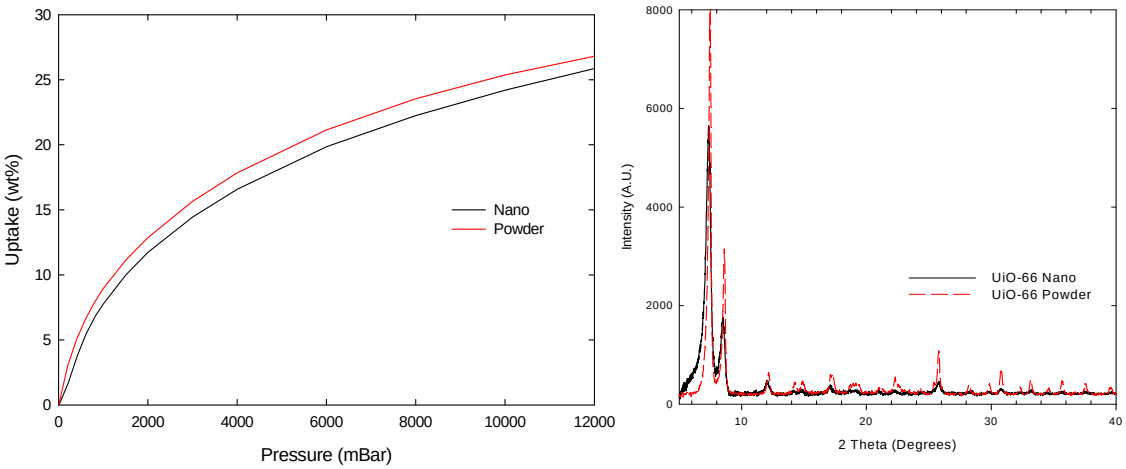

Figure A.1. Comparison of microwave synthesized, 'Nano', and solvothermal, 'Powder', versions of UiO-66 CO_2 adsorption isotherms collected at 298K (left) and

66 synthesis was successfully completed in 45 s compared to the 24 h originally published[6] by simply placing a 5 mL aliquot of the originally published reactant solution in the aforementioned digestion vessel. The solution was centrifuged[7] for ca. 10 min., decanted, and suspended in a more volatile solvent, $CHCl_3$. A few drops of the resultant solution were then placed on respective sample holders, and powder XRD followed by SEM was collected following solvent evaporation. The UiO-66 structure was confirmed via pXRD in Fig. A1, and the sample was termed 'nano' due to the particle size discussed later. Approximately 10 mg of unactivatedUiO-66 was formed from the 5 mL of reactant solution in the microwave vessel. A resultant 24% decrease in surface area between the microwave and solvothermal synthesized versions of UiO-66 was noted following BET modeling of N_2 adsorption at 77K (1,160 and 994 m^2/g for the powder and nano samples, respectively) . The surface area reduction was apparent when comparing CO_2 adsorption at 298K of the two UiO-66 products, Fig. A.1, and possibly due to crystal-structure defects from the more rapid synthesis. However, from an application perspective, the reduced cost from decreasing the reaction time by over three orders of

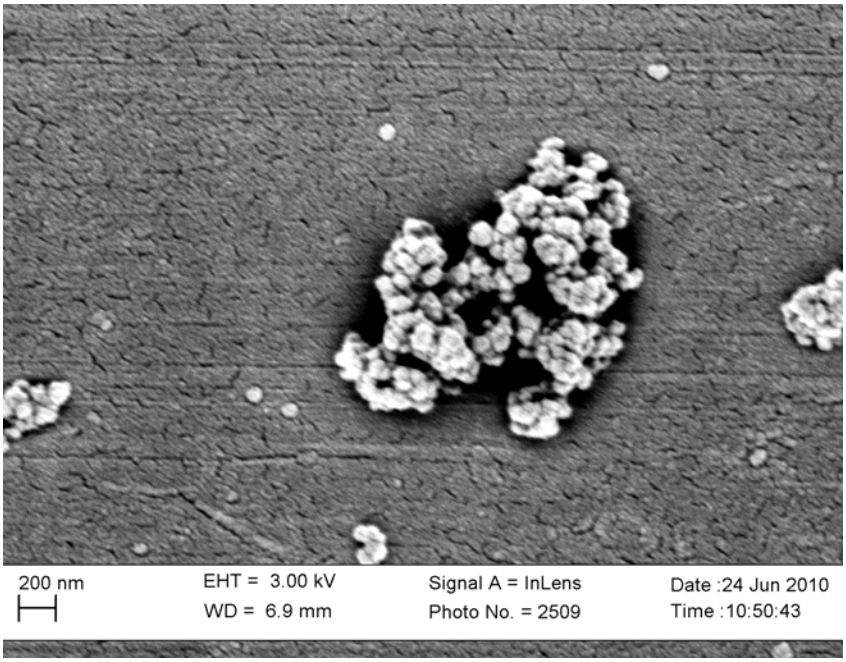

Figure A.2. SEM micrograph of UiO-66 microwave-assisted product, 'nano'

magnitude may justify the 13% decrease in CO_2 uptake at 1 bar. The microwave synthesized material formed was relatively monodisperse crystals of less than 100nm (~34 nm)[8], a true nano-MOF (Fig. A.2.), which may be useful for further applications not discussed herein.[9] However, analogous trials of UiO-66-NH_2 synthesis were not successful and more advanced techniques were sought. Horcajada et al.[10] have successfully synthesized MOFs constructed of the same ATPA ligand via microwave exposure. One notable difference was microwave irradiation power. The published synthesis utilizes a programmable microwave and synthesis occurs at 400 W of microwave irradiation versus the constant output 1,000 W microwave used above.

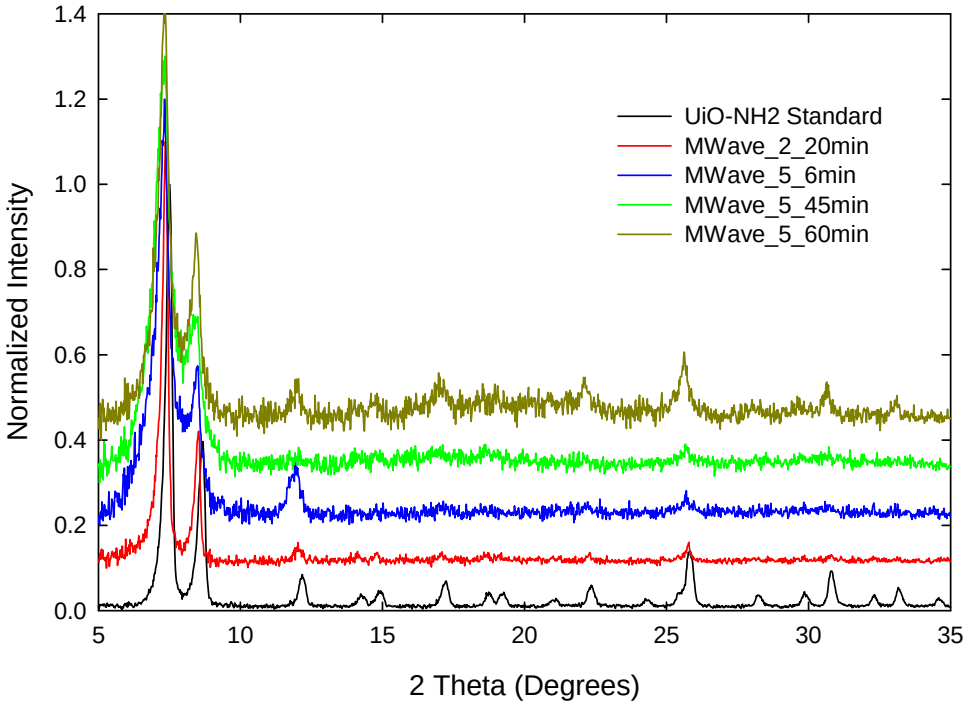

Figure A.3. UiO-66-NH_2 microwave-assisted syntheses pXRD comparison to standard synthesis. MWave_2_20min (Concentration ratio-2, synthesis time-20 min.)

A programmable microwave, MDS-2100 from CEM, capable of temperature and pressure control was procured and used for further attempts to synthesize amine-functionalized UiO-66.

A five-fold array of equimolar concentrations of $ZrCl_4$ and ATPA (5-25 mmol/L) as well as multiple synthesis times (6-60 min) were attempted at 393 K. pXRD was used to confirm the formation of the desired product, and BET modeling of N_2 adsorption for the optimal samples was planned. Figure A.3 illustrates some of the better pXRD results from the trials, but also shows the seemingly stochastic nature of microwave-assisted syntheses. For a singular trial at '5' concentration ratio higher angle XRD peaks originally formed by 6 min. disappear by 45 min. and reappear at 60 min. synthesis time.

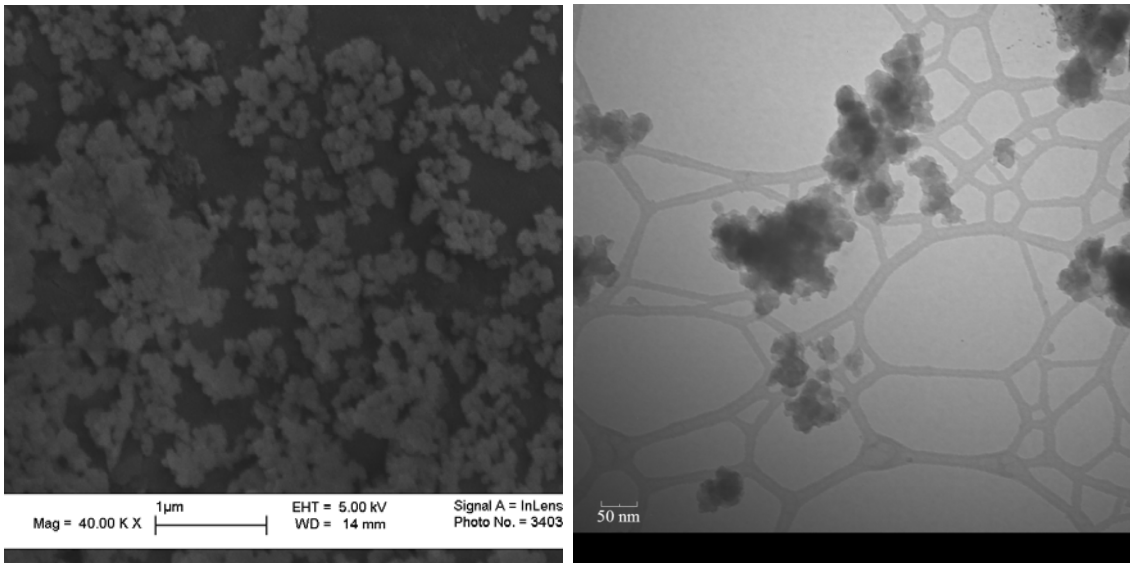

Figure A.4. UiO-66-NH_2 (4_60 min) microwave-assisted syntheses SEM (left) and TEM (right) results.

Two original samples, 4_60 min and 5_60 min were large enough (>/= 10 mg) for N_2 adsorption characterization, and BET modeling of the isotherms predicted 230 and 480 m^2/g, which is a significant reduction from the original product of ca. 1,000 m^2/g. Again true nanoMOF size particles are identified via SEM and TEM (Figure A.4). Further inconsistencies were noted while trying to recreate syntheses for surface area characterization. When the identical synthesis procedure was followed no obtainable product was formed. After evaluating possible sources of error including DMF and ATPA degradation or impurities, the inconsistencies were determined to be inherent to microwave-assisted synthesis itself.

Conclusions

The accelerated synthesis technique appears to propagate any experimental inconsistencies and produce lower quality crystals. Therefore, the current configuration was not considered a viable option for large scale high-throughput production.

References

1. Haque E, Khan NA, Park JH, Jhung SH. Synthesis of a Metal-Organic Framework Material, Iron Terephthalate, by Ultrasound, Microwave, and Conventional Electric Heating: A Kinetic Study. *Chem.-Eur. J.* 2010;16(3):1046-1052.

2. Khan NA, Haque MM, Jhung SH. Accelerated Syntheses of Porous Isostructural Lanthanide-Benzenetricarboxylates (Ln-BTC) Under Ultrasound at Room Temperature. *European Journal of Inorganic Chemistry.* Nov 2010(31):4975-4981.

3. Lee JS, Halligudi SB, Jang NH, Hwang DW, Chang JS, Hwang YK. Microwave Synthesis of a Porous Metal-Organic Framework, Nickel(II) Dihydroxyterephthalate and its Catalytic Properties in Oxidation of Cyclohexene. *Bulletin of the Korean Chemical Society.* Jun 2010;31(6):1489-1495.

4. Ni Z, Masel RI. Rapid Metal Organic Framework Molecule Synthesis Method. *United States Patent Application Publication.* 2009;11/785,102.

5. Parr. Models 4781 & 4782 Microwave Acid Digestion Vessels, 23 & 45 mL http://www.parrinst.com/products/sample-preparation/acid-digestion/microwave-acid-digestion-vessels-models-4781-4782-23-45-ml/. Accessed August 30th, 2012.

6. Cavka JH, Jakobsen S, Olsbye U, et al. A new zirconium inorganic building brick forming metal organic frameworks with exceptional stability. *Journal of the American Chemical Society.* Oct 2008;130(42):13850-13851.

7. SCSI FOCS. Vanguard V6500 Centrifuge. http://www.cecocablingsystems.com/centrifuge.htm. Accessed July 1st, 2010.

8. Patterson AL. The Scherrer formula for x-ray particle size determination. *Phys. Rev.* Nov 1939;56(10):978-982.

9. Spokoyny AM, Kim D, Sumrein A, Mirkin CA. Infinite coordination polymer nano- and microparticle structures. *Chem. Soc. Rev.* 2009;38(5):1218-1227.

10. Horcajada P, Chalati T, Serre C, et al. Porous metal-organic-framework nanoscale carriers as a potential platform for drug delivery and imaging. *Nature Materials.* Feb 2010;9(2):172-178.

APPENDIX B

THIN FIILM GROWTH OF UIO-66

Introduction

The array of reported MOFs can modify specific surface properties including electronic, optical, and wetting especially when present as an anchored thin-film. The coated surfaces can in turn be used in applications including catalysis, gas separation and sensing, as well as drug delivery. [1-3] With the demand for MOF thin-films now understood, recent research is targeted at synthesis method development. The methods can be categorized by substrate preparation and growth method.

Popular substrate preparation methods include using unaltered substrates, seeded-growth, and functionalized surfaces.[1] Sub-micron scale MOF seed crystals are deposited on substrates by methods including drop-wise techniques, dip coating, and spin-coating.[4] The complexity of the seed deposition method is often selected based on a desired orientation of the thin-films. Self-assembled monolayers, SAMs,[5] are used to anchor MOFs to the substrate and facilitate patterned film growth. SAMs are often deposited via a vacuum chamber and silane-based compounds. However, SAMs are also readily prepared by less hazardous organo-thiol deposition on Au surfaces, which can provide functional sites capable of tethering many MOFs including –COOH, $-CF_3$, and –OH.[6]

Multiple film-growth techniques are also currently reported. The first and most simplistic thin-film synthesis technique involves submersing a substrate in the reactant solution and conducting solvothermal synthesis identical to that for the powder.[6] Liquid phase epitaxy (LPE) is also implemented to produce MOF thin-films. Based on the layer-by-layer technique developed by Lanmuir and Blodgett,[7] LPE can reportedly

synthesize MOF thin-films of controlled thickness.[1] Electrochemical synthesis techniques similar to those used for high-throughput synthesis are also reported for HKUST-1 and MOF-5 film growth.[8] Other film-growth methods include gel-layer synthesis,[9] colloidal deposition method,[10] and microwave synthesis techniques.[11]

UiO-66 Thin-Film Growth

Utilizing the prior success synthesizing nano-crystals of UiO-66 (see Appendix A), seeded film growth was attempted. Seed crystals were thermally deposited while suspended in $CHCl_3$ in a drop-wise manor on Anopore™ aluminum oxide substrates. The substrate was heated to 100 °C under vacuum for ca. 5 minutes. Excess crystals were rinsed off with $CHCl_3$ and the process was repeated 3x until an visually even coating of crystals was observed. Then, the seeded substrate was placed in a 23 mL Parr acid digestion vessel[12] containing 15 mL of UiO-66 reactant solution. The substrate was orientated vertically to mitigate gravitational affect on the thin-film growth. The vessel was then subjected to the originally published[13] solvothermal synthesis procedure of heating at 393 K for 24 h. The substrate was removed and excess product was rinsed off with DMF.

The SEM image of UiO-66 thin-film (Fig. B.1) is from the best of three iterations of the above described procedure, and each trial resulted in more thorough coverage. However, significant cracks in the film were still present. Moderate deflection of the substrate was noted even during gentle handling and was a likely source of the film cracking. Other potential causes included thermal expansion coefficient differences between film and substrate, non-uniform seeding, and rapid cooling rates following synthesis.

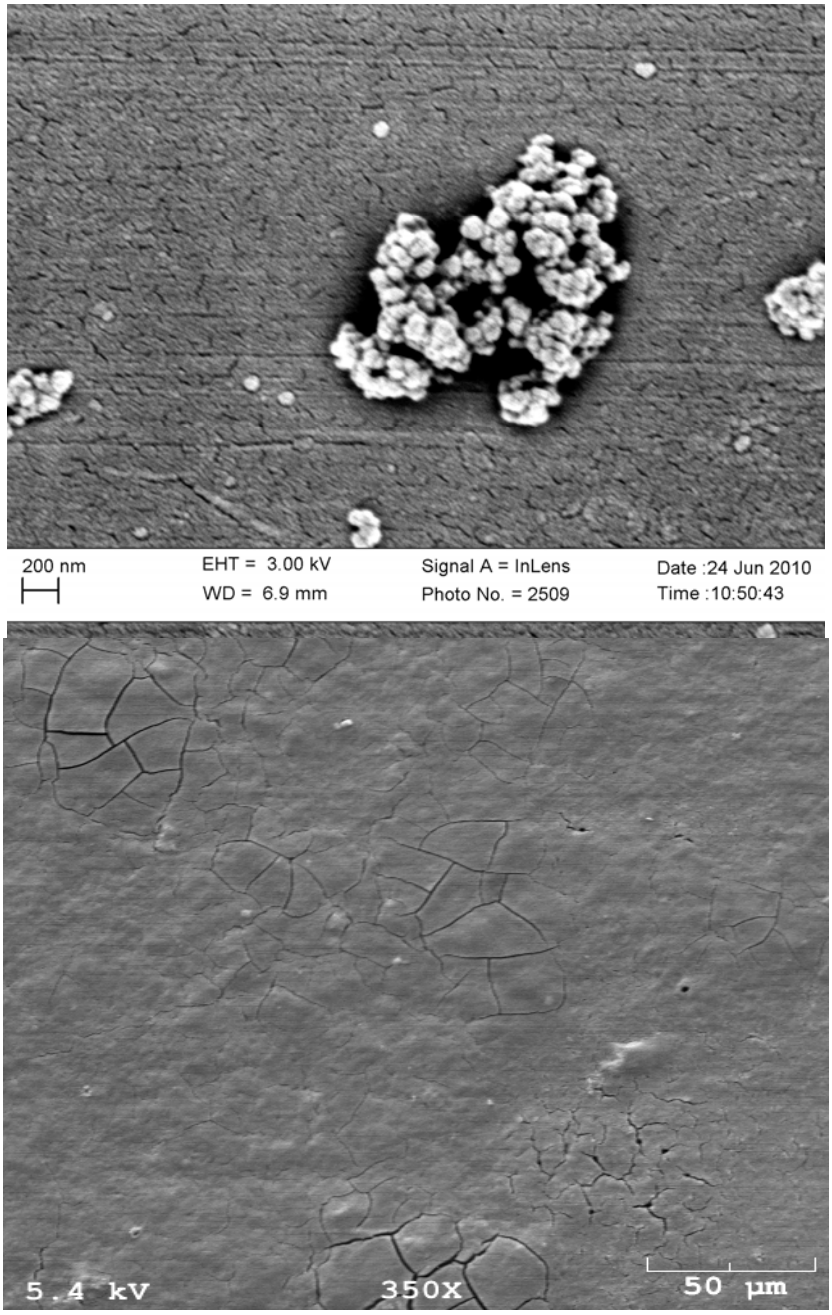

Figure B.1. SEM images of UiO-66 thin film (top) on Anopore Aluminum Oxide substrate and nano-MOF crystals from the microwave synthesis (bottom).

Conclusions and Recommendations

Numerous iterations would likely be required to provide a more uniform MOF coating. As mentioned in current literature and illustrated above MOF thin-films are often subject to cracking.[11] In attempt to alleviate the cracks, more rigid substrates could be implemented. The resulting films would provide direct conclusions about the substrate flexibility and its affect on the crack development. If more rigid substrates do not provide crack-free films, alternative drying and activation methods could be employed. For example, a slower drying process under a solvent-saturated environment may prevent crack formation. More sophisticated seed-crystal or precursor deposition methods may also be explored if crack problems still persist. The idea being that a more uniform layer of seed crystals may form a more uniform film and prevent cracking.

References

1. Shekhah O, Liu J, Fischer RA, Woll C. MOF thin films: existing and future applications. *Chem. Soc. Rev.* 2011;40(2):1081-1106.

2. Golzhauser A, Woll C. Out of the Vacuum-Through the Liquid Into the Cell. *ChemPhysChem.*11(15):3201-3213.

3. Ferey G. Some suggested perspectives for multifunctional hybrid porous solids. *Dalton Trans.* 2009(23):4400-4415.

4. Zacher D, Shekhah O, Woll C, Fischer RA. Thin films of metal-organic frameworks. *Chem. Soc. Rev.* 2009;38(5):1418-1429.

5. Allara DL, Nuzzo RG. Spontaneously organized molecular assemblies Formation, dynamics, and physical-properties of normal-alkanoic acids adsorbed from solution on an oxidized aluminum surface. *Langmuir.* 1985;1(1):45-52.

6. Hermes S, Schroder F, Chelmowski R, Woll C, Fischer RA. Selective nucleation and growth of metal-organic open framework thin films on patterned COOH/CF3-terminated self-assembled monolayers on Au(111). *Journal of the American Chemical Society.* Oct 2005;127(40):13744-13745.

7. Blodgett KB, Langmuir I. Built-up films of barium stearate and their optical properties. *Phys. Rev.* Jun 1937;51(11):0964-0982.

8. Ulrich Muller, Hermann Putter, Michael Hesse, et al. Method for Electrochemical Production of a Crystalline Porous Metal Organic Skeleton Material. *United States Patent Application Publication.* 2004;10/580,407.

9. Schoedel A, Scherb C, Bein T. Oriented Nanoscale Films of Metal-Organic Frameworks By Room-Temperature Gel-Layer Synthesis. *Angew. Chem.-Int. Edit.* 2010;49(40):7225-7228.

10. Horcajada P, Serre C, Grosso D, et al. Colloidal Route for Preparing Optical Thin Films of Nanoporous Metal-Organic Frameworks. *Adv. Mater.* May 2009;21(19):1931-1935.

11. Yoo Y, Varela-Guerrero V, Jeong HK. Isoreticular Metal-Organic Frameworks and Their Membranes with Enhanced Crack Resistance and Moisture Stability by Surfactant-Assisted Drying. *Langmuir.* Mar 2011;27(6):2652-2657.

12. Parr. Acid Digestion http://www.parrinst.com/products/sample-preparation/acid-digestion/. Accessed August 25th, 2012.

13. Cavka JH, Jakobsen S, Olsbye U, et al. A new zirconium inorganic building brick forming metal organic frameworks with exceptional stability. *Journal of the American Chemical Society.* Oct 2008;130(42):13850-13851.

APPENDIX C

NITRIC OXIDE DELIVERY VIA NONO-MOFS

Introduction

Nitric oxide (NO) is a gaseous free radical present in many biological processes. Following the discovery that NO and endothelium-derived relaxing factor (EDRF) are one in the same by Moncada et. al.[1] and Ignarro et. al.,[2] a surge in NO based research has occurred,[3] which leads to the discovery of a plethora of therapeutic properties associated with NO. NO plays an intricate role in many biological processes including anti-bacterial, anti-thrombotic, vasodilation, wound healing, and inflammation treatment. [4-7]

Due to the benefits of NO and the development of nanomaterials, much research is now aimed at creating agents capable of controlled release of NO to a targeted area.[6,8] Current prospective materials for NO delivery include silica and metal nanoparticles,[6,9] peptide-containing polymers,[10,11] and photoactive micelles.[12] Porous solids, such as MOFs, offer another viable option to store and deliver NO. Benefits of porous materials for NO delivery include lower pressures required to store the same quantity of NO, decreased potential for NO related safety problems, and easier handling. [13] With the nearly infinite set of structures available and the potential of post-synthetic modification, MOFs offer one of the most promising options for medical NO delivery.

Background of NO Delivery With MOFs

Some of the more promising MOFs are those containing open-metal sites or CUSs, which provide a preferential adsorption site for polar molecules such as NO. For example, HKUST-1 or Cu-BTC exhibits high adsorption capacity of NO at 298 K and 1

bar of 3 mmol/g. This is mainly due to the strong adsorption interaction, $\Delta H_{ads.}$ ca. 90 kJ/mol, between the open-metal sites and adsorbate molecules. However, the strong affinity for NO proves detrimental when examining the release of NO, and HKUST-1 is only capable of delivering ~1μmol/g of NO.[14] Other CUS containing MOFs, the Co and Ni forms of MOF-74, which are composed of the dihydroxy benzene dicarboxylate (DOBDC) ligand exhibit even higher uptakes of ~ 7mmol NO/g at 298 K and 0.8 bar and also show nearly complete release of the adsorbed NO when exposed to air at 11% RH. The release shows an initial 'burst' of NO from the phsysisorbed portion followed by a slower, sustained release of the chemisorbed portion.[15] In general, release of both phsysisorbed and chemisorbed NO from MOFs is very rapid, and complete release is often difficult due to strong binding energies.

Post-synthetic modification (PSM) of MOFs facilitates pore size and functional group adaptation to fit target applications. Recent developments in PSM show exposure of amine-functionalized MOFs to NO at 100 psig can yield diazeniumdiolate (NONOate) functionalized porous materials.[4] NONOates readily decompose when exposed to an aqueous environment releasing two moles of NO per equivalent mole of NONOate (Figure C.1). Therefore, the resultant MOF exhibits both NO storage properties as well as biologically triggered release capablities.

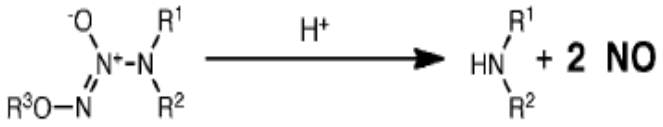

Figure C.1. NONOate degradation reaction in the presence of aqueous solutions.[4]

In an attempt to increase the amount of NO released by HKUST-1, Rosseinsky et al.[16] post-synthetically modification via gas phase addition of 4-methyl amino-pyridine (4-map). The resultant amine-functionalized MOF is exposed to NO to form a NONOate complex. More complete release of NO is observed versus the parent structure of HKUST-1, but 4-map is also reported to leach out of the MOF during release testing.[16] Cohen et. al. report successful post-synthetically modification (PSM) of two amine-functionalized MOFs, UMCM-1-NH_2 and IRMOF-3, which are based on the 2-amino terephthalic acid ligand. UMCM-1-NONO and IRMOF-3-NONO release 0.1 and 0.5 mmol NO/g respectively, which are an order of magnitude lower than those reported for Co and Ni-MOF-74. One possible interference source during the NO detection is the reported degradation of both MOFs in the presence of water. Also, the NONOate materials may still be capable of a more sustained release, which is not discernable using the chosen analysis method, Griess assay.[4]

Investigation of NONO-MOF Performance

Following the recent report from Cohen et al.[4] discussing the synthesis of NONOate-functionalized MOFs for NO delivery DMOF-1-NH_2 and UiO-66-NH_2 were examined for the same purpose. In order to gain further insight into the transport of NO from NONOate decomposition, the amine-containing ligand, 2-amino terephthalic acid (ATPA), of both prospective MOFs as well as two NONOate MOFs reported previously[4] was first examined for NO release potential. Synthesis of ATPA-NONO was attempted via the reported procedure of exposure to 100 psig of NO[4] for approximately 48 hours.

Color change from bright yellow of the parent ATPA to a light brown, potentially ATPA-NONO, was noted.

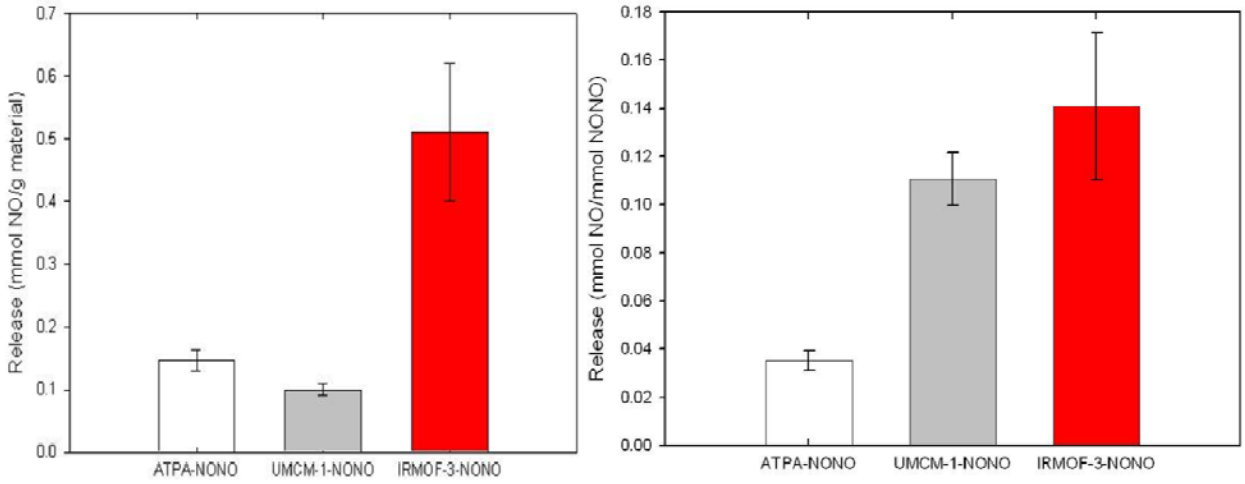

Figure C.2. Total NO release results (left) of ATPA-NONO compared to UMCM-1-NONO and IRMOF-3-NONO reported by Cohen et. al.[4] Normalized total release results (right) accounting for number NONOate sites per material.

Total release of NO from the ATPA NONO was monitored via the Griess assay. An often used NO detection technique, Griess assay used a buffer solution to promote nitrate, NO_3^-, formation from emitted NO, which was detectable with UV-Vis spectroscopy.[4,17] The experiment took place under simulated biological conditions of 37 °C and in PBS with a pH of 7.4. Three samples were collected after complete release was apparent, about 15 minutes, and NO concentrations were determined from a calibration curve collected immediately beforehand. Reliable examination of the release of phsysisorbed and chemisorbed NO requires minimal exposure to ambient air. Even low humidity levels, 11% RH, have been shown to trigger rapid

release of adsorbed NO in MOFs.[15,18] ATPA was not isolated from lab conditions. Therefore, the release reported was expected to be due to mainly NONOate degradation, which permits direct comparison to previously published NONO-MOF results.

Mass-based results showed ATPA-NONO releases 0.15 +/- 0.02 mmol NO/g, which is slightly higher than reported results of the mesoporous UMCM-1-NONO (Fig. C.2 (left)) and well below IRMOF-3-NONO.[4] MOF degradation, inadvertent release, and large pore size are potential sources of the poor performance of UMCM-1.[19] Also, when the release results are plotted on a mmol of NONO basis (assuming 100% conversion of amine sites to NONOates), the MOFs exhibit a three-fold increase in total NO released versus the ligand, ATPA-NONO (Fig. C.2 (right)). This directly demonstrates the benefits of using a porous media with amine-functionality for NO delivery versus non-porous amine-containing ligand. However, IRMOF-3-NONO and UMCM-1-NONO are not the best MOFs for NO delivery applications. Both exhibit instability in the presence of water, and UMCM-1-NONO is a meso-porous material with a relatively low number of possible NONOate sites per mass.[20]

With this in mind, post-synthetic modification of water stable MOFs, UiO-66-NH_2 and DMOF-1-NH_2, was attempted following an identical procedure of exposure to 100 psig of NO. Again, color change during the procedure was noted for both materials. Structure retention after NO exposure is verified using XRD, and complete peak position agreement is noted. PSM structure confirmation via IR spectroscopy of UiO-66-NH_2 before and after modification was inconclusive. However, from literature[4] we find that inability to detect identifying NONOate peaks does not predicate modification failure.

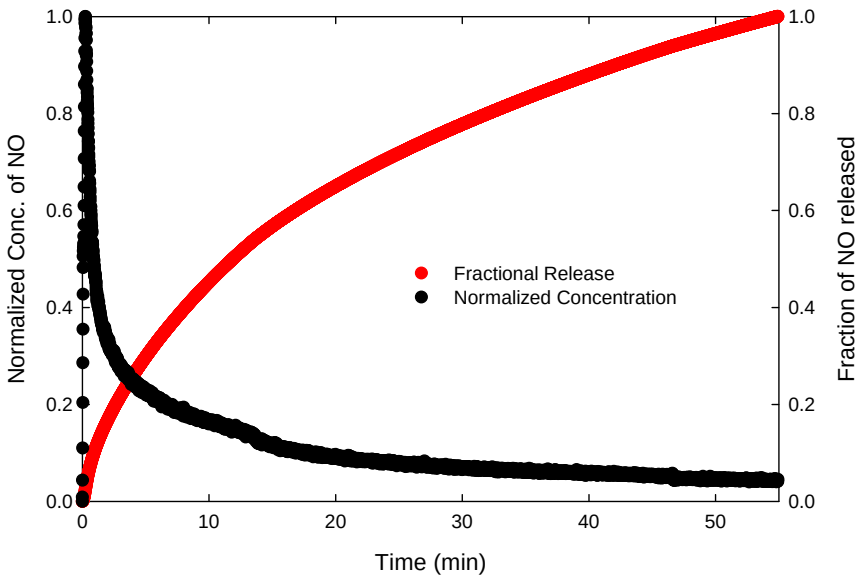

Figure C.3. Kinetic NO release of DMOF-1-NONO

In order to confirm that the desired kinetic release results are available for NONOate functionalized MOFs, samples of UiO-66-NONO, DMOF-1-NONO, and ATPA-NONO were stored under ambient conditions and shipped to GE Power & Water in Boulder, CO. A Sievers Nitric Oxide Analyzer (NOA 280i) was used to directly detect the released NO via ozone-chemiluminescence.[21] Preliminary kinetic release results were returned. Figure C.3 illustrates the most sustained released from preliminary kinetic studies, which is from DMOF-1-NONO. UiO-66-NONO showed virtually no release and ATPA-NONO showed a very quick release, which was completed within 3 minutes. A standard NO calibration was not collected, which precludes determination of NO flux or total amount release. As the poor performance of UiO-66-NH_2 illustrates, further iterations may be necessary to provide the optimum product consisting of the maximum fraction of NONOate to NH_2 functional sites. Also, minimizing the exposure to humid air is imperative for further NO release experiments.

References

1. Palmer RMJ, Ferrige AG, Moncada S. Nitric-oxide release accounts for the biological-activity of endothelium-derived relaxing factor. *Nature.* Jun 1987;327(6122):524-526.

2. Ignarro LJ, Byrns RE, Buga GM, Wood KS. Endothelium-derived relaxing factor (edrf) released from artery and vein appears to be nitric-oxide (no) or a closely related radical species. *Federation Proceedings.* Mar 1987;46(3):644-644.

3. Moncada S, Palmer RMJ, Higgs EA. Nitric-oxide - physiology, pathophysiology, and pharmacology. *Pharmacological Reviews.* Jun 1991;43(2):109-142.

4. Nguyen JG, Tanabe KK, Cohen SM. Postsynthetic diazeniumdiolate formation and NO release from MOFs. *Crystengcomm.* 2010;12(8):2335-2338.

5. Hinks NJ, McKinlay AC, Xiao B, Wheatley PS, Morris RE. Metal organic frameworks as NO delivery materials for biological applications. *Microporous Mesoporous Mat.* Apr 2010;129(3):330-334.

6. Seabra AB, Duran N. Nitric oxide-releasing vehicles for biomedical applications. *J. Mater. Chem.* 2010;20(9):1624-1637.

7. Lyons CR. The role of nitric oxide in inflammation. *Advances in Immunology, Vol 60.* Vol 60. San Diego: Academic Press Inc; 1995:323-371.

8. Frost MC, Reynolds MM, Meyerhoff ME. Polymers incorporating nitric oxide releasing/generating substances for improved biocompatibility of blood-contactincy medical devices. *Biomaterials.* May 2005;26(14):1685-1693.

9. Stevens EV, Carpenter AW, Shin JH, Liu JS, Der CJ, Schoenfisch MH. Nitric Oxide-Releasing Silica Nanoparticle Inhibition of Ovarian Cancer Cell Growth. *Molecular Pharmaceutics.* May-Jun 2010;7(3):775-785.

10. Taite LJ, Yang P, Jun HW, West JL. Nitric oxide-releasing Polyurethane-PEG copolymer containing the YIGSR peptide promotes endothelialization with decreased platelet adhesion. *J. Biomed. Mater. Res. Part B.* 2008;84B(1):108-116.

11. Jun HW, Taite LJ, West JL. Nitric oxide-producing polyurethanes. *Biomacromolecules.* 2005;6(2):838-844.

12. Caruso EB, Cicciarella E, Sortino S. A multifunctional nanoassembly of mesogen-bearing amphiphiles and porphyrins for the simultaneous photodelivery of nitric oxide and singlet oxygen. *Chem. Commun.* 2007(47):5028-5030.

13. Wheatley PS, Butler AR, Crane MS, et al. NO-releasing zeolites and their antithrombotic properties. *Journal of the American Chemical Society.* Jan 2006;128(2):502-509.

14. Xiao B, Wheatley PS, Zhao XB, et al. High-capacity hydrogen and nitric oxide adsorption and storage in a metal-organic framework. *Journal of the American Chemical Society.* Feb 2007;129(5):1203-1209.

15. McKinlay AC, Xiao B, Wragg DS, Wheatley PS, Megson IL, Morris RE. Exceptional behavior over the whole adsorption-storage-delivery cycle for NO in porous metal organic frameworks. *Journal of the American Chemical Society.* Aug 2008;130(31):10440-10444.

16. Ingleson MJ, Heck R, Gould JA, Rosseinsky MJ. Nitric Oxide Chemisorption in a Postsynthetically Modified Metal-Organic Framework. *Inorganic Chemistry.* Nov 2009;48(21):9986-9988.

17. Ignarro LJ, Fukuto JM, Griscavage JM, Rogers NE, Byrns RE. Oxidation of nitric-oxide in aqueous-solution to nitrite but not nitrate - comparison with enzymatically formed nitric-oxide from l-arginine. *Proc. Natl. Acad. Sci. U. S. A.* Sep 1993;90(17):8103-8107.

18. Liu HA, Balkus KJ. Novel Delivery System for the Bioregulatory Agent Nitric Oxide. *Chem. Mat.* Nov 2009;21(21):5032-5041.

19. Mu B, Schoenecker PM, Walton KS. Gas Adsorption Study on Mesoporous Metal-Organic Framework UMCM-1. *Journal of Physical Chemistry C.* Apr 2010;114(14):6464-6471.

20. Schoenecker PM, Carson CG, Jasjuja H, Flemming CJJ, Walton KS. Effect of Water Adsorption on Retention of Structure and Surface Area of Metal-Organic Frameworks *Ind. Eng. Chem. Res.* 2012.

21. GE Analytical Instruments, Inc. Sievers, Nitric Oxide Analyzer (NOA 280i). 2010.

APPENDIX D

RAW DATA

All reported pXRD data are available as .xrdml files on the Walton Group shared folder under the following extension: research\Walton group\Experimental Data\pXRDs_PMS_2012

Chapter 3: Toxic industrial chemical adsorption using MOFs

Mg MOF-74 CO_2 Uptake

Mg MOF-74 (Loaded 'Wet')

Uptake(wt%)	Pressure (mbar)
000.515930	004.596
011.111330	024.642
023.108970	110.703
026.323410	213.336
028.146800	315.701
029.387420	409.781
030.528950	517.359
031.534730	618.388
032.462100	722.357
033.209970	814.031
034.056620	919.203
034.664300	1001.256
035.356270	1100.013
035.356270	1100.013
034.664520	994.707
033.226320	798.797
031.566860	598.743
029.596380	397.754
026.834650	197.834
002.753090	004.596

Mg MOF-74 (Loaded 'Dry')

P(mbar)	Uptake (wt%)
3.527	0.00
32.392	2.78
225.898	5.43
423.546	7.27
618.789	8.60
819.243	9.63
1017.693	10.34

Chapter 4: Water stability of MOFs

Water Adsorption at 298 K

UIO-66-NH2

%RH	mol/kg
0.0000	0.0000
6.4000	3.8017
11.2630	6.5056
16.0860	10.9904
20.9540	16.3643
25.8080	18.1469
30.6480	18.7927
40.3570	19.6089
50.0240	20.1966
59.7200	20.7028
69.4160	21.2813
79.1230	21.5803
88.7740	21.8949
79.1200	21.6310
59.7180	21.0242
40.3530	20.2118
20.9510	17.9422
0.0000	2.8425

UIO-66

%RH	mol/kg
0.0000	0.0000
11.2280	1.2698
20.9300	3.4024
30.6140	18.4395
40.3360	19.4738
50.0120	20.1788
59.7080	20.6904
69.4050	21.1420
79.1160	21.6471
88.7870	25.1501
79.1150	24.5953
59.6870	23.6849
40.3360	20.2934
20.9240	8.4400
0.0000	1.6556

CUBTC

mol/kg	%RH
0.0000	0.0000
16.5618	11.2550
22.7995	20.9480
24.4762	30.6430
25.0869	40.3760
25.5960	50.0400
26.1094	59.7230
28.4738	69.4220
28.7484	79.1220
32.6065	88.7910
32.0151	79.1330
31.2262	59.7540
29.5661	40.3510
22.5288	20.9410
3.0332	0.0000

DMOF-1-NH2

mol/kg	%RH
0.0000	0.0000
1.5866	11.2750
2.3735	20.9530
2.9351	30.6620
3.5276	40.3760
3.8499	50.0550
4.6786	59.7320
5.4280	69.4180
6.3113	79.1190

UMCM-1

%RH	mol/kg
0.0000	0.0000
11.2610	1.6288
20.9400	2.4390
30.6510	3.1221
40.3540	3.7970
50.0430	4.9950
59.7310	5.9339
69.4260	6.9728
79.1120	9.7691
88.8140	13.5189

Mg-MOF-74

mol/kg	%RH
0.0000	0.0000
29.1675	6.4090
29.8918	11.2710
30.7343	16.0810
31.4638	20.9570
32.1528	25.7970
32.6999	30.6340
33.6393	40.3560
34.5299	50.0470
35.2292	59.7010
35.8529	69.4080
36.3161	79.1110
36.7340	88.7770
36.4320	79.0900
35.8561	59.7160
34.9174	40.3450
33.1674	20.9380
6.1444	0.0000

DMOF-1

mol/kg	%RH
0.0000	0.0000
0.1081	10.6250
0.2084	20.4910
3.4295	30.3350
4.7058	40.1820
2.4052	59.8610
2.4835	79.5420
2.5929	89.3810
2.5929	89.3810
2.4973	79.5330
2.4144	59.8660
2.3587	40.1830
2.2791	20.5120
2.1111	0.0000

	Vol. Soln. cc	Yield g	cm2/cc	gMOF/L soln
PTFE	66.0000	0.6104	1.1623	9.2485
PTFE	65.0000	0.6258	1.1655	9.6277
PTFE	25.0000	0.2284	1.7963	9.1360
PTFE	12.0000	0.1148	2.0091	9.5667
PTFE	10.0000	0.0855	2.0909	8.5500
Glass	153.0000	1.4889	0.8826	9.7314
Glass	103.0000	0.8900	0.9579	8.6408
Glass	101.0000	0.9887	0.9625	9.7891
Glass	196.0000	1.7160	0.8485	8.7551
Glass	10.0000	0.0720	2.1041	7.2000
Glass	15.0000	0.1356	1.9469	9.0400
Glass	20.0000	0.1706	1.8684	8.5300
Glass	5.0000	0.0414	2.5755	8.2800
Glass	20.0000	0.1615	1.8684	8.0750
Glass	10.0000	0.0945	2.3142	9.4500
Glass	14.9000	0.1256	2.2108	8.4295
Glass	20.0000	0.1681	2.1571	8.4050
Glass	8.0000	0.0672	2.3927	8.4000
Glass	15.0000	0.1237	2.2094	8.2467

120C

Time (h)	Yield (g/L)		
4.0000	1.6200	1.6600	1.5200
8.0000	2.5100	2.7300	2.5100
12.0000	2.5500	2.7000	2.4500
16.0000	2.3500	2.5100	2.4000
20.0000	2.7300	2.6600	2.4600
24.0000	2.5800	2.6000	2.6900
28.0000	2.8000	2.7100	2.5100

110C

Time(h)	Yield (g/L)		
4.0000	0.0000	0.0000	0.0000
8.0000	1.6300	1.7900	1.6100
12.0000	2.4100	2.3100	2.4200
16.0000	2.5600	2.4100	2.4100
20.0000	2.5100	2.6900	2.3800
24.0000	2.6200	2.5800	2.6500
28.0000	2.6900	2.5400	2.5300
32.0000	2.4800	2.6100	2.6300
36.0000	2.7300	2.5600	2.6200
40.0000	2.5200	2.5700	2.4300

100C

Time(h)	Yield (g/L)		
4.0000	0.0000	0.0000	0.0000
8.0000	0.3500	0.4000	0.2800
12.0000	1.0000	1.2000	1.0600

16.0000	1.3500	1.2200	1.2800
20.0000	1.9800	1.8300	2.0200
24.0000	2.0000	2.0100	1.8700
28.0000	2.1100	2.4300	2.3100
32.0000	2.6600	2.4300	2.4100
36.0000	2.5300	2.4000	2.7000
40.0000	2.6300	2.5900	2.4700

Chapter 6: Flow-through synthesis optimization

Yield Data

Trial	**2.1**	**2.2**	**3.1**	**3.2**	**3.3**	**4.1**
Tau (/12 h)	**Yield (g/L)**					
1.0000	0.0000	2.3100	0.9132	0.3567	0.3250	0.0550
2.0000	0.0410	2.9545	0.1916	1.7917	0.9633	0.1217
3.0000	0.0000	3.0368	0.2205	1.2717	2.3383	0.2483
4.0000	0.0000	2.9600	0.0464	0.2067	3.3583	1.1726
5.0000	1.9455	3.7571	0.0566	0.7767	0.1900	0.4417
6.0000	1.7250	0.6889	0.0263	1.0267	1.4967	0.3636
Reactor	0.0830	3.8830	0.5570	3.3170	1.5067	0.5858

pXRD-fit analysis

	XRD Quantification				# of peaks	
	5-35 Degrees 2 theta cif file has				19	
	Original UIO-NH2 sample has				19	
	# of Peaks					
	2.1	2.2	3.1	3.2	3.3	4.1
3 tau	2	1	12	15	4	10
4 tau	1	2	2	12	16	14
5 tau	3	2	9	11	16	16
6 tau	1	2	19	4	8	10
Average Value	1.75	1.75	10.5	10.5	11	12.5
Relative Peak Agreement						
Average Value	0.09	0.09	0.55	0.55	0.58	0.66

ZIF-65 Scale-Up Data

120C			
Time (h)	Yield (g/L)		
0.0000	2.7100	2.7100	2.7100
6.0000	9.5100	9.5800	9.3000
12.0000	7.6800	7.5400	7.3400
24.0000	5.0800	5.2600	5.3900
36.0000	4.8800	4.8600	4.9500
48.0000	4.1200	4.0800	
60.0000	4.2900	4.0600	4.0500
72.0000	3.9400	3.8100	3.8800

110C			
Time(h)	Yield (g/L)		
0.0000	2.7100	2.7100	2.7100
6.0000	6.6200	6.3300	5.9400
12.0000	9.3500	9.5300	9.9700
24.0000	9.5400	9.6900	9.3200
36.0000	7.7800	7.6000	7.7800
48.0000	6.5100	6.6500	6.1800
60.0000	6.5100	6.6900	6.3300
72.0000	6.3700	6.1000	6.4800

100C			
Time(h)	Yield (g/L)		
0.0000	2.7100	2.7100	2.7100
6.0000	3.2500	3.3800	
12.0000	5.7700	6.4000	6.4100
24.0000	10.2700	10.4200	9.9600
36.0000	10.2200	10.3900	10.6000
48.0000	9.5300	9.3800	9.4600
60.0000	9.4000	9.1600	9.4100
72.0000	8.7900	8.7200	7.9500

MIL-125-NH_2 Scale-Up Data

MIL-125_NH2					
Name	Material	Vol (cc)	Yield (g)	SA/V(1/cm)	Normalized Yield (g/L)
PI	PTFE	85	1.2931	1.1154	15.2129
PII	PTFE	50	0.7571	1.2295	15.142
P1	PTFE	12	0.1817	2.0091	15.1417
HG	PTFE	18	0.289	1.8727	16.0556
_3	PTFE	20	0.3227	1.8454	16.135

P2	PTFE	31	0.4384	1.7583	14.1419
_9	Glass	5	0.0735	3.2145	14.7
_10	Glass	3	0.029	3.4111	9.6667
_7	Glass	21	0.3105	1.8337	14.7857
_5	Glass	23.5	0.3392	2.1512	14.434
_6	Glass	15	0.2272	2.2255	15.1467
J1	Glass	100	1.5175	0.9649	15.175
J2	Glass	204	3.0369	0.8437	14.8868
J3	Glass	50	0.7541	1.2024	15.082
J4	Glass	400	5.8805	0.7867	14.7013

120C

Time (h)	Yield (g/L)		
0.0000	0.0000	0.0000	0.0000
4.0000	17.6100	16.4900	15.3600
8.0000	19.2000	18.9200	18.5700
12.0000	18.6200	17.3000	
24.0000	18.3300	18.8000	18.0300

110C

Time(h)	Yield (g/L)		
0.0000	0.0000	0.0000	0.0000
4.0000	17.4700	15.9700	17.5900
8.0000	16.1000	18.5100	18.3000
12.0000	17.4000	17.7800	
24.0000	17.0900	19.4600	

100C

Time(h)	Yield (g/L)		
0.0000	0.0000	0.0000	0.0000
4.0000	15.2000	15.2800	15.1900
8.0000	14.7800	17.9000	17.3700
12.0000	17.9400	17.9800	19.9800
24.0000	15.9900	18.1400	18.1600

Mg MOF-74 Scale-Up Data

Mg MOF74

Sample Name	Material	Yield (g)	Normalized Y(g/L)	SA/V (1/cm)	Vol. of Soln. Added (cc)
PI	PTFE	0.0795	1.9875	1.2987	40
PII	PTFE	0.1633	2.1773	1.1371	75
P1	PTFE	4.00E-04	0.08	2.5817	5

P3	PTFE	0.033	1.5	1.8231	22
HG	PTFE	0.0126	0.84	1.9272	15
_1	Glass	0.0124	3.1	3.2882	4
_2	Glass	0.021	3.2308	3.1465	6.5
_3	Glass	0.0569	3.7933	1.9272	15
_4	Glass	0.0371	3.5	2.3107	10.6
_6	Glass	0.0523	5.5053	2.3443	9.5
_7	Glass	0.0793	5.2867	2.2255	15
_8	Glass	0.7733	3.8665	0.8461	200
_9	Glass	1.597	3.9925	0.7867	400
_10	Glass	0.1718	3.436	1.2024	50
_11	Glass	0.4329	3.7643	0.9339	115

125 C

Time (h)	Normalized Yield (g/L)		
0.0000			
6.0000	0.8000	0.3200	0.7600
8.0000	2.0700	2.2700	1.9300
10.0000	3.1800	3.3000	3.2300
12.0000	3.1900	3.2700	3.5600
16.0000	3.6000	3.2400	3.5700
20.0000	4.1900	3.7500	3.6000
24.0000	3.7400	4.0100	4.1500
28.0000	4.0000	4.3400	3.9400

115 C

Time(h)	Normalized Yield (g/L)		
0.0000	0.0000	0.0000	0.0000
6.0000	0.0000	0.0000	0.0000
8.0000	0.0000	0.0000	0.0000
10.0000	0.6500	0.9600	1.2200
12.0000	2.1600	2.1300	1.4900
16.0000	2.6500	3.0700	3.1600
20.0000	3.0300	3.9800	1.6800
24.0000	3.7600	3.5400	3.6500
28.0000	4.0200	3.0200	3.9800

105 C

Time(h)	Normalized Yield (g/L)		
0.0000	0.0000	0.0000	0.0000
6.0000	0.0000	0.0000	0.0000
8.0000	0.0000	0.0000	0.0000
10.0000	0.0000	0.0000	0.0000
12.0000	0.0000	0.0000	0.0000

16.0000	1.2300	1.2400	1.5500
20.0000	1.7800	2.1500	1.7200
24.0000	2.9700	3.2200	1.5300
28.0000	2.6400	2.3500	1.9800

Chapter 8: ZIF-65 (SOD) adsorption and stability

Water adsorption data

Weight	MFC_A	Uptake wt%	Uptake mmol/g
42.1621	0	0	0
42.201	6.377	0.0923	0.0512
42.2083	11.223	0.1095	0.0608
42.2854	16.097	0.2924	0.1623
42.3297	20.955	0.3975	0.2207
42.3797	25.804	0.516	0.2864
42.4183	30.668	0.6076	0.3373
42.518	40.349	0.844	0.4685
42.6414	50.034	1.1367	0.631
42.9159	59.72	1.7879	0.9925
44.0347	69.413	4.4414	2.4654
46.4113	79.102	10.0782	5.5943
46.9037	88.775	11.246	6.2426
46.5733	79.083	10.4624	5.8076
44.1578	59.7	4.7333	2.6274
43.0611	40.346	2.1322	1.1836
42.6803	20.939	1.229	0.6822
42.4041	0	0.5738	0.3185

Single gas adsorption data

Nitrogen

25 C P (mbar)	Weight (mg)	mmolN2/g	**35 C** P (mbar)	Weight (mg)	mmolN2/g	**45 C** P (mbar)	Weight (mg)	mmolN2/g
0	27.4806	0	0	27.4885	0	0	27.4837	0
20.452	27.482	1.77E-03	16.977	27.4963	0.0101	20.452	27.494	0.0135
24.327	27.4819	1.64E-03	23.793	27.4967	0.0106	25.797	27.4928	0.0119
57.736	27.4848	5.44E-03	49.451	27.4983	0.0127	55.331	27.4945	0.0141
111.859	27.4888	0.0106	98.496	27.5011	0.0163	106.915	27.496	0.0161
211.953	27.4966	0.0208	204.068	27.5075	0.0246	208.612	27.5006	0.022
403.721	27.5083	0.036	407.195	27.519	0.0395	407.73	27.5096	0.0337
603.373	27.5214	0.053	604.042	27.5291	0.0527	605.378	27.5185	0.0452
808.372	27.5357	0.0716	801.957	27.5399	0.0668	802.625	27.527	0.0564
1005.084	27.5486	0.0883	999.739	27.5508	0.0808	1004.149	27.535	0.0667
2000.675	27.6081	0.1656	2000.942	27.5984	0.1427	2001.209	27.5738	0.1171
2997.868	27.6616	0.2352	2999.339	27.6469	0.2057	2996.265	27.6128	0.1678
3994.662	27.7105	0.2987	3998.537	27.687	0.2578	3997.869	27.6608	0.2301
5993.994	27.7995	0.4143	5996.935	27.7746	0.3716	5997.603	27.7362	0.328
7993.461	27.8784	0.5168	7994.53	27.851	0.4708	7998.672	27.8038	0.4158
9992.526	27.9491	0.6086	9993.729	27.916	0.5552	9994.798	27.869	0.5006
13997.34	28.0743	0.7714	13995.73	28.0371	0.7125	13996.27	27.9866	0.6533
19987.05	28.2227	0.9641	19998.28	28.1854	0.9051	19998.94	28.1402	0.8529
14997.21	28.0937	0.7966	14987.18	28.0676	0.7521	15004.96	28.0398	0.7225
11992.26	28.0166	0.6963	11983.71	27.9805	0.6389	11987.98	27.9373	0.5893
7998.806	27.8791	0.5177	7998.806	27.8469	0.4655	7983.17	27.8134	0.4283
5999.607	27.8044	0.4206	5997.603	27.7698	0.3653	5999.607	27.7411	0.3344
3998.938	27.7125	0.3013	3998.136	27.6815	0.2506	3998.938	27.6705	0.2427
2000.407	27.61	0.1681	1999.205	27.5927	0.1353	2000.274	27.579	0.1239
999.338	27.551	0.0914	1000.14	27.5438	0.0717	998.536	27.5429	0.0769
496.732	27.5177	0.0482	496.865	27.5145	0.0337	498.87	27.5221	0.05
248.035	27.5014	0.027	248.836	27.5006	0.0157	248.569	27.5107	0.0352
98.095	27.4911	0.0137	97.56	27.4919	4.35E-03	98.095	27.5036	0.026
0	27.4867	0	0	27.4829	0	0	27.4837	0

Carbon Dioxide

25C P (mbar)	Weight (mg)	mmol CO2/g	**35 C** P (mbar)	Weight (mg)	mmol CO2/g	**45C** P (mbar)	Weight (mg)	mmol CO2/g
0	27.5025	0	0	27.5043	0	0	27.4937	0
17.245	27.5394	0.0305	20.185	27.5381	0.0279	15.641	27.52	0.0218
29.673	27.569	0.0549	28.069	27.5527	0.04	27.535	27.5352	0.0342
51.99	27.6172	0.0948	53.193	27.5949	0.0748	52.792	27.5668	0.0604
103.173	27.7262	0.1849	100.901	27.6731	0.1394	99.966	27.6237	0.1074
201.796	27.9182	0.3435	208.478	27.8344	0.2727	208.077	27.7475	0.2097
400.246	28.262	0.6275	407.329	28.1032	0.4947	409.066	27.9539	0.3803
603.24	28.5551	0.8696	604.175	28.3307	0.6827	604.576	28.1313	0.527
815.722	28.8114	1.0814	806.634	28.5331	0.8499	813.182	28.3006	0.6669
1002.812	29.0065	1.2426	1009.093	28.7085	0.9948	1020.051	28.4516	0.7916
2002.278	29.7173	1.8299	2006.555	29.3496	1.5244	2005.753	29.0287	1.2686
2999.472	30.1536	2.1904	3010.297	29.7774	1.8779	3006.689	29.4194	1.5915
4005.754	30.4639	2.4467	4001.878	30.0892	2.1354	4004.15	29.7202	1.8401
6004.685	30.8869	2.7962	5993.059	30.5199	2.4913	5998.671	30.148	2.1936
7998.94	31.1887	3.0455	7999.341	30.8365	2.7528	7996.534	30.4839	2.4712
9994.932	31.4249	3.2406	9996.936	31.0735	2.9486	9998.94	30.7367	2.6802
13984.91	31.8094	3.5583	13995.2	31.448	3.258	14003.75	31.1353	3.0096
19990.79	32.3581	4.0117	20000.01	31.882	3.6166	19997.07	31.601	3.3944
14986.65	31.8717	3.6098	15000.95	31.5077	3.3073	15003.22	31.2296	3.0875
11998.14	31.6314	3.4113	11995.07	31.2637	3.1058	11995.07	30.9727	2.8752
7998.806	31.189	3.0458	7993.728	30.8274	2.7453	7991.59	30.5073	2.4906
5994.262	30.9051	2.8112	5999.607	30.5199	2.4913	5993.994	30.1741	2.2152
3998.804	30.4781	2.4584	3999.74	30.0825	2.13	3998.404	29.7279	1.8464
1999.605	29.746	1.8535	2001.075	29.3433	1.5193	1999.605	29.0159	1.258
999.605	29.0323	1.2639	998.67	28.6972	0.9855	997.868	28.446	0.787
498.202	28.4452	0.7788	499.538	28.209	0.5821	499.404	28.0507	0.4603
248.836	28.0346	0.4396	247.901	27.8866	0.3158	246.965	27.8021	0.2549
98.496	27.7343	0.1916	99.03	27.6632	0.1312	98.362	27.6344	0.1163
0	27.5094	0	0	27.4963	0	0	27.5044	0

Henry's Law Constants for ZIF-65

.

IAST 25C

Partial P (mbar)	Pressure mbar	CO2 Uptake (mmol/g)	N2 Uptake (mmol/g)	Kco2	Kn2
0	0	0	0		
0.5	1	7.00E-04	0	0.0014	0
50.5	101	0.0646	2.30E-03	0.1278	0.0046
100.5	201	0.1218	4.30E-03	0.1144	0.004
150.5	301	0.1748	6.20E-03	0.106	0.0038
200.5	401	0.2247	8.00E-03	0.0998	0.0036
250.5	501	0.272	9.70E-03	0.0946	0.0034
300.5	601	0.3172	0.0113	0.0904	0.0032
350.5	701	0.3606	0.0129	0.0868	0.0032
400.5	801	0.4022	0.0144	0.0832	0.003
450.5	901	0.4424	0.0158	0.0804	0.0028
500.5	1001	0.4812	0.0172	0.0776	0.0028

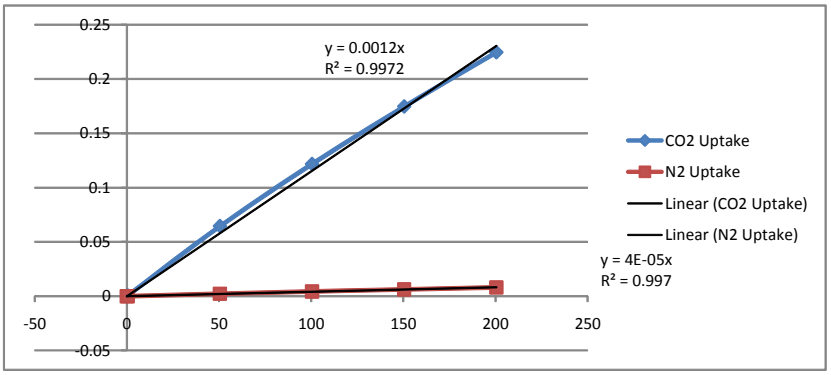

ATCl et al. 2012

Partial P (mbar)	P (mbar)	CO2 Uptake (mol/u.c.)	CO2 (mmol/g)	KCo2
0	0	0	0	0.001769
50	100	0.83	0.088442623	0.001215
100	200	1.4	0.149180328	0.001705
150	300	2.2	0.23442623	
1000	6.1	0.65	0.65	
			Converted by hand from .cif file info	
	6.111111111		0.106557377	
	(from estimating plot)			
	0.833333333			
	1.388888889			
	2.222222222